SEDIMENTOLOGY AND GEOCHEMISTRY OF REGRESSIVE AND TRANSGRESSIVE SURFACES IN THE GUNFLINT FORMATION, NORTHWESTERN ONTARIO

CHRISTOPHER IRA YIP

Submitted in partial fulfilment
of the requirements for the degree of

Master's of Science

Department of Geology
Lakehead University
Thunder Bay, ON
June 2016

1 ABSTRACT

The 1.878 Ga Gunflint and equivalent iron formations of the Animikie Basin were deposited during the period after the rise in atmospheric oxygen during the Great Oxidation Event, which began at approximately 2.4 Ga. The atmospheric composition, and especially oxygen content, during this period after the rise in atmospheric oxygen, is not well known. The Gunflint and correlative formations, having been deposited in a shallow-marine setting, might provide information on oxygen levels present in the atmosphere-ocean system at this time. This is further made possible as the rocks that make up these formations are excellent records of transgression and regression of the sea. This record is reflected in up-section changes in lithology of the rocks that make up these formations. Further, the strata show evidence of exposure indicative of maximum regression. This exposure would have allowed the sediments and rocks to interact chemically with the atmosphere and meteoric water at the time.

Stromatolites developed in the near-shore deposits and the rocks upon which the stromatolites grew show evidence of exposure during the repeated relative sea level low stands. These rocks have an alteration pattern that depends on their lithology. The rocks that comprise the Archean crystalline basement below the Gunflint show an intense alteration pattern that includes the formation of large corestones as well as increases in Fe and Mn content. Their geochemistry is largely the result of alteration by basin derived fluids. The exposure surfaces in the grainstones that make up the Gunflint and equivalent formations exhibit cementation and brecciation of the grainstones directly beneath the stromatolites.

Geochemical analysis performed on these rocks targeted the concentration of redox sensitive oxides and elements; Fe_2O_3, MnO, V, Cr, Mo and U. Also considered were the Ce and

Eu anomalies present. These oxides and elements react differently in oxidizing vs. reducing fluids. Subsequently, this analysis showed a shift in the Ce anomaly throughout the stratigraphy. The change from negative Ce anomalies in the basal samples to the positive Ce anomalies in the middle and upper lowstand layers indicate a shifting redox boundary, where the lowest stromatolite layers had produced enough oxygen to balance the flux of Fe^{2+}- rich seawater in a position away from them, whereas the middle and upper stromatolite areas had redox boundary at the surface of the stromatolite themselves. Enrichment in Cr and V, as well as depleted Eu anomalies in strata associated with lowstands, points to the mixing of oxic freshwater, probably a combination of surface runoff from the craton and diffusion of groundwaters, and the anoxic seawaters filling the basin.

2   TABLE OF CONTENTS

3 LIST OF FIGURES

x

4   LIST OF TABLES

5 ACKNOWLEDGEMENTS

I first would like to extend my biggest thank you to my advisor Dr. Philip Fralick, whose advice, guidance, support and patients has been invaluable throughout this process. Next thank you to my anonymous external editor, your edits and advice on my thesis have been much appreciated.

Next, I would like to thank the Lakehead Geology faculty members. Your knowledge and passion for sharing this knowledge has been inspiring to me during my time at Lakehead.

Anne Hammond, Kristi Tavener, Matt Svensson and the technicians down at LUIL; thank you for all your help from sample prep to analysis.

Lastly, to my family and friends you are far too numerous to list but your love and support throughout this time has meant the world to me

Thank You All!

1. INTRODUCTION

BIFs have often been described as bizarre or unusual rocks, and correspondingly exceptional conditions have been advanced to explain their presence in the stratigraphic record

-Trendall (2002)

1.1   Iron Formations

The chemical sediments comprising large- scale banded iron formation are among the principal sources of the global iron supply. Deposits around the world have been classified by James (1966) as rocks with ≥ 15 wt% metallic iron. Iron formations (IF) are commonly thinly laminated, mostly comprised of chert, and fundamentally different from the generally younger ironstones, which are more aluminum-rich and less- laminated. The largest deposits formed during the Precambrian from the Late Archean-to-Paleoproterozoic (Figure 1). There are two main classifications for the Precambrian iron formations, "Superior-type" and "Algoma-type" deposits. The "Algoma-type" iron formations were formed in deep water environments near vents sites, whereas the Superior-type IFs were formed in shallow water environments (Ohmoto, 2002). There are three major basins in which Superior-type iron formations have been deposited, as well as some smaller basins. These are the Hamersly Basin in Australia, the Transvaal System in South Africa and the North American circum-Superior Labrador Trough - Animikie Basin. Due to the lack of modern analogies to Superior type iron formation there is currently no consensus on the depositional chemistry, as well as the paleogeographic and paleoclimatic significance during deposition. James (1954) has divided the Precambrian Superior-type iron formations into four distinct stratigraphic unit, which are all based on the mineralogy of the iron-bearing mineral; sulfide, carbonate, oxide, and silicate. The sulfide stratigraphic unit are represented by the occurrence of pyritic carbonaceous slate. The carbonate stratigraphic unit of

the Superior-type iron formations are defined by a majority of iron carbonate, either ankerite or siderite. Oxide stratigraphic unit are either comprised of hematite or magnetite-rich rocks.

The large-scale Precambrian banded iron formations are present in all continents around the world. They have an intriguing temporal distribution. The oldest IF is about 3.8 Ga and present in some of the oldest cratons and greenstone belts such as the Isua BIF in Greenland. The majority of the large iron formations start to appear at approximately 2.8 Ga; these are present in supra-crustal sequences including greenstone belts, mostly from the continents of Gondwana (Trendall, 2002). The rise in the iron formations around this time coincides with the appearance of photosynthetic oxygen (Nisbet et al., 2007; Fralick and Riding, 2015), which allowed the precipitation of dissolved ferrous Fe in the oceans. A subsequent rise in iron formation abundance at approximately 2.5 Ga can be linked to the dramatic increase in oxygen immediately prior to and during the Great Oxidation Event (GOE). Deposition of massive iron formations in the shallows of the oceans continued sporadically until about 1.8 Ga when the oceans, or at least their near-shore areas, became euxinic and increasing sulphur content in shelf areas allow it to overwhelm the REDOX system and to banish oxide stratigraphic unit iron formation to the deeper areas of the ocean (Canfield, 1998; Poulton et al., 2004; 2010; Kendall et al., 2011).

There is no agreed upon model for the formation of the large-scale iron formations due to the lack of modern analogs. We know that at the time of iron formation deposition the oceans were enriched in both iron and silica, but the sources of these two are one of the questions plaguing researchers. Early models for iron formation deposition and source of iron and silica, include Dimroth (1976) who noticed that granular iron formations were deposited in a distinctive manner similar to that of modern carbonate environments and concluded that they must have

been deposited in carbonate environments, in which the silica and iron were derived by wholescale diagenetic replacement of the carbonates (Dimroth, 1968; Dimroth 1976; Dimroth and Chaivel, 1978). Others who advocated this model include Kimberly (1974), and to a limited extent, Sommers et al. (2000). This model has been dismissed due to the presence of textural features such as dehydration cracks found by Simonson (1987), as well as the lack of carbonate deposits that show a progressive, large-scale change to iron and silica. Other rejected hypotheses include deposition in lacustrine or non-marine environments that were originally championed by researchers, i.e., Hough (1958), Eugster and Chou (1973) and Garrels (1987); who suggested that the smaller iron formations were deposited in lakes and environments that were completely isolated from the world ocean. There are also Precambrian evaporate models that suggest that evaporation of seawater allowed for the deposition of iron and silica in either marine (Trendall, 1973) or non-marine evaporite settings (Eugster and Chou, 2973). Some models have more of a consensus with researchers who favor a hydrothermal source of solutes, which suggest that the iron and silica were placed at and above saturation in the ocean by hydrothermal sources, much like Algoma-type iron formations (Goodwin et al., 1985). As per water chemistry, the currently accepted model is that Superior-type iron formations were deposited in a stratified water column in which the deep oceanic waters that upwelled onto the shelf were saturated with dissolved ferrous iron and the surface waters were too oxygenated to allow for the transportation of the iron (Trendall, 2002). The silica saturation in the Precambrian seawaters suggests the lack of silica fixing organisms (Maliva et al., 1989) and that silica concentrations in seawater during the Precambrian were up to 60ppm (Siever, 1992). Some proposed precipitation mechanism for the silica includes biological inducement (LaBerge et al., 1987), evaporation, co-precipitation with iron (Ewers, 1983), as well as polymerization due to electrolyte changes (Morris, 1993). The

most accepted model for silica precipitation is that precipitation occurred in the pore water at or near the sediment/water interface (Simonson, 1987).

Currently, modern work on iron formations is trying to answer two questions. The first is deciphering the original mineralogy of iron formations. This was started when Moorhouse (1960) and Lougheed (1983) proposed that the grainstones and stromatolites of the Gunflint Lower Stromatolitic Member were orginally comprised of cabonate precipitates, which where then later diagenetically altered to silica. Sommers et al,, (2000) reinterpreted this propoasal due to the presence of ghosted carbonate, quartz crystals and euhedral specular hematite that cross-cut stromatolitic and grainstone boundaries. This relationship has been interpreted to be due to the silicification of the original carbonate. Recently Shapiro and Konhauser (2015) have suggested that the iron present in Gunflint Formation stromatolites was derived during the emplacement of the Duluth complex, in which oxidized iron-rich fluids precipitated the iron oxides present in the stromatolites.

The second question concering iron formations their distribution and link to the evolution in the oxygenation of atmosphere and oceans, especially coincident with the Great Oxidation Event (Figure 1). Iron formation probably first appeared on Earth as pyrite- and magnetite-rich deposits present on and near spreading ridges associated with volcanism. The rise in photosynthetic oxygen around 2.8 Ga coincided with the large-scale appearance of iron formations (Nisbet et al., 2007). Deposition of large-scale iron formations peaked around 2.5 Ga when a shift from deep water deposition to deposition on unrimmed platforms occurred immediately prior to the GOE (Cloud, 1973; Klein, 2005; Pufahl, 2010: Bekker et al., 2010). Iron formation deposition declined following the GOE due to a previous increase in oxidized Fe precipitation from seawater, as well as a reduction in Fe and Si being delivered into the ocean at

the time (Pufahl and Hiatt, 2012). Widespread euxinia within the oceans at approximately 1.8 Ga

ended continental deposition of iron formations (Canfield, 1998: Poulton et al., 2004; 2010;

Kendall et al., 2011). Iron formations make a brief reapperance in the Neoproterozoic during

"snowball" glaciations (Klein, 2005; Reddy and Evans, 2009; Bekker et al., 2010).
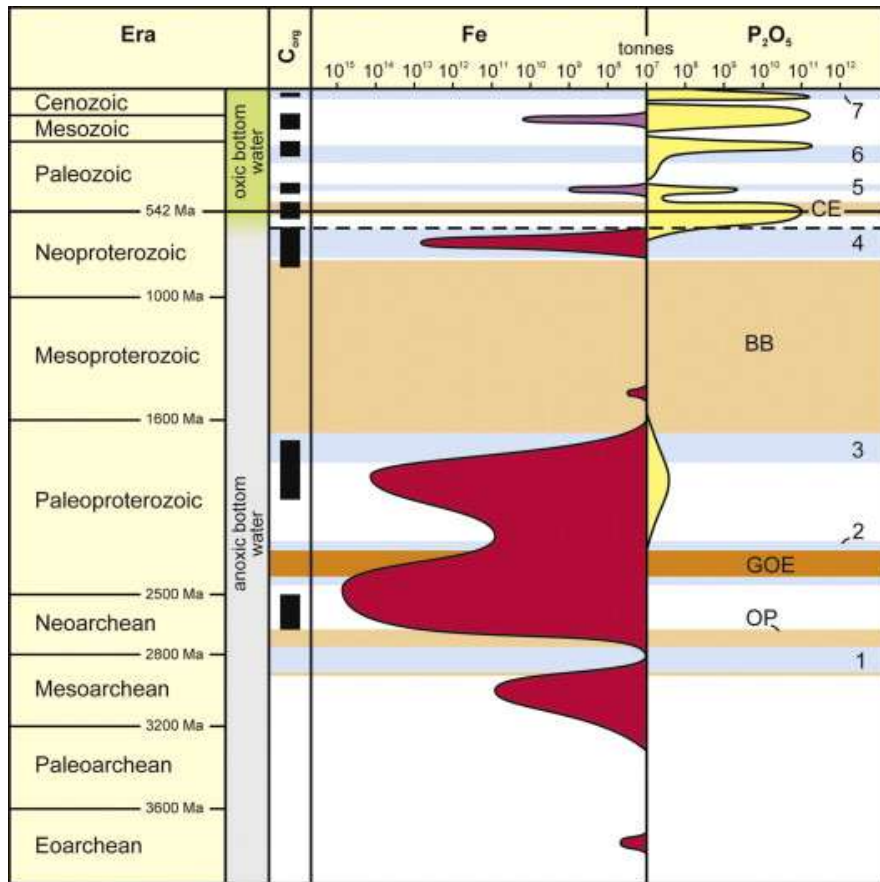
Figure 1: The temporal distribution of bioelemental sediment deposits including: iron formation (red), ironstones (purple), phosphorite (yellow) and black shale (black). Data collected on deposit age, resource estimate and timing of Earth events from Glenn et al. (1994), Kholodov and Butuzova, (2004), Condie et al.,(2001), Klein, (2005), Reddy and Evans, (2009) and Bekker et al., (2010). Legend: OP=appearance of oxygenic photosynthesis: GOE=Great Oxidation Event, BB=Boring Billion, CE=Cambrian explosion. Glaciations: 1=Mesoarchean; 2=Huronian; 3=Paleoproterozoic; 4=Neoproterozoic 'Snow Ball'; 5=Ordovician; 6=Permian; 7=Neogene (Taken from Pufahl, (2010)).

1.2   Atmospheric Oxygenation

One of the most engaging debates going on in geology today is on the oxygenation of the Earth's atmosphere and oceans during its early evolution. Atmospheric oxygenation is important because it appears to coincide with the rise in eukaryotic life during the same period and deposition of the large Superior-type iron formations. The early discussion of the timing started in 1964 at a NASA conference in Goddard when Brancazio and Cameron (1964) presented "The origin and evolution of atmospheres and oceans", suggesting that an abiotic process was solely involved in the rise in oxygen levels. This hypothesis continued until Cloud (1973) proposed in 1973 that oxygen derived from the photosynthetic activity of cyanobacteria was responsible for the deposition of the large Paleoproterozoic iron formations. Another hypothesis regarding the evolution of oxygen has been put forth by Holland (2002) who suggested that the aerobic biosphere was not just the result of a decrease in volcanic outgassing but a change in the chemistry of the volcanic gasses from reducing to more oxidizing. A more recent hypothesis is that the decrease in atmospheric methane acted as the catalysts for oxygen accumulation (Zahnie et al., 2006; Konhauser et al., 2009). The time which saw the biggest rise in the oxygenation of the Earth's atmosphere and oceans has been referred to by Holland (2002 and 2006) as the GOE. Holland (2006) has divided the evolution of oxygenation on Earth into five separate stages. Stage 1: This ranges from 3.85-2.45 Ga. This time has the earliest presences of oxygen. The oxygen level at this stage was less than 10^{-5} PAL (present atmospheric levels), which is about 2 ppm (Kasting et al.,2001; Pavlov and Kasting, 2002). This early oxygen level was probably a result of photosynthetic activities of cyanobacteria. At this point in time there was a stratified ocean in that the deep ocean was anoxic, with widespread banded iron formation and manganese deposits indcating that the deep waters had to be reducing so to allow for the concentration of Fe^{2+} and

Mn^{2+} to build up in order for it to be upwelled and deposited in the oxygenated portion of the ocean (Roy 1997).

Stage 2: 2.45 -1.85 Ga, this period surrounds the Great Oxidation Event. This drastic change in the environment has been highly debated for years, and answers remain inconclusive (Canfield, 2005). During this thime there was the cessation of BIF deposition around 2.44 Ga. Deposition does not reappear for another 360 Ma. The oxygen level in the atmosphere at approximately 2.0 Ga is still poorly defined with estimates calculated from 2.2-1.9 Ga paleoweathering surfaces to be around 15% PAL (Yang and Holland, 2003). This suggests that the oxygen content of the atmosphere would have been much higher at the beginning of the GOE but returned to about 0.21 atm by the end of the event. At this time the shallow ocean would have been at equilibrium with the atmosphere. The deep oceans would have been anoxic, allowing for the ongoing concentration of Fe^{2+} and Mn^{2+} within the anoxic waters. The presence of the first evaporitic deposits containing either gypsum or anhydrite shows that the concentration of SO_4^{2-} in the oceans had increased during the GOE due to the weathering of sulphides and was not totally removed from the deep oceans (Melezhik et al., 2005; Gellatly and Lyons, 2005). This increase in sulphate concentrations in the oceans allowed for an increase in the rate at which the sulphate was being reduced. When the rate of sulphate reduction exceeded the rate at which sulphide-reduced Fe entered the system, the amount of dissolved iron disappeared, depressing iron formation deposition (Canfield, 1998).

Stage 3: The period from 1.85-0.85 Ga has been described by Holland, (2006) as the "boring period" and represents the final cessation of large-scale BIF deposition. During this time, the oxygen content of the atmosphere was around 10-15% PAL. The ending of BIF deposition was not due to the either the oxidation of the deep water, as suggested by Holland, (1984), or due

to formation of the "Canfield Ocean", which is a sulphidic deep ocean, (Canfield, 1998) but due to a fluctuation of Fe^{2+} to the deep oceans, which allowed for deeper oxidation removing the Fe before it was transported elsewere (Holland, 2006).

Stage 4: The period from 0.85-0.54 Ga is more eventful than that of Stage 3. During this time, the Earth saw three of the largest ice ages that have been observed in the evolution of the Earth all of which were followed by periods of extreme heat (Hoffman and Schrag, 2003). This stage also shows a small resurgence in the deposition of BIF and marine Mn deposits, with the majority of them tied to glacial deposits. This period also saw the appearance of animals with hard parts during the Cambrian explosion (Knoll et al., 2006; Conway Morris, 2005).

Stage 5: The present stage of atmospheric evolution. During this period the oxygen content has reached, and at times, exceeded present atmospheric levels. This increase in atmospheric oxygen content was probably due to the evolution of large vascular plants which allowed for the rise in O_2 production, increasing the O_2 levels, before they returned to the present levels. The shallow oceans would have followed a similar pattern; whereas the deep oceans would have had a more complex evolution. The deep Phanerozoic oceans would have probably been oxygenated at a much deeper level than previously. During the Cretaceous there was a worldwide sea level rise and warming allowing for the transformation of the ocean into an anoxic deep ocean (Arthur et al., 1985).

Further research into the GOE evolution by Pufahl and Hiatt (2011) and others involve using chemical proxies such as major oxides, rare earths elements, trace elements and stable isotopes to investigate iron formations. These studies are combined with existing studies looking at the various phases present in the rock record, such as the appearance of iron mineral abundances and the disappearance of the detrital pyrite and uraninite, as well as the appearance of red beds in

continental rock records. Using this combined data Pufahl and Hiatt (2011) concluded that changes in the hydrodynamic, paleoenvironment and oceanography are visible in the changes in the geochemical trends occurring in the lithostratigraphic unit and stratigraphic sequence boundaries.

The Great Oxidation Event (GOE) mentioned previously is the period between 2.4 to 2.0 Ga. This event is noted by a change in the rock record caused by the irreversible appearance of oxygen in the atmosphere, which allowed for the switch to more highly oxidizing sub-aerial conditions. Within the rock record this transition is marked by both physical and geochemical changes. Physically, the start of the GOE is characterised by the disappearance of redox-sensitive minerals, such as detrital uraninite and siderite, from sedimentary rocks along with the oxidation of pyrite present in the terrestrial environment, all of which were indicative of the widespread anoxic environment prior to this period (Roscoe and Minter, 1993; Canfield, 1998; Canfield and Raiswell, 1999; Bekker et al, 2004, Holland, 2006; Konhauser et al., 2011). These losses in the rock record were replaced by the presence of hematite-rich redbeds, oxidised shallow water iron formations, and $CaSO_4$-rich evaporites. (Cloud, 1968; Roscoe, 1969; Chandler, 1988; Fleet, 1998; El Tabakh et al., 1999; Rasmussen and Buick, 1999; Hanzen et al., 2008).

During the widespread anoxia of the Archean, prior to the GOE, the atmospheric oxygen level ranged from 10^{-12} to 10^{-14} PAL, with the presence of volcanic gases rich in CO and H_2, and could have reached up to 4×10^{-8} PAL during periods of the decreased output of reducing volcanic gases (Kasting and Walker 1981). Atmospheric levels of oxygen during the GOE have yet to be precisely constrained (Holland 2006). Studies of the 2.25 Ga Hekpoort Paleosol, Botswana gave PAL values of 0.1-5% (Yang and Holland, 2003). A value of 15%PAL of the

2.2-1.9 paleoweathering profile in Griqualand West, South Africa bracket the GOE, indicating

that the oxygen level was lower at the start of the GOE and rose throughout (Holland, 2006).

Geochemically the mass-independent fractionation (MIF) of sulphur isotopes present in

sulphide and sulphate minerals is an excellent tool for tracking the change in atmospheric oxygen

(Bekker et al., 2004). MIF uses the four sulphur isotopes of 32S, 33S, 34S and 36S to show the

mixing of the gaseous sulphur species and the coeval mixing with seawater, which had a low

sulphur content (Farquhar et al., 2000; Canfield et al., 2000). Large MIF isotope signatures are

present in samples collected that are older than 2.41 Ga. After this time MIF isotope signatures

completely disappear from the record (Bekker et al., 2004; Holland, 2006).

MIF signatures present in samples with ages older than 2.41 Ga are indicative of a low

level of oxygen in the atmosphere. The lack of oxygen in the atmosphere hindered the production

of ozone thus allowing for UV rays to penetrate deeper towards the Earth. The UV rays

dissociated the SO_2 in the atmosphere into its elemental and water soluble S species (Farquhar et

al., 2000). The elemental and water soluble S then could not exchange with the Archean

atmosphere allowing for preservation in the rock record (Pavlov and Kasting, 2002). In the

modern atmosphere (i.e. oxygen content levels > 10^{-5} PAL (Pavlov and Kasting, 2002) the

sulphur dissociated species formed are oxidised to sulphate and lose their MIF signature (Bekker

et al. 2009).

1.3   Animikie Group Rocks

The Animikie Group rocks represent Paleoproterozoic sedimentary rocks that were deposited within the Animikie basin that had flooded what is now Northwestern Ontario and the majority of the North central United States. These sediments are divided into two segments which contain the seven major iron ranges. The segments, and their corresponding iron ranges, are the northwestern segment that has the Gunflint (Ontario), Mesabi (Minnesota) and Cuyuna (Minnesota) ranges, and the southeast segment comprised of the Gogebic (Wisconsin), Marquette (Michigan), Iron River-Crystal Falls (Michigan) and the Menominee (Wisconsin) ranges (Figure 2). The Gunflint, Mesabi, and Gogebic ranges are the predominant iron ranges and are composed of nine individual formations. These formations are grouped together according to their location and their stratigraphic position; the basal units are represented by the Kakabeka Conglomerate (Gunflint), Pokagama Quartzite (Mesabi) and the Palms Formation (Gogebic). The iron formations within these major ranges are the Gunflint (Gunflint), Biwabik (Mesbai) and Ironwood (Gogebic). At the top of the Animikie groups are the Rove (Gunflint), Virginia (Mesabi) and Tyler (Gogebic) (Figure 3). The sediments forming these formations are the result of the repeated transgression-regression of the ancient Animikie Sea that flooded the area (Morey, 1983).
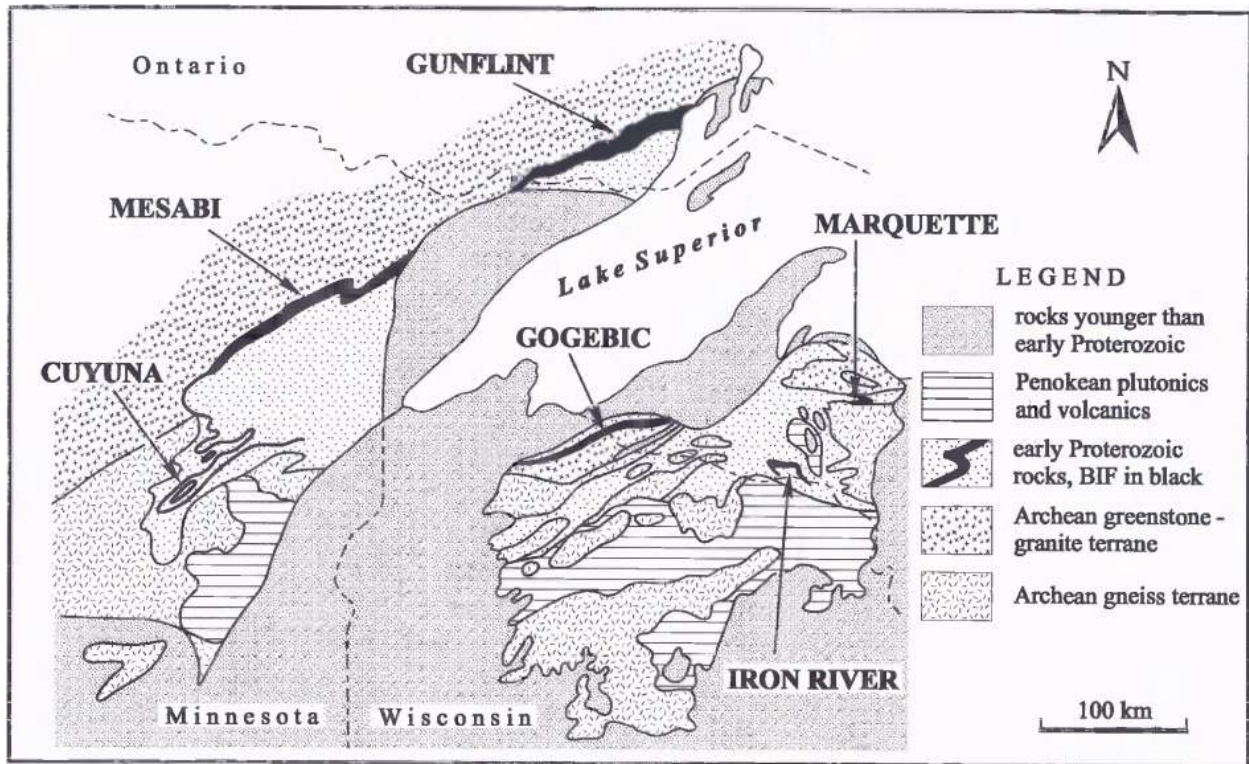
Figure 2: Bedrock map of the major iron ranges of the Animikie Basin in the Lake Superior region (Pufahl et al., 2004).
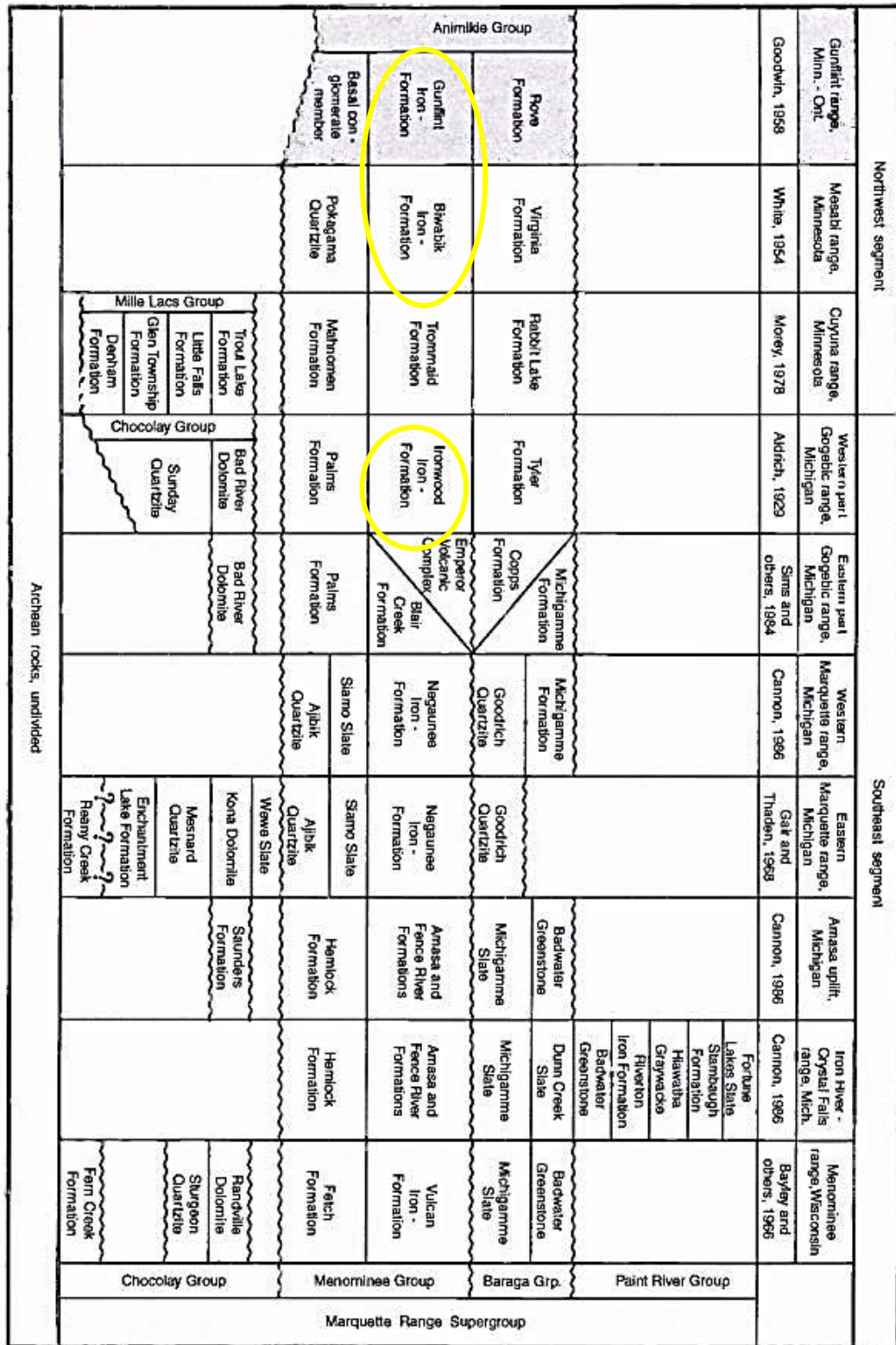
Figure 3: The proposed correlation of the sediments of the Animikie group. The iron formations studied are circled in yellow (Modified from Pufahl et al., 2000).

The Kakabeka, Pokegama, and Palms formations are clastic rocks, that uncomfortably overlie Archean basement rocks making up the Superior Province. These three basal formations contain stratified deposits. These formations are comprised of clasts of Archean granites and volcanic rocks, as well as quartz that have been reworked by storm-generated waves forming roughly stratified, matrix supported, supratidal, pebbly beach deposits that represent the initial transgression of the Animikie Sea (Ojakangas, 1983; Cannon and Fralick, 2010).

Conformably overlying the basal formations are the three main iron ranges: Gunflint; Biwabik; and Gogebic (Dolence, 1961). With a thickness ranging from 120 to 185m dipping 5° to the south, the Gunflint formation is 170km long, continuously extending from Gunflint Lake, Minnesota northeast and ending in the Loon Lake area, Ontario. From there, erosional remnants occur at Schreiber, Ontario, about 100km northeast (Goodwin, 1956). In northeastern Minnesota, the Biwabik iron range has been truncated by the intrusion of 1.1 Ga gabbros of the Midcontinent Rift resulting to the southwest of this intrusion in a narrow, 0.4 to 4.8km wide, band covering 200km. The dip of the Biwabik ranges from 2 to 10° at the southeastern portion of the range to dips of 8 to 45° near the Duluth complex (Gruner, 1946). The Ironwood formation is a 150m thick iron formation. Unlike the other two formations mentioned the Ironwood represents a slightly deeper water environment that still records sea level fluctuations (Pufahl and Fralick, 2004). At the top of the Gunflint and Biwabik formations there is a limestone unit, which represents a drastic change in the depositional environment (Burton and Fralick, 2007). Accretionary lapilli derived from the Sudbury impact event can be found on the limestone unit in both the Gunflint and Biwabik formations (Addison et al., 2005; Cannon and Addison, 2007).

Discontinuously overlying the Gunflint and Biwabik iron formations are the Rove and Virginia. The Ironwood formation is overlain by the Empress Volcanic complex. The Rove and

Virginia Formations are thinly bedded to laminated, fine-grained mudstone and turbiditic sandstone ranging in thickness from 380 to 1000m. A detailed sedimentology and sequence stratigraphy study of the Rove and Virginia Formations was conducted by Maric (2006). The Empress Volcanic Complex that overlies the Ironwood Formation is mostly comprised of tuffaceous beds with interlayered nonmagnetic shales (Schmidt, 1980).

A highly debated question is the tectonic setting of the Animikie Basin. With a lack of evidence there have been two primary models for the tectonic setting. The first model is the foreland basin model suggested by Hoffmann (1987), Southwick and Morey (1991) and Ojakangas et al. (2001). This model proposed that a northward migrating foreland basin was formed north of the Penokean fold and thrust belt, as a response to crustal loading caused by the Penokean orogeny at approximately 1.85 Ga. The second model put forth by Hemming et al. (1995) and Fralick et al., (2002) proposed the formation of a backarc basin north of the Wisconsin Magmatic terrane. During the Penokean orogeny, this backarc basin evolved into a foreland basin, accommodating the Rove formation (Hemming et al., 1995; Ojakangas et al., 2001).

1.4   The Gunflint and Equivalent Formations.

The earliest record of the Gunflint formation can be traced back to the 1880's by Ingall (1888), who described the Silver Mountain-Whitefish River area of Northwestern Ontario in an annual mining report. During the turn of the 20th century there were minor amounts of work on the Gunflint by Smith (1905) and Silver (1906) until the 1920's when Tanton (1923) began comprehensively mapping the area. Detail descriptions of the stratigraphy were completed by

Gill (1926), who also developed one of the original theories on the deposition of the Gunflint (Gill, 1927).

The Gunflint was initially divided by Goodwin (1956) into two depositional cycles, six individual sedimentary stratigraphic unit and four members. The original members are a Basal conglomerate member, Lower Gunflint, Upper Gunflint and Upper Limestone. A study of the mineralogy, geochemistry and economic potential, as well as detailed geological mapping, were undertaken by Moorehouse and Goodwin (1960). This further refined the stratigraphy by dividing it into two members: the lower and upper members. The Lower member is comprised of the Basal Conglomerate, Lower Stromatolitic Chert, Lower Shale, Lower Taconite and localized lava Flows. The upper member is composed of Upper Stromatolitic Chert, Upper Jasper, Upper Shale, and Upper Taconite, capped off by the Limestone member. Further redefinition of this stratigraphy was undertaken by Fralick and Barrett (1995) who simplified the stratigraphy in which the lower and upper members are divided into stromatolitic cherts and cherty grainstones.

The Biwabik iron formation was first divided into four divisions by Wolff (1917) and Broderick (1920): the Lower Cherty, Lower Slaty, Upper Cherty and Upper Slaty. These divisions were based on their primary lithology in which the cherty stratigraphic unit are comprised of granular iron formation that is rich in iron oxides and cherts, with the slaty stratigraphic unit comprised of mudstone and iron-rich siliciclastics composed of iron silicates, iron carbonates, and localized chert beds. The Ironwood has been divided into five stratigraphic unit based on similar lithologies to the Biwabik: Plymouth (slaty), Yale (slaty), Norrie (cherty), Pence (slaty) and Anvil (cherty) (Hotchkiss, 1919; Aldrich, 1929; Huber, 1959; Marseden, 1978). Severson et al. (2009) have published a review of the Biwabik and Gunflint formations,

correlating each stratigraphically using tuffaceous layers present in the upper portions of the two formations.

The sediment of the Gunflint and equivalent iron formations represent the transgression and regression of the ancient sea that flooded the Animikie basin (Pufahl et al., 2000). The boundaries that reflect the changes in sea level, especially in the initial transgression as well as a change from transgression to regression, are marked by definite changes in the lithologies and the presence of stromatolite colonies in some of the outcrops. The first stromatolite zone, which marks the initial transgression of the Animikie Sea, is found at the base of the Gunflint sitting on top of the Kakabeka Conglomerate. The second stromatolite zone is present 45m above the basal contact forming the first unit of the upper member. This stromatolite colony reflects the transgression of the Animikie Sea, with the stromatolites sitting on a diastem or maximum regression of the Animikie Sea (Fralick and Barrett, 1995). Stromatolite growth occurred solely in shallow water (Pufahl et al., 2000) which means that sediments and rocks of the underlying Gunflint were probably exposed to the atmosphere at the time of maximum regression (Fralick and Barrett, 1995). Recently a third horizon within the Gunflint, Biwabik, and Gogebic Formations has been identified as a possible exposure surface. This layer is found approximately 40m from the erosional contact at the top of the formations and is overlain by stromatolites and oncolites (Arts, 2015).

U-Pb ages were obtained from zircons found in the volcanic tuffs present in the Gunflint and provide an absolute age of 1878.3 ± 1.3Ma (Fralick et al., 2002). A U-Pb age of 1874 ± 9Ma was obtained from correlative volcaniclastic beds present in the Gogebic (Schneider et al., 2002).

The Gunflint stratigraphy represents deposition at and near the shoreline of the basin and any change in the sea level would be noted in the rock record. The surfaces that represent the

shift from transgression to regression and regression to transgression are identified three times within the Gunflint Stratigraphy. These surfaces are:

 1) The base of the Gunflint marking the initial transgression,

2) 45m above the base of the Gunflint marking regression-transgression and,

3) 40m below the erosive top of the Gunflint marking another period of regression-transgression.

Extending from the base of the Kakabeka Conglomerate up into the first 20m of the Gunflint, the basal transgression marks the initial flooding of the shelf by the Animike Sea. This initial transgression is made up of the extraformational conglomerate of the Kakabeka, marking a storm affected beach deposits. The fining-upward grainstones of the basal Gunflint represents the deepening of the Animike Sea (Fralick and Barrett, 1995). The shift from initial transgression to regression of the Animike Sea is marked by a change in the grainstones. At 20m above the base of the Gunflint, there is a change in which the grainstones shift from fining-upward to coarsening-upward marking the transition from flooding to retreating of the Animike Sea. The regressive surface, as well as the diastem (maximum point of regression), are characterised by the presence of the stromatolite/oncolite colonies present within the grainstones. Transgression again is marked by the fining-upward grainstones and continues up until the regression-transgression sequence 40m below the erosional surface at the top of Gunflint. This surface has just been recognised by Arts (2015) and not been written about extensively, but this surface is also overlain by stromatolite/oncolite colonies within the grainstones.

The noticeable transgressive-regressive surfaces present in the Gunflint stratigraphy are not as evident in other iron formations of similar make-up, and thus, not readily studied and

published on. Any data present in the literature on possible exposure surfaces in other studies looking at material peripheral to that of the transgression-regression surface (i.e. Planavsky et al., (2009) which sampled of stromatolites and surrounding iron formation inthe Gunflint and Biwabik). The data in their research show that the majority of the stromatolite and surrounding Gunflint samples plot with expected Ce anomalies, but the majority of the iron formation samples plot with nil negative anomalies, especially away from the transgressive-regressive surfaces. These nil Ce anomalies indicate that the majority of the standard Gunflint samples represent an anoxic environment during deposition, with minor siliciclastic component.

The presence of the stromatolite/oncolite colonies within the Gunflint stratigraphy is a key indicator of the transgressive-regressive surfaces. These "laminated, benthic, microbial deposits" are present in some of the oldest sedimentary deposits dating back to 3 Ga (Riding, 1991).

Forming in the nearshore marine environments of the Gunflint formation, the stromatolites are comprised of mostly alternating layers of fine-grained iron oxide and, silica with minor amounts of carbonates present. This composition is different from the composition of modern stromatolites, which are comprised of carbonate grains with less cement. There are two unique methods of stromatolite formation. One method of formation is trapping and binding by agglutination of surrounding carbonates grains by extra polymeric substance (EPS), which is a sticky substance produced by the microorganisms present (Decho, 1990; Riding, 1991). The other method of stromatolite formation is through precipitation. The precipitation of the minerals that make up the stromatolites was driven by one of two precipitation mechanisms. Biologically controlled mineralisation (BCM) in which the minerals are precipitated directly within the cell walls as a vital component of the cell (Lowenstam, 1981; Lowenstam and Weiner, 1983; Frankel

and Bazylinski, 2003). The other mechanism for precipitation is biologically induced mineralisation (BIM). During BIM, the minerals are precipitated within the EPS of the cell (Frankel and Bazylinski, 2003). The stromatolites formed within the shallow water on top of hard surfaces which allowed them to stay anchored to the ground making them key indicators of subaerial exposure during transgression-regression.

1.5   Scope of Research

The overall focus of this thesis was to examine exposure surfaces present in the Gunflint and other equivalent formations in the Animikie Group, and to use the collected physical attributes and geochemical data to interpret the conditions and environment immediately before, during and after the time of exposure. The first step was to identify the outcrops and diamond drill hole sections that best represent the three possible exposure surfaces present in the Gunflint or equivalent formation's stratigraphy. Next, samples were collected from the outcrops and drill holes, while noting the overall characteristics of the outcrops and cores. The samples were used to macroscopically and microscopically characterize the alteration pattern in rocks immediately below exposure surfaces using both macroscopic and microscopic descriptions. The geochemistry of the samples was examined using ICP-AES and MS with particular attention paid to REDOX sensitive elements that can serve as proxies for the environment at the time of deposition, or allow for an interpretation of the environment at the time of exposure. To accomplish this, samples were collected from nine outcrops and three drill holes that represent each of the three possible exposure surfaces present in the Gunflint stratigraphy (Figure 4 and Table 1).
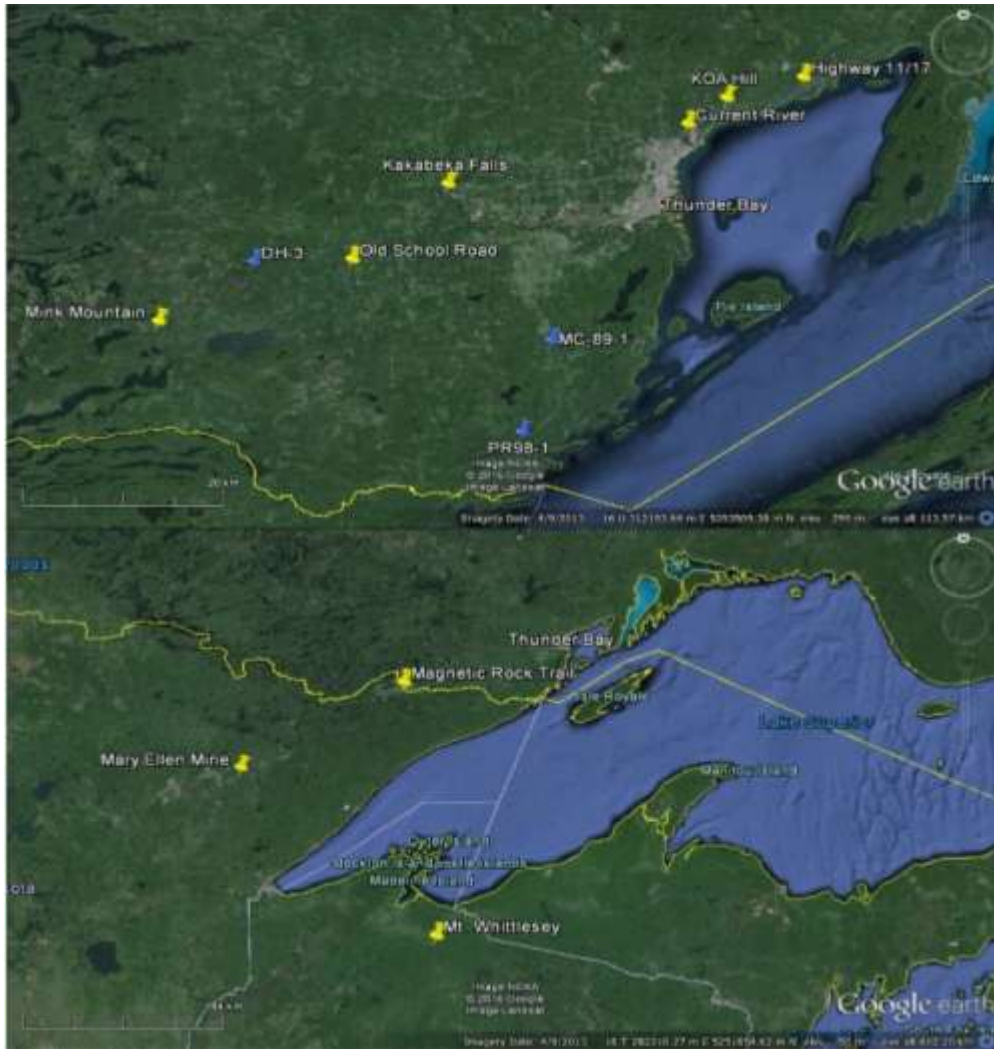
Figure 4: Map of the sample location selected for this project. 1) Thunder Bay area sample sites. B) Minnesota and Wisconsin sample sites.

Table 1: Sample sites selected for this project. This table shows whether the sites it is an outcrop or a drill hole, the sample site location within the Gunflint stratigraphy, the nearest known city, and the UTMs of the outcrop or drill hole (NAD 83)

Study Site	Outcrop or Drill Hole	Stratigraphic Location	Location	UTMs (NAD 83)
Highway 11/17	Outcrop	Basal	Thunder Bay, ON	0353131, 5376455, 16N
KOA Hill	Outcrop	Basal	Thunder Bay, ON	0342770, 5374259 16N
Kakabeka Falls	Outcrop	Basal	Thunder Bay, ON	305201E, 5364740N 16N
Whitefish Channel	Outcrop	Basal	Nolalu, ON	289167E, 5351919N 16N
Mink Mountain	Outcrop	Middle	Soumi, ON	710621E, 5346233N 15N
Old School Road	Outcrop	Middle	Nolalu, ON	291713E, 5354771N 16N
Current River	Outcrop	Middle	Thunder Bay ,ON	337466E, 5370543N 16N
DH 87-3	Drill Hole	Middle	O'Connor Twp, ON	
Magnetic Rock Trail	Outcrop	Middle	Gunflint Trail, MN	662473E, 5329219N 15N
MC-89-1	Dill Hole	Middle	Neebing, ON	316715E, 5340523N 16N
PR98-1	Drill Hole	Upper	Neebing, ON	578923E, 5275160N 16N
Mount Whittlesey	Outcrop	Upper	Mellen, WI	683144E, 5130188N 15N
Mary Ellen Mine	Outcrop	Upper	Biwabik, MN	578504E, 5279565N 16N

2 METHODS AND MATERIALS

2.1 Imaging

The samples that were collected from the outcrops and drill holes were cut and crushed to a fine powder, using an agate mill, at the Lapillary, Lakehead University. Thin sections and scanning electron microscope discs for petrographic analysis were prepared by the Geology Department technicians for selected samples. Some of the hand and diamond drill core samples were polished for better binocular microscopic imaging. Petrographic analysis and imaging was performed on the Olympus BX51 polarizing microscope with an Olympus DP70 digital camera. Standard photographs were taken by either a Sony α390 digital camera with an 18-55 mm lens or a Canon EOS Rebel T3i with an 18-55mm lens. Macroscopic images were taken with a Pentax WG-II camera. Imaging of the samples was used to help determine the composition of the samples, as well as document the changes that occurred in the samples during Paleoproterozoic exposure.

SEM-imaging was performed on polished thin sections. The SEM utilized was a Hitachi SU-70 Schottky Field Emission scanning electron microscope with an Oxford AZtec 80mm/124ev EDX. Data was processed on with the AZtec software. The X-ray spectrographic analysis involved elemental semi-quantitative mapping for chemical variations in the samples taken from outcrops with most alteration.

2.2 Definition

Due to the similar nature that Superior-type iron formation have to carbonate environments, it is commonplace to use carbonate geology terms to help describe the composition and formation of the main components. Using Dunham's Carbonate Classification

grainstones are defined as grain supported with no matrix mud, and not bound together during

deposition. Unless otherwise stated the grainstones mention throughout this project refer to

interclastic grainstone. Simonson (1987) described the framework grains of the grainstones. In

this paper grain composition is split into two groups: non-oolitic and oolitic grains. Oolitic grains

are rounded grains with concentric layering surrounding a nucleus. Non-oolitic grains do not

show this concentric layering around the nucleus and range is shape from angular to rounded.

They can also be referred to as a peloid or interclastics. Quartz textures of both the grains and the

cement use Folk's (1968) definition of chert and microquartz. Microquartz crystals are crystals

less than 35um long. Chert is a chemically-precipitated sedimentary rock comprised of

microcrystalline and/or chalcedonic quartz, with subordinate amounts of megaquartz and minor

amounts of impurities (Folk, 1968).

2.3   Geochemistry
2.3.1   *Analysis*

The majority of the samples were analyzed using both Inductively Coupled Plasma

Atomic Emission Spectrometry (ICP-AES) and Inductive Coupled Plasma Mass Spectrometry

(ICP-MS). Some the early analysis of the samples taken before the start of the project was

performed at the Ontario Geosciences Laboratory in Sudbury Ontario. The samples collected

during the study period were analysed at the Lakehead University Instrument Laboratory

(LUIL). ICP-AES analyses were performed on a Varian Vista Pro Radial atomic emission

spectrometer. ICP-MS analysis was performed with a Perkin-Elmer Elan DRC-e quadrapole

mass spectrometer.

Sample preparation for ICP-AES and MS analysis were performed at Lakehead University using an open crucible 2 acid dilution method. Samples selected for geochemical analysis were cut using a rock saw. Samples were first hand crushed using a titanium mortar and pestle; this was followed by mechanical crushing with an agate puck in an agate bowl. The resultant powders were then collected. For digestion, rock powders were measured out to 0.250g to 0.500g and placed in Teflon beakers. Hot plates used for analysis were heated to approximately 90°C. The beakers were then filled with 10ml of double distilled water (DDW), followed by 5ml of nitric acid and then placed on the hot plates for 12-24 hours, until completely evaporated. Next, the beakers were removed from the hot plate and filled with 10ml of nitric acid and 5ml hydrofluoric acid. The beakers were placed back on the hot plate and allowed to evaporate. This process are repeated two more times. On the last day the beakers were removed from the hot plate. Two ml of nitric acid was added to the beakers, and they were placed back on the hot plates and allowed to simmer. After 20 minutes, 15ml of DDW was then added to the beakers which were simmered for 10 more minutes. The digested samples were then transferred to 100ml volumetric flasks using DDW. The flasks were placed on the hot plate and warmed for two hours. After cooling, the flasks the volume of the flask was adjusted to 100ml with DDW. The solution in the flasks was then transferred to 50ml vials. For ICP-AES analysis, a 200 or 400x dilution was used. ICP-MS analysis used a 1000x dilution. The 1000x dilution is created by adding 10ml of the solution into a 50ml vial and topped off with a 2% nitric solution.

The extracts were analysed for redox sensitive oxides, trace and rare earth elements using ICP-AES analysis was used for major oxide and trace element concentrations. ICP-MS analysis was used for rare earth elements and minor trace element concentrations. The major oxides studied were Fe_2O_3 and MnO. The trace elements investigated were Cr, V, U, and Mo. Taylor

and McLennan's (1985) Post-Archean Australian Shale values were used for rare earth element normalization.

Accuracy, Precision and Lower Detection limit

For the ICP-AES samples, the precision was calculated from multiple analyses of the same samples and results were within the expected limits within 15% of the measure standard. The accuracy was calculated using the USGS standards [BHVO-2] a Hawaiian basalt and [QLO-1a] a quartz latite from Oregon and were found to be within the acceptable limits for the elements used in this study (Al, Ca, Fe, K, Mg, Mn, Na, P, Ti, Cr and V). ICP-MS analysis for REEs as well as Mo and U was also evaluated for accuracy and precision using the same BHVO-2 and QLO-1a standards and the results were within the acceptable limits and are presented in Figure 5. Expected data was provided by the USGS along with the samples. The BHVO-2 data was provided by Wilson, (2000). The details of the collection, preparation and testing are provided by Wilson (2000). The QLO-1 data was based on the international data compilation (Abbey, 1983; Gladney, 1983; Gladney and Roelandts, 1987; Govindaraju, 1994). Background information for QLO-1 was provided by Flanagan (1976).
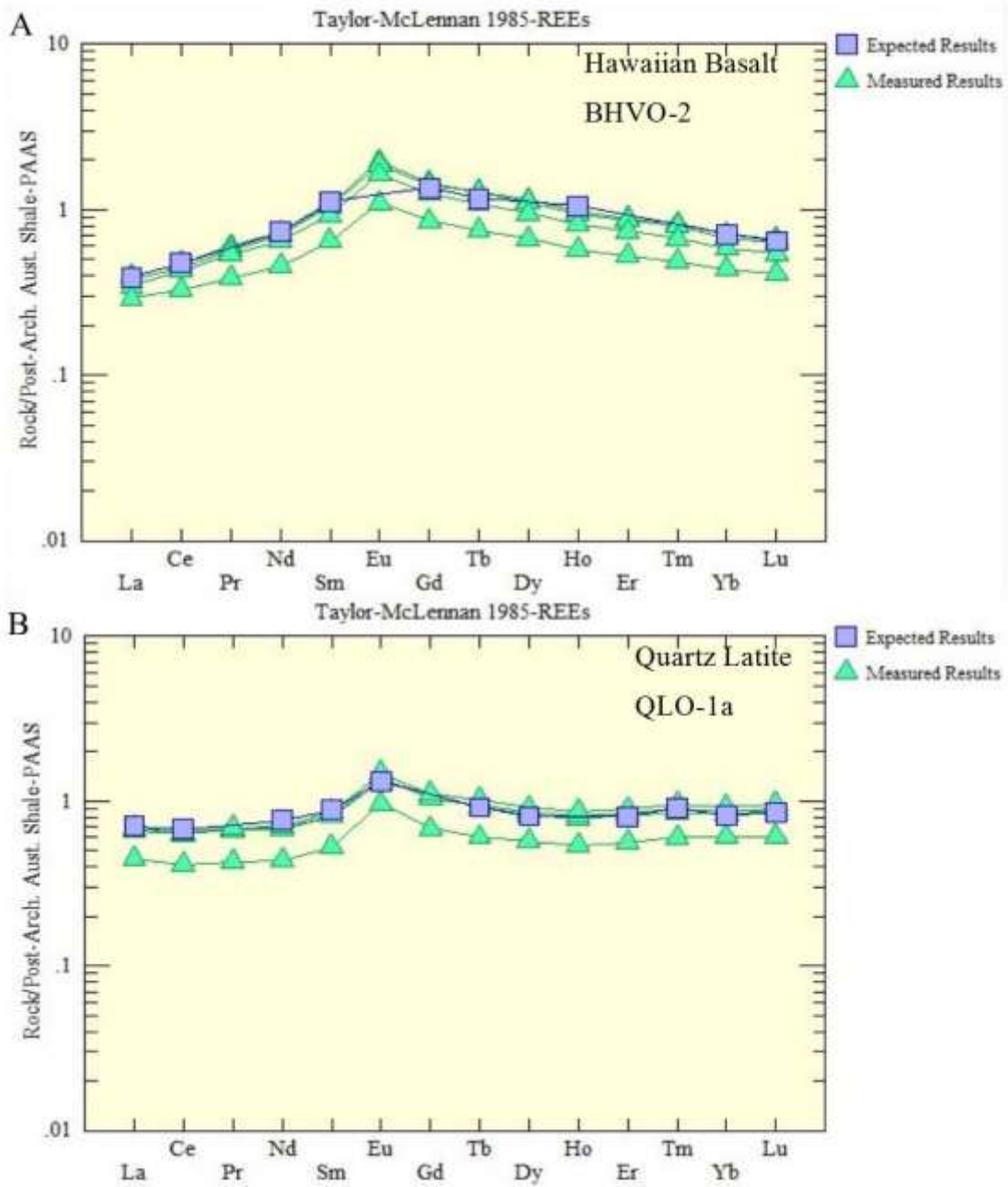
Figure 5: Accuracy and prescion of the standard used for rare earth element analysis. All measured standards show accurate curves and precise results. A) Hawaiian basalt standard, B) Quartz latite standard. Element with no data indicate that no expected values was given with the samples.

The lower detection limits were also calculated for AES and MS analysis using the average blank for selected runs are presented in Table 2

Table 2: Lower detection limits for major oxides (wt %), trace element and rare earth elements (ppm).

	Lower Detection		Lower Detection
Al_2O_3	273.6	La	1.102
CaO	194.2	Ce	2.079
Fe_2O_3	308.6	Pr	0.211
K_2O	165.2	Nd	0.697
MgO	54.04	Sm	0.095
MnO	2.4	Eu	0.009
Na_2O	389.04	Gd	0.095
P_2O_5	12.4	Tb	0.009
TiO_2	3.76	Dy	0.033
Cr	0.09	Ho	0.007
V	0.002	Er	0.012
		Tm	0.003
		Yb	0.011
		Lu	0.002
		Mo	1.849
		U	0.153

2.3.2 Behaviour of REDOX Sensitive Elements Oxides and Trace Elements

REDOX sensitive oxides and elements are divided into two distinct groups, those that are relatively immobile when oxidized, and those that are relatively immobile when reduced. The oxides Fe_2O_3 and MnO are relatively immobile and formed when reduced iron and manganese enter oxidizing fluids. The elements that are relatively immobile when reduced act in a different manner. These elements include V, U, Cr, and Mo.

The elements V and U are both highly soluble in oxidizing fluids and will precipitate when the fluid becomes reduced (Sugiyama, 1989; Wehrli and Stumm, 1989; Shiller and Mao 1999, 2000). The solubility can also be increased if V or U form sulfate complexes (Wanty and Goldhaber, 1992). V content is an excellent marker of organic content present. Oxyhydroxides will precipitate V^{3+} which is reduced from either vanadate (V) or vanadyl (IV). Uranium acts in a similar manner to V in that oxidation and reduction will allow for its precipitation (Brown, 2003).

In anoxic conditions and in neutral pH fluids, chromium exists in a 3^+ state and is immobile. If there is enough oxygen available to oxidize Mn to MnO, the MnO can oxidize the Cr from its 3^+ state to a 6^+ state, allowing for it to become mobile and easily transported. If this oxidized fluid suddenly becomes reduced the mobile Cr (VI) will revert to Cr (III) causing it to precipitate (Eary and Rai, 1987; Oze et al., 2007; and Frei et al., 2009).

In a REDOX sense, the precipitation and removal of Mo from solution can occur in both oxygenated and reducing environments. The main source of Mo in today's oceans is riverine input as dissolved MoO_4^{2-} (molybdate) derived from the weathering of the continetal crust (Bertine and Turekian, 1973; Taylor and McLennan, 1995). In oxygenated environments, the molybdate is precipitated with Mn-oxyhydroxides (Bertine and Turekian, 1973). Removal of Mo in oxygenated environments is not the most efficient mechanism of Mo removal, resulting in a loss of about 35% of dissolved Mo from the modern riverine input (Scott et al., 2008). The most efficient way of removing dissolved Mo is through sulphidic conditions. The presence of high amounts of sulphide changes the molybdate to thiomolybdates ($MoO_xS_{4-x}^{2-}$) and it is removed by organic matter and reduced sediments at a rate of 200-5000 times faster than Mo removal in oxygenated environments (Helz et al., 1996). This range in removal speed is determined by

hydrogen sulphide concentrations. The lower end occurs in areas where the H_2S is restricted to the sediments, while the uppervalues are due to the presence of sulphide and tetrathiomolybdate ion within the water columns (Scott et al., 2008).

Rare Earth Elements

Ce and Eu are the only two rare earth elements that can behave somewhat differently than the other REEs due to alternate valance states at surface temperatures and pressure. Normally Ce and Eu act in the same nature as the rest of the REEs in that they are commonly present in the trivalent state. Unlike the other REEs when introduced to oxidizing conditions Ce oxidized from the Ce (III) to Ce (IV). In this state, the Ce can either be removed from the solution by direct precipitation or by scavenged by Fe and Mn oxyhydroxides. This is through either (1) oxidation of the dissolved Ce(III) to form the oxide cerianite (CeO_2), which will adhere to minerals present in Mn oxide-rich areas, or (2) oxidation allows for scavenging of the dissolved Ce(III) by the Mn oxyhydroxides and Fe oxyhydroxides (Rankin and Childs, 1976; Lei et al., 1986; Marsh, 1991; Koppi et al., 1996; Braun et al., 1998; Bau, 1999, Ohta and Kawabe, 2001; Ji et al., 2004).

When calculating Ce anomalies for PAAS normalized REE distribution plots a problem can arise due to La forming positive anomalies. This problem can be eliminated by not using the La value when calculating the Ce anomaly

$$\text{Ce anomaly (Pr/Pr*)} = Pr_{PAAS}/ (0.5Ce_{PAAS}+0.5Nd_{PAAS})$$

However, the equation for the La anomaly does have the Ce component in it leading to a forced correlation between calculated La and Ce anomalies:

$$\text{La anomaly (Ce/Ce*)} = Ce_{PAAS}/ (0.5La_{PAAS}+0.5Pr_{PAAS})$$

The rare earth element Eu acts in a completely different manner to Ce. Within the basaltic oceanic crust, the percolating Mg-rich seawater will start to rise in temperature as it nears a heat source within the crust. The Eu ion is the only REE that can exist in the 2^+ state, is roughly the same size as the Ca^{2+} ion, and is present in high amounts within the plagioclase feldspar of mid-ocean ridge basalts. When the heated Mg-rich seawater exchanges Mg for Ca it will also pick up Eu^{2+} ions allowing for an increase in the Eu content of vented hydrothermal fluids. The Archean and Paleoproterozoic inherited this positive Eu anomaly. Eu anomalies present in PAAS normalized REE distribution plots represent deposition in an oceanic environment (Peter, 2003). The Eu/Eu* anomaly explored in this project is expressed as (Bau and Duluski, 1996):

$$Eu/Eu* = Eu_{PAAS} / (0.67Sm_{PAAS} + 0.33Tb_{PAAS})$$

3   BASAL CONTACT SAMPLE SITES:

The outcrops present at three sample sites studied show the exposure surface present at the basal contact of the Gunflint Formation. The three sites chosen were two outcrops present on the shoulder of Highway 11/17 east of Thunder Bay and the third is present on the shoulder of Highway 588 on the border of Kakabeka Falls Provincial Park near Kakabeka Falls, Ontario. These outcrops mark the initial transgression of the ancient sea that flooded the basin in which the iron formations were deposited. The rocks that makeup these outcrops show alteration that may reflect the changes that occurred when the rocks were exposed to the Precambrian atmosphere. The alteration is reflected in both physical attributes and geochemical changes. The outcrops present at the sample sites can be divided into three distinct stratigraphic unit 1) an unaltered basal layer in the Archean basement, 2) an altered horizon, and 3) the basal layer of the Gunflint Formation. Unaltered Stratigraphic unit: The unaltered stratigraphic unit of the outcrop represent the original composition of the outcrop before being exposed to the Precambrian atmosphere and any later alteration. Altered stratigraphic unit: The altered stratigraphic unit of the outcrops represent the near surface portion of the outcrop that was exposed to the Precambrian atmosphere. These stratigraphic unit differ from site to site due to the starting composition expressed in the unaltered layer. Figure 6 shows that the alteration stratigraphic unit vary at the outcrop level. The variability of the alteration stratigraphic unit ranges from what appears to be intense weathering and rounding of core stones of the unaltered layer to slight microscopic alteration of the mineral makeup of the outcrop. The grainstone, plus or minus microbialites, is representative of the basal contact that makes up the start of deposition of the Gunflint Formation at these sites. The basement at one of the sites is composed of siliceous microbialite with stromatolites overlain by carbonate grainstone.
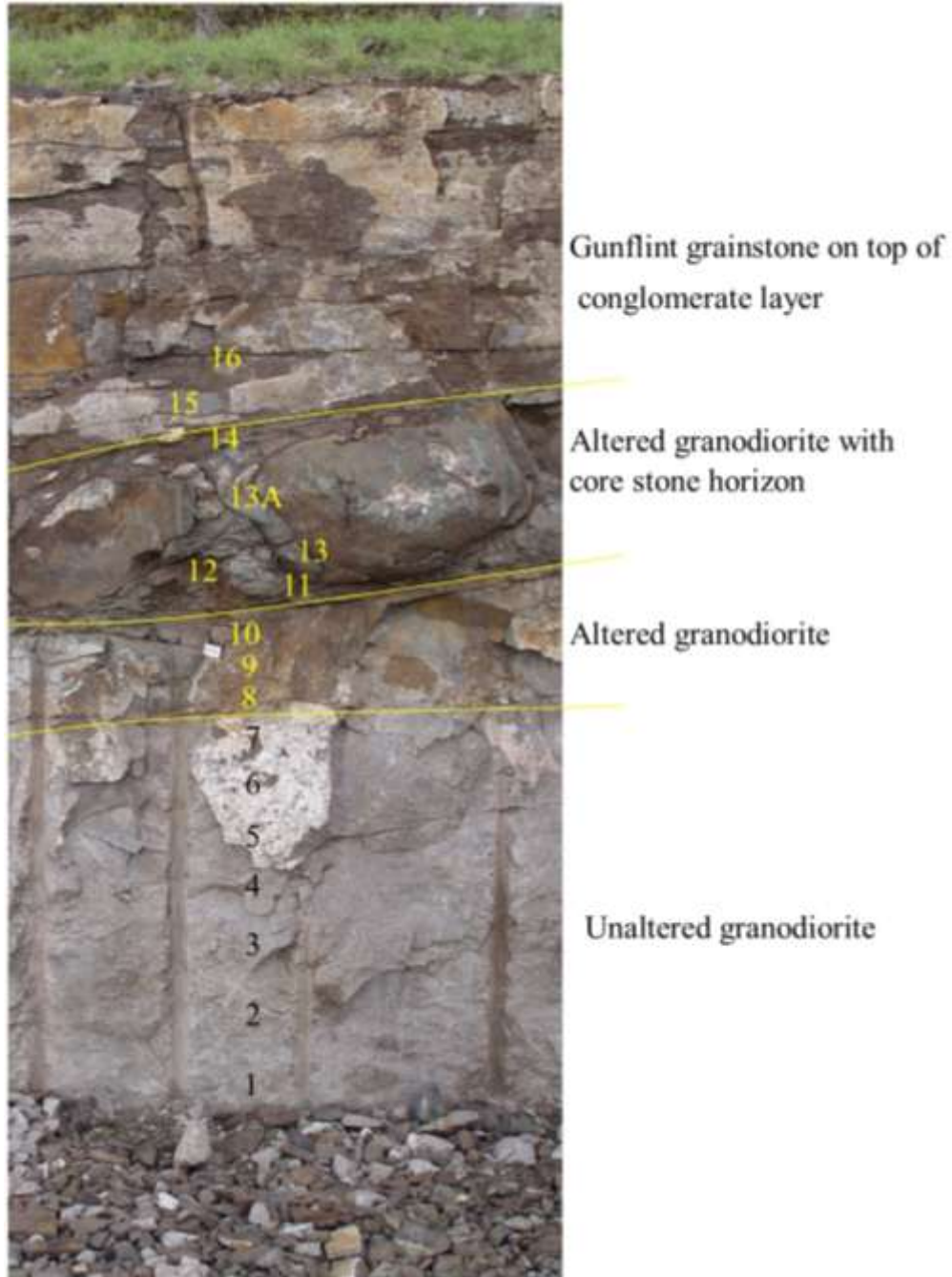
Figure 6: The stratigraphy of the Highway 11/17 outcrop with the approximate location of the samples taken from the outcrop.

3.1 Sample Sites

3.1.1 *11/17 Sample Site*

The outcrop present at the Highway 11/17 sample site exhibits a very distinct alteration pattern, showing the breakdown of the granodiorite that makes up the majority of the outcrop (Figure 6). Samples 1- 7 were selected from the unaltered stratigraphic unit of the 11/17 outcrop comprising the lowest 200 cm of the outcrop (Figure 7). The fresh granodiorite is composed of mostly medium grained plagioclase, potassium feldspar, quartz, and biotite. There is also minor amounts of amphibole, apatite and magnetite as well as some very coarse-grained potassium feldspar present throughout the unaltered stratigraphic unit. In thin section, the grains have subhedral grain boundaries (Figure 8). There is some minor sericite zonation appearing on the feldspar and some of the biotite is chloritized.

Figure 7: The unaltered layer from the Highway 11/17 outcrop. A) The entire unaltered stratigraphic unit of the 11/7 outcrop grading up into the altered layer. B) Close up of the unaltered granodiorite showing the pink potassium feldspar and waxy plagioclase with minor amounts of quartz and biotite.
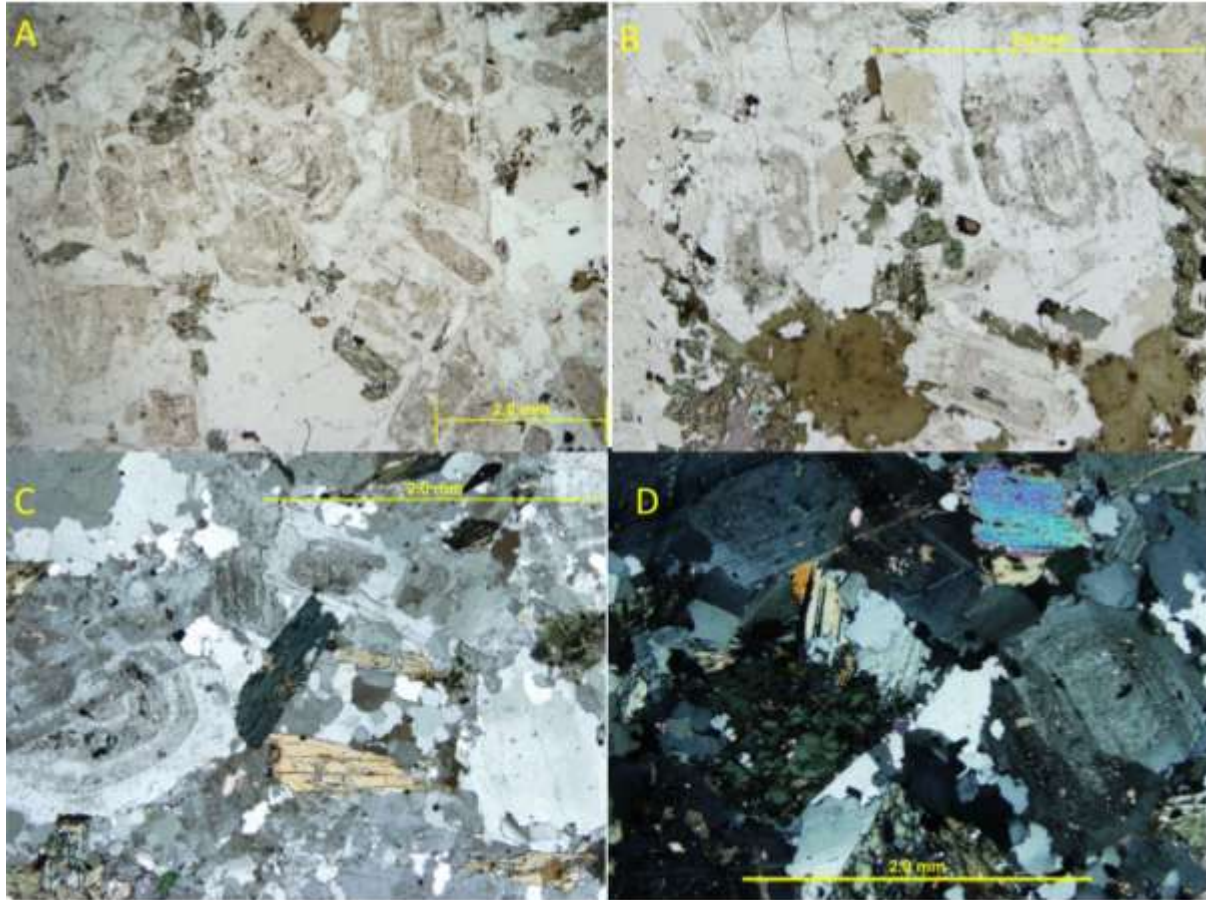
Figure 8: Photomicrographs of the unaltered stratigraphic unit of the Highway 11/17 outcrop. A and B) Plane polarized photomicrographs showing the minor alteration present replacing areas of the plagioclase as well as some of the biotite and amphibole. C and D) XPL photomicrographs showing the main mineral composition of the granodiorite. The minor amounts of alteration can be seen in the zoning of the plagioclase as well as chloritization of the biotite.

The granodiorite layer begins to show alteration at about 205 cm above the base of the outcrop. Samples 8, 9 and 10 were taken from the altered granodiorite layer that has taken on a green hue as opposed to the pink of the fresh samples. This change in colour is due to the replacement of the original minerals while retaining the original textures. The original plagioclase and potassium feldspar have been replaced by sericite, and the biotite is altered to

chlorite. In thin section, the fine-grained sericite have replaced the feldspar especially the highly fractured ones. The quartz also begins to show rounding of its edges.

Moving up the altered layer of the Highway 11/17 outcrop there is a very distinct and sharp transition at 226cm above the base in which the altered stratigraphic unit granodiorite begins to form large boulders or core stones (Figure 9A). The alteration has exfoliated the core stones removing the outside layers of the boulders. These layers consistently fill the spaces between the boulders giving the material surrounding the boulder a scaly pitted apperance. Hand samples show replacement of the feldspar by chlorite (Figure 9B). In thin section, the samples show extensive alteration compared to the slightly altered layer below the horizon, in that virtually everything except for the pre-existing chlorite and quartz has been replaced by chamosite (Figure 9C). The quartz also appears rounded and highly fractured. A core stone was also removed from the weathered layer. Hand samples and thin sections taken from the core stone have similar textures to the altered granodiorite from below the core stone horizon with a little more chamosite replacing the sericite (Figure 9D and F). Sample 12, which is from between the core stones, shows a secondary overprinting of the granodiorite. This sample is different from the other samples from this horizon in that it is more conglomeratic in nature comprised of rounded quartz with secondary carbonate replacing the sericite and chlorite of the altered granodiorite (Figure 9E).
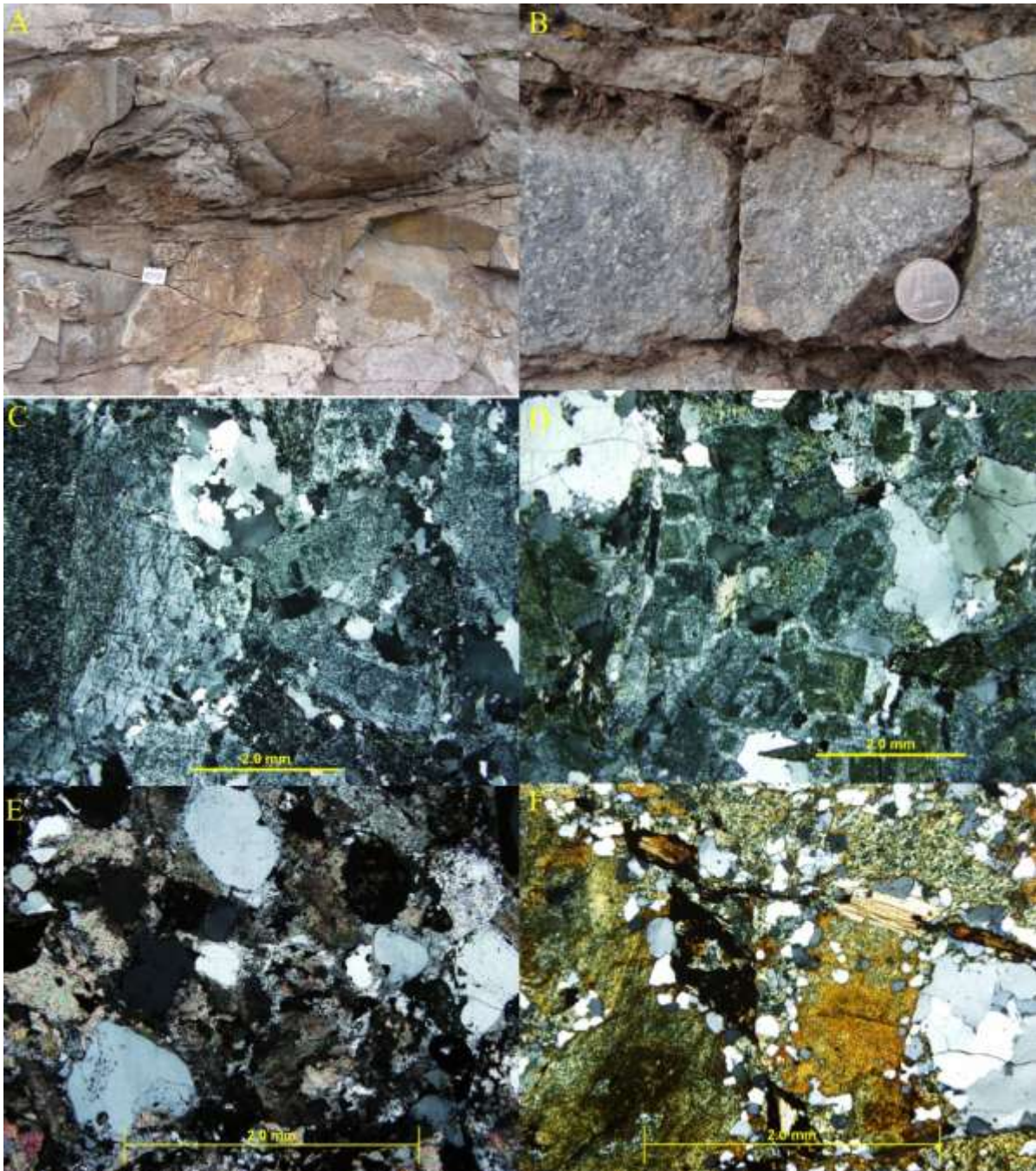
Figure 9: A) The altered stratigraphic unit of the Highway 11/17 outcrop showing the rounding of the granodiorite core stones. B) The pebble conglomerate layer overlying the altered zone that is derived from the breakdown of the original granodiorites. C and D) Photomicrographs of the altered layer below the highly altered boulder layer. The photos show that everything except for the quartz was replaced by fine-grained sericite, with some progressive replacement by chamosite. Photomicrograph E is from sample 12 showing secondary carbonate replacing the matrix. Photomicrograph F shows the chamosite overprinting everything except quartz in a sample of core stone from the boulder layer of the outcrop.

The top of the Highway 11/17 outcrop is composed of resedimented breakdown products of the core stones. Samples 14, 15 and 16 were taken from this horizon, which represents the Kakabeka Conglomerate overlain by Gunflint Formation grainstones. Samples 14 and 15 are comprised of an immature pebble conglomerate (sample 14) that fines into an immature clay-rich sandstone (samples 15). The pebble conglomerate is made up of fine-to pebble-sized quartz grains in a fine-grained sericite matrix. The sandstone is made up of fine-to coarse-grained quartz with minor amounts of clay between the quartz grains. The outcrop is capped off by a chert and carbonate grainstone of the basal Gunflint grainstone.

Scanning electron microscope backscatterd elemental mapping of Highway 11/17 samples reflect the change in the alteration up the stratigraphy of the outcrop (Figure 10). Samples 1,7,8 and 11 were selected to represent the change from the freshest granodiorite samples at the base of the outcrop to the most altered from the core stone horizon. Sample 1 represents the freshest granodiorite; the elemental maps show that K, as well as Na, are the predominant elements due to both K-feldspar and plagioclase being the dominant minerals present in the sample. The minor amounts of Fe and Mg are hosted in the biotite. Sample 7's map shows the first appearance of alteration, though K is still the dominant element in the sample. Fe and Mg have increased in concentration appearing as alteration products of the plagioclase and replacing biotite as it altered to chlorite. Sample 8 is from immediately above the transition from slighlty altered granodiorite to the very altered granodiorite. The alteration is marked by the overprinting of the entire sample by both Mg and Fe (there is no Mg or Fe in sericite) in chlorite replacing the biotite and felddspars. The minor amount of K left represents the last of the unaltered microcline with sericite replaced areas. Sample 11 was taken from the

core stone horizon and shows the most altered granodiorite. The alteration of the outcrop has

replaced everything except quartz and some accessory minerals with Fe and Mg.
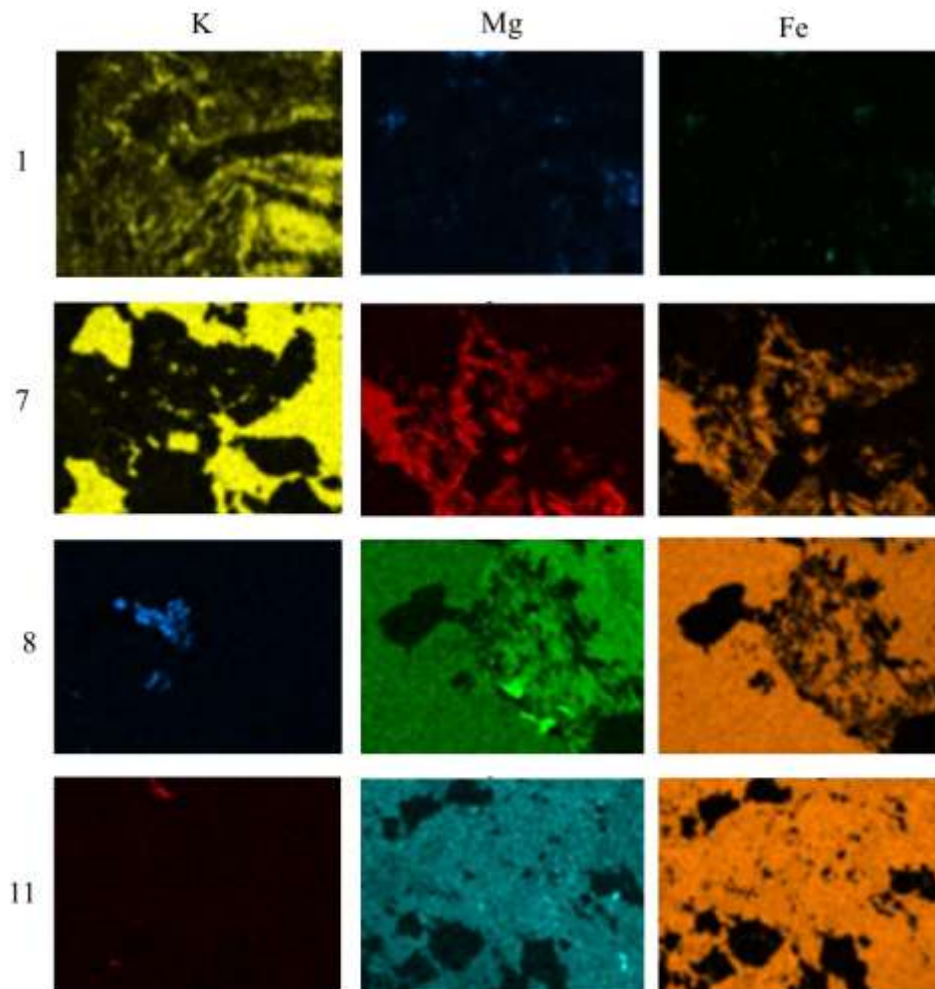
Figure 10: Scanning electron microscope (SEM) backscatter false colour elemental maps of K, Mg and Fe in samples 1,7,8,11 from the Highway 11/17 outcrop. Sample 1 is fresh material at the base of the outcrop. The other samples are from progressively higher levels culminating in sample 11 from the highly altered zone.

3.1.2 Kakabeka Falls Outcrop

The outcrop present on the shoulder of Highway 580, outside of Kakabeka Falls

Provincial Park, consists of a basement exposure surface comprised of an Archean granitic body.

The granitic body is overlain by a siliceous microbialite with stromatolites, capped by an

ankerite grainstone (Figure 11). The unaltered stratigraphic unit of this outcrop is composed of

granodiorite (Figure 12A). Sample KF-11-01 was taken from the base of the outcrop and is a

white granodiorite comprised of holocrystalline, medium-grained crystals, predominantly of

quartz, plagioclase, and biotite (Figure 12 B and C). Petrography shows that there are also minor

amounts of microcline present in the sample (Figure 12 D).
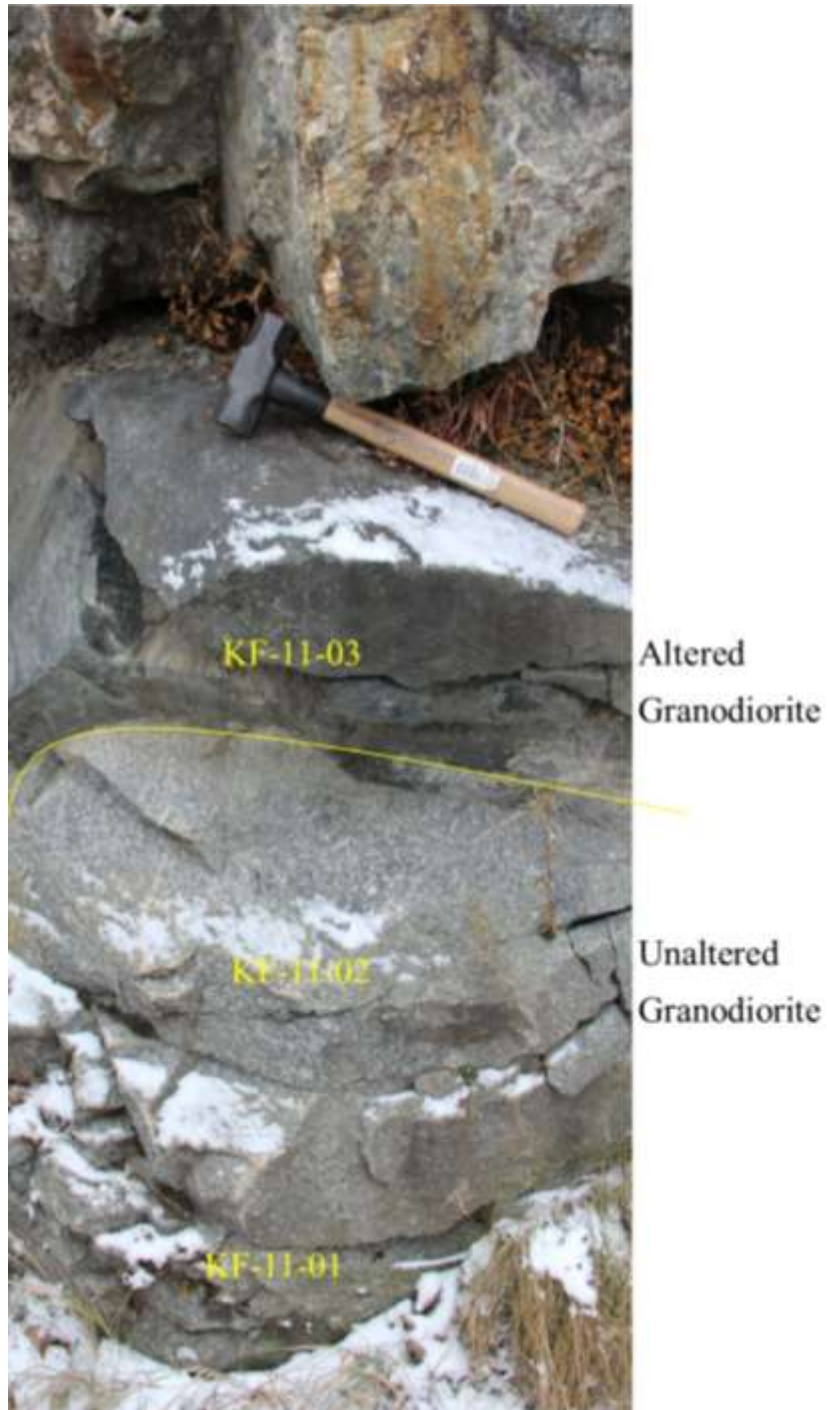
Figure 11: A stratigraphic section with approximate sample locations on the exposure surface present near Kakabeka Falls.The alteration stratigraphic unit is noted by the distinct change in color from the grey pink granodiorite to the dark green replacement minerals.
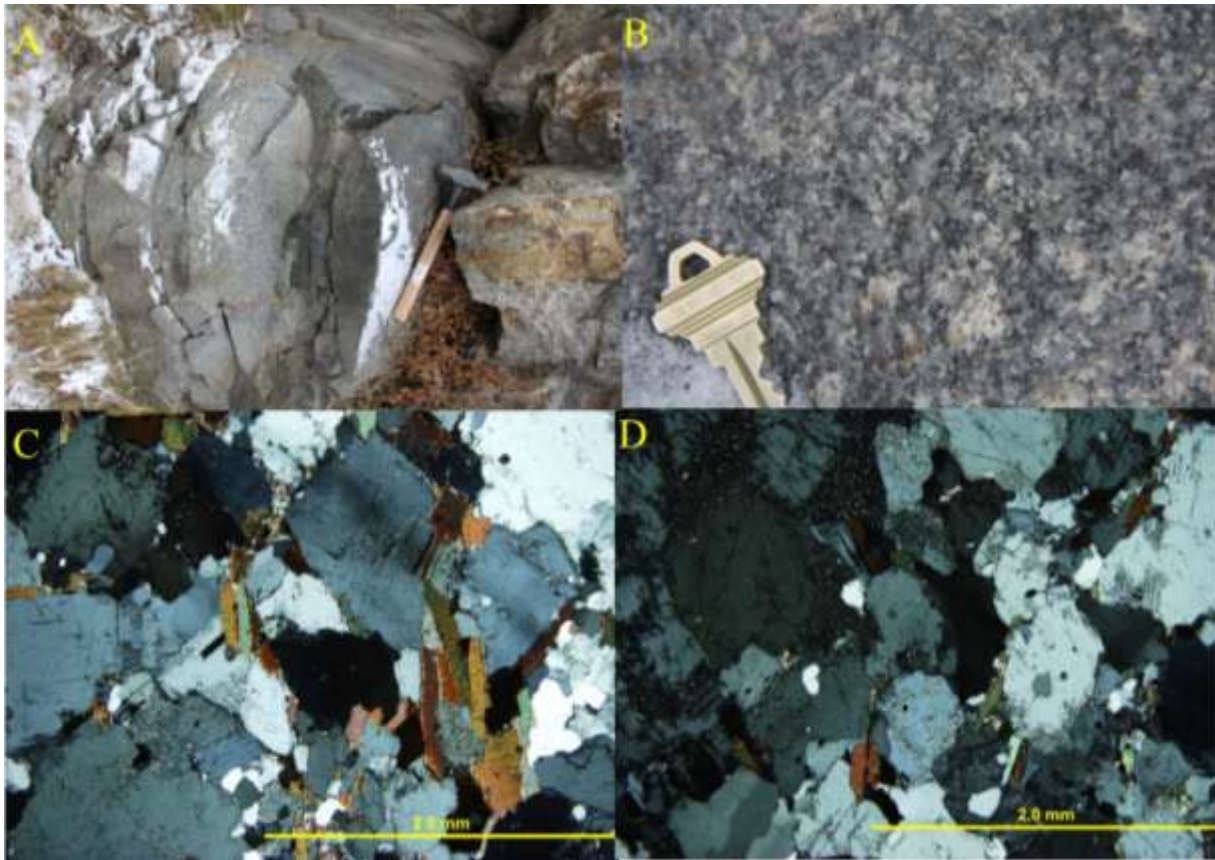
Figure 12: A) The unaltered stratigraphic unit of the Kakabeka Falls outcrop on the shoulder of Highway 588 outside of Kakabeka Falls. B) This figure is a close up view of the unaltered layer of the Kakabeka Falls outcrop showing the waxy plagioclase, glassy quartz, and the black biotite. C and D) Photomicrographs of the unaltered stratigraphic unit from the Kakabeka Falls outcrop showing the modal composition of the stratigraphic unit.

The alteration stratigraphic unit of the Kakabeka Falls outcrop is seen in the top 70cm of the granodiorite (Figure 13A). The alteration is marked by the change in colour from the fresh white granodiorite to a waxy yellow colour of the feldspar seen in KF-11-02 (Figure 13B). The progressively altered granodiorite in the top 10cm of the unit has a greenish hue. KF-11-03 was taken from this area. The visible alteration has replaced the feldspar and biotite with the green chamositie material. In thin section, the alteration minerals are chlorite replacing the feldspar and

biotite (Figure 13 C and D).
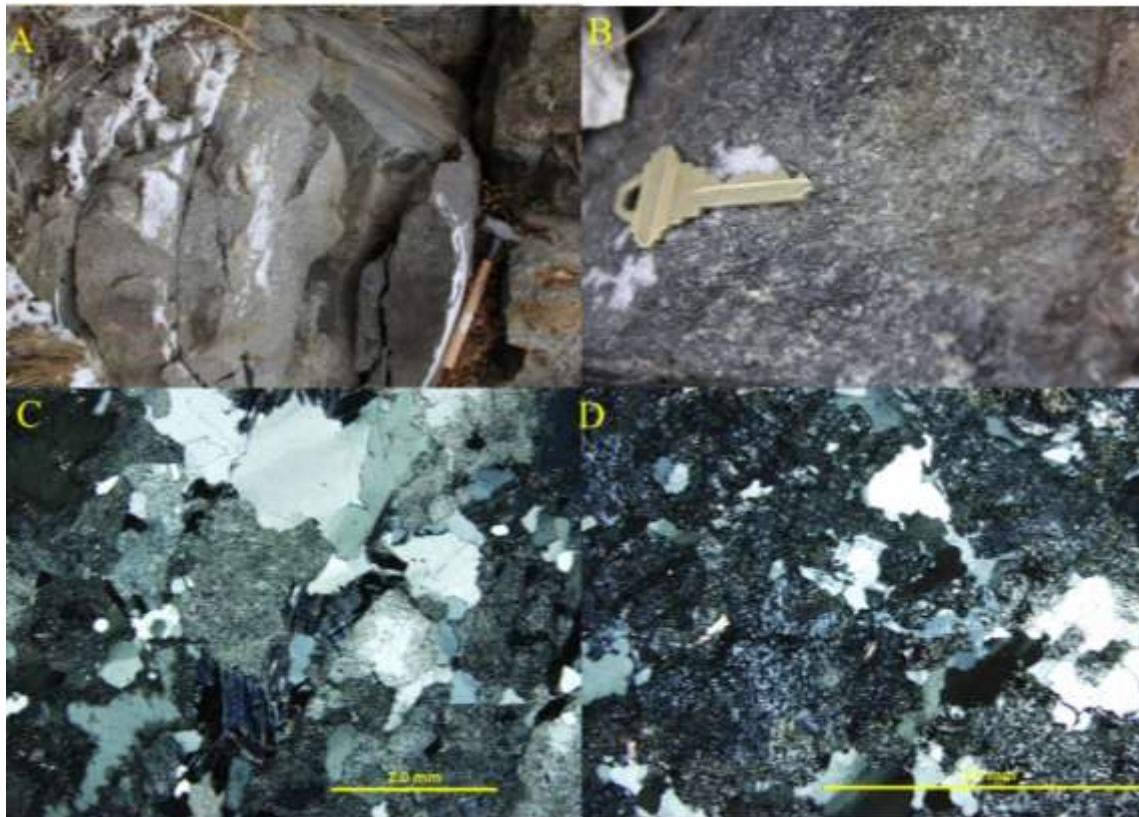
Figure 13: The alteration stratigraphic unit of the Kakabeka Falls outcrop. A) There is a lack of physical change in the altered portion of the outcrop, but the alteration can be seen (B) as the feldspar are replaced by fine-grained yellow or green minerals. C) and D) are photomicrographs of the alteration layer from Kakabeka Falls. Figure C shows the transitionary sample KF-11-02 from between the fresh and altered samples. The feldspar have been replaced by fine-grained mica, and the biotite have started to alter to chlorite. D) Sample KF-11-03, was selected from the altered layer and shows that everything except for the quartz has been replaced by the fine-grained chlorite.

3.1.3 KOA Hill Outcrop

The third basal outcrop studied was on the shoulder of Highway 11/17 across from the KOA Park outside of Thunder Bay. Unlike the other Highway 11/17 and Kakabeka Falls' outcrops, the unaltered stratigraphic unit of the KOA hill outcrop is not igneous in nature, but a metasedimentary unit (Figure 14). This stratigraphic unit has a distinct foliation, which is a vertical schistosity striking at 70˚ (Figure 15A). The samples, KOA-01 to 03, show that the unaltered metasedimentary rocks are made up of fine-grained quartz and chlorite. These sediments have some overprinting by larger quartz grains. The altered stratigraphic unit of this outcrop is 1.5m above the base. The alteration is present as a distinct change in the foliation present. The alteration changes from the vertical schistosity to one with no distinct foliation direction. In thin section the alteration is reflected by an increase in the quartz overprinting. Sitting on top of the altered stratigraphic unit is a conglomerate unit that is comprised of allochthonous clasts, including slate, quartz, and feldspar. The conglomerate becomes finer grained up the stratigraphy forming a conglomerate comprised of clast hosted in a sericite matrix. The Gunflint is comprised of medium-grained ankerite grainstone with fine-grained hematite.
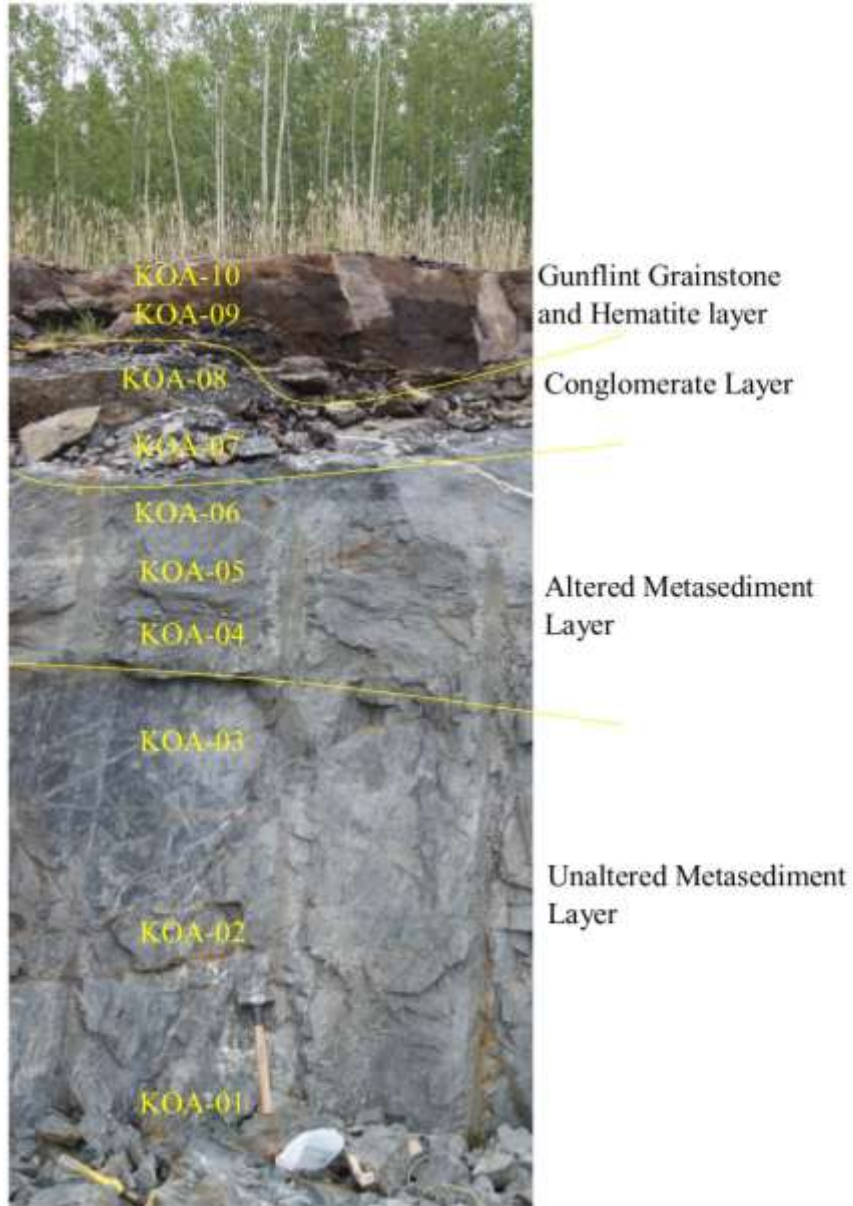
Figure 14: Stratigraphy of the exposure surface forming the KOA Hill outcrop with the approximate location of samples.
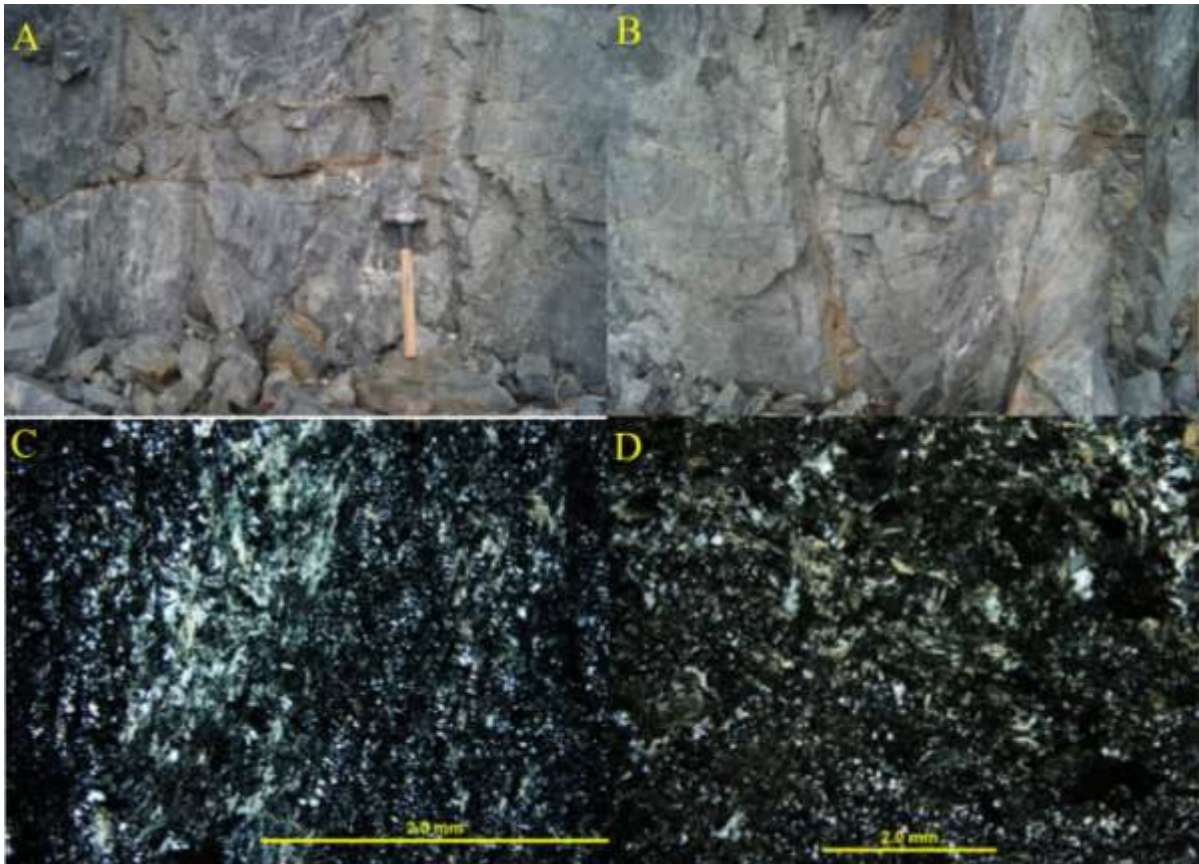
Figure 15: A) The unaltered stratigraphic unit of the KOA Hill outcrop on the shoulder of Highway 11/17 east of Thunder Bay Ontario. B) The vertical schistosity present at the KOA outcrop. C and D) Photomicrographs of the KOA Hill outcrop showing it is composed of fine-grained quartz with mica defining its foliation.
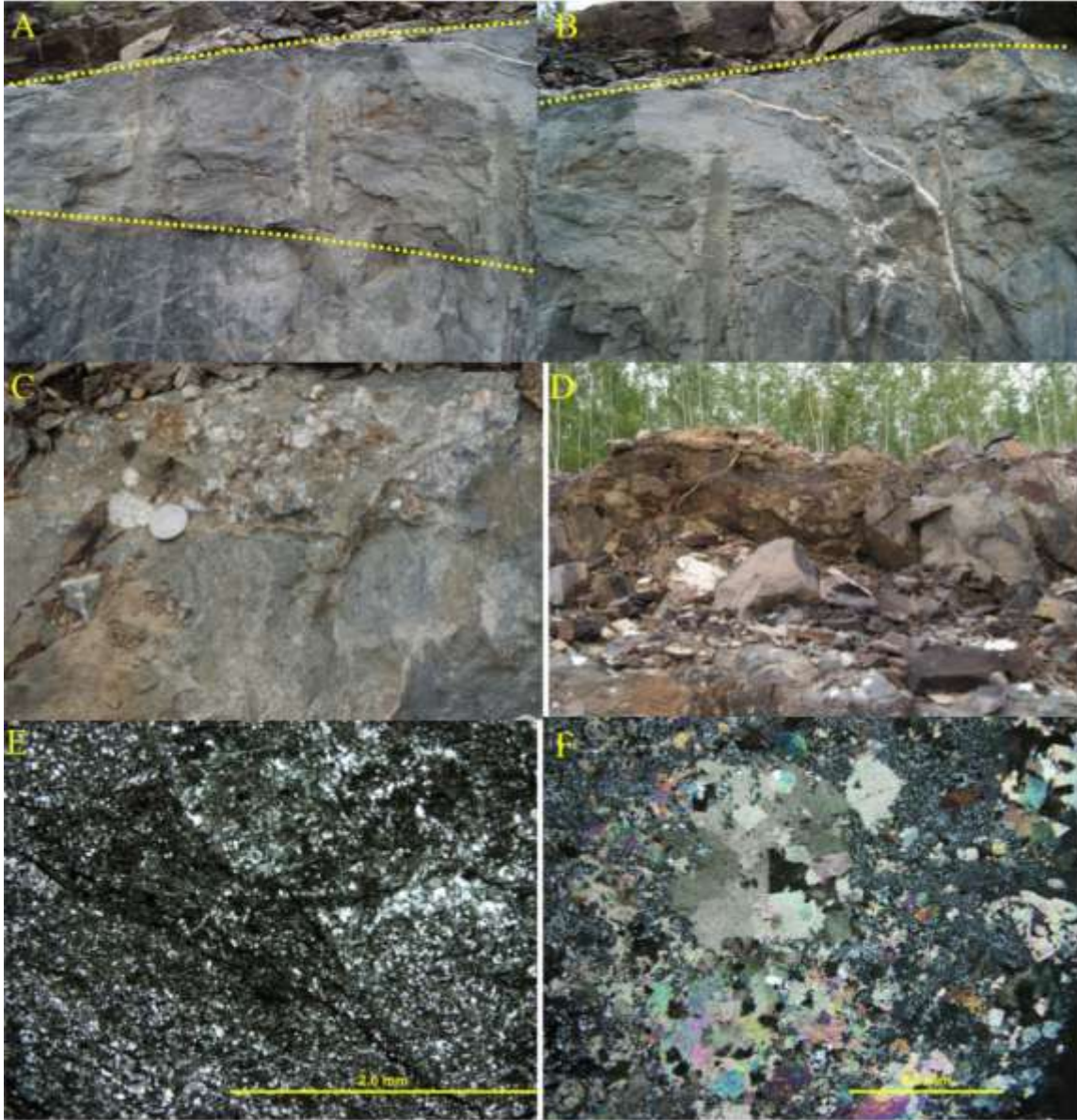
Figure 16: The altered stratigraphic unit of the outcrop at KOA Hill on the shoulder of Highway 11/17 outside of Thunder Bay. Photos A and B are of the altered layer with A showing the change in schistosity from the vertical schistosity of the unaltered layer to the rubble flaky layer of the altered stratigraphic unit.C) The conglomerate layer overlying the altered zone showing the allochthonous clasts. D) Hematite/grainstone present on top of the KOA Hill outcrop. E) Photomicrograph of the altered stratigraphic unit showing quartz overprinting, as well as the fracturing of the original material. F) Photomicrograph of the grainstone layer showing carbonate and quartz replacing the grainstone layer.

3.2 Whole Rock Geochemistry of the Basement Exposure Surfaces

3.2.1 *Highway 11/17 outcrop*

Alteration of an outcrop can be tracked using the chemical index of alteration (CIA) (Nesbitt and Young, 1982), which measures the amount of loss of Na, K and Ca relative to Al. Fresh rocks score 35 to 50 whereas totally leached rocks score 100. Here these values are used along with an A-CN-K feldspar ternary diagram, which employs the molar components of feldspar, to track the loss and gain of these components during alteration (Nesbitt, 2003). The calculated CIA values for the samples collected from the Highway 11/17 outcrop show that samples 1-7 are fresh having CIA values from 39 to 41. The altered samples, 8 to 15, with the exception of sample 12, which has had secondary addition of Ca, have values ranging from 79 at the beginning of the alteration horizon to 91 from the samples in the core stone horizon. Figure 17 is a Feldspar Diagram for these samples. The diagram reflects the alteration present in the CIA values. Samples 1-7 all have fresh compositions and they plot in the middle of the diagram, where fresh granodiorite lies. With increasing alteration samples 8 and 9 become depleted in CaO, Na_2O, and, to a lesser extent, K_2O. The most altered samples, 10-15, plot along the Al_2O_3 - $CaO+Na_2O$ tie line. The two anomalous samples that plot at or near the $CaO+Na_2O$ vertex are samples 16 and 12 respectively. Sample 12 plots on the $CaO+NA_2O$ tie line and is from the altered material between the rounded granodiorite core stones and exhibits replacement of the matrix by secondary carbonates, increasing the CaO content. Sample 16 is from the grainstone layer with significant carbonate.
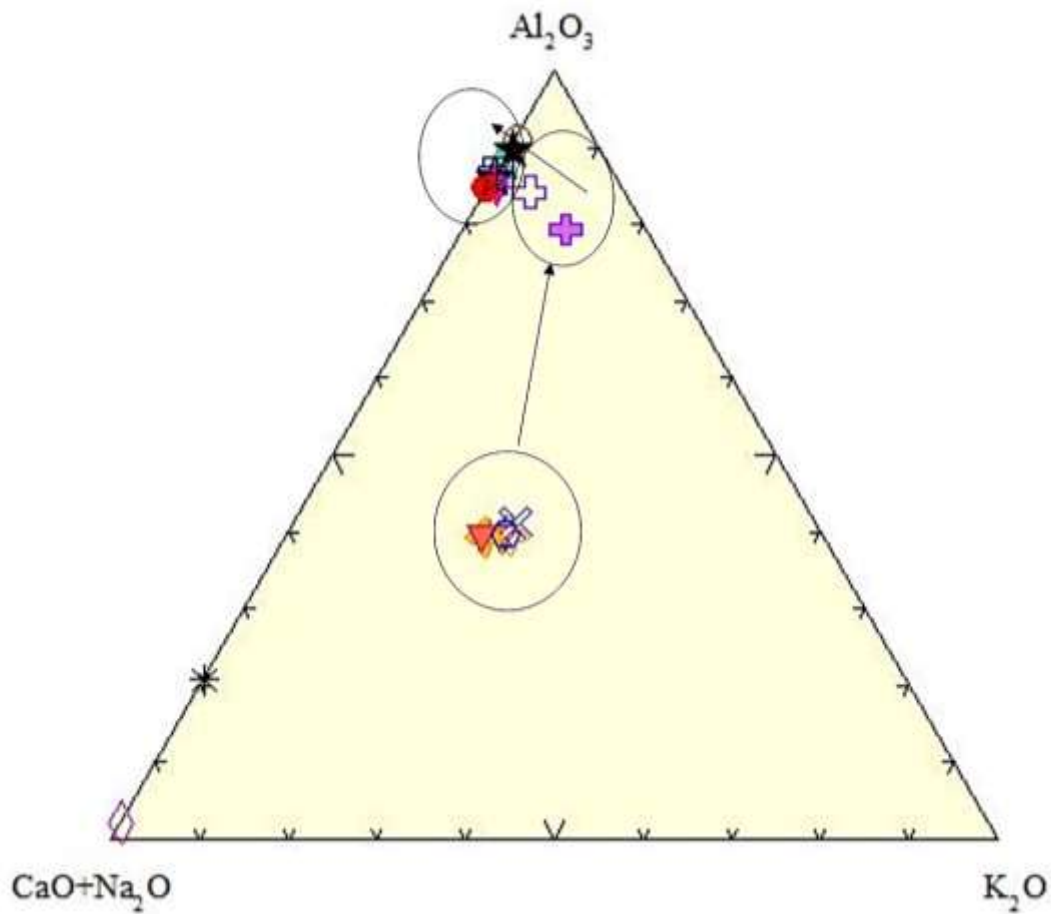
Figure 17: The Al_2O_3-(CaO+Na_2O)-K_2O feldspar plot for the Highway 11/17 samples. The fresh samples plot in the middle of the diagram with the alteration trend first moving towards Al_2O_3, with less loss of K than Na and Ca. Compositions then move towards the CaO+Na_2O-Al_2O_3 tie line and finally towards the Al_2O_3 vertex along the CaO+Na_2O tie line, showing that the alteration of the outcrops was substantial. The two anomalous samples that plot at and near the CaO+Na_2O vertex are samples 12 and 16 which come from material that was replaced by carbonate and the carbonate grainstone (open diamond). Arrows denote the weathering trend of the fresh granodiorite samples.

Plotting the mafic components of the whole rock geochemistry of the samples also reflects the alteration pattern. Figure 18 shows the same division of samples as in the feldspar diagram in that the fresh samples, 1-7, plot with consistent values as granodiorites. The altered products all plot close to the Fe_2O_3+MgO tie line with sample 8 (closed-cross) showing the least

alteration of members of this group, similar to Figure 17 where sample 8 and sample 9 (open

cross) plot with less K loss than the main group of altered samples. The plot show that the

depletion of the K, Na and Ca as seen in the feldspar diagram is balanced by an increase in Fe_2O_3

and MgO content. The two anomalous samples are again sample 12 and 16 which have been

replaced by secondary carbonate (Sample 12) or are recrystallized carbonate grainstone (Sample

16).
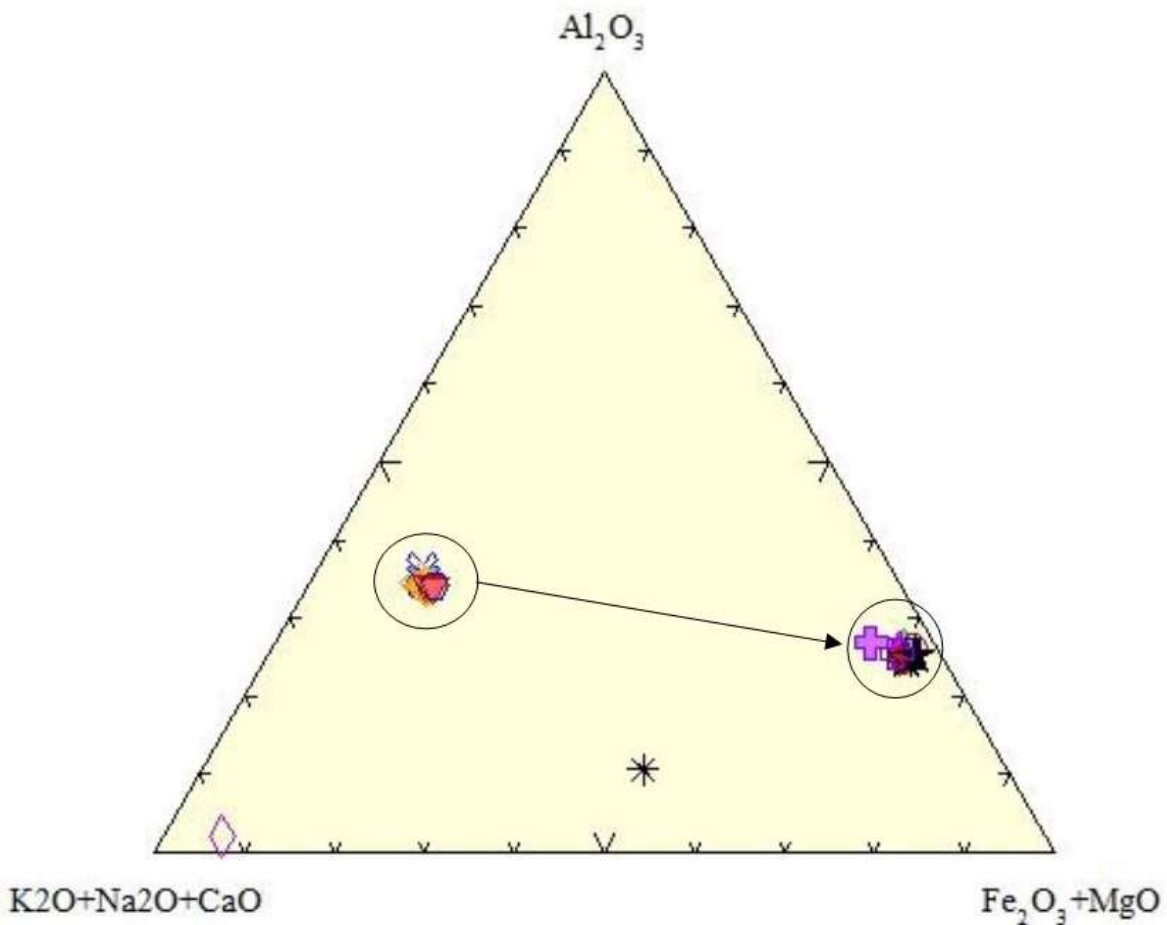
Figure 18: The A-CNK-FM mafic diagram, which plots the change in the mafic components of
the altered outcrop. The diagram shows that the fresh samples are plotting where fresh
granodiorite is expected to plot. The altered samples have grouped along the Al_2O_3-Fe_2O_3+MgO
tie line, this shows that the Ca, Na and K are being replaced by Fe and Mg. Samples 12 and 16
are anomalous samples with high CaO from the presence of carbonate. Line denotes the
alteration trend of the fresh granodiorite.

The mass percent change was calculated from the whole rock chemistry. These plots show the changes that have occurred during the alteration of the granodiorite. The mass loss plots give a better visual representation of the alteration than CIA and A-CN-K diagrams. Using the first sample as the freshest sample the plot reflects whether the overlying granodiorite has undergone the addition of oxide mass (positive values) or undergoes a loss in oxide mass resulting in negative values. Figure 19 is a plot of the percent mass change in the Fe_2O_3 content of the samples collected from the outcrop stratigraphy. The plot shows that samples selected from the fresh, unaltered stratigraphic unit all plot at the zero percent line. As alteration becomes present in the hand samples the Fe_2O_3 content increases to 800% and continues to climb to about 1000%.
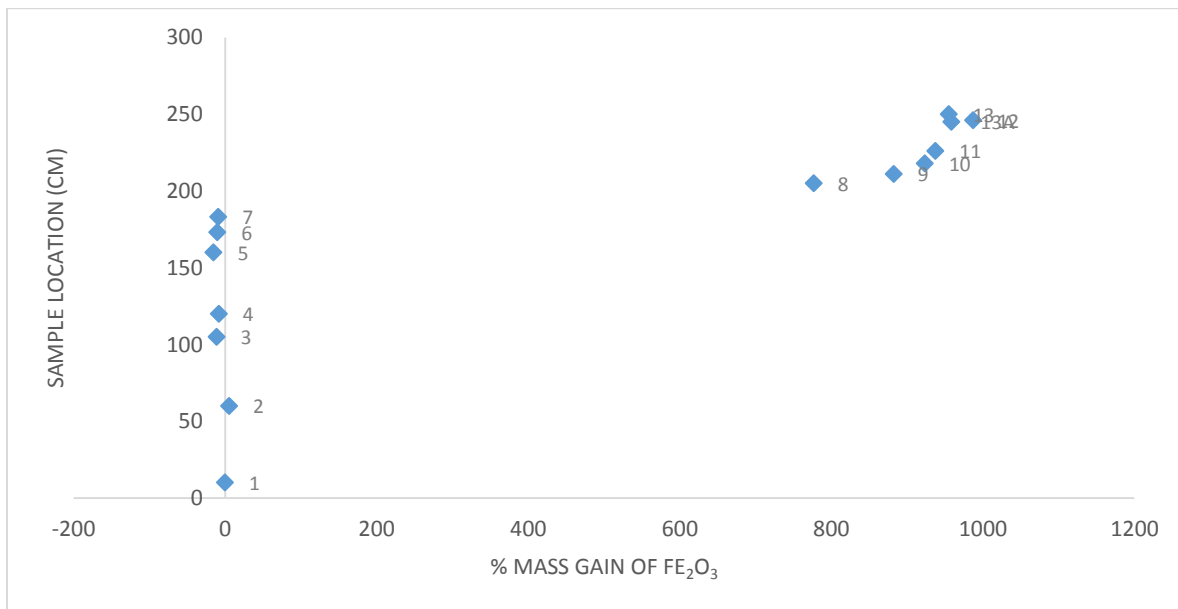
Figure 19: Plot of the percent mass change in iron of samples collected from the Highway 11/17 outcrop.

Figure 20 shows the percent mass change in K_2O for the 11/17 samples. The plot exhibits the opposite trend to that of the Fe_2O_3 mass change. The unaltered samples 1-7 plot near the zero percent mark again, but as soon as alteration appears in sample 8 the K_2O mass percent become depleted by 100%. The rest of the samples will decrease to almost 128% loss of K_2O within the altered samples. Again sample 12 shows a drastic decrease in K_2O concentration, due to the overprinting of carbonate in the sample.
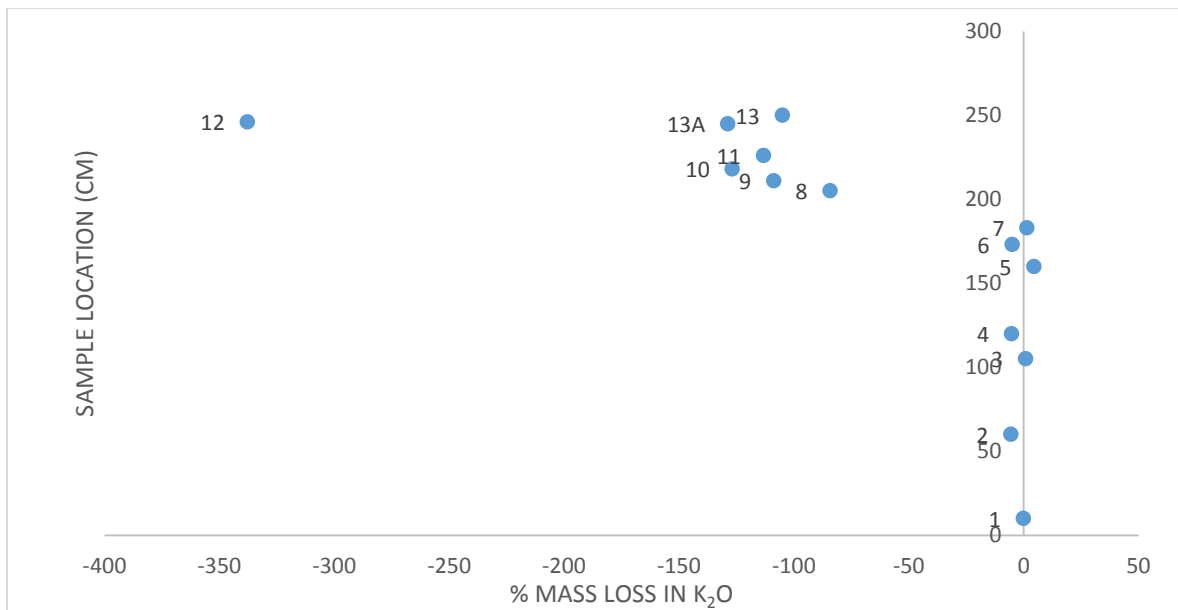
Figure 20: The depletion in K_2O mass in the samples collected from Highway 11/17 outcrop. The plot shows that fresh samples all plot near the zero percent line. Samples 8-13 exhibit alteration present with depletion of K_2O. Sample 12 is the sample that has been replaced by secondary carbonate.

Figure 21A shows the ratio of the mean of the altered portion of the oxide divided by the mean of the Al_2O_3 portion in the altered samples. This is plotted against the ratio of the mean of the unaltered portion of the same oxide divided by the mean of the of the Al_2O_3 in the unaltered portion. The plot shows the actual gain and loss of selected oxides. A line from the origin with a slope of one reflects the immobility of an oxide. The oxides plotting along or near the line show immobility compared to those oxides that plot away from the line. The oxides that show gains

during alteration plot above this line. These oxides include Fe_2O_3, which has the most drastic increase during alteration, MgO, and MnO. The oxides that plot beneath the line had a loss during alteration. These oxides include Na_2O, CaO, and K_2O.
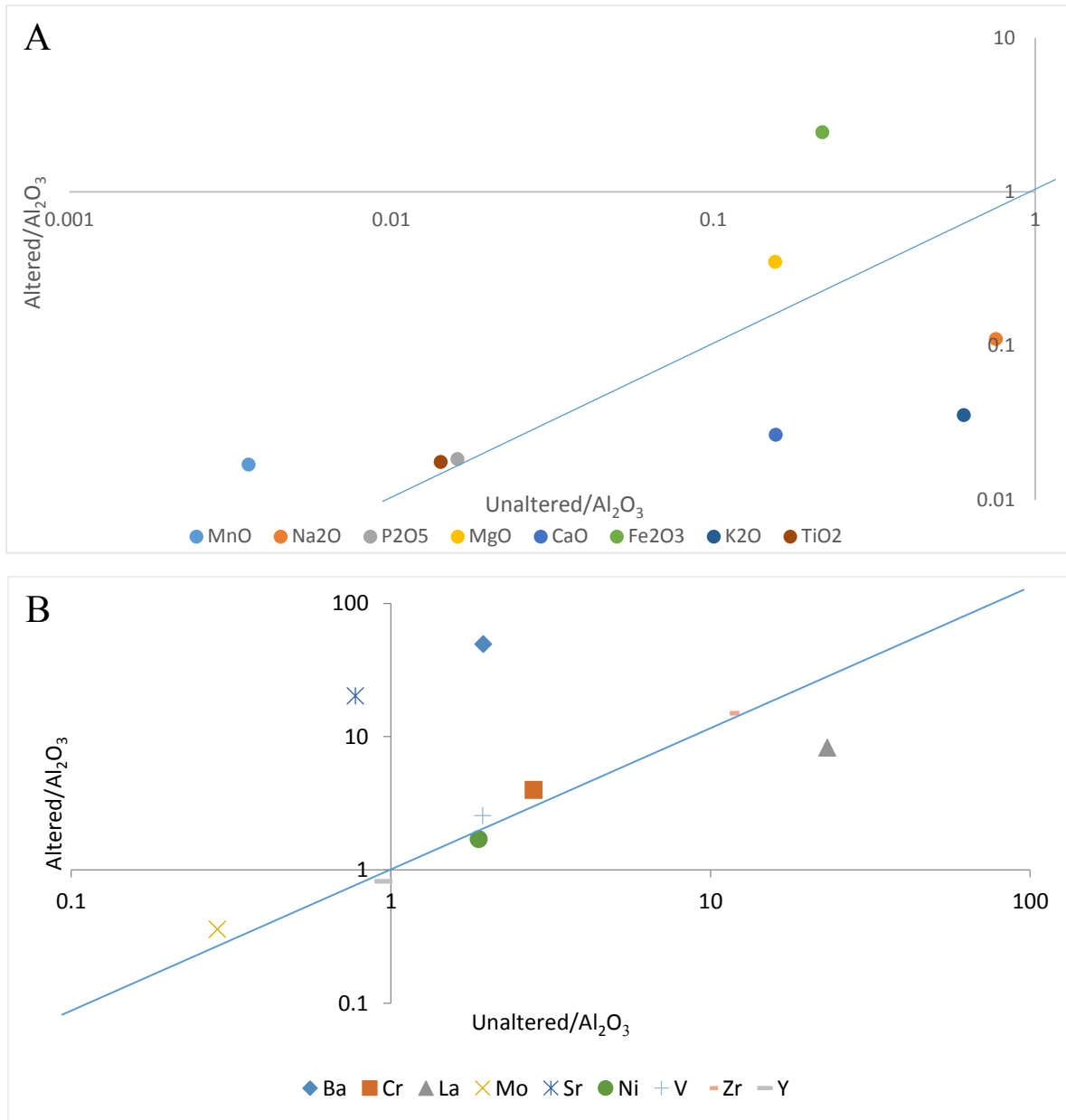
Figure 21: A) Scatter-plot showing the ratio of the mean of an oxide in the altered samples divided by the mean of the Al_2O_3 in the altered samples plotted against the ratio of the mean of an oxide in the unaltered samples divided by the mean of the of the Al_2O_3 in the unaltered samples. B) The plot of the trace elements using the same method described above.

The second plot reflects the same construction as the oxide plot above except that it uses the trace elements from the Highway 11/17 samples (Figure 21B). This plot shows that Ba, Sr and La plot away from the 1:1 line showing there is a gain in composition during alteration for both Sr and Ba, whereas there is a loss in La during alteration. The elements and oxides that were immobile are: Al_2O_3, TiO_2, P_2O_5, Cr, Mo, Ni, V, Y and Zr.

3.2.2 Kakabeka Falls

The feldspar diagram for the samples collected from the Kakabeka Falls outcrop shows a standard weathering pattern for granodiorite samples. The alteration of this outcrop is reflected in a more uniform trend (Figure 22). This trend shows that the fresh sample (green triangle) has more Al_2O_3 and less K_2O than the granodiorite in the 11/17 site. In fact even the relatively fresh sample has a CIA of 58 indicating that it has lost some K, Na and/or Ca. The position of sample KF-11-02 (open square on the figure) shows that alteration has begun to deplete the sample in both CaO and Na_2O. The most altered sample, KF-11-03, has become extensively depleted in both CaO and Na_2O.
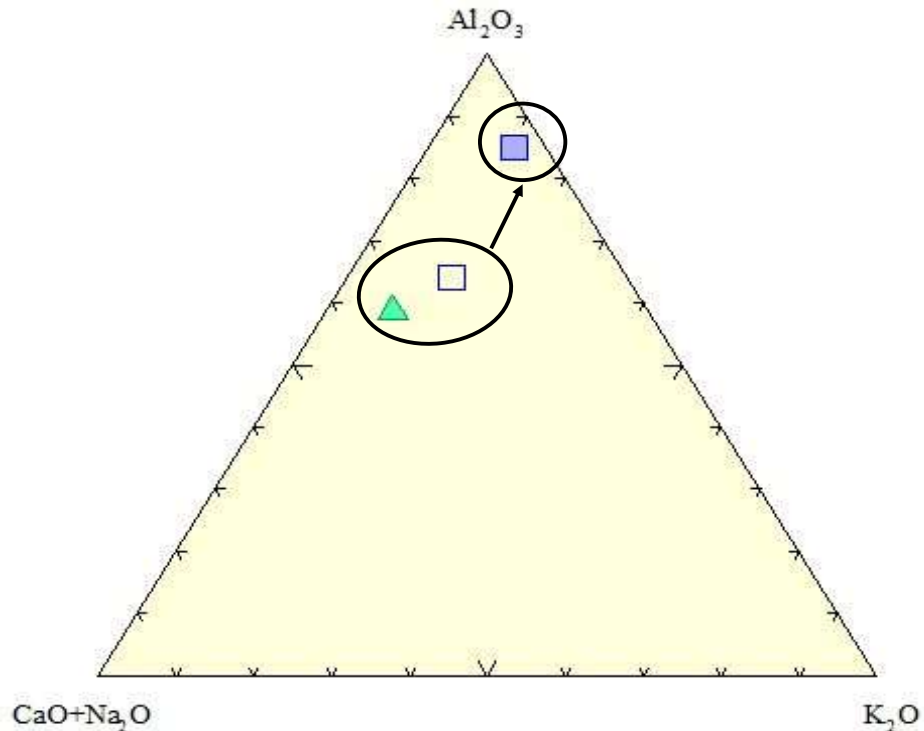
Figure 22: The Al_2O_3-CaO+Na_2O-K_2O feldspar diagram for the Kakabeka Falls samples. The fresh sample KF-11-01 (Green triangle) plots with above standard CaO+Na_2O and Al_2O_3 and low K_2O. As alteration increases up the stratigraphy, the sample KF-11-02 (open square) begins to show a depletion in CaO and Na_2O. Sample KF-11-03(closed square) represents the most altered sample showing that alteration has depleted most of the CaO and Na_2O.

The mafic diagram for the Kakabeka Falls outcrop shows the alteration of the outcrop exhibits a similar pattern to that of the Highway 11/17 mafic diagram in that the loss of Ca and Na are balanced by the addition of Fe and Mg (Figure 23).
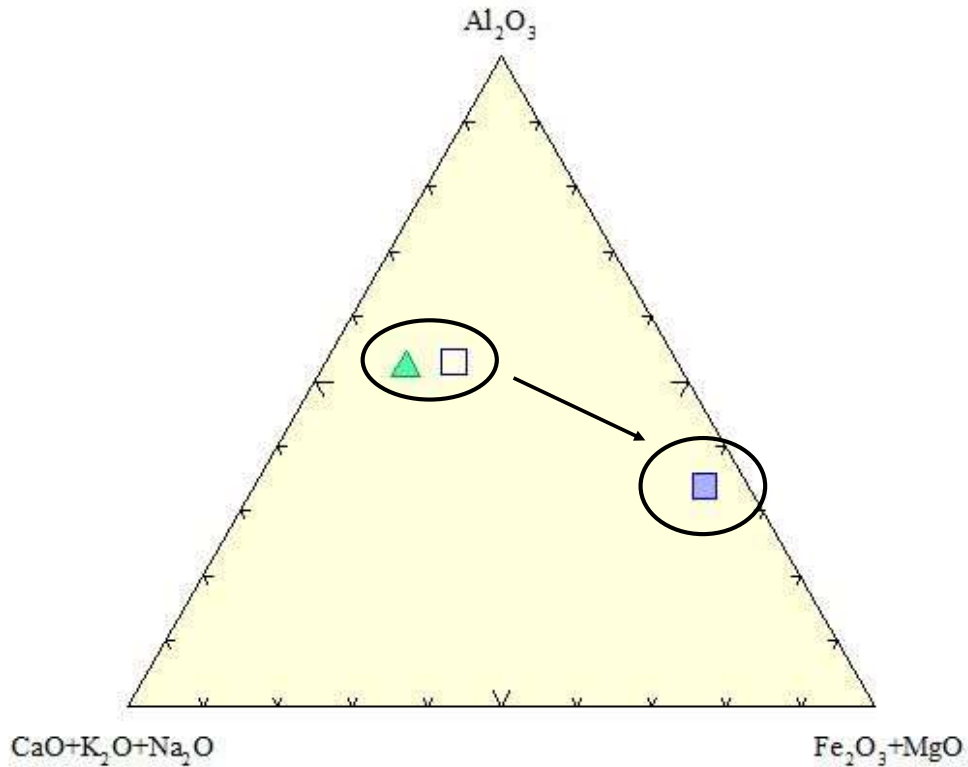
Figure 23: The mafic diagram for the Kakabeka Falls outcrop. The diagram shows that the increase in alteration that depletes the samples of CaO and Na_2O is balanced by an increase in Fe and Mg.

The Fe_2O_3 percent mass gain plot for the samples from the Kakabeka Falls outcrop (Figure 24) shows the increase in Fe_2O_3 going from the freshest sample KF-11-01. Sample KF-11-02 is representative of the slightly altered portion of the outcrop and has an increase in Fe content of 43% compared to the most altered sample that increased by 930% (Figure 24).
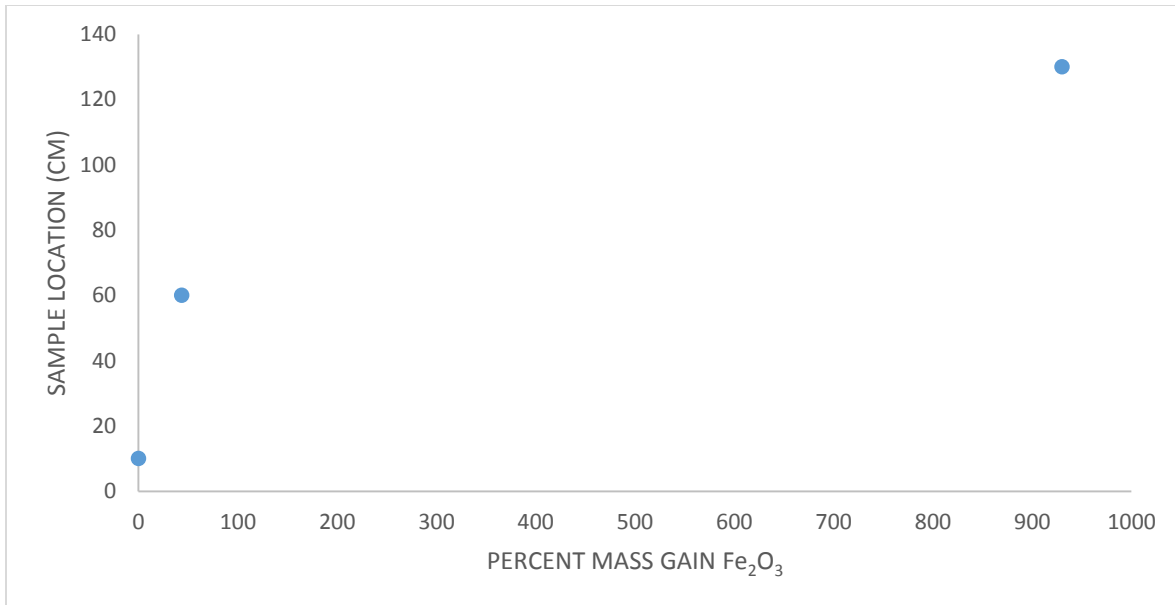
Figure 24: The percent mass gain of Fe_2O_3 in the samples from the Kakabeka Falls outcrop.

Figure 25 shows the percent mass loss of CaO from the Kakabeka samples due to alteration of the outcrop. The alteration depletes the fresh samples by 50% in the slightly altered samples to 95% in the completely altered sample.

Ratio plot for samples from the Kakabeka Falls outcrop area shows that, like the 11/17 outcrop, there is a drastic increase in the Fe_2O_3 content, and to a lesser extent Mg content, as well as a drop in the CaO and Na_2O. The plot shows that the Kakabeka Falls outcrop does not have a significant change in K_2O (Figure 26A). Figure 26B is a similar plot to that of the oxide plot above it but is made using trace element data. The trace element data shows that there is some alteration especially in Cr and Ni, which are slightly enriched away from the 1:1 line, and Sr, which is depleted. Both plots show that Al_2O_3, TiO_2, P2O5, La Mo, V, Y are the immobile elements within the Kakabeka Falls samples.
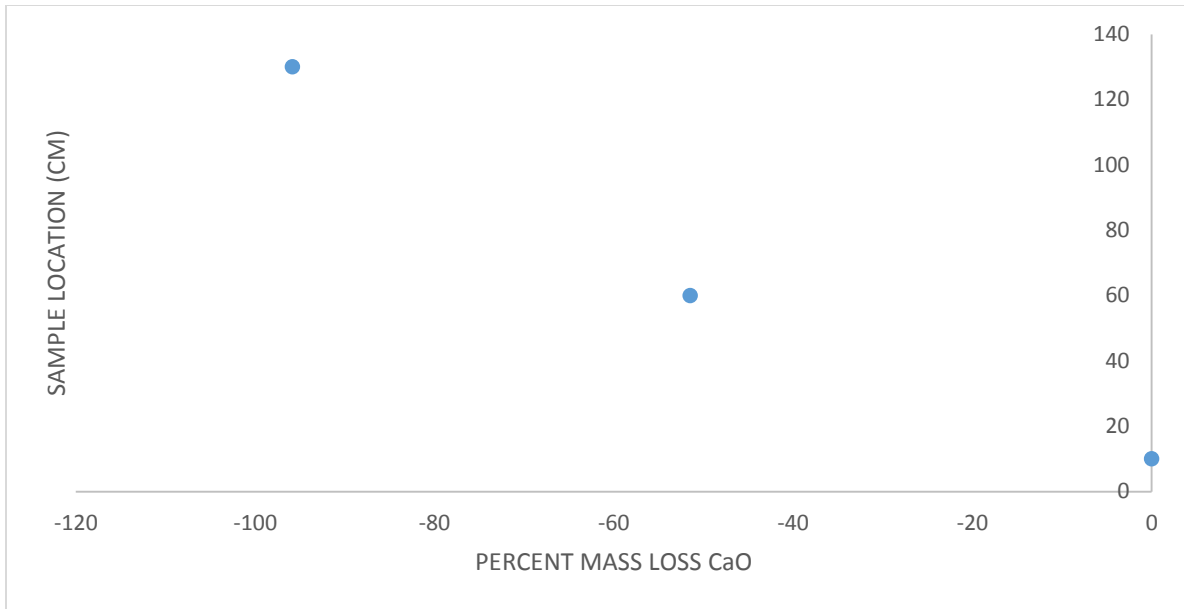
Figure 25: The percent mass loss of CaO in samples from the Kakbeka Falls outcrop.
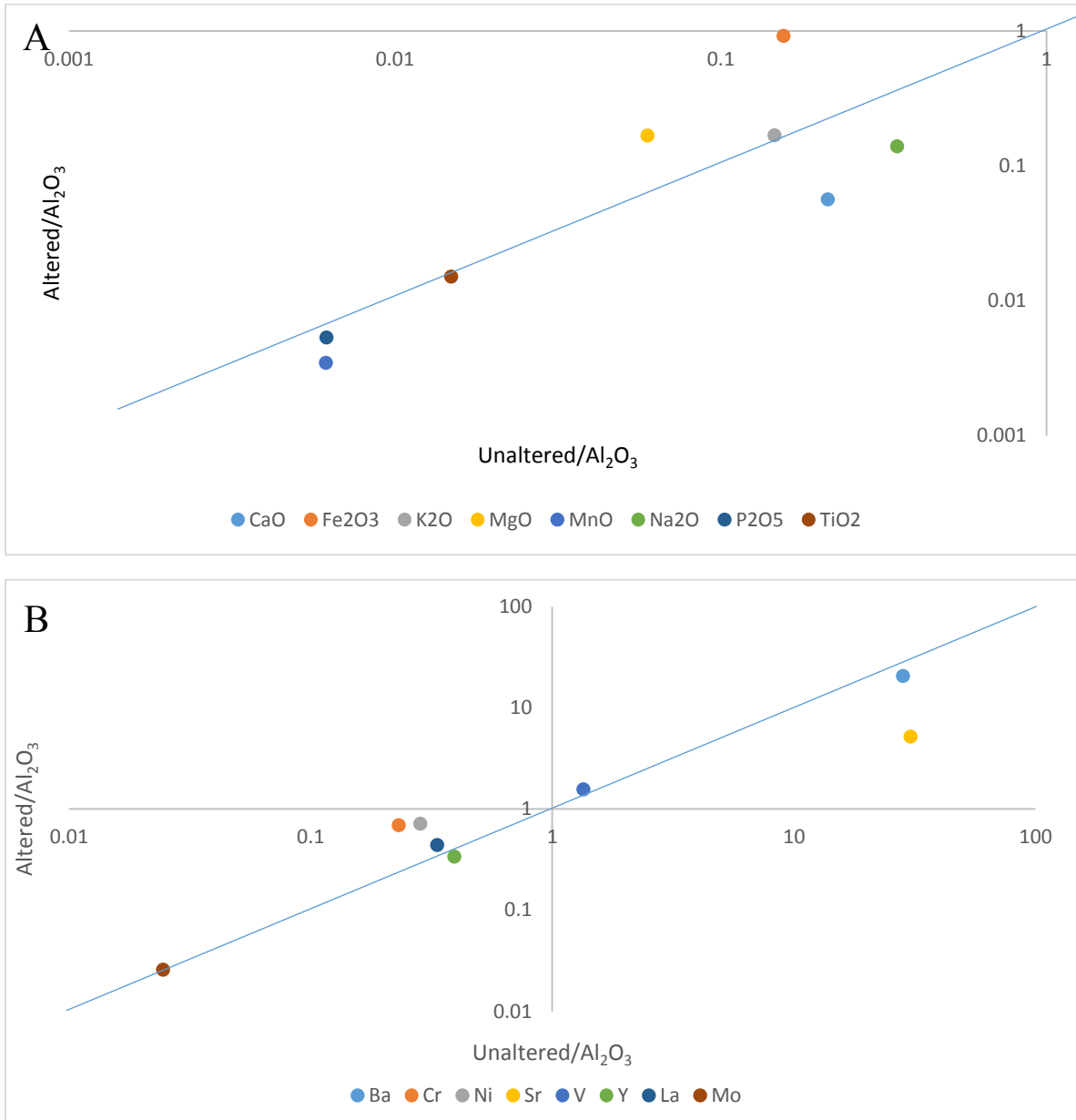
Figure 26: Altered vs. unaltered plot for the Kakabeka Falls outcrop. A) The major oxides B) The trace elements.

.

3.2.3 KOA Hill outcrop.

The Archean metasedimentary rocks of the KOA Hill outcrop are different from the two previous outcrops and this can be seen in the alteration trend present in the KOA Hill's Al_2O_3-$CaO+Na_2O+K_2O$ feldspar diagram (Figure 27). As the Archean basement is composed of metasandstones, which contain preweathered debris, the fresh samples plot with very low Ca, Na and K concentrations. The samples from the altered horizon plot near the Al_2O_3-K_2O tie line horizontally across from the fresh sample cluster. The sample taken from the conglomerate with chlorite and minor amounts of sericite at the top directly below the hematite and grainstone layer plots with low Ca, Na and K. The two anomalous samples are from the top of the outcrop and represent sample KOA-09 (asterix) which is the massive hematite layer and sample KOA-10 (open star) the grainstone layer overlying the hematite layer.
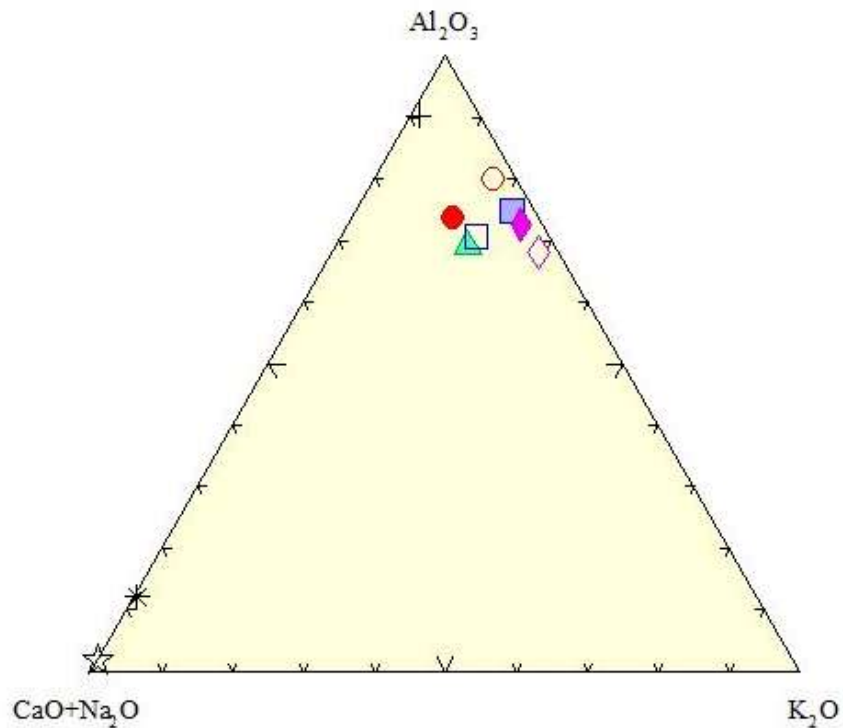
Figure 27: The feldspar diagrams for the samples from KOA Hill.
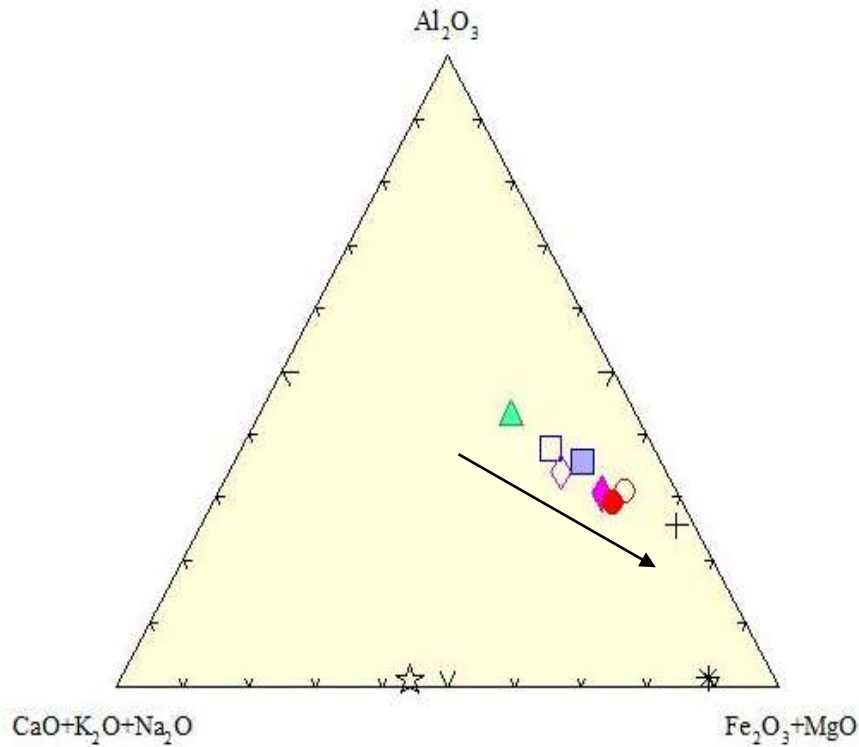
Figure 28: The mafic diagram for the samples taken from the KOA Hill outcrop.

The mafic diagram for the KOA Hill samples exhibits a clearer alteration trend than the feldspar diagram (Figure 28). The plot shows a gradual increase in Fe_2O_3 and MgO up through the metasedimentary rocks and into the conglomerate. The sericite conglomerate sample that appears away from the alteration trend in the feldspar diagram plots along the alteration trend here. The two anomalous samples present in the diagram are the two samples KOA-09(asterix) and KOA-10 (open star) which come from the massive hematite layer and the grainstone layer respectively.

Figure 29 contains the alteration plots constructed in the same manner as the plots above. Figure 29A is of the major oxides, showing that both CaO and Na_2O are depleted and Fe_2O_3, MnO and P_2O_5 slightly enriched during alteration. The trace element alteration plot (Figure 29B) shows that La is the only trace element that is enriched. Both Ba and Sr are depleted during

alteration. The two plots shows that Al_2O_3, TiO_2, MgO, P_2O_5, MnO, V, Cr, Y, Mo and Ni are all immobile.
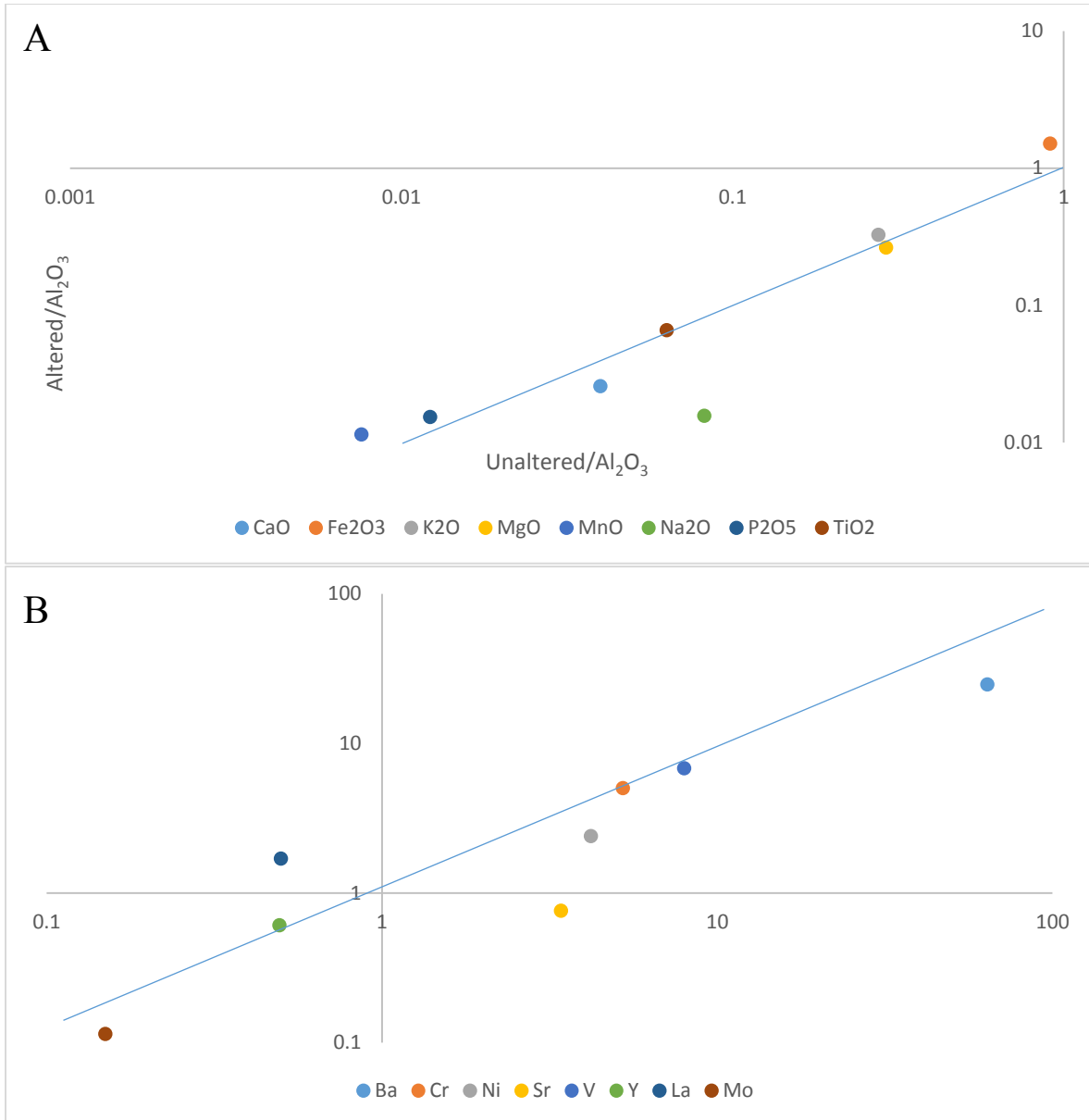
Figure 29: The alteration plots for the KOA Hill samples. A) Alteration of the major oxides and B) trace elements.

3.3 Rare Earth Elements
3.3.1 *Highway 11/17*

Rare earth elements (REE) were analyzed for all samples using inductively coupled plasma mass spectroscopy. The samples are normalized to Taylor and McLennan (1985) post-Archean Australian shale values. Figure 30A and B shows the values obtained for the samples selected from the unaltered up into the altered stratigraphic unit just below the conglomerate layer of the Highway 11/17 outcrop. Samples 1-7, taken from the unaltered granodiorite layer, show identical patterns and concentrations, in which the LREEs are enriched compared to the HREEs, with a slightly positive Ce anomaly and a distinctly positive Eu anomaly. The REE distribution plots shows that as alteration increases, The rocks represented by samples 8 to 13 become progressively depleted in REE concentration, and in particular light rare earth elements are lost. Figure 31 is of the REE patterns for samples 14, 15 and 16, which were taken from above the altered faces and represent the conglomerate and sandstone as well as the grainstone layer that caps the outcrop. This diagram shows that the lower concentration of REEs continues up into the conglomerate and clay-rich sandstone. Sample 15, which was taken from the clay-rich immature sandstone, shows a slight enrichment of HREEs compared to LREEs but still has the flat Ce anomaly and slightly positive Eu anomaly. The grainstone sample (sample 16) shows a slight depletion of the HREEs compared to LREEs with a very slightly negative Ce anomaly and positive Eu anomaly.
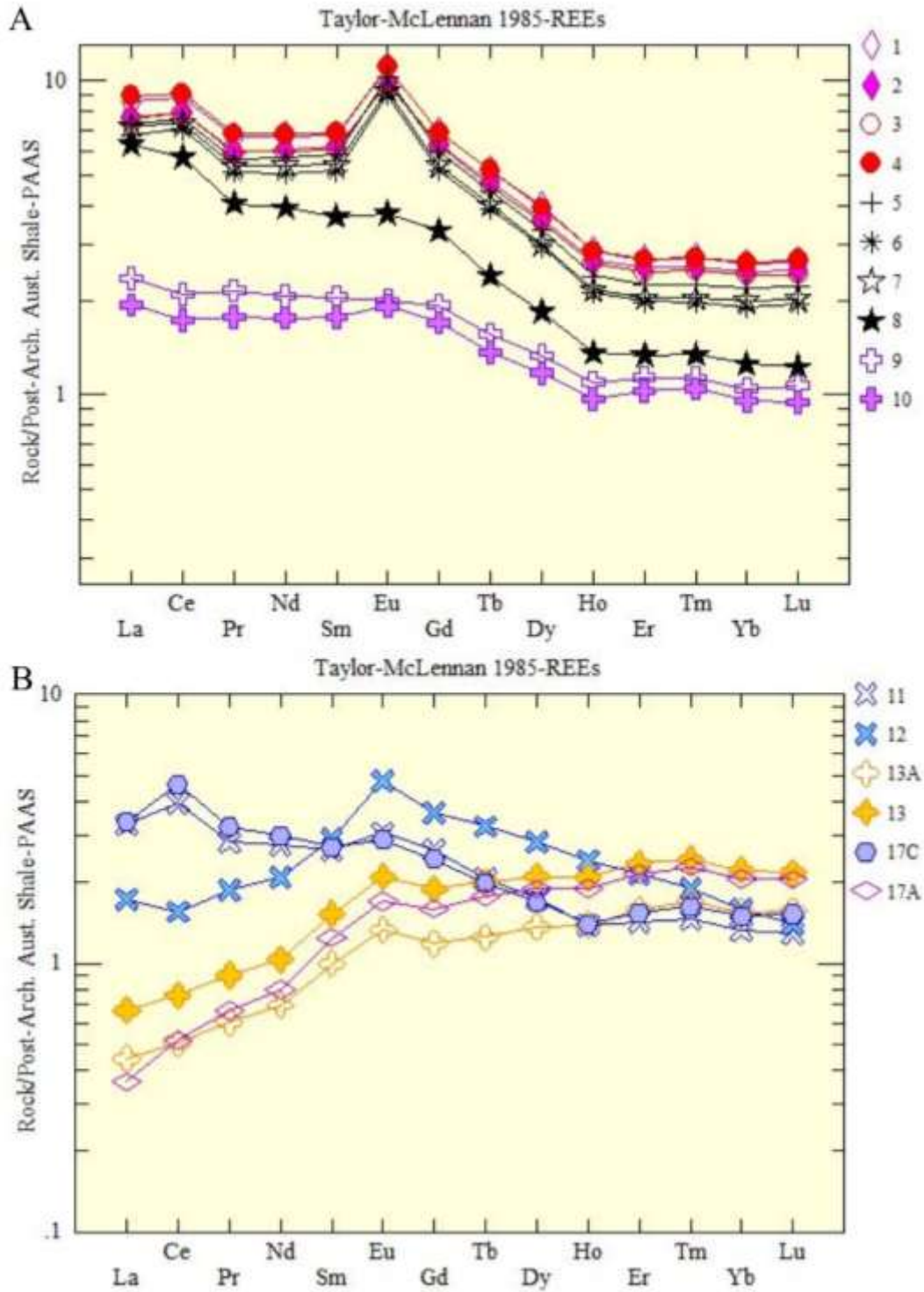
Figure 30: PAAS normalized REE distribution plots diagrams of the samples taken from the Highway 11/17 outcrop. A) The plot of the unaltered to altered samples just below the intense alteration surface. B) The PAAS normalized diagram for the samples from the intensely altered corestone area.
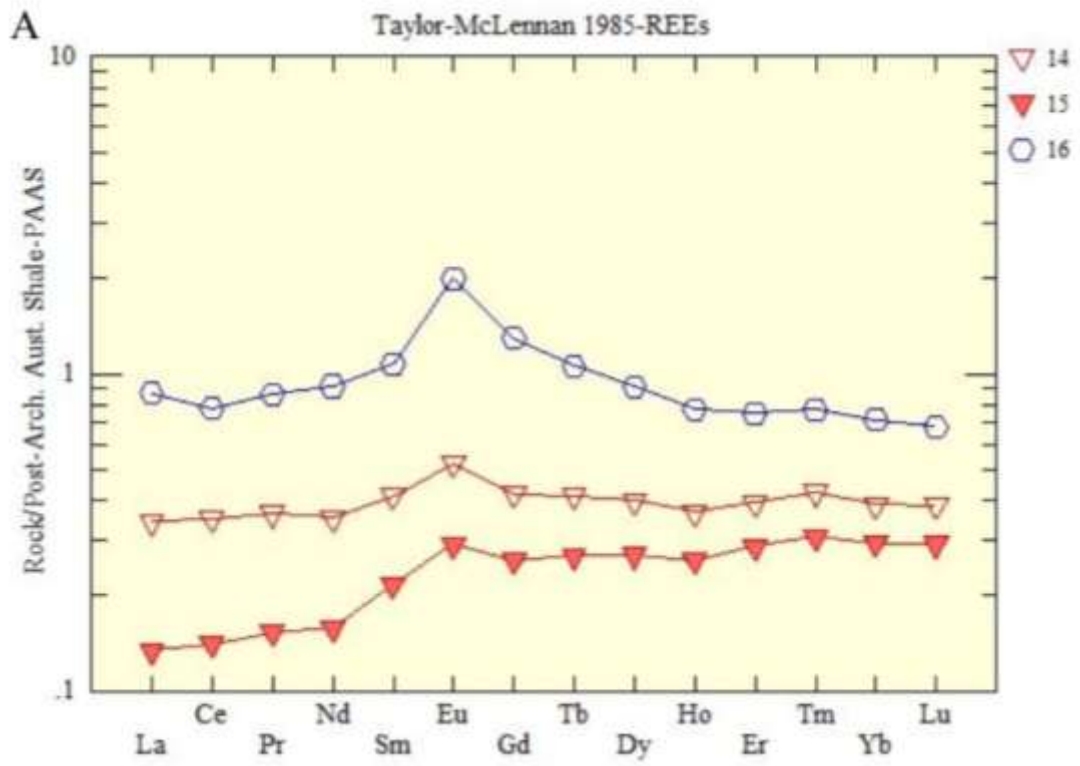
Figure 31: The PAAS normalized diagram for the Kakabeka conglomerate and Gunflint grainstone samples from the top of the Highway 11/17 outcrop.
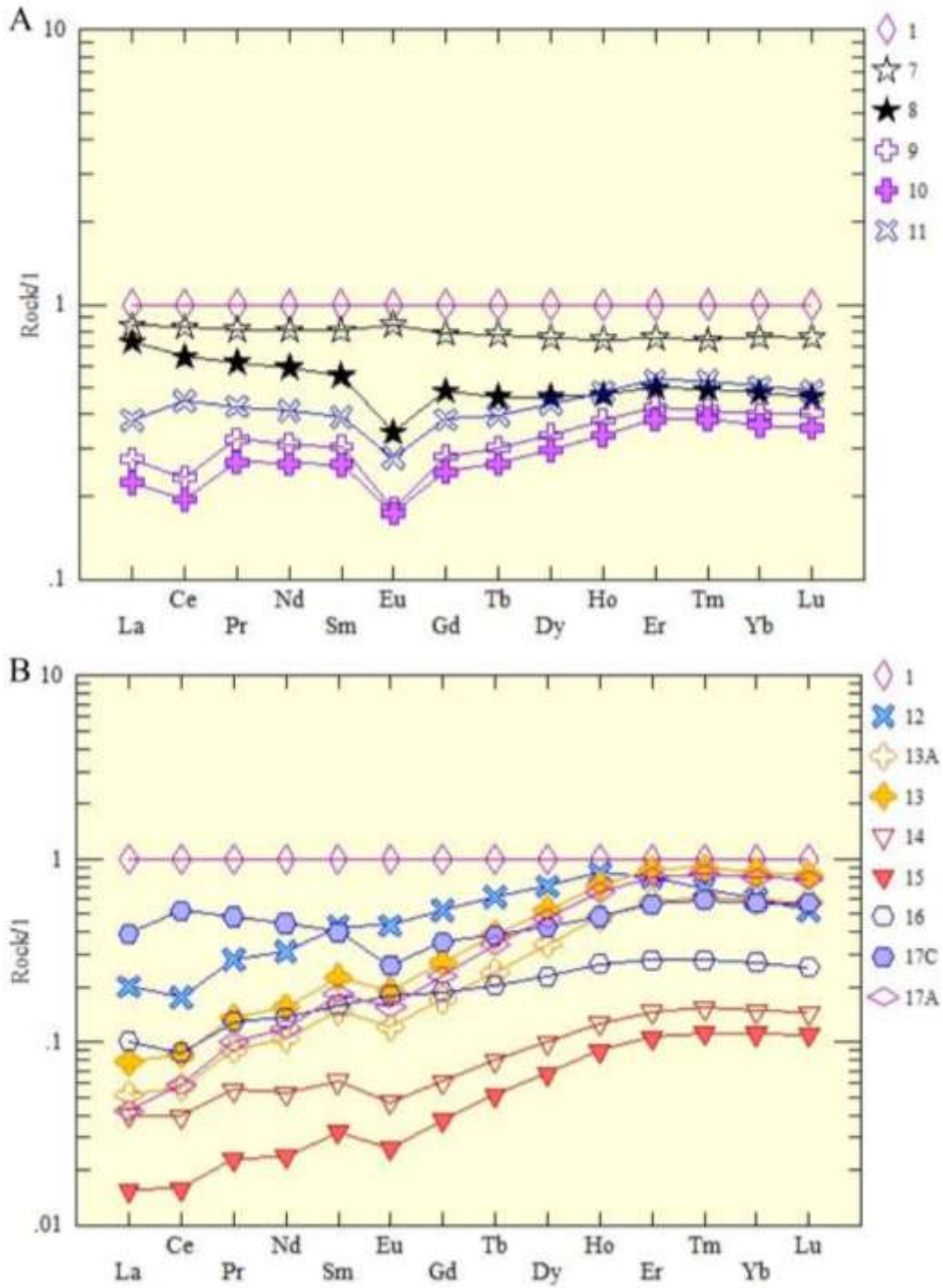
Figure 32: Granodiorite normalized REE distribution plots for the samples from Highway 11/17. A) Altered samples from below the core stone horizon. B) Samples from the corestone horizon and above the granodiorite.

When normalized to a fresh granodiorite sample, REE distribution plots can be used to show which of the rare earth elements are the most affected during alteration. Figure 32A shows the altered samples from Highway 11/17 normalized to sample 1. As alteration intensifies up the stratigraphy of the outcrop, there is a decrease in the total REE concentration. There is also preferentially leaching of Eu, and in some of the samples, Ce below the core stone horizon (Figure 32B). The plot shows that there is differential leaching of the LREE compared to the HREE in the samples from the core stone horizon and above.

3.3.2 Kakabeka Falls

Figure 33 shows the PAAS normalized REE distribution plots for the samples collected from the granodiorite unit that makes up the basement at the Kakabeka Falls outcrop. The plot shows that the samples collected underwent a similar but not as drastic depletion in REE concentration as seen in the samples from Highway 11/17. The plot also has a flat Ce anomaly as well as a positive Eu anomaly. The pattern shows that in the fresh sample the HREEs are depleted when compared to LREEs. The altered sample has a flatter pattern with a slight enrichment in HREEs along with the distinct positive Eu anomaly.

The granodiorite normalized REE distribution plots for the Kakabeka Falls samples shows that the most altered sample has a lower concentration of light REEs compared to the fresher samples (Figure 34). The Ce anomaly shows no change from the fresh sample to the altered sample. The Eu anomaly shows a decrease in concentration from the fresh to altered samples. The alteration of the outcrop has caused a change in the REE pattern slope in that there is an enrichment in HREE concentrations while the LREEs become depleted.
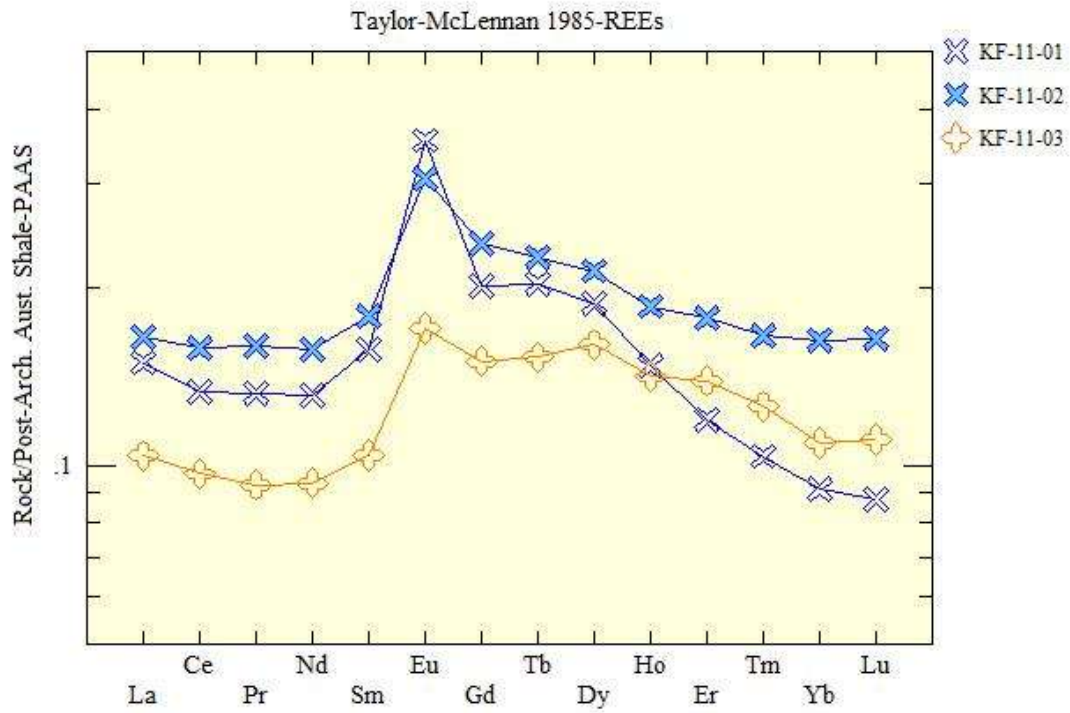
Figure 33: PAAS normalized REE distribution plots of the samples collected from the granodiorite of the Kakabeka Falls outcrop.
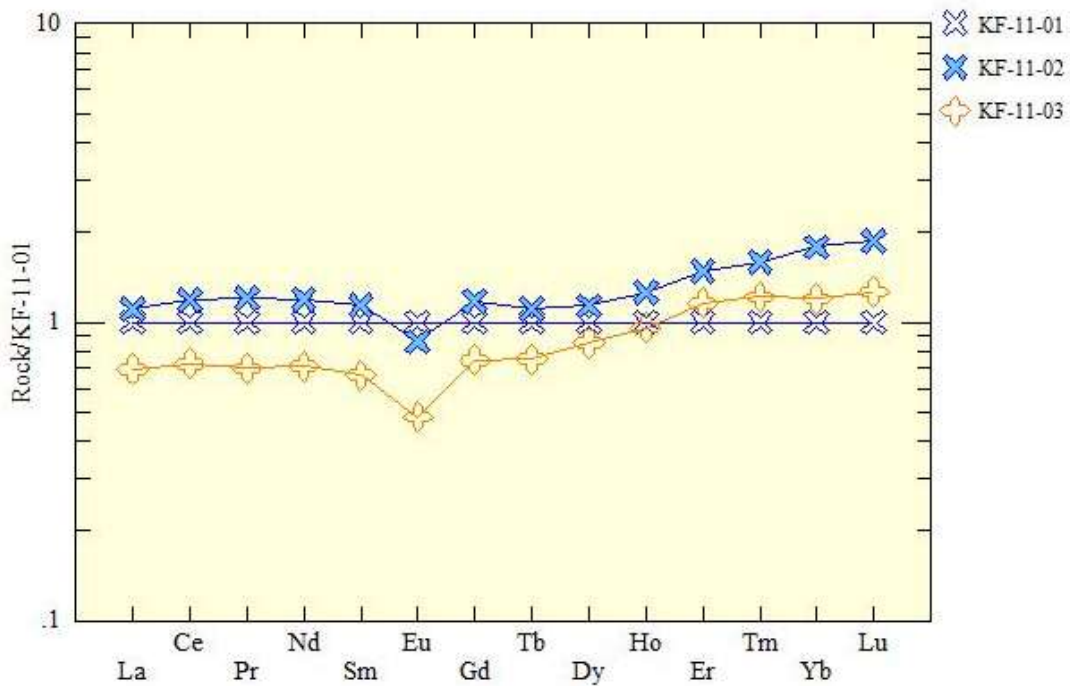
Figure 34: Sample KF-11-01 normalized REE plots for the Kakabeka Falls outcrop.

3.3.3   KOA Hill

The measured REE values for the samples collected from the KOA hill outcrop were normalized to Taylor and Mclennan's (1985) Post Archean Australian Shale values and plotted. The plots in Figure 35 are divided by their stratigraphic unit; the fresh samples in A and the altered samples in B. The plots of the unaltered samples, KOA-01 to KOA-03, show a consistent pattern among the three samples with similar concentrations of LREEs and HREEs, a flat Ce anomaly, as well as a distinct positive Eu anomaly. The samples KOA-04, 05 and 06 are from the weathered zone of the outcrop, these samples show a depletion of HREEs compared to LREEs. The distinct positive Eu anomaly has decreased in size, but the flat Ce is still present. Figure 36A and B are the PAAS normalized distribution plots for the samples collected from the top of the KOA hill outcrop and represent the Kakabeka conglomerate and the Gunflint hematite and grainstone layer that cap off the outcrop. The conglomerate sample are KOA-07 and 08. These two samples show different patterns from each other and the other samples. Sample KOA-07 is from the conglomerate directly above the weathered stratigraphic unit and shows equivalent concentrations in LREEs and HREEs with a slight enrichment in the MREEs, a distinct negative Ce anomaly and a slight positive Eu anomaly. Sample KOA-08 which is from the conglomerate in which the matrix is clay-rich, has a REE pattern that shows a depletion of LREEs compared to the MREEs and HREEs. There is also a slightly noticeable negative Ce anomaly as well as a slightly positive Eu anomaly. The samples KOA-09 and 10 were taken from the top of the outcrop. The KOA-09 hematite sample shows enrichment of the HREEs compared to the LREEs. The plot also shows a positive Eu anomaly as well as no Ce anomaly. Sample KOA-10 is from the Gunflint grainstone layer, the plot shows a consistent pattern with the other grainstone layers present at the 11/17 and Kakabeka Falls outcrops in which there is a slight

enrichment of HREEs compared to the LREEs along with a negative Ce anomaly and a positive Eu anomaly.

The sample normalized REE plots for the KOA Hill samples shows that the samples collected from the fresh metasedimentary rocks have a slight depletion in the LREEs. The HREEs of the fresh metasedimentary rock plot around 1 which shows that there is little to no change in concentration (Figure 37A). The altered metasedimentary rocks have a slight increase in the LREEs compared to the HREE and show little to no change in concentration from the sample used for normalizing (Figure 37B). The PAAS normalized plots have no Ce anomaly present in the metasedimentary rocks, and this is reflected in the sample normalized plot. The Eu anomaly present in the metasedimentary rocks does not change in concentration even during alteration. The sample normalized plots for the top conglomerate; hematite/grainstone layers shows that the LREEs are depleted relative to the fresh sample. Two of the four samples have pronounced negative Ce anomalies. The Eu anomaly is negative in the conglomerate and hematite sample, with a slight positive Eu anomaly present in the grainstone sample (Figure 37B).
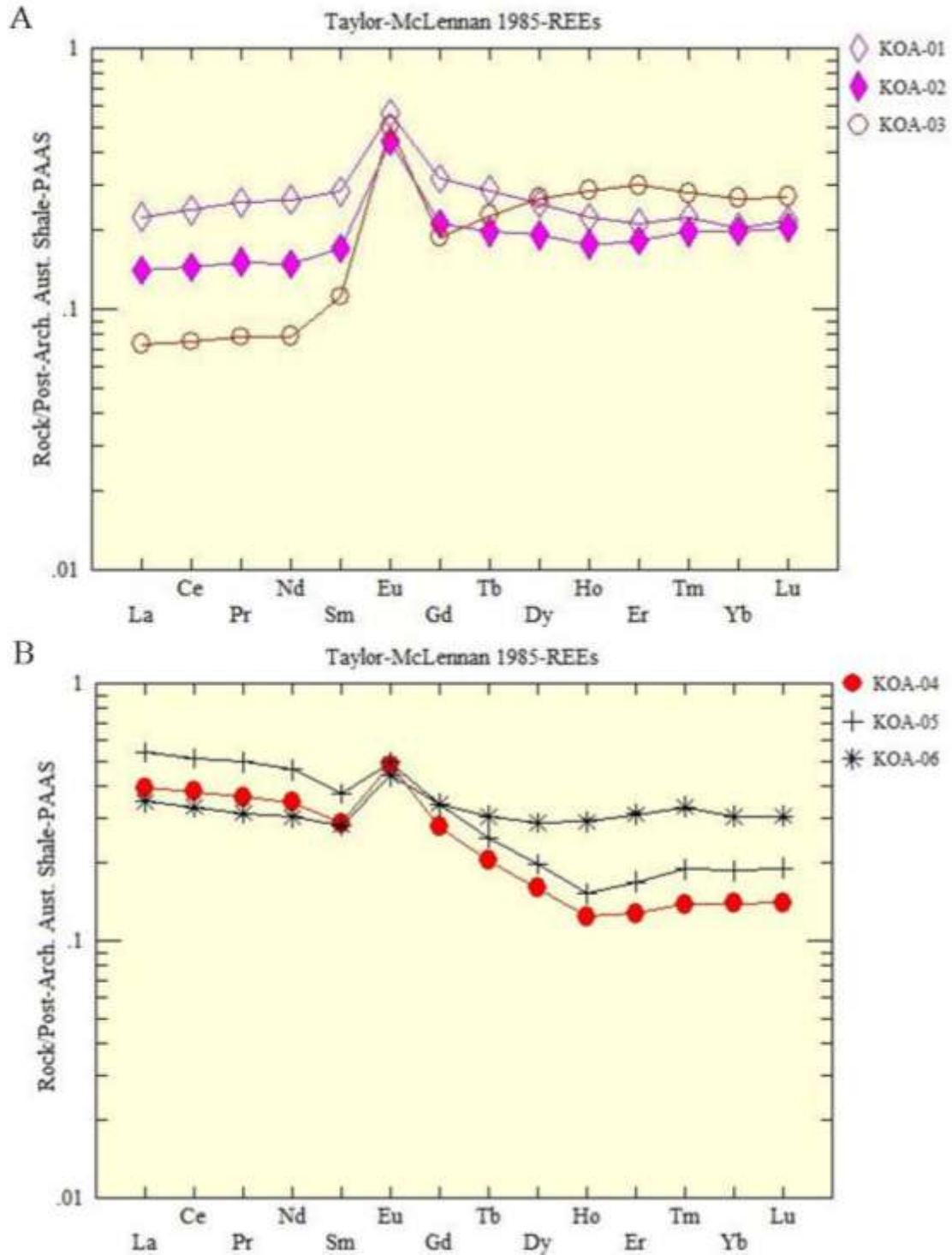
Figure 35: PAAS normalized REE distribution plots for samples collected from the outcrop at KOA Hill. A) Fresh rocks (KOA-01, -02 and -03). B) Samples KOA-4, -5, and -6 from the altered rock.
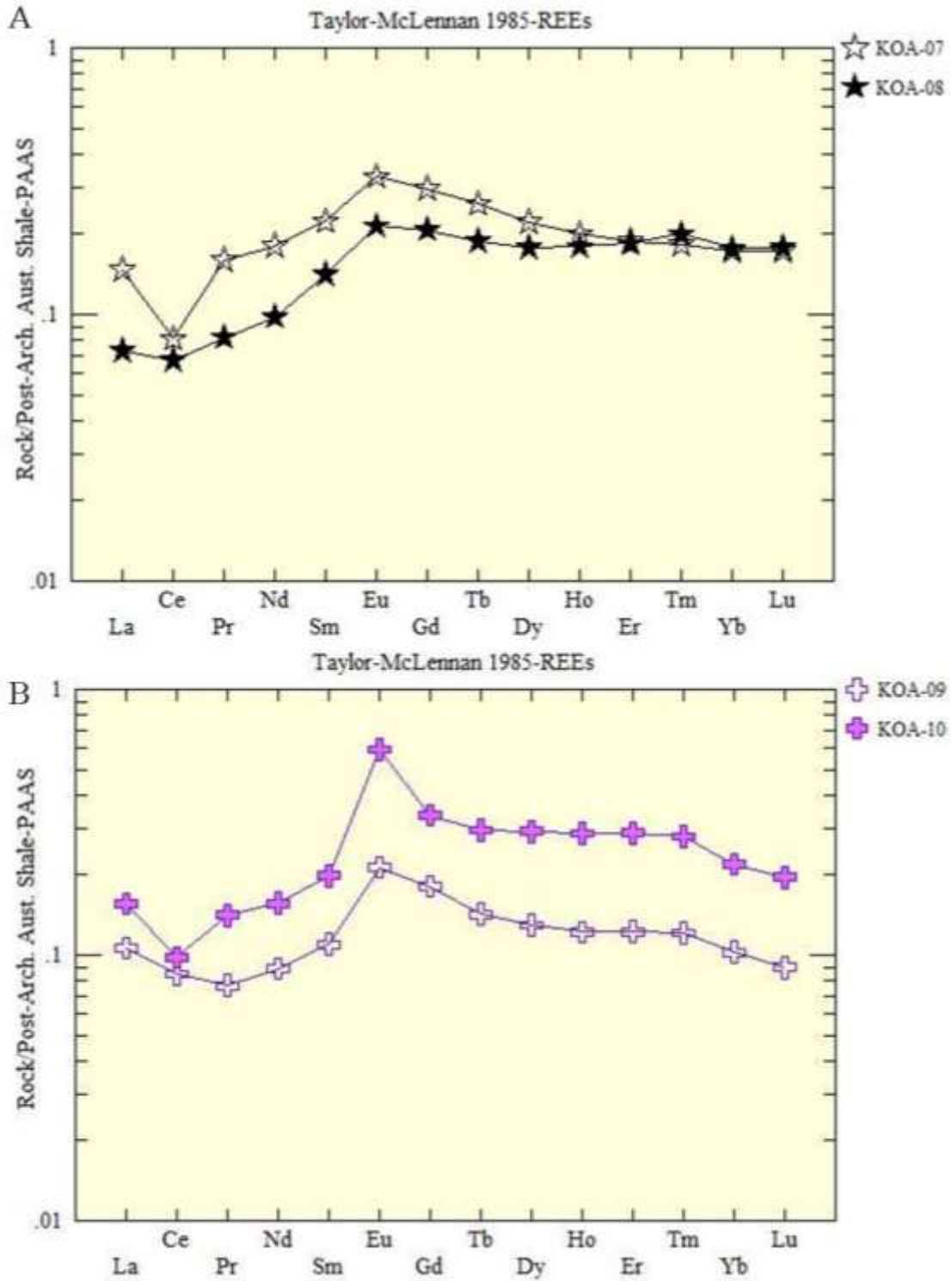
Figure 36: PAAS normalized REE distribution diagrams for the plots from A) the conglomerate and B) rocks from the hematite (KOA-09) and grainstone layer (KOA-10).
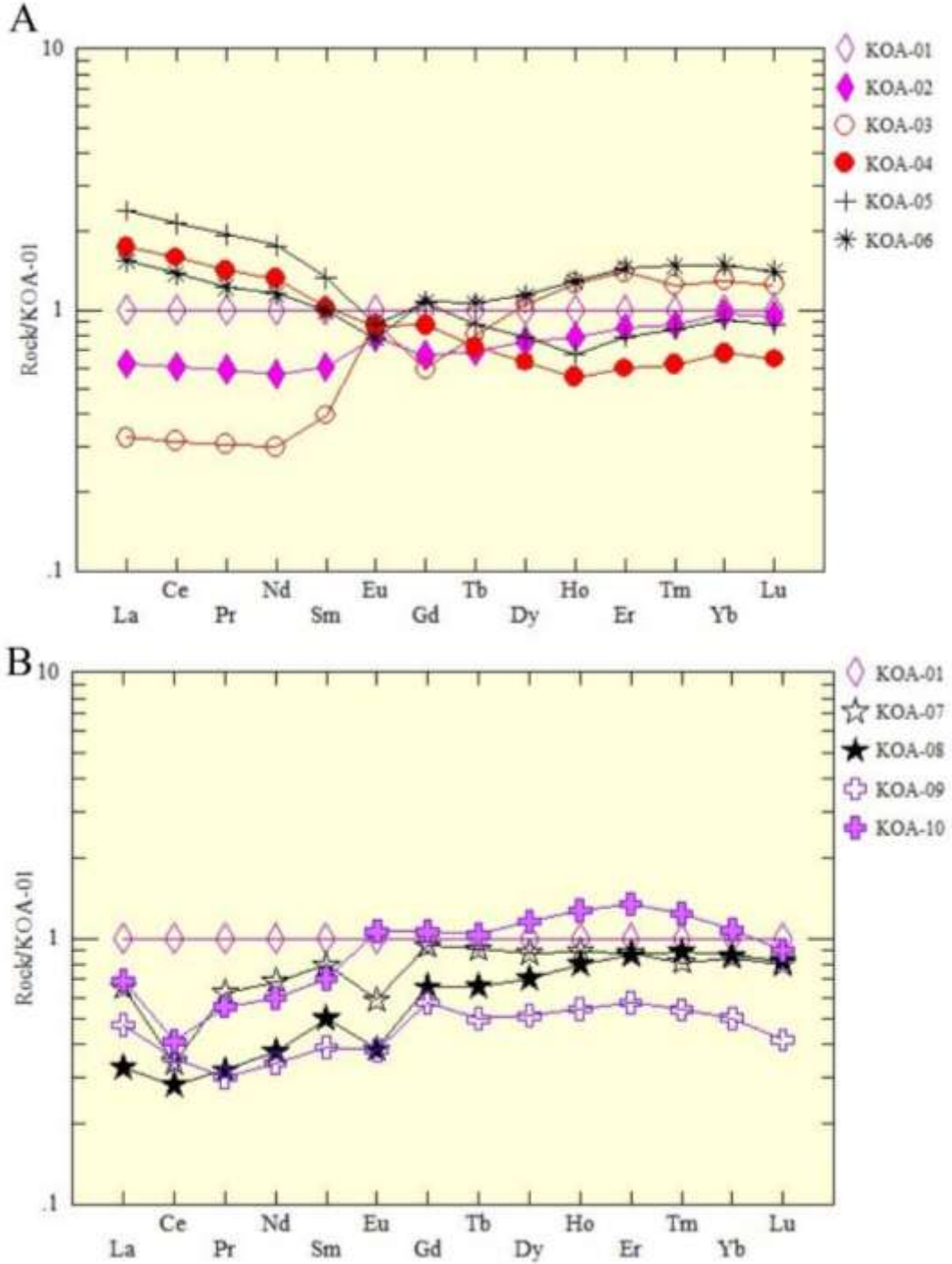
Figure 37: REE distribution plots normalized to the fresh sample for the KOA Hill samples. A) The samples were taken from the metasedimentary rocks. B) The samples were taken from the conglomerate and hematite grainstone layers overlying the metasedimentary rocks. Sample 7 and 8 are from the conglomerate. Sample 9 is from the hematite and sample 10 is from the grainstone.

4   BASAL GUNFLINT GRAINSTONE

Some of the outcrops studied contained the basal units of the Gunflint Formation. Limited data from two of these where erosive truncation of the Gunflint precluded detailed study were presented in the previous section. Two other outcrops studied show an extensive section of the overlying stromatolites as well as the grainstone deposited around them. These two sample sites are near Kakabeka Falls and the Whitefish Channel outcrop.

4.1   Sample Sites
4.1.1   Kakabeka Falls

At the base of this outcrop is the nonconformity composed of the Archean granodiorite below the Gunflint Formation chert microbialite, chert stromatolites and ankerite grainstone. This sequence contains an excellent example of subaerial exposure of the Gunflint grainstone during deposition. A chert microbialite consisting of a very flat mat with scattered pinicles overlies the granodiorite and is itself overlain by stromatolites. An ankerite grainstone has been depositied alongside and overlying the stromatolites. The top of the outcrop consists of a brecciated silicified ankerite grainstone with broken clasts of the chert laterally in ankerite grainstone.

An indicator of the presence of subaerial exposure at this outcrop are vadose silt layers deposited at the bottom of quartz cement filled cavities within the ankerite grainstones (Figure 38A). The vadose silt layer occurs at the bottom of the dissolution cavities and is overlain by blocky quartz cement (Figure 38B). The vadose silt layers are comprised of a combination of fine-grained carbonates with pyrite and scattered detrital quartz grains (Figure 38C).

A second possible example of subaerial exposure is present in the top 30cm of the outcrop (Figure 39A). It is reflected in the aforementioned brecciated grainstone stratigraphic unit

comprised of silicified patches of grainstone that have been brecciated and filled by ankerite

grainstone (Figure 39B). It is possible that the underlying vadose silt may have formed during

development of this hard-ground.
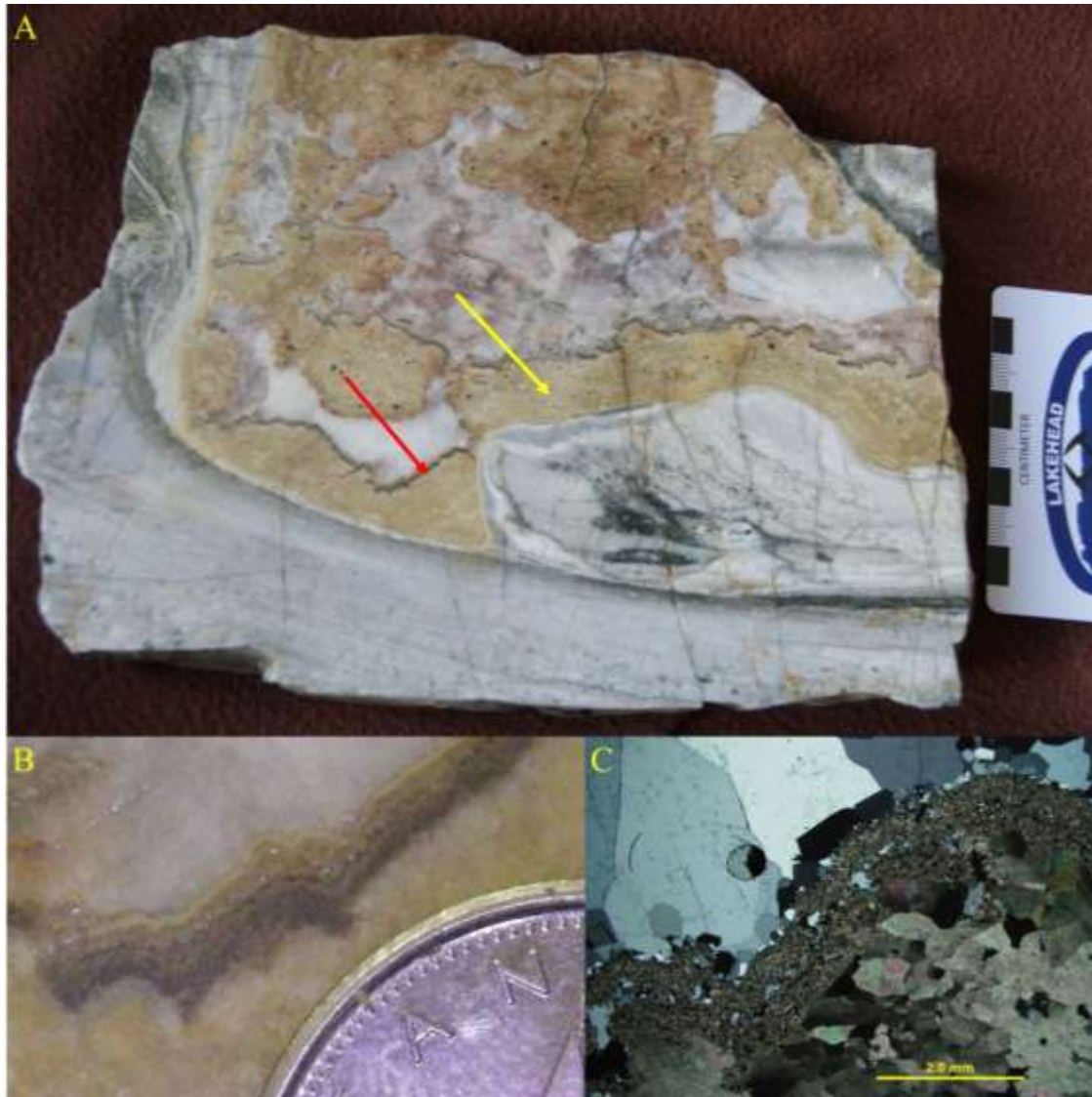
Figure 38: Vadose silt layer present at the Kakabeka Falls outcrop. A) A polished slab which shows the ankerite grainstone (yellow arrow) with void filling white quartzt cement overlying microbialite and a large fragment of microbialite. The vadose silt layer (red arrow) underlies the quartz filling the cavities. B) The fine grained carbonate and pyrite of the vadose silt layer at the bottom of the quartz-filled cavity. Dime for scale. C) Photomicrograph of the vadose silt layer showing the composition of fine-grained ferroian dolomite, detrital quartz grains and pyrite.

Figure 39: A) The silicified and brecciated portion of the uppermost ankerite grainstone found at the top of the Kakabeka Falls outcrop. B) Eroded pieces of silicified grainstones in ankerite grainstone.

4.1.2   Whitefish Channel

This outcrop is on the banks of the Whitefish River channel outside of Nolalu, Ontario to the west of Thunder Bay, Ontario. The Whitefish channel outcrop is comprised of a series of large low-lying bioherms draped by a grainstone on-top of a crystalline basement (Figure 40A). The bioherms are comprised of large domal stromatolites at the base, on top of which thin digitate stromatolites form (Figure 40 B and C). The grainstone that was deposited on top of the bioherms is composed of fine-grained chert. Evidence of very early silicification of, primary chert deposition forming the bioherms is the presence of large chert clasts that have fractured and been broken off, with the space filled by the grainstone overlying grainstones (Figure 40D). This suggests that the grainstones that are associated with the stromatolites had to be cemented by quartz before being overlain by the grainstones.

Petrographically the grainstones present in the Whitefish channel outcrop are comprised of fine-grained cherts and a minor amount of blocky quartz (Figure 41A). The thin sections show replacement by fine- to -coarse grained ferroan dolomite (Figure 41B). Much like the grainstone the digitate stromatolites present at Whitefish channel are comprised of fine-grained cherts. Stromatolitic layering is rarely preserved but when present shows shows that the stromatolites are comprised of mostly chert and fine-grained iron oxides (Figure 41C). Interspaces present between stromatolite columns are filled by chert non-oolitic peloids (Figure 41D).

Figure 40: Photographs of the Whitefish channel outcrop near Nolalu, Ontario. A) The underlying basement below the bioherms and grainstone. B) Chert bioherms with draping grainstones. C) Grainstone draped bioherms near the river. D) Large silicified brecciated grainstone clast fractured and filled by the overlying grainstone.
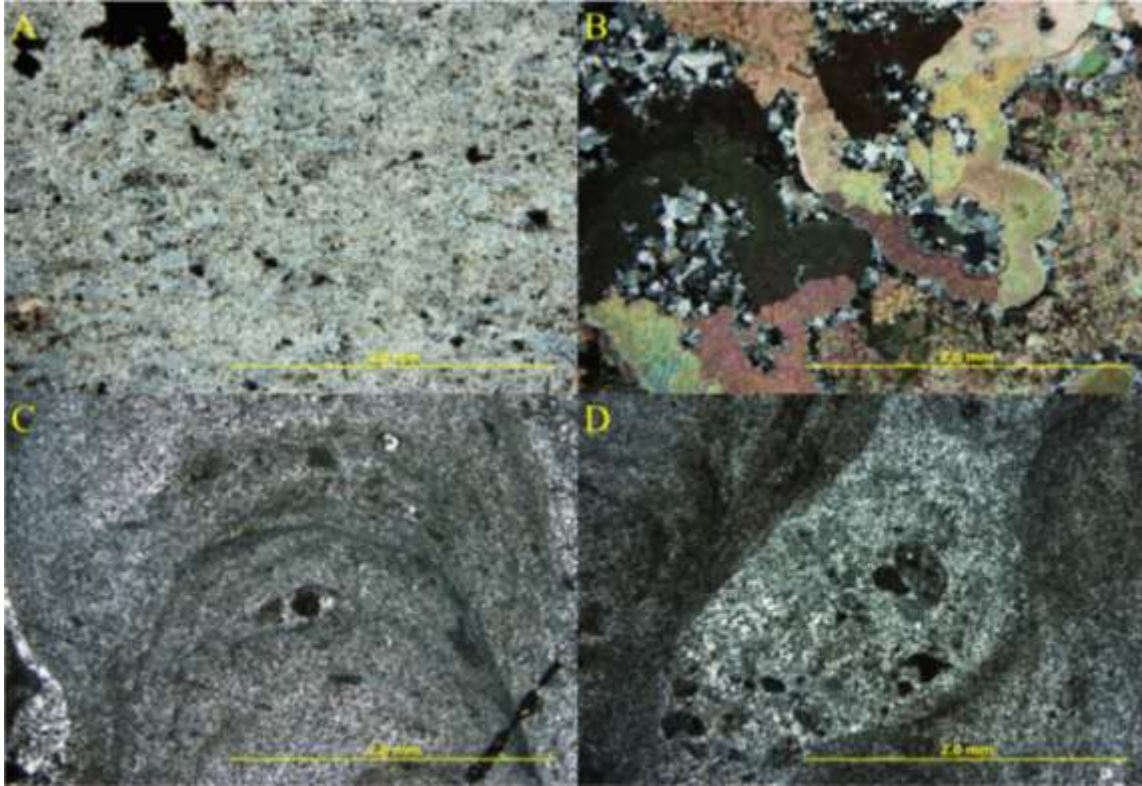
Figure 41: Photomicrographs of samples taken from the Whitefish Channel sample site. A) Carbonate and chert grainstone. B) Ferronan dolomite is replacing chert grains. C) The poorly preserved digitate stromatolite is showing chert and fine-grained iron oxide composition. D) Chert non-oolitic peloids present in the interspace between stromatolite columns.

4.2   Geochemistry
4.2.1   Kakabeka Falls

Four samples from the grainstone and stromatolitic sample found at the Kakabeka Falls outcrop, as well as samples collected from previous work done by Simon Horner (2012) were analysed for both whole rock and rare earth elements. Simon Horner's sample were sent for analysis to the OGS Lab in Sudbury, Ontario and analysed using XRF and ICP-MS. The rest of the samples were analyed using ICP-AES as well as ICP-MS at LUIL. The samples selected for analysis are shown with a brief description in Table 3.

Table 3: Sample number and a brief description of the samples chosen for analysis from the Kakabeka Falls outcrop.

Sample	Description
KF-A	Domal Stromatolite samples (light laminae)
KF-B	Domal Stromatolite sample (dark laminae)
KF-C	Basal microbialite sample (light laminae)
KF-S	Basal microbialite sample (dark laminae)
SH-2	Stromatolitic chert
SH-3	Ankerite grainstone over basal mat
SH-4	Ankerite grainstone over basal mat
SH-5	Silicififed carbonate grainstone from above the stromatolites
SH-6	Layered chert from the top of the outcrop
SH-10	Layered microbialite

Figure 42 shows major REDOX oxides and elements plotted against the siliciclastic component of the samples represented by Al_2O_3. Possible positive trends are visible in the plots of Fe_2O_3 vs. Al_2O_3, V vs. Al_2O_3 and U vs. Al_2O_3 (Figure 42A, C, D) with no trends visible in the plot of MnO vs. Al_2O_3 (Figure 42B).
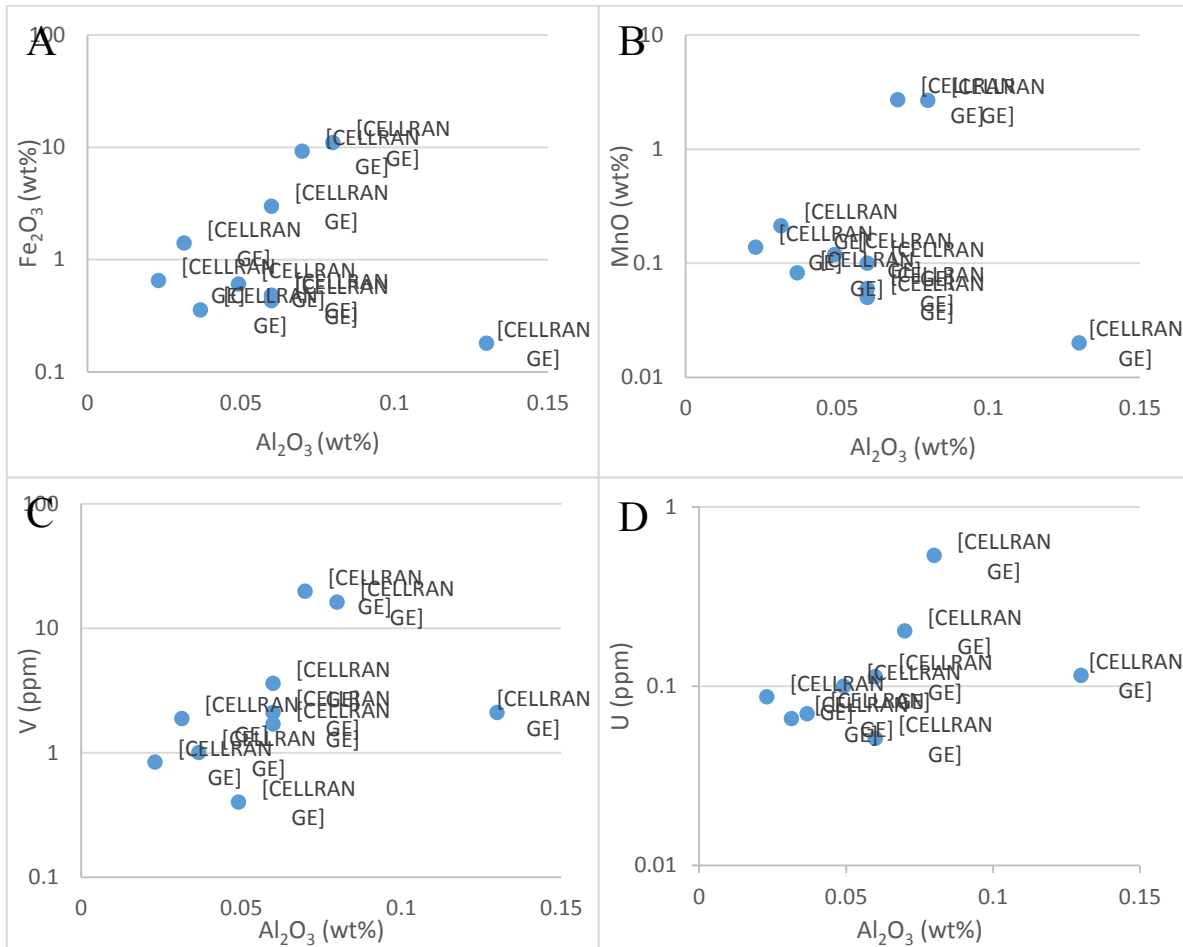
Figure 42: Redox sensitive elements vs. siliciclastics. A) Fe_2O_3 vs. Al_2O_3, B) MnO vs. Al_2O_3, C) V vs. Al_2O_3 and D) U vs. Al_2O_3. Possible trends are visible in the plots of Fe_2O_3 vs. Al_2O_3, V vs. Al_2O_3 and U vs. Al_2O_3. No trends are visible in MnO vs. Al_2O_3

The major redox sensitive elements are Fe_2O_3, MnO and V. Figure 43 shows the plot of Fe_2O_3 vs. MnO, Fe_2O_3 vs. V and MnO vs. V. Possible positive trends are visible in the plots of Fe_2O_3 vs. MnO and Fe_2O_3 vs. V (Figure 43A and B). Whereas the plot of MnO vs. V shows no distinct trends between the two (Figure 43C).
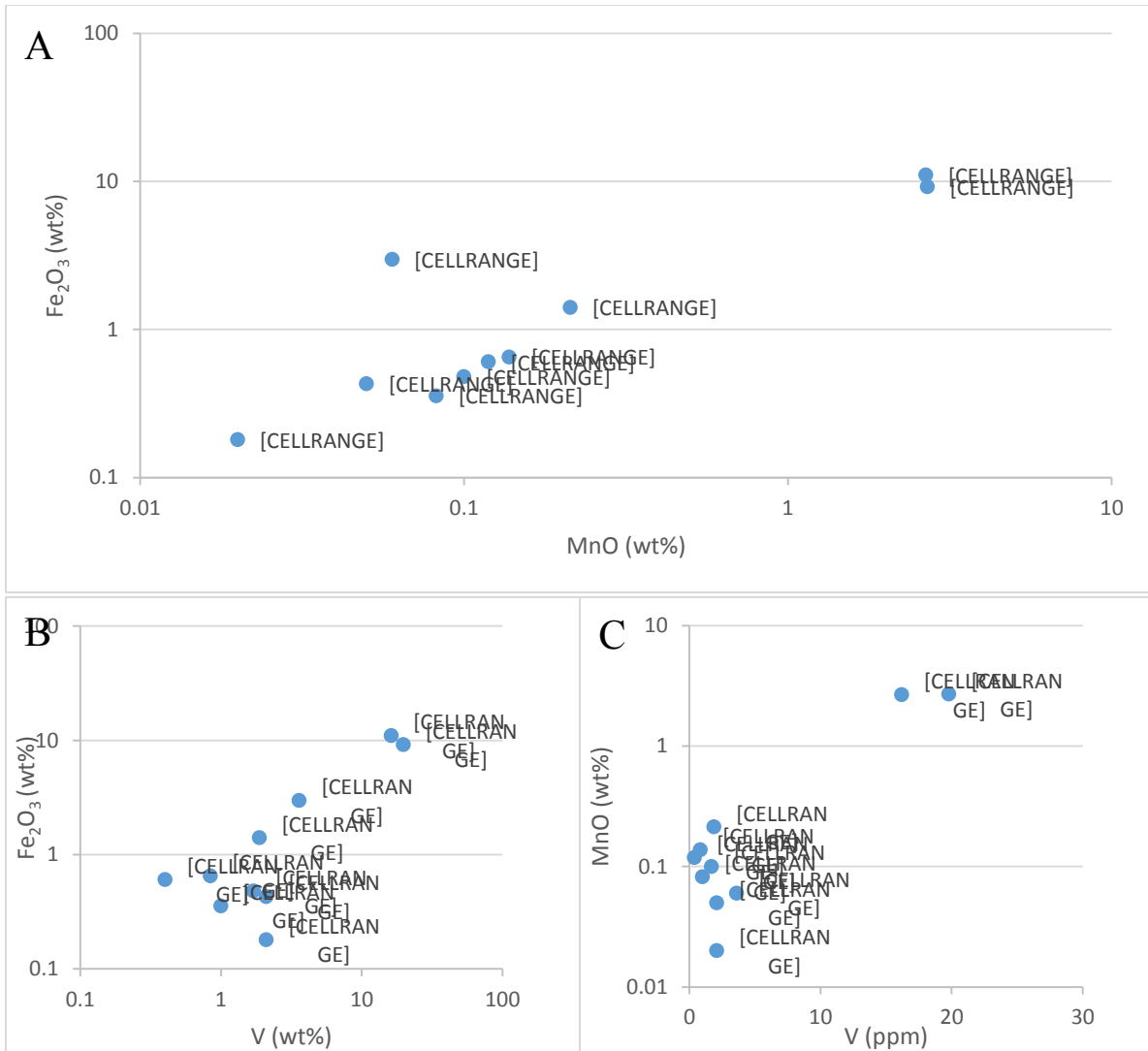
Figure 43: Redox sensitive oxides and elements plotted against each other. A) Fe_2O_3 vs. MnO showing a positive trend forming between the two oxides. B) Fe_2O_3 vs. V showing a positive trend. C) MnO vs. V showing no trend.

Figure 44 shows the plots of the minor redox sensitive elements Cr, U, Mo plotted against V and Cr. Some of the samples have chromium values below detection, which are plotted at zero. The plots of Cr vs V, U vs. V and Mo vs. V do not show any trends forming between any of the elements (Figure 44A, B, C). The plot of U vs. Cr does show a possible positive trend forming between these two redox sensitive elements (Figure 44D).
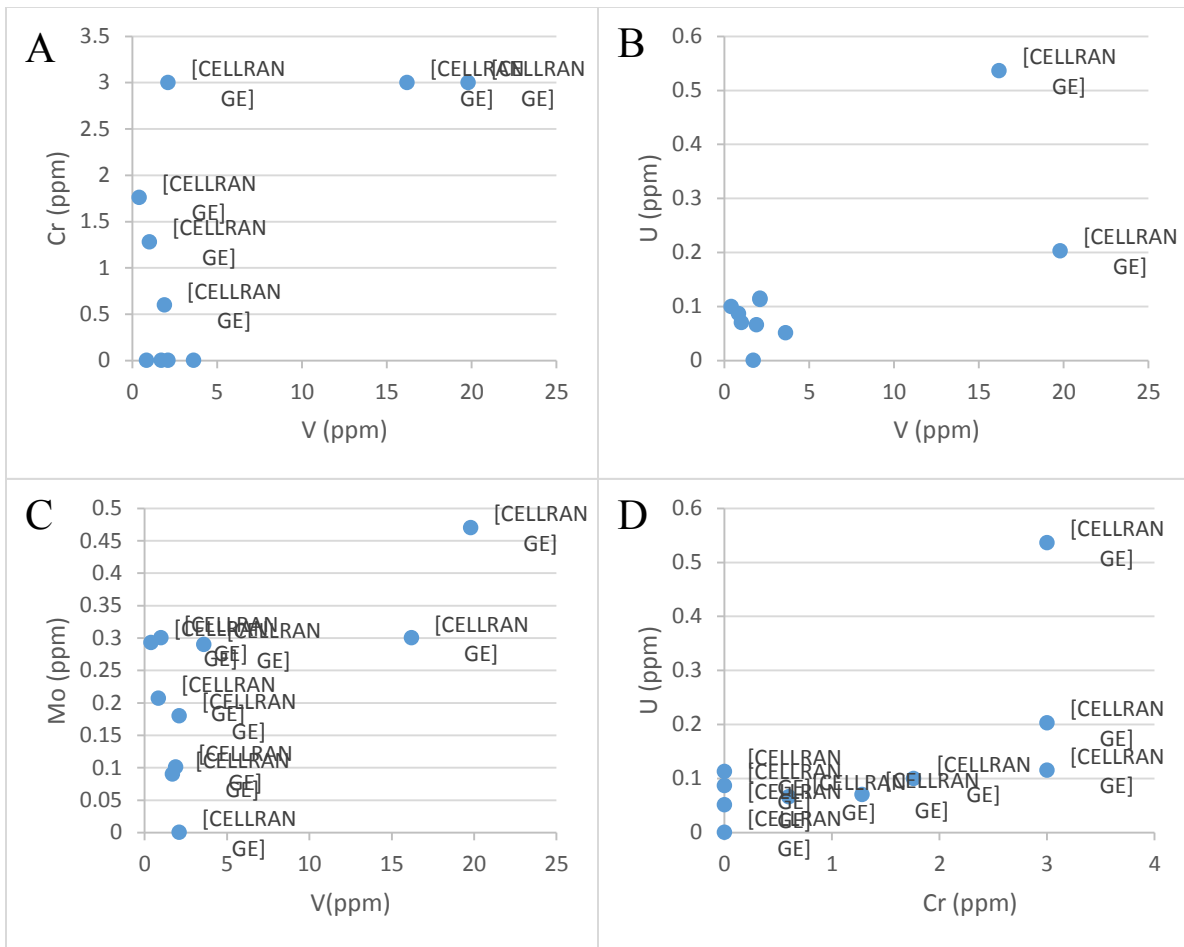
Figure 44: Redox sensitive elements plotted against V and Cr. A) Cr vs. V, B) U vs. V, C) Mo vs. V showing no visible trend D) U vs. Cr showing a possible positive trend.

4.2.2 *Whitefish Channel*

Ten samples were selected from individual layers present at the Whitefish channel outcrop. The samples were taken from the crystalline basement, the bioherms and the grainstones draping the bioherms. These samples were analysed for major oxide, trace element and rare earth concentrations. The samples selected for analysis are presented with a brief description in Table 4.

Table 4: The samples analysed from the Whitefish channel sites

Sample number	Description
WF-CY-01 (1)	Grainstone from between the stromatolites
WF-CY-02 (2)	Chert from stromatolite bioherm
WF-CY-03 (3)	Grainstone draping bioherm
WF-CY-04 (4)	Grainstone draping bioherm
WF-CY-05 (5)	Red chert stromatolite
WF-CY-06 (6)	Grainstone draping bioherm
WF-A	Jasperlitic chert stromatolites
WF-B	Jasperlitic chert stromatolites
WF-3	White chert
WF-10	White chert

Figure 45 is of the plots of the major redox components Fe_2O_3, MnO, V and U plotted against the siliciclastic component represented by Al_2O_3. The Fe_2O_3 vs. Al_2O_3 plot, seen in Figure 45A, shows no trend forming between the two oxides. The lack of any trend can be seen in the plots of MnO vs. Al_2O_3 (B), V vs. Al_2O_3 (C), and U vs. Al_2O_3 (D)

The whole rock and trace element geochemistry provides evidence on the redox environment at the time of deposition. The next group of plots look at the redox sensitive elements (Figure 46). These plots are of Fe_2O_3 vs. MnO (A), and Fe_2O_3 and MnO vs. V (B and C). Positive trends are visible in all three plots, especially in the plot of MnO vs. V (C) in which

sample four plots along the line were as the previous two plots sample WF-CY-4 plot with high

MnO and V compared to Fe_2O_3 (B).
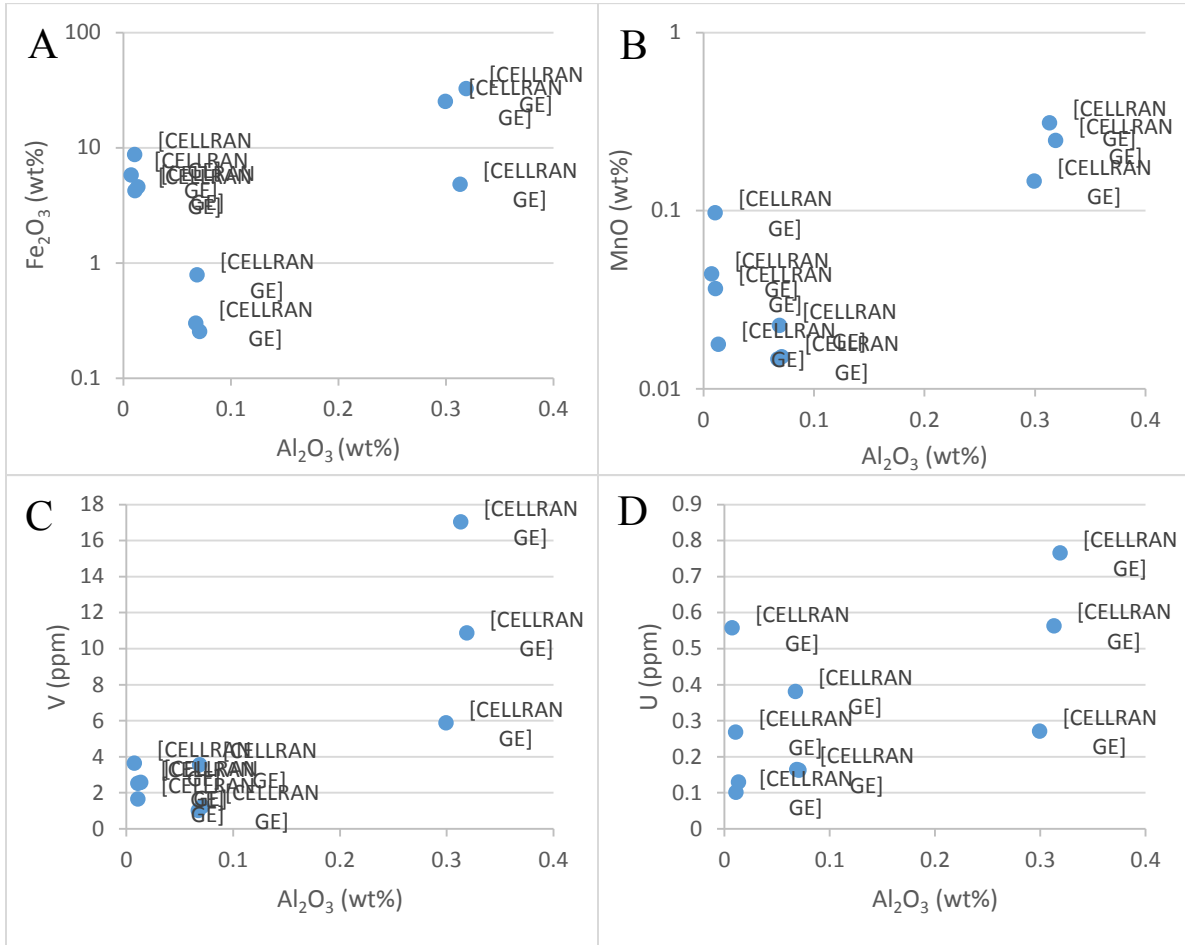
Figure 45: Scatterplots of the redox sensitive oxides vs. siliciclastic content of the Whitefish channel. The plots showing no distinct patterns forming in any of the plots, though the samples with larger amounts of Al also have larger amounts of Fe, Mn and V. A) Fe_2O_3 vs, Al_2O_3 B) MnO vs.Al_2O_3. C) V vs. Al_2O_3 D) U vs. Al_2O_3.
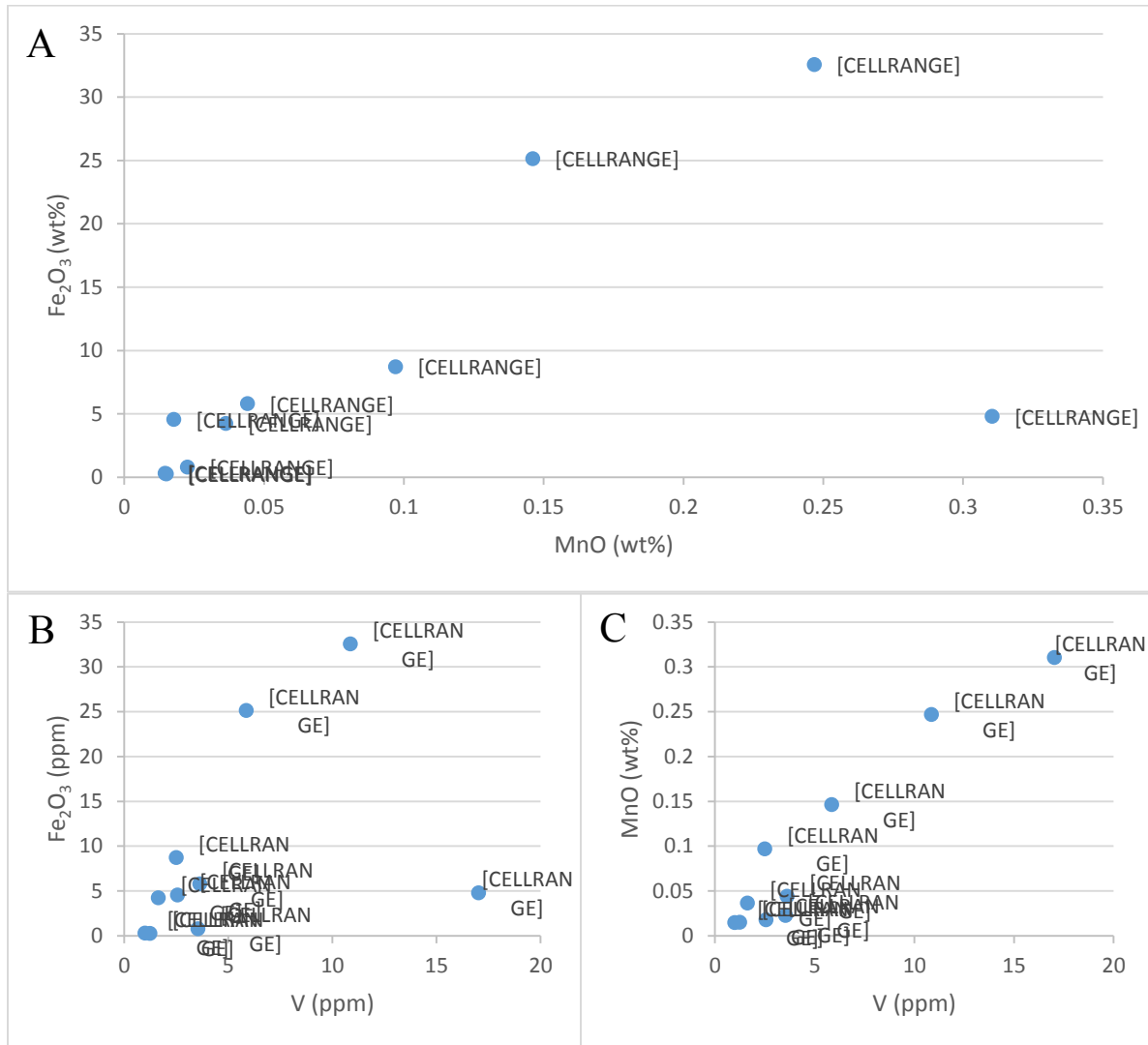
Figure 46: redox sensitive elements Fe$_2$O$_3$, MnO and V plotted against each other. A)Fe$_2$O$_3$ vs. MnO showing a positive trend-between the two. B) A similar trend can be seen in the plot of Fe$_2$O$_3$ vs. V. C) MnO vs. V shows a very distinct positive trend between the two elements.

The plots seen in Figure 47 are of the minor redox sensitive elements Cr, U and Mo ploted against V and Cr. The plot of Cr vs. V shows no visible trend forming between the two elements (Figure 47 A). The plot of U vs. V shows a possible positive trend forming between the two elements (Figure 47 B). The last two plots of Mo vs. V and Cr vs. U show no correlation between the elements (Figure 47 C and D).
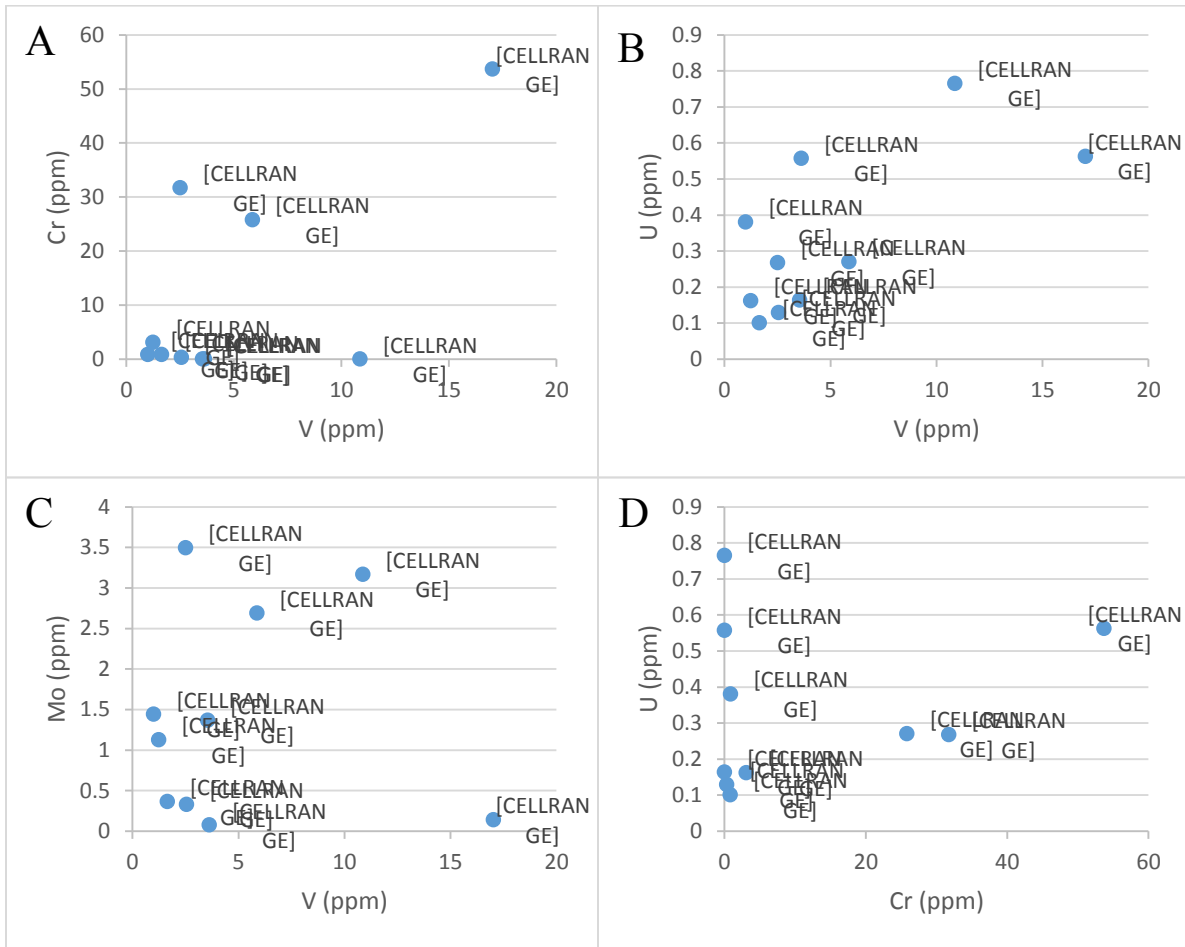
Figure 47: The plots of redox sensitive elements Cr, U and Mo plotted against V and Cr. No trends are visible in the plot Cr vs. V (A), Mo vs. V (C) and U vs. Cr (D). With some of the data a positive trends is visible in the plot of U vs. V (B).

4.3   Rare Earth Elements

4.3.1   Kakabeka Falls

ICP-MS analysis was performed on the same ten samples collected by Simon Horner and myself and are listed in Table 3. The concentrations were normalized to Taylor and McLennan (1985) PAAS values and plotted in the following diagrams (Figure 48). The majority of the stromatolite samples show a similar concentration except for SH-2, which plots lower than the stromatolites.

A plot of the PAAS normalized La and Eu anomaly values plotted against PAAS normalized Ce anomalies is shown in Figure 49. Figure 49A shows the Ce anomaly vs. La anomaly. The plot shows that two of the samples show distinct positive Ce anomalies along with positive La anomalies. Whereas the rest of the sample show negative Ce anomalies. Figure 49B is a plot of Eu anomaly vs. Ce anomaly. This plot shows that there is a slight correlation between the Ce anomaly and the Eu anomaly.

When the redox sensitive oxides and elements are plotted against the PAAS normalized Ce values, the plots show that there is no correlation between the Ce anomaly and the REDOX sensitive elements Fe_2O_3, MnO, V and U (Figure 50).
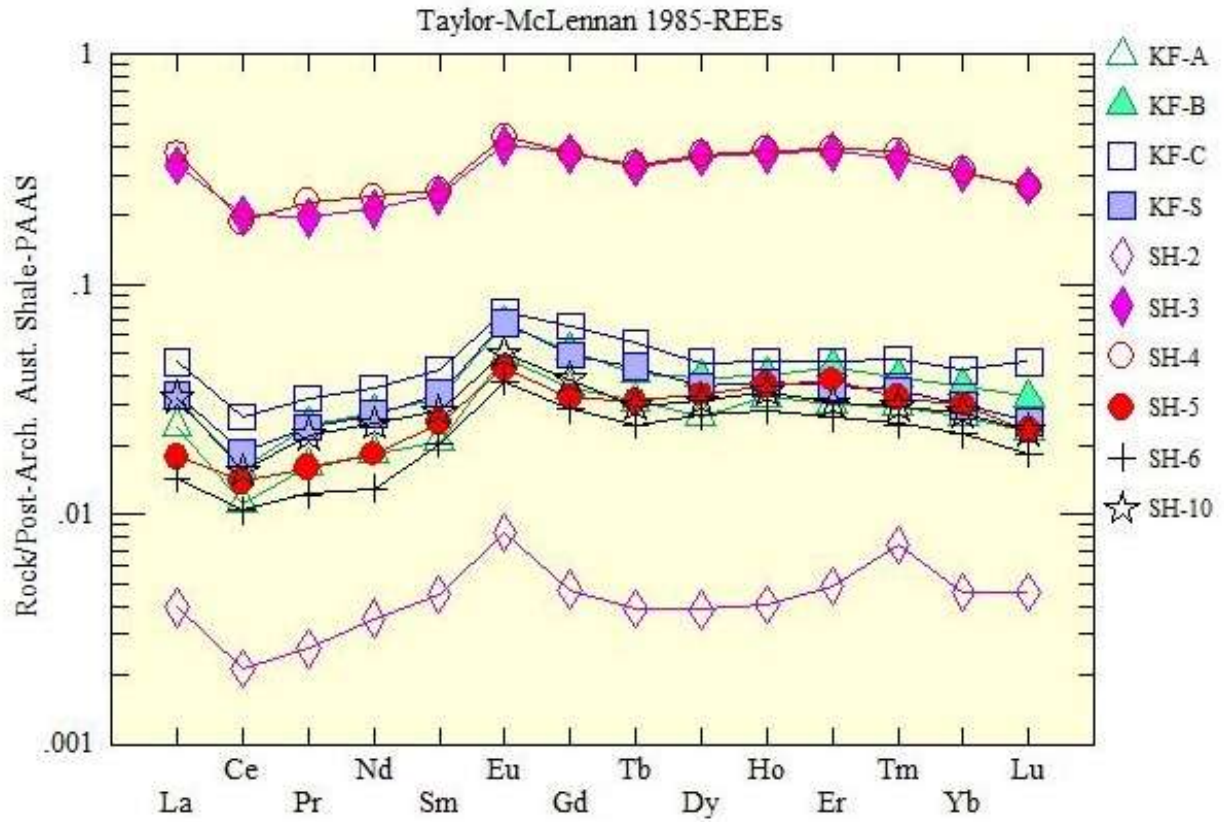
Figure 48: PAAS normalized rare earth element concentration plot for the samples collected from the basal Gunflint Formation at the Kakabeka Falls outcrop.
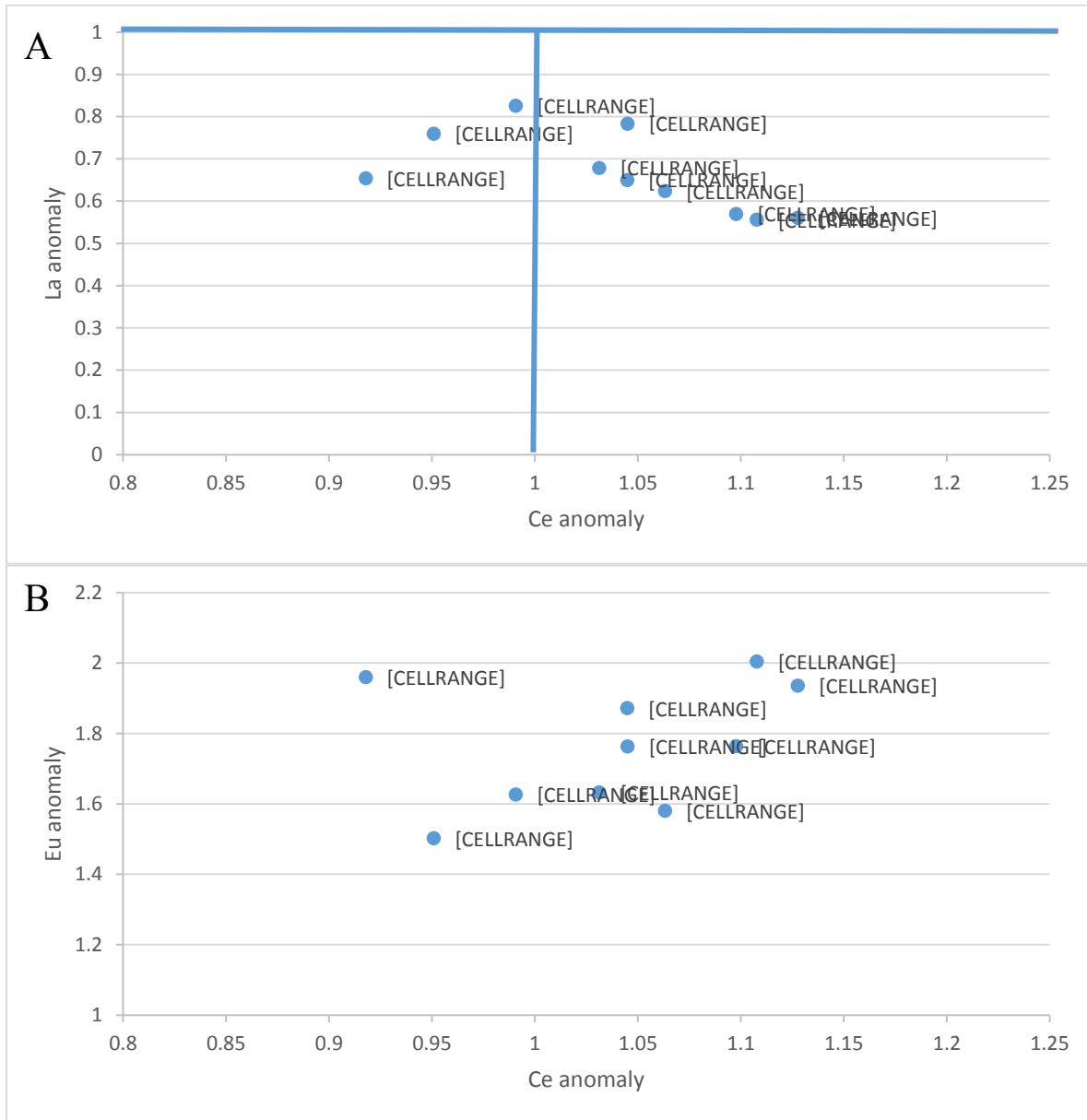
Figure 49: PAAS normalized La and Eu anomalies vs. PAAS normalized Ce anomaly. A) La vs Ce anomaly plot showing that the negative Ce anomalies seen in the grainstones taken from above the stromatolites show a slight positive Ce. Samples 2 and 3 have positive Ce anomalies, whereas the rest have no to large negative Ce anomalies and are positively correlated with positive La anomalies, though this is likely the result of Ce being in the formula for La anomalies. B) Eu vs. Ce anomaly. There is a slight trend between increasing negative Ce anomaly and increasing positive Eu anomaly.
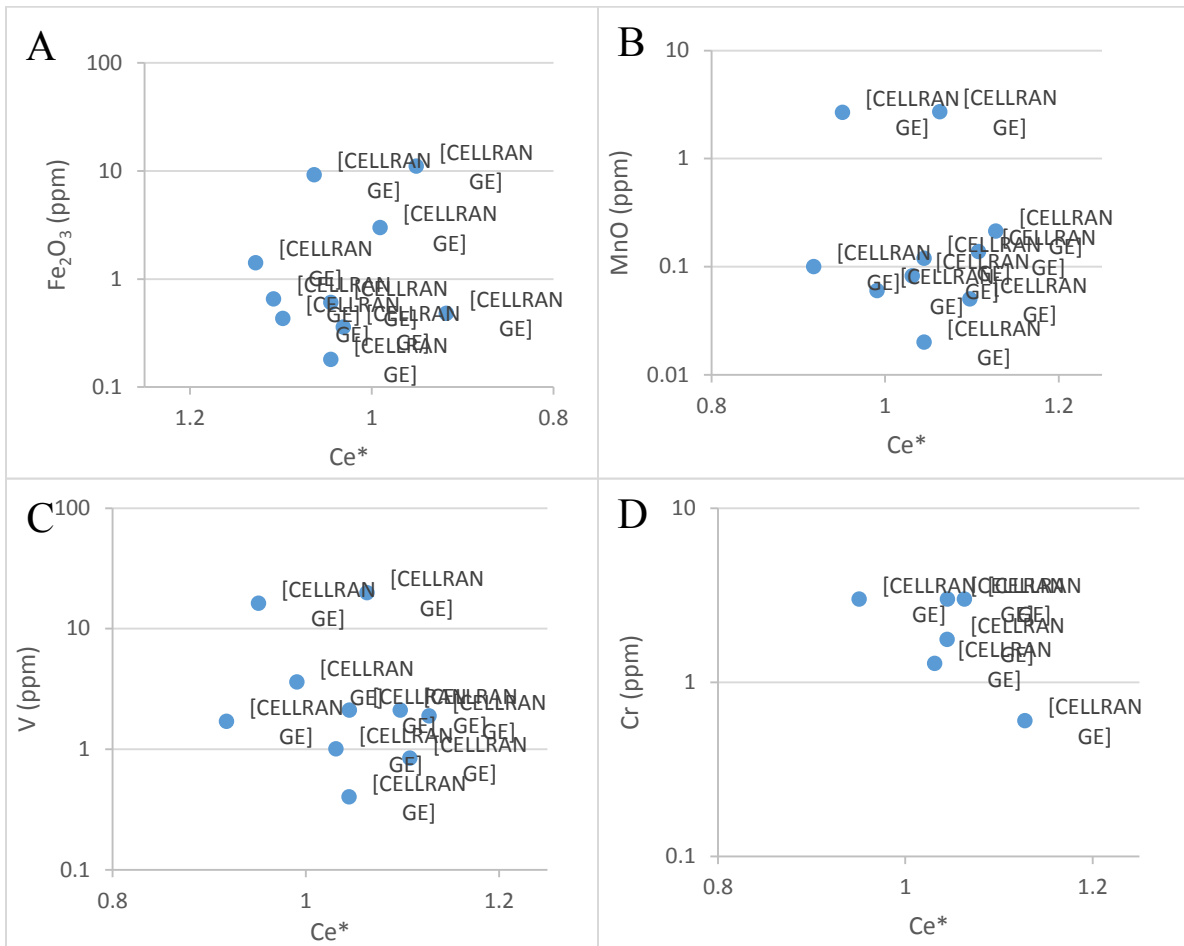
Figure 50: redox sensitive elements vs. PAAS normalized Ce anomaly values (Ce*). No trends can be seen in any of the plots. A) Fe₂O₃ vs. Ce*. B) MnO vs. Ce*. C) V vs. Ce* and Cr vs. Ce*.

4.3.2 *Whitefish Channel*

The ten samples were analysed for their rare earth element concentrations (Table 4). The values were PAAS normalized and plotted (Figure 51). This plot shows that the stromatolite samples all have similar concentrations whereas the grainstone samples from above the stromatolites have varying concentrations. All the Whitefish samples have slightly heavy enriched patterns with most having negative Ce anomalies as well as distinct positive Eu anomalies.

Figure 52 are the plots of the PAAS normalized La, Eu values vs. PAAS normalized Ce values. The Ce and La anomalies were calculated and plotted against each other (Figure 52A). The plot shows a trend forming between the two anomalies. The plot shows that the Ce anomaly become plot towards the zero for the grainstone samples and from the negative Ce anomaly seen in the samples collected from the stromatolites. The plot of PAAS normalized Eu values vs. PAAS normalized Ce values shows no trend between the two anomalies, thus there is no correlation between the two anomalies (Figure 52).
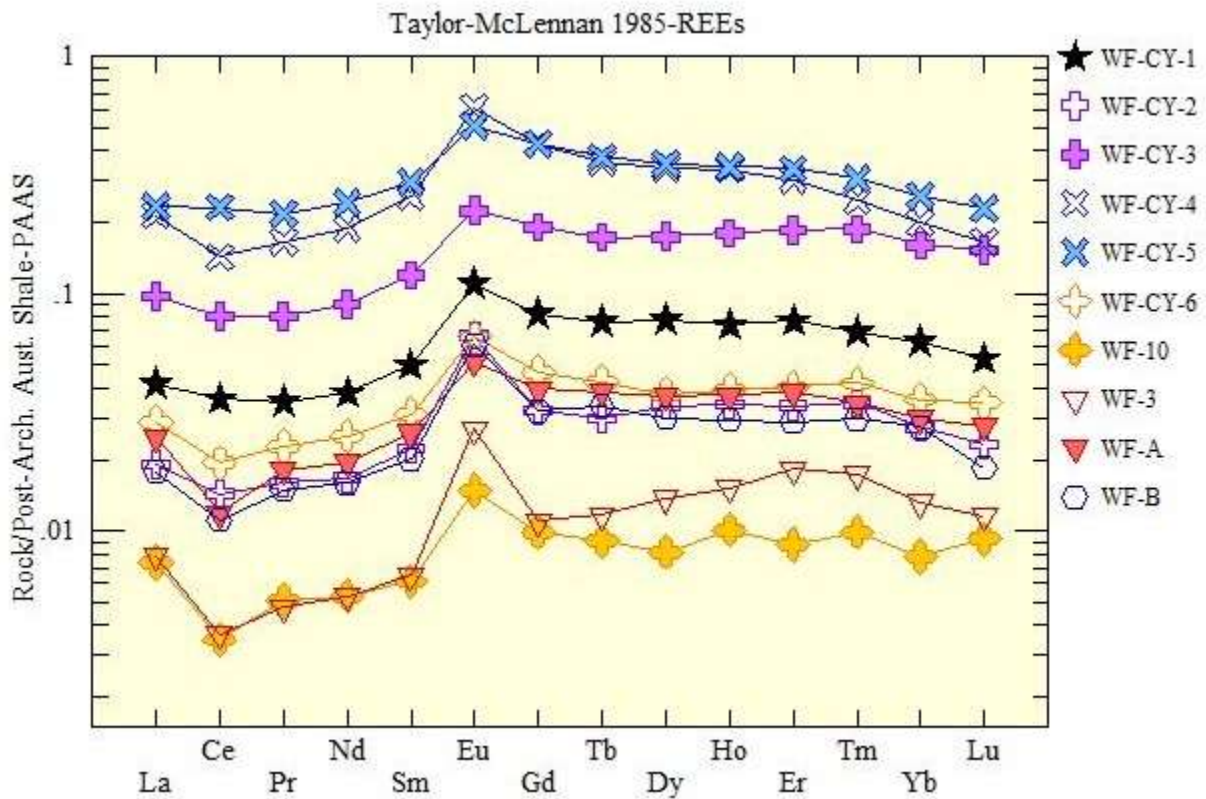
Figure 51: The PAAS normalized rare earth element concentration plot for the samples collected from Whitefish Falls. The samples all show a flat pattern with negative Ce anomalies and positive Eu anomalies.
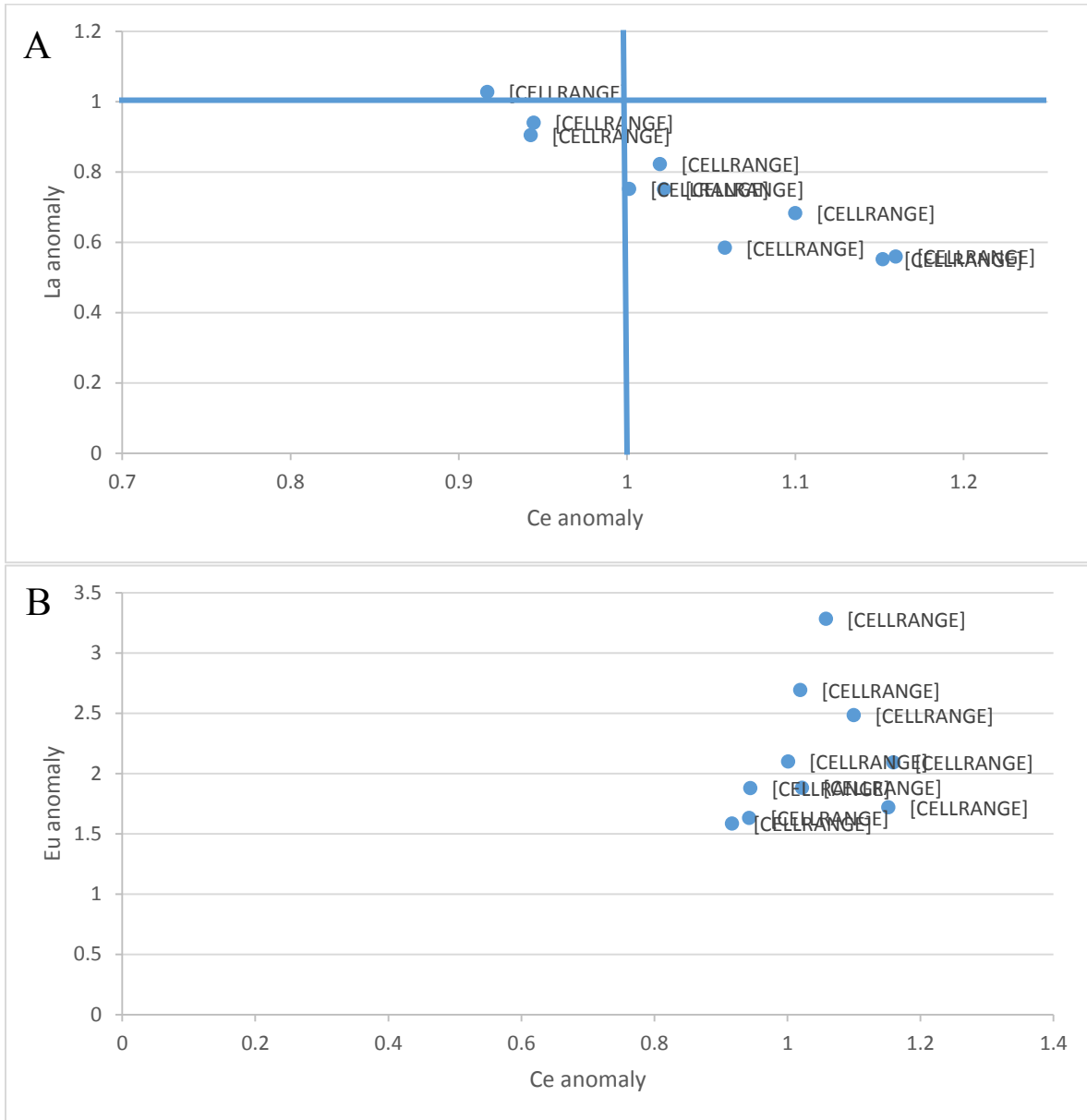
Figure 52: PAAS normalized La and Eu values plotted against PAAS normalized Ce values. A) The Ce anomaly vs. La anomaly plot for the samples taken from Whitefish Falls. Stromatolites show the highest negative anomaly, with the grainstones showing no Ce anomaly. B) PAAS normalized Eu values vs. PAAS normalized Ce values showing no trend forming between the two anomalies

The plots of the redox sensitive elements vs. the PAAS normalized Ce values. Possible trends are visible in the plots of Fe_2O_3 vs. Ce* and V vs. Ce* (Figure *53* A and C). There are no visible trend seen in the plots of MnO vs. Ce* and Cr vs. Ce* (Figure *53* B and D).
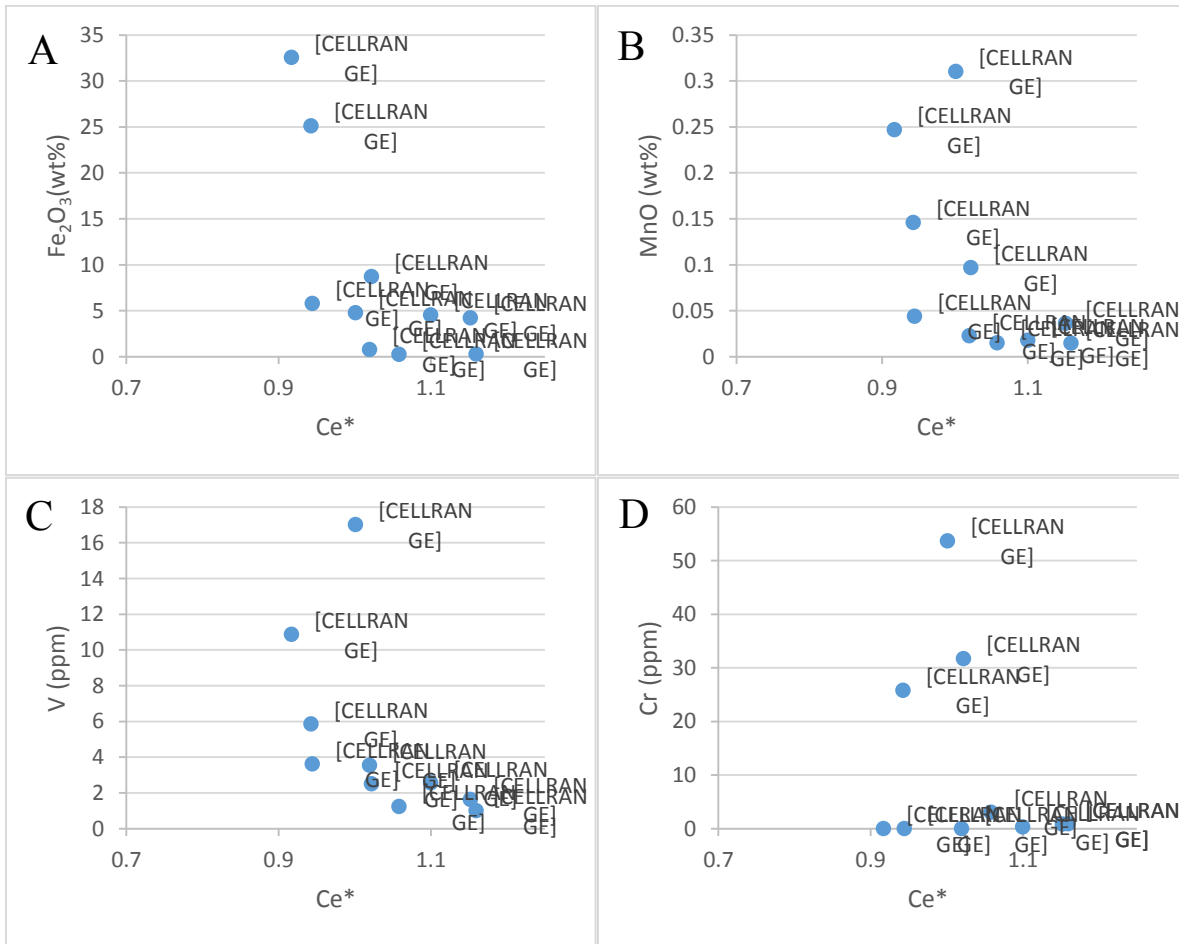
Figure 53: Redox sensitive element vs. PAAS normalized Ce values (Ce*). A) Fe_2O_3 vs. Ce showing a possible trend. B) No trend visible in MnO vs. Ce* C) V vs. Ce* shows a possible trend between the two. D) No trend present in Cr vs. Ce*

5 MIDDLE STROMATOLITIC UNIT

Following the initial transgression, the lower regressive succession of the Gunflint, and

equivalent formations in the area, is a 20m thick sequence, with the maximum lowstand surface

approximately 45m above the basal contact. This section of the Gunflint reflects the shallowing

due to the retreat of the ancient sea that deposited Gunflint sediments (Fralick and Barrett, 1995).

The outcrops chosen for this study were from a few meters above and below the surfaces that

were created during the maximum retreat of the sea. The chert grainstone below this surface

becomes coarser-grained during sea level retreat, and was occasionally affected by storms

(Fralick and Barrett, 1995). At some of the study sites the maximum regression surface has

microbiolites forming directly on it, whereas others do not have preserved stromatolites but still

contain possible alteration patterns.

5.1 Sample Sites
5.1.1 Mink Mountain

The Mink Mountain outcrop lies just north of Whitefish Lake, near Suomi Ontario. The

outcrop shows a section of the middle regressive surface starting from the grainstone, up into a

stromatolite and oncolite unit. The 353cm thick outcrop is very informative due to the drastic

brecciation of the grainstone that stromatolites and oncolites capping off the outcrop.

5.1.1.1 Grainstone layer

The outcrop behind Mink Mountain is comprised of a medium- to coarse-grained grainstone

(Figure 54). At the outcrop level, the grainstones are composed of brown to blue non-oolitic

chert grains. The grains of the grainstone are tightly packed and cemented by chert. Sporadic

muds, comprised of either hematite or jasper, can be seen throughout this layer.

Figure 54: The grainstone layer present at the outcrop behind Mink Mountain showing the change between the solid grainstone (yellow arrow) and the brecciated grainstone with hematitic mud (red arrow).

Thin sections of the grainstone samples taken from the outcrop behind Mink Mountain clearly show the composition of the layer (Figure 55). The grainstone layer is made entirely of non-ooltic medium- to -coarse grains that are mostly sub-rounded to angular in shape (Figure 55A). The grains are comprised of fine-grained, mosaic cherts, which show a range of hematite coatings, from a thin coating surrounding the edge of the grain to complete replacement (Figure 55B and C). The cement that holds the grains together has varying textures. The main cements are drusy pallisade crystals around the edges of grains and mosaic cherts cement in the space

between grains. Some of the samples taken from the outcrop show spherulitic chalcedony fans

forming in what had been open space between the grains (Figure 55D).
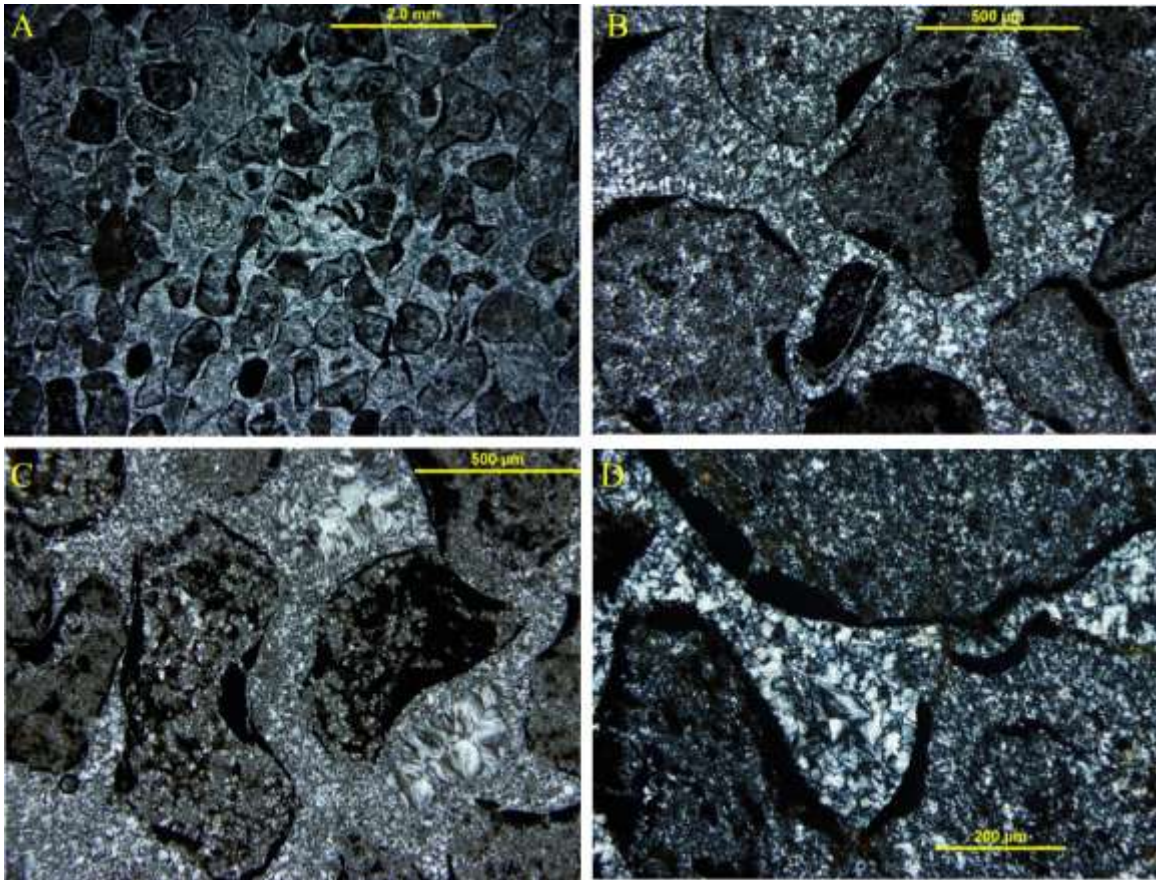
Figure 55: Thin section photomicrographs of the grainstone layer taken from the outcrop behind Mink Mountain. A) Sub-angular grains that make up the Mink Mountain grainstones. B) Drusy and mosaic cherts forming the primary cements with chalcedony fans visible in C). Photomicrographs of the chert grains and cements. D) Coating and replacement of chert grains.

5.1.1.2   The brecciated layer

There is a 30cm thick brecciated layer overlying the bedded grainstone at the outcrop behind

Mink Mountain. This is a thick rubble layer of grainstone in direct contact with the stromatolites.

It is comprised of large grainstone blocks that have been both overturned and broken up from the

intact grainstone below. The large grainstone blocks show both rotation and movement from the

grainstone layer (Figure 56). The brecciated grainstone layer reflects the breakup and post-lithification alteration of the grainstone. The open spaces between the grainstone blocks are filled with hematite and jasper (Figure 56B). The stromatolites above form directly on top of these brecciated grainstone blocks (Figure 56C). Thin sections taken from these samples show that the grainstones are recemented by the hematite and jasper (Figure 57). The brecciated grainstones still are composed of the non-oolitic grains but the cement has change. The red jasper that fills the spaces between the grainstone blocks are represented by very fine-grained cherts with the hematite inclusions forming a dark tint to the chert (Figure 57A). The jasper that intruded the grainstone blocks is comprised of fine-grained cherts with disseminated hematite grains (Figure 57B). The cement between the grains seems to be a combination of microcrystalline quartz forming on the edges of the grains. Open spaces created between the grains are filled by a combination of blocky quartz and some spherulitic fans of chalcedony (Figure 57C). The breccia also has clasts of the fine-grained cherts present along with the grainstone fragments (Figure 57D).

Figure 56: The brecciated grainstone layer of the outcrop behind Mink Mountain. A) Breccia directly below the stromatolite layer. The jasper and hematite fill open spaces between grainstone blocks. B) Blocky intrusions of jasper and hematite between grainstone blocks. C) Grainstone block directly beneath the stromatolites.
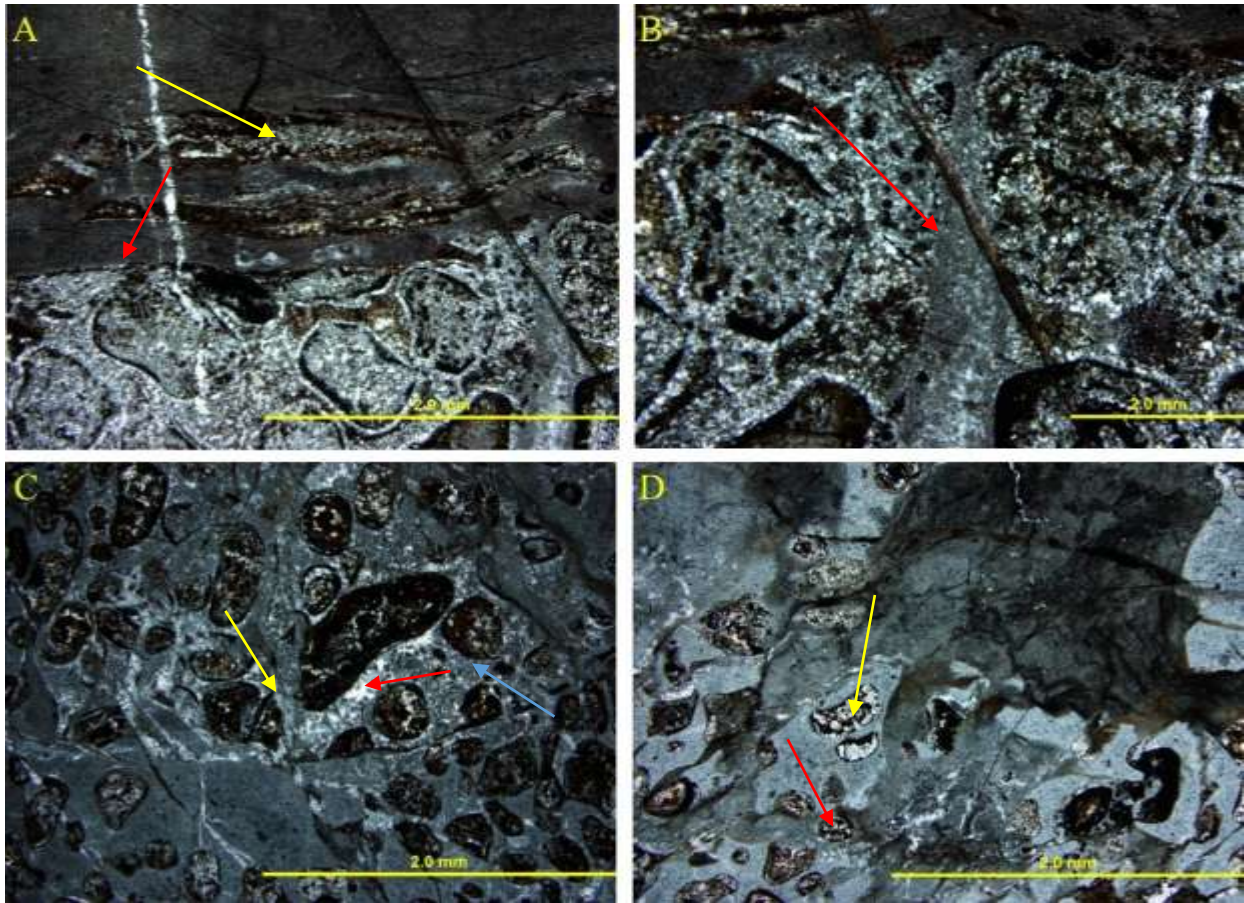
Figure 57: Photomicrographs of thin sections from samples from behind Mink Mountain taken from the brecciated grainstones. A) The contact between a jasper intrusion (red arrow) and the grainstone. Sections of the grainstone cement can be seen within the jasper intrusion (yellow arrows). B) A secondary intrusion (red arrow) is feeding from the jasper intrusion along a breccia surface in the grainstone. C) Grains hosted in the fine-grained jasper showing the microquartz drusy cement (blue arrow). Open voids filled by blocky quartz (red arrow) and chalcedony fans (yellow arrow). D) The jasper intrusions with grains showing both non-oolitic grains (blue arrows) and chert clast (yellow arrow).

5.1.1.3 The stromatolite layer

The stromatolites present at Mink Mountain have formed directly on top of the pre-lithified grainstone layer. Within the outcrop, there are varying generations of stromatolite growth, with the stromatolites appearing to grow in random directions due to the fracturing and rotation of the grainstone blocks ending the formation of one stromatolite and allowing for the growth of

stromatolites with a different up direction. The morphology of the stromatolites is mostly large decimeter-sized domes, which are comprised of thin digitate stromatolites. All of which grew off flat mat stromatolites, forming on the grainstone blocks (Figure 58 A, B, C)

Figure 58: The varying morphologies of the stromatolites from behind Mink Mountain. A) Domes. B) Digitate structures and C) Flat lying microbialite.

Petrographically, the stromatolites from the outcrop behind Mink Mountain, are comprised entirely of chert and iron oxides (Figure 59A). The layering of both flat mat and digitate stromatolites are well preserved (Figure 59B). Some of the stromatolites show open gaps between the layers, which are filled with either cherts or hematite. Interspaces between the stromatolites show infilling by rounded chert grains (Figure 59 C and D).
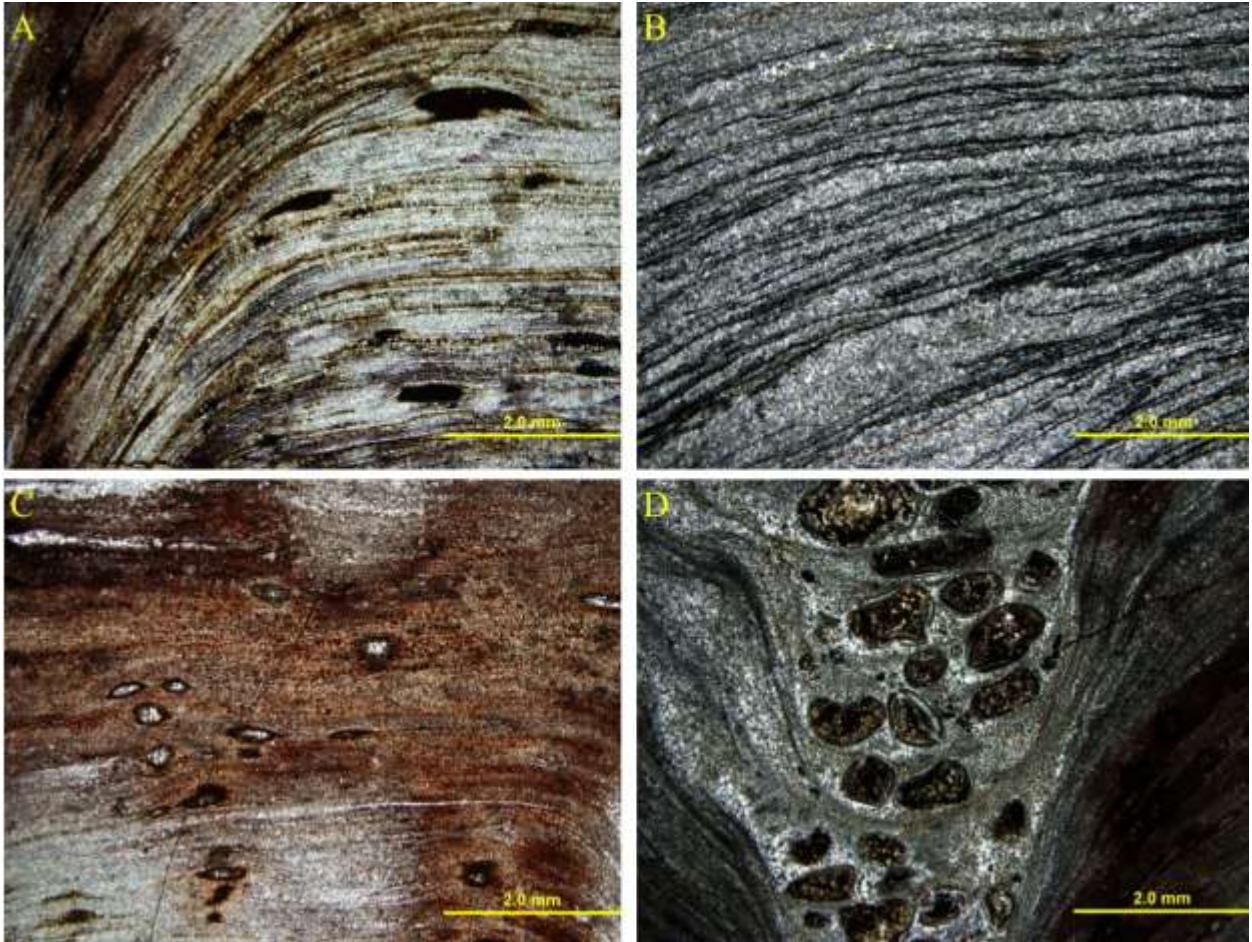
Figure 59: A and B) Well preserved layering of the stromatolites from behind Mink Mountain.C) Chert filled the open spaces between the stromatolite layers. D) Coarse chert grains filling the interspaces between the stromatolites with bridging laminae.

An ooid grainstone layer is present covering and filling the open spaces formed between the stromatolites and broken pieces of stromatolites throughout the outcrop (Figure 60). The majority of this layer is comprised of ooids and oncoids that are looser packed than the grainstone layer below the stromatolites, but are also cemented by chert (Figure 61A) and jasper (Figure 61B).
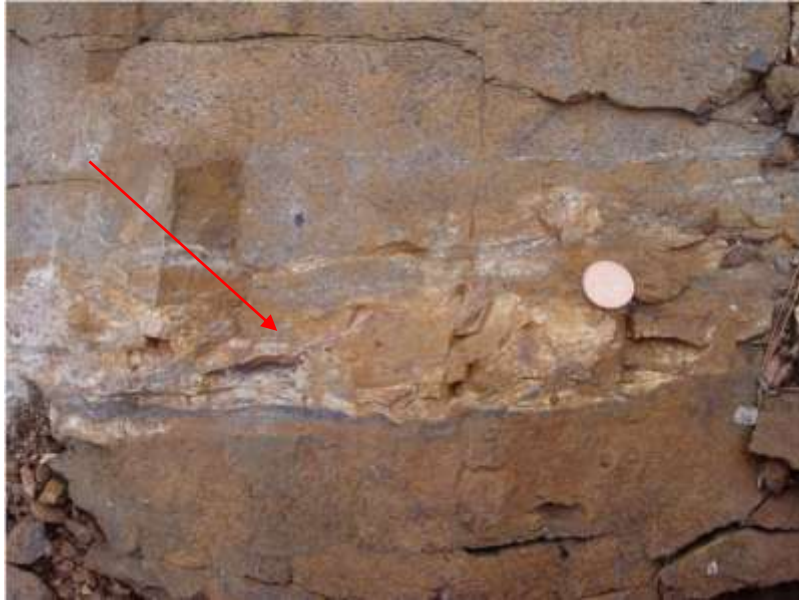
Figure 60: Ooid grainstone overlying the stromatolites at the outcrop behind Mink Mountain. The ooid grainstone can be seen surrounding the stromatolitic material in the middle layer in the photo (red arrow).
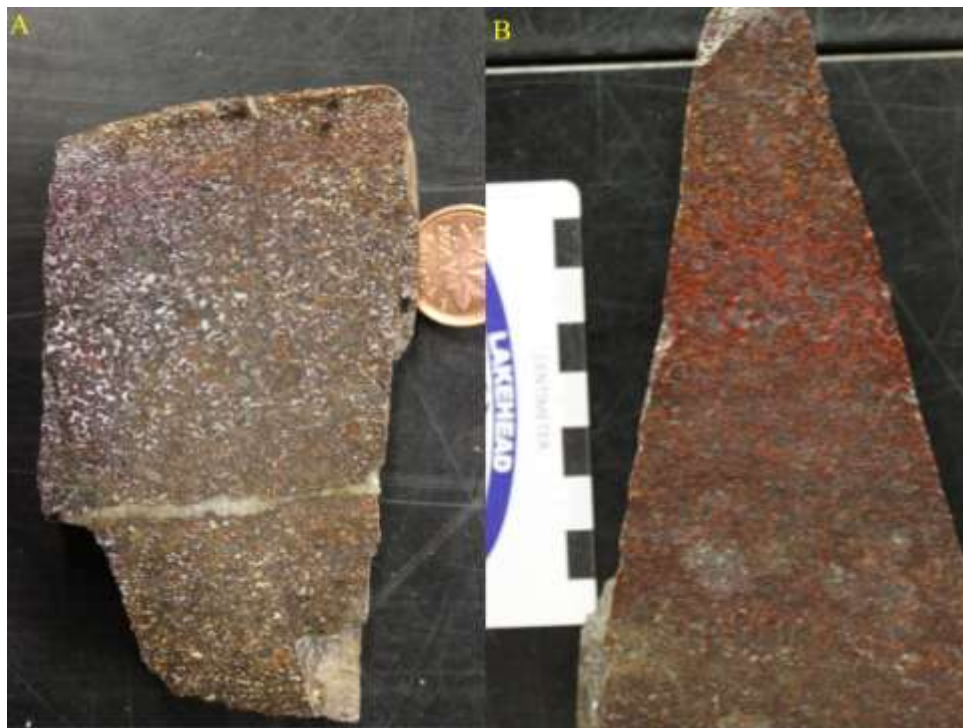
Figure 61: Polished samples of ooid grainstones from the outcrop behind Mink Mountain. A) The ooids hosted in a white chert cement. B) A red jasper cement is hosting the ooids.

Petrographically, ooids and oncoids are silicified, with the majority of them having one nucleation sites rimmed by concentric layers of iron oxides (Figure 62A). The nuclei are comprised of mosaic cherts ranging in grainsize from fine-grained mosaic cherts to blocky quartz cement forming the nuclei of the larger oncoids (Figure 62B). The cement that bonds the ooids together is much coarser-grained than the cement in the grainstone layer. The gains are mostly rimmed by chalcedonic overlays followed by blocky mosaic chert filling the open spaces; there are also some spherulitic chalcedony fans (Figure 62C). The layering within the larger oncoids shows dehydration cracks forming perpendicular to the layering. These cracks are filled with cement and show matching edges (Figure 62D).
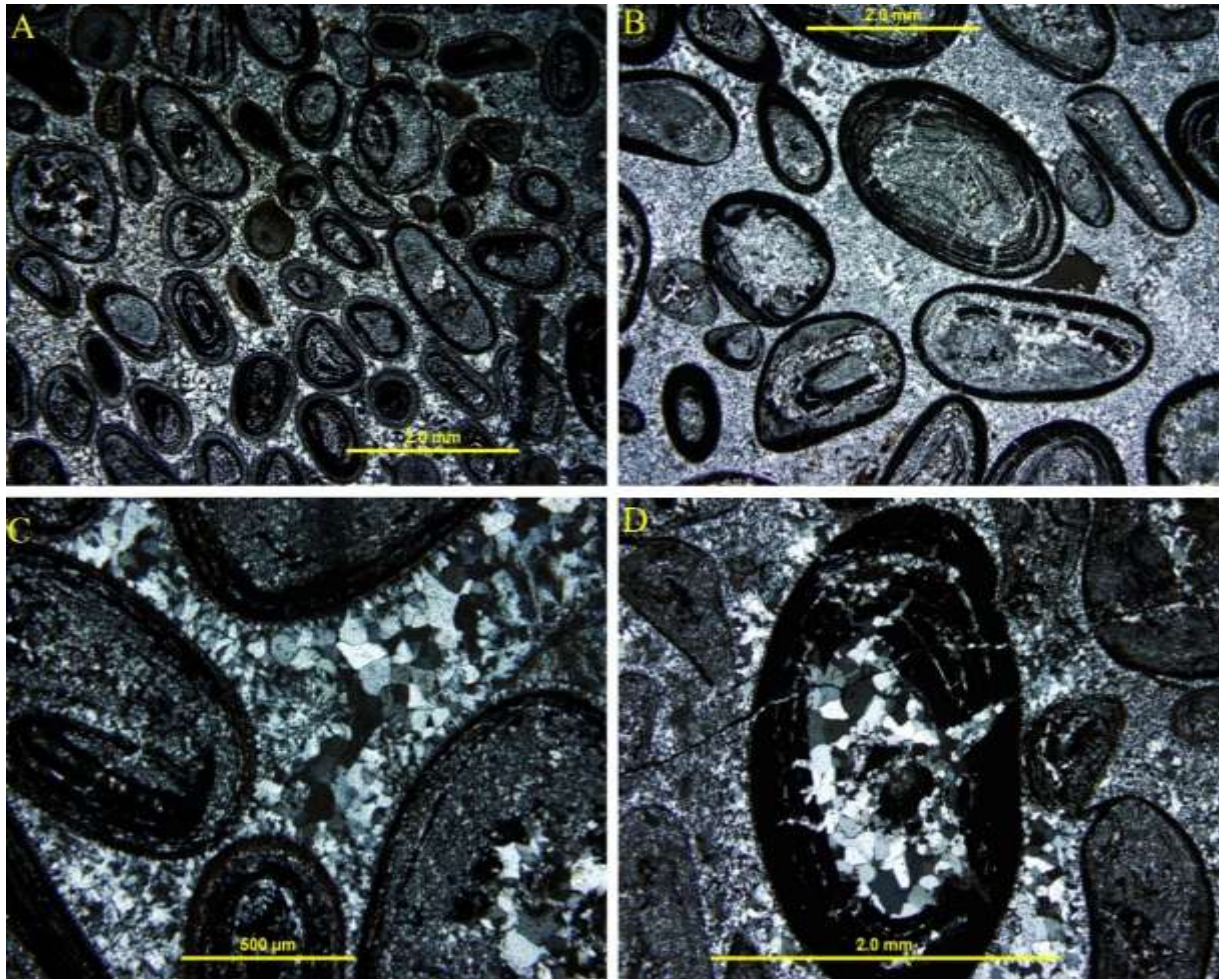
Figure 62: Ooid grainstone in samples taken from the outcrop behind Mink Mountain. A) This shows the range of grains from ooids to small oncoliths. B) The different nuclei that form the ooids and oncoliths. C) The change in cement from drusy cement around the edges of grains, to the chalcedony overlay surrounding the ooids to blocky quartz cement filling the open spaces to chalcedony spherulitic fans. D) Dehydration cracks with cement filling the dehydration cracks.

5.1.2 Old School Road

The outcrop is found on the shoulder of Old School Road, near Nolau, Ontario. This outcrop has a similar composition to that of the outcrop behind Mink Mountain, just 1.5km down the road. The samples taken from the outcrop show that it is comprised of a grainstone layer, which becomes brecciated before the formation of the overlying stromatolites. This is all capped by an oolite layer, similar to that of the outcrop behind Mink Mountain.

5.1.1.4 Grainstone and Breccia Stratigraphic unit

The Old School Road grainstone shows a similar composition to the grainstone layer found behind Mink Mountain (Figure 63A). The grainstones from the Old School Road outcrop are comprised of bluish tinted, medium-sized grains. The grains are tightly packed within a chert cement. There are thin veins crossing the grainstone, mostly comprised of chert and jasper (Figure 63B). There are two sets of these fractures that cross the grainstone layer directly beneath the stromatolites (Figure 64A). One fracture set with veins runs through the entirety of the grainstone but terminates at the stromatolite contact. The second set of veins runs entirely through the grainstone and terminates after cutting across the lower portion of the stromatolite layer (Figure 64B). This second set of fractures is thicker and mostly comprised of jasper and hematite. The veining within the grainstone is related to the brecciation of the grainstone layer. The brecciated layer of the Old School Road outcrop was best seen in a large sample taken from the flat-lying outcrop. A rotated large fragment capped off by microbiolite shows that the brecciation is similar to that of the Mink Mountain outcrop in which the grainstone layer was brecciated before the formation of the overlying stromatolites. Injections of hematite and jasper form the matrix of the breccia, filling the voids created by the breaking up of the grainstone.

Petrographically, the grainstone shows a similar composition to that of Mink Mountain. The grainstone is made up of non-oolitic, sub-angular grains (Figure 65A). The grains are comprised of mosaic cherts. Similar to that of the Mink Mountain grainstone, the majority of the grains in the grainstone show a range of coatings, with most only having a thin iron oxide coating around the grain (Figure 65B). The cement of the grainstone is mostly comprised of mosaic cherts. Dolomite grains, probably ferronian, are present within the cement (Figure 65C). The vein set that crosses the grainstone layer and terminates at the stromatolite are composed of chalcedony (Figure 65D).

Figure 63: The grainstone, brecciated layer and the stromatolites of the Old School Road outcrop. A) A grainstone block beneath the stromatolite layer, with the large voids being filled in by jasper veins (injections). B) The brecciated grainstone stratigraphic unit of the outcrop directly beneath the stromatolite. Dotted lines show the outlines of the grainstone blocks.
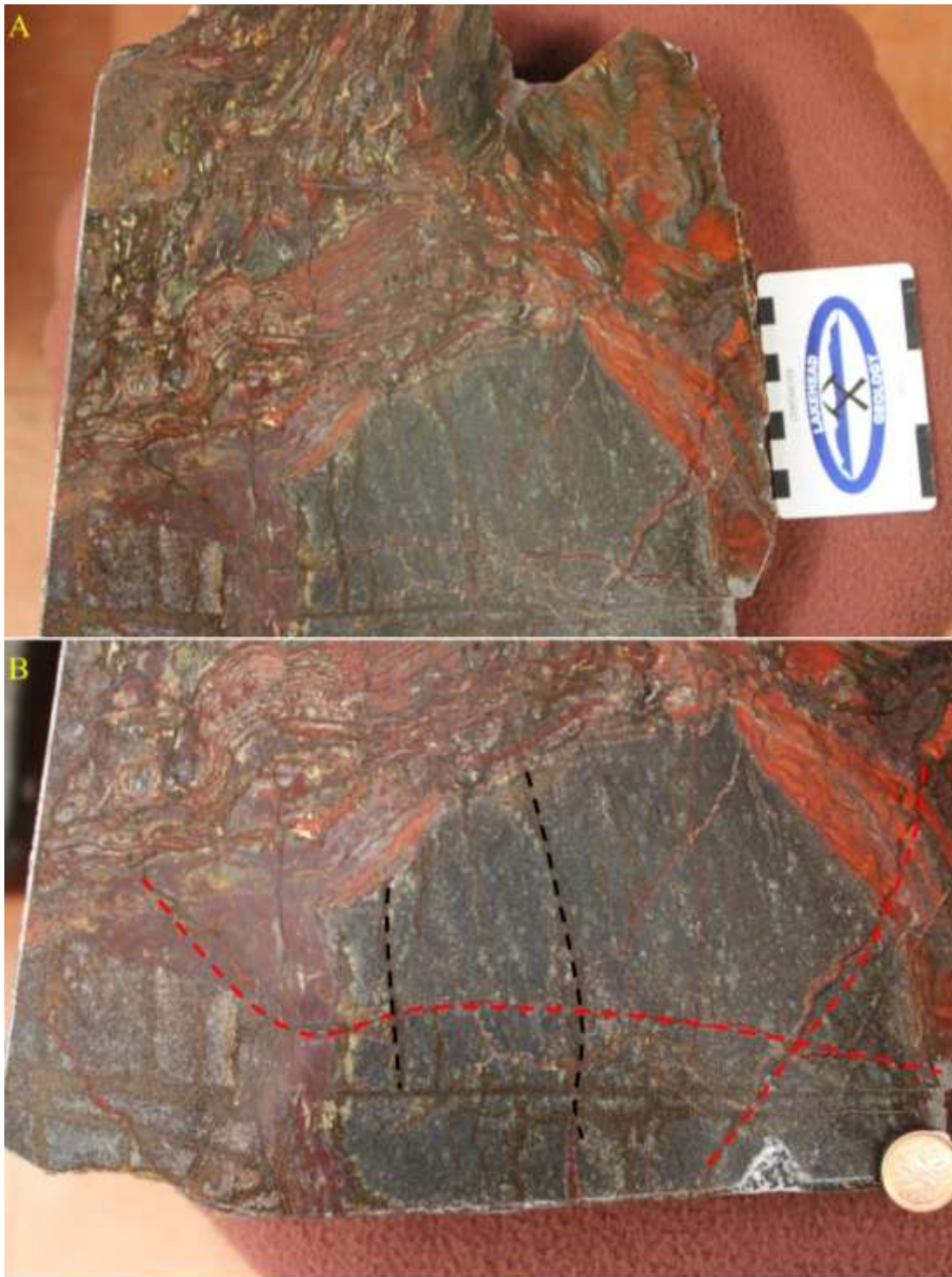
Figure 64: A polished slab of the brecciated grainstone layer in contact with the stromatolite from the Old School Road outcrop. A) The contact between the stromatolite and the grainstone showing the brecciation and filling by the large jasper and hematite veins. B) The veining of the grainstone layer. The ones that terminate at the stromatolite layer are dashed lines in black, and the red dashed lines are the veins that are continuous through the lower portion of the stromatolite.
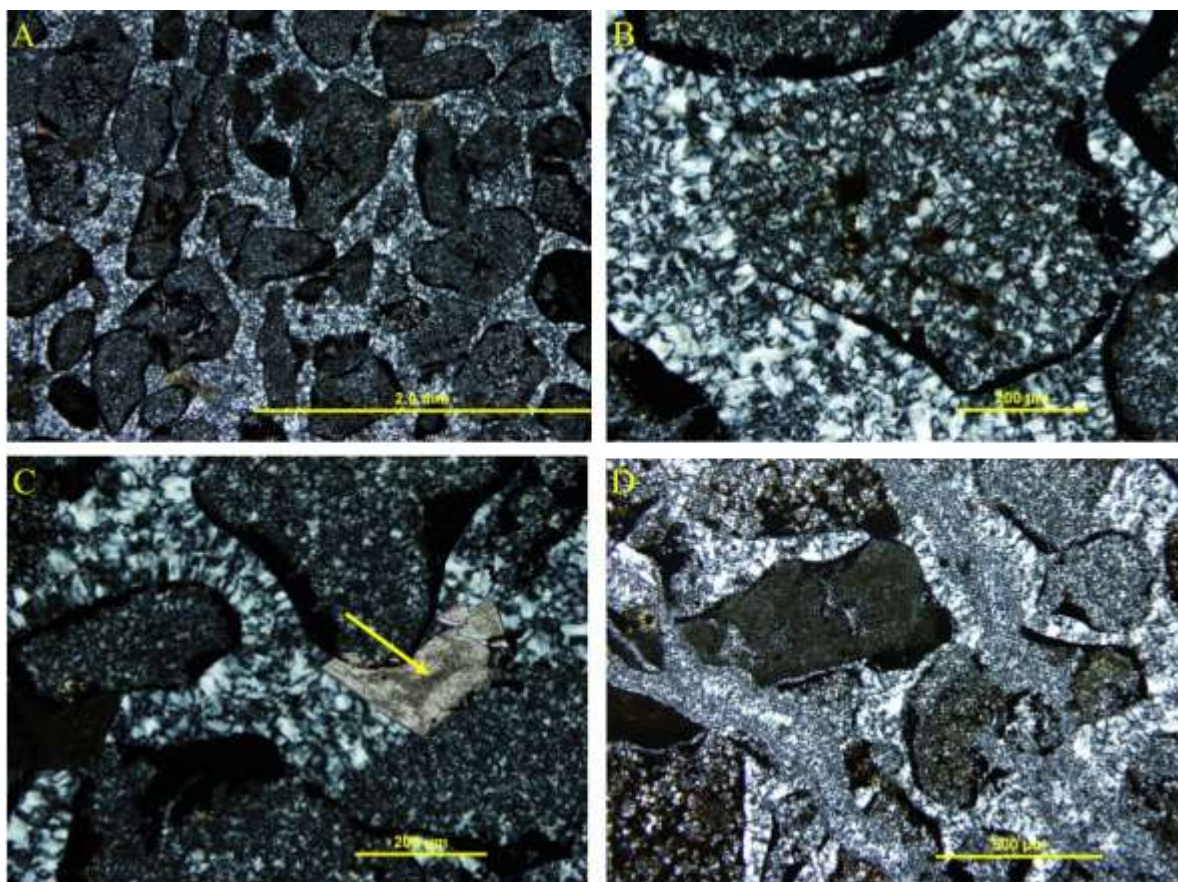
Figure 65: Photomicrographs of the Old School Road grainstone layer. A) Angular, non-oolitic grains showing various levels of coating and rounding. B) The primary cement of the grainstone layer showing the chalcedony drusy quartz rounding the edges of the grains as well as fans forming between grains. C) Dolomite rhomb (arrow) replacing some of the cement between the grains. D) Chalcedony filled fractures running through and breaking up the grainstone layer.

5.1.1.5 *Stromatolite Stratigraphic unit*

The Old School Road samples contain stromatolite morphologies ranging from flat-lying stromatolites, forming on the contact with the grainstone layer (Figure 66A) and growing up into digitate stromatolites near the top (Figure 66B and C). Much like the outcrop behind Mink Mountain, samples taken from the Old School Road outcrop show several generations of stromatolite growth intermixed with the angular shard-like grains and ooids from the overlying oolite grainstone. Petrographically, the red columnar stromatolites are comprised of fine-grained

mosaic cherts (Figure 67A). The layering of the stromatolites is not well preserved by iron oxides and opaques (Figure 67B). There are rounded non-oolitic grains present in the interspaces between the stromatolite columns. There the grains are cemented by the same fine-grained mosaic chert, with some coarse chert grains overprinting down the middle of the interspace between the bridging laminae (Figure 67C). Similar to the angular grainstone layer beneath the stromatolites there are rhombs of dolomite, probably ferronian, present in both the interspace and between the layering of the stromatolites (Figure 67D).
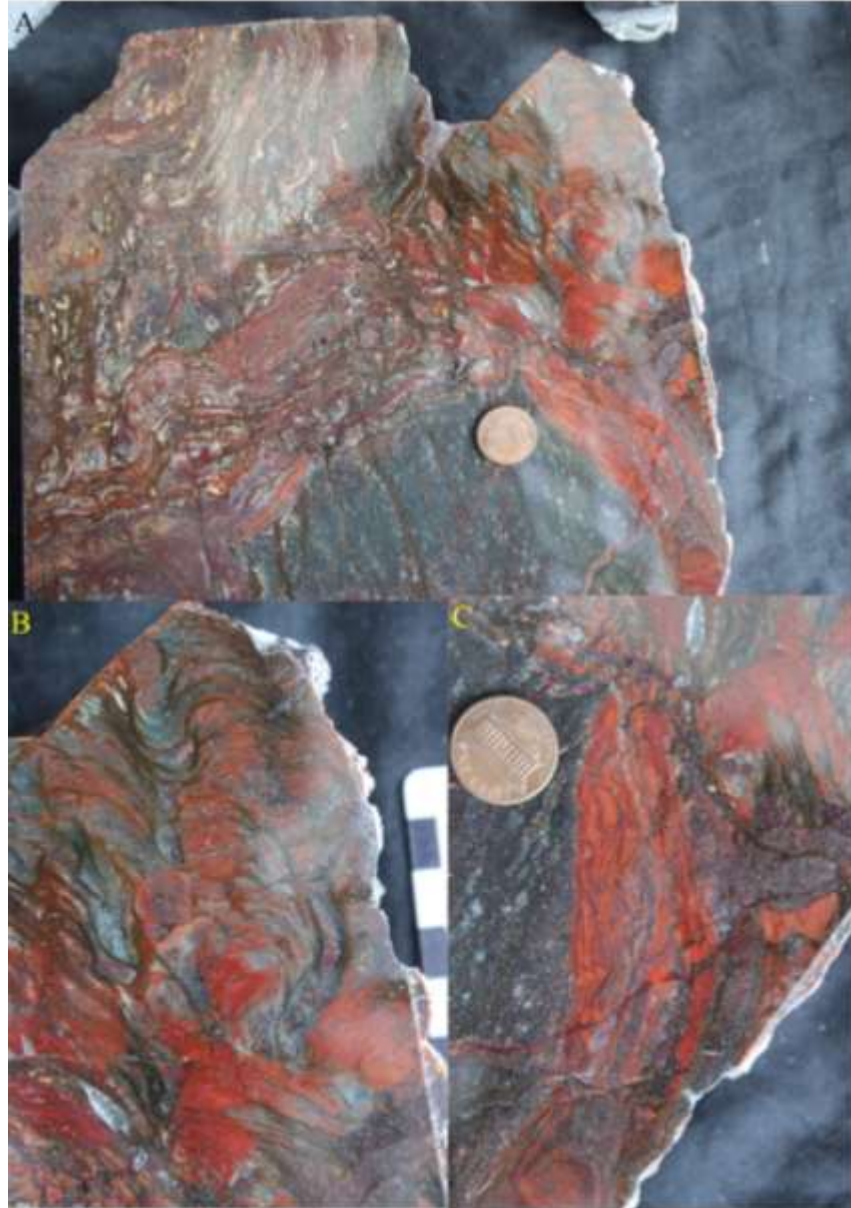
Figure 66: Photographs of the stromatolites from Old School Road. A) The stromatolites from Old School Road showing the different morpholgies including well formed digitates on the right, flat lying stromatolites at the contact with the boulder and broken up stromatolites to the left. B) Red digitate stromatolites C) Flat lying stromatolites at the contact with the boulder.
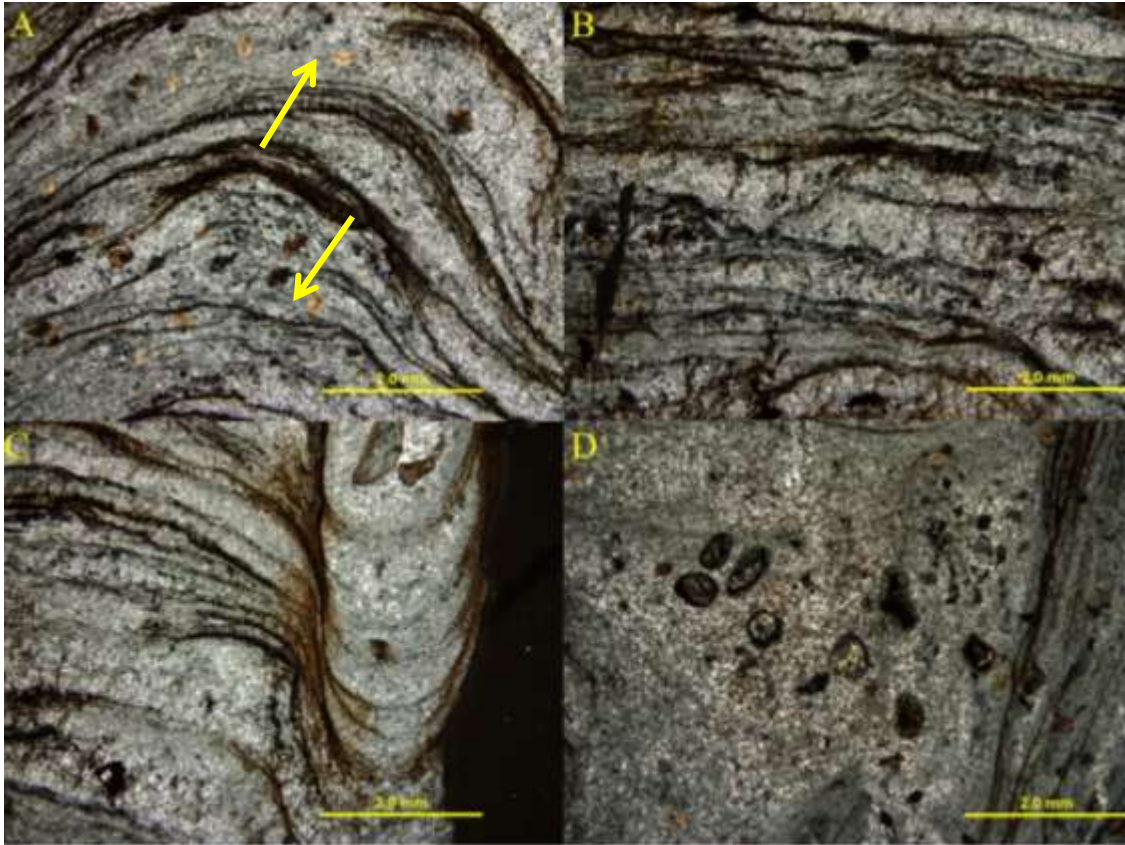
Figure 67: Photomicrographs of the stromatolites from Old School Road. A) The layering of the stromatolites showing the presence of dolomite rhombs. B) Well preserved layering of the stromatolites. C) Layering into the interspace with bridging laminae D) Grains found within the interspace of a stromatolite.

5.1.1.6 *Ooid Grainstone*

The ooid grainstone from the Old School Road outcrop shows a similar composition to the

ooid grainstone from the outcrop behind Mink Mountain (Figure 68A). These ooids are found

between the interspaces of stromatolites and rip-ups of the stromatolites can be seen within the

grainstone layer (Figure 68B). The ooids are coarse- to very coarse- grained and show concentric

layering around a chert nuclei (Figure 68 C).
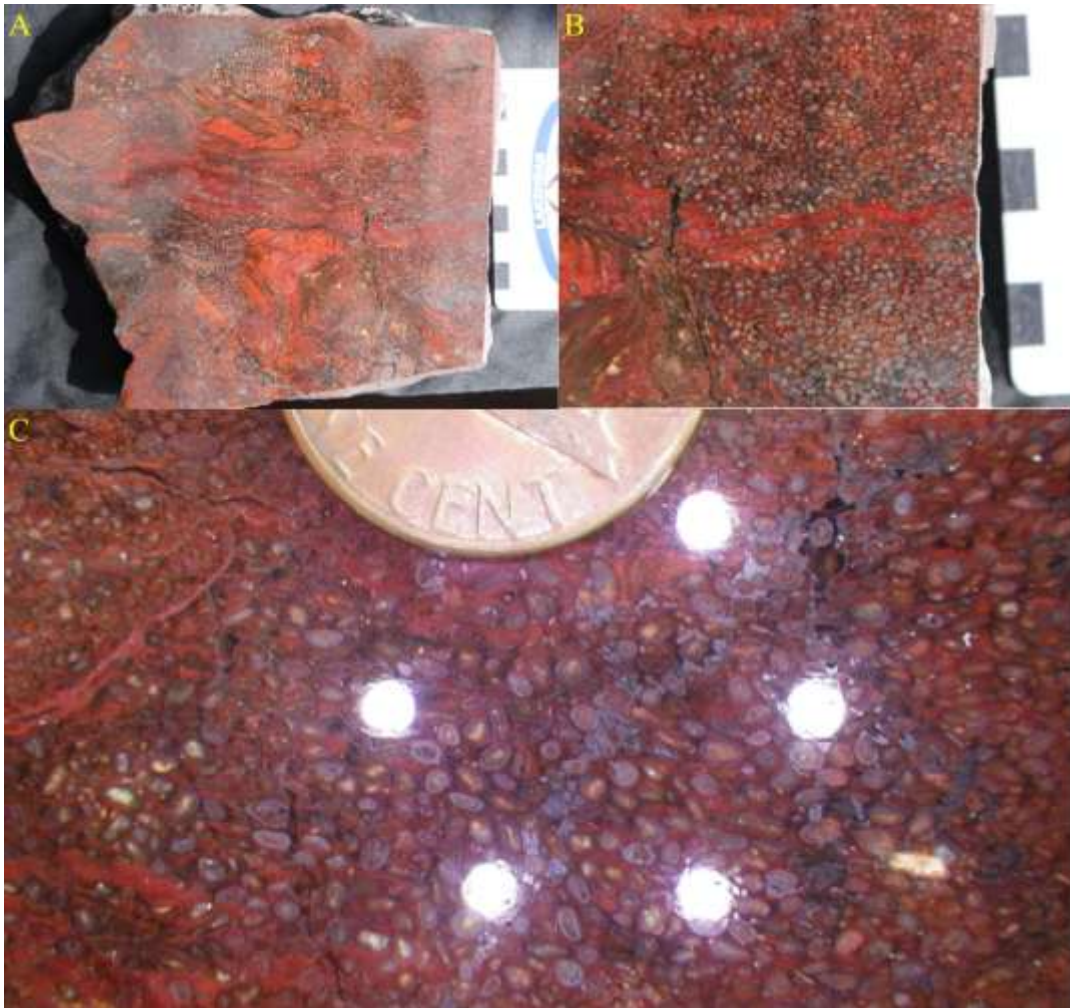
Figure 68: Photographs of the oolite grainstone from the Old School Road outcrop. A) A polished sample showing the ooilite grainstone and stromatolite. B) Close up of the ooid grainstone showing the predominate grains are ooids. Also seen are stromatolite ripups and microbial texture. C) Layering in ooids, jasper cement and wispy mat development. White circles are reflected camera lights.

5.1.3   Magnetic Rock Trail

The Magnetic Rock Trail outcrop is located on the Magnetic Rock hiking trail off the

Gunflint Trail in the Superior National Forest north of Grand Marais Minnesota. This series of

outcrops, on the side of the trail, shows the complete cycle of grainstones deposited during

regression upon which the stromatolites are formed. Further trangression lead to the depostion of

grainstone and allowing for the deposition of the volcanogenic lapilli stratigraphic unit on top.

The proximity of the Magnetic Rock outcrop to the Duluth complex and resultant thermal

metamorphism has resulted in an appearance different from that of the previous sites.

Figure 69: The outcrops found on the Magnetic Rock trail, in the Superior National Forest, Minnesota A) The grainstone underlying the capping brecciated layer (top of cliff) and stromatolites. B) The top of the Magnetic Rock trail outcrop showing the lapilli layer (red arrow) overlying the stromatolites.

5.1.1.7   Grainstone Stratigraphic unit
The exposed grainstone stratigraphic unit of the Magnetic Rock Trail outcrop is 444cm thick

and comprised of an interlayering of grainstones and fine-grained chemical sediments (Figure

69A). The grains that comprise the grainstone stratigraphic unit are medium to coarse magnetite

grains. The grains are bound together in a quartz cement.

5.1.1.8 *Brecciated Stratigraphic unit*

The brecciated layer present at the outcrop on the Magnetic Rock Trail is a 30cm layer directly beneath the stromatolites. This stratigraphic unit is different from the brecciated stratigraphic unit beneath the stromatolites behind Mink Mountain and Old School Road, in that instead of the brecciated grainstone and jasper, the brecciated stratigraphic unit is comprised of rip up clasts from the grainstone layer cemented by ferroactinolite grains.

5.1.1.9 *Stromatolite Stratigraphic unit*

The stromatolite layer of the Magnetic Rock Trail outcrop is about 100cm thick and lies directly above the brecciated grainstone layer (Figure 70 and Figure 71). Figure 70A shows that the majority of the stromatolites formed at the Magnetic Rock outcrop are comprised of thin digitate stromatolites which grade into low lying flat laminated stromatolites (Figure 70B and C). Unlike the red stromatolites of Mink Mountain and Old School Road, the stromatolites found on the Magnetic Rock Trail range in colour from light green to dark green with white and black areas (Figure 70D). Thick chert layers can be seen between the layers of the darker stromatolite.. Petrographiclally the stormatolites are comprised mostly of fine-grained mosaic cherts (Figure 71). The stromatolitic layering is not as well preserved as at the other sites. Fine-grained crystals of actinolite are present within the stromatolite mosaic cherts. Ooids can be seen within the interspace of the stromatolites. These ooids are comprised of iron oxide replacing cherts around a chert nucleus. The layering surrounding the nucleus shows dehydration cracks that are filled by chert cement.

Figure 70: Photographs of polished hand samples from Magnetic Rock Trail. A and B) Showing the light coloured digitate stromatolites grading into the darker coloured flat lying stromatolites. C) The flat lying stromatolite completely underlying digitate stromatolites. D) Close up of the digitate stromatolites with pelloids in between the digitate heads.

Figure 71: In situ stromatolites at Magnetic Rock Outcrop. A) Flat lying light green-grey stromatolites. B) Darker stromatolites with chert between the stromatolitic layering. C) Crinkly, flat stromatolites. D) 3D view of the Magnetic Rock stromatolites.

5.1.1.10 Lapilli stratigraphic unit

The stromatolites of the Magnetic Rock trail outcrop are capped off by a layer comprised of lapilli lenses and grainstone (Figure 72 A). This layer is in a similar stratigraphic position to the oolite layer present at both Mink Mountain and Old School Road. There are two distinct lapilli lenses; they are found between medium-to coarse- grained grainstones, with the top layer being overlain by a massive magnetite layer (Figure 72B). The grainstone that is present between the lapilli lenses is comprised of medium-to coarse- grained rounded granules in a chert cement (Figure 72C).
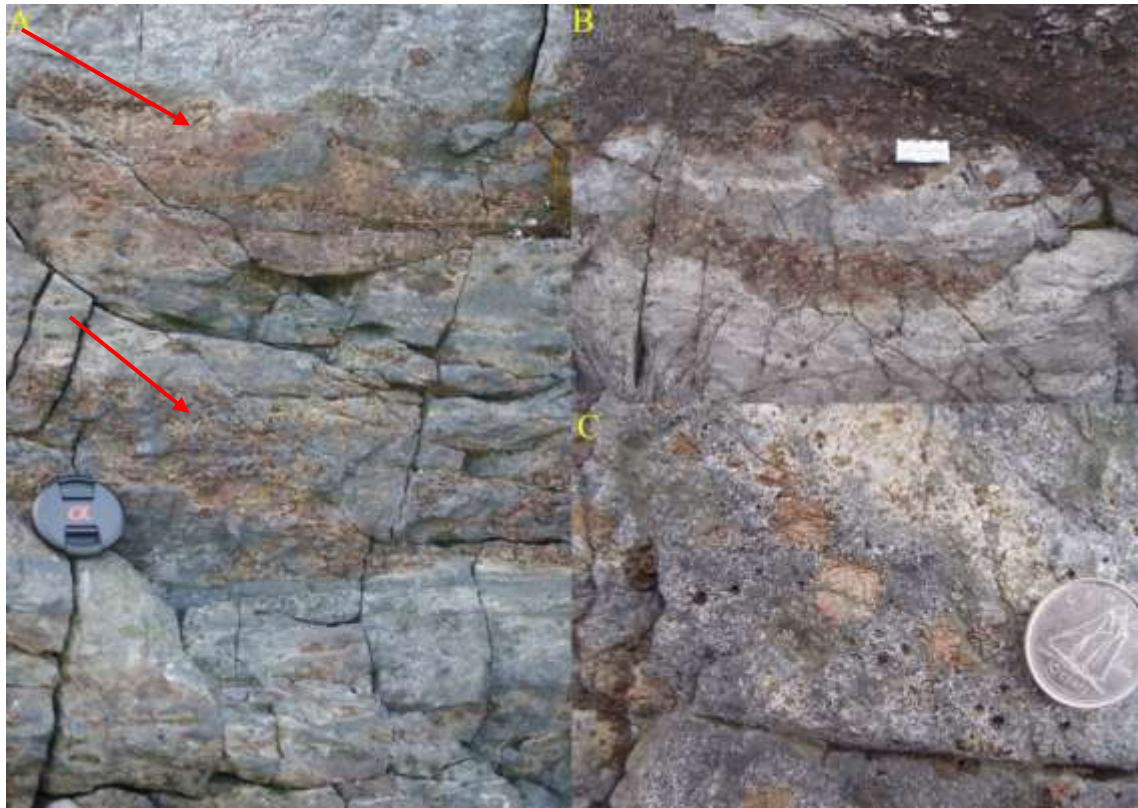
Figure 72: Images of the lapilli layers above the stromatolites at Magnetic Rock Trail. A) The two distinct lapilli lenses (red arrows). B) The magnetite layer above the lapilli layer. C) Close up of the lapilli comprised of minnesotaite. Layers of medium grained grainstones with chert cement is present between the lapilli.

5.1.4 Current River

There are two outcrops containing stromatolites loctated on the edge of Current River in the northeastern portion of Thunder Bay, Ontario. The first outcrop is present on the edge of Boulevard Lake and the second is located beneath the Arundel Street bridge to the north of Boulevard Lake, approximately 3m stratigraphically above the first. These outcrops have distinctly different grainstones, breccias and stromatolites.

5.1.1.11 Grainstone stratigraphic unit

At the first study site the stromatolites are found at the mouth of Current River as it flows into Boulevard Lake (Figure 73). The grainstones at this site were originally comprised of fine-grained ferroan dolomite (ankerite) grains (Figure 73A and B). The grains were rapidly silicified in places, and then cemented by a blocky quartz cement resulting in the presence of the silicified pods present within the grainstone (Figure 73D).

The second grainstone site under the Arundel Street Bridge, was originally comprised of ferroan dolomite grains. These grains were then completely silicified resulting in the complete replacement of the ferroan dolomite. Three distinct agate filled fractures are present within this layer. This 1m thick grainstone layer sites immediately above the ferroan dolomite grainstones present at the Boulevard Lake site (Figure 74A).

Figure 73: The outcrop at the mouth of Current River. A, B) and ferroan dolomite grainstone beneath the stromatolites. C) Domal stromatolite comprised of chert. D) Chert clast present in the ferroan dolomite.

5.1.1.12 *Brecciated stratigraphic unit*

The brecciated stratigraphic unit at the two Current River outcrops are quite different from each other. The Boulevard Lake outcrop contains silicififed stromatolite and grainstone clasts within the ferroan dolomite grainstone (Figure 73D). These broken fragments are more numerous near the chert stromatolites and were derived from them during the storm events which deposited the grainstones (Fralick, 1988).

The brecciated stratigraphic unit present below the stromatolites under the Arundel Street bridge (Figure 74A) is composed of brecciated grainstone fragments that have, in places, been

replaced by pyrite (Figure 74B). The grainsize decreases upwards towards the stromatolites (Figure 74C).

Figure 74: The stromatolite layer beneath the Arundel Street Bridge showing the brecciated stratigraphic unit. A) The outcrop portion showing the silicified layer (yellow arrow) and the brecciated layer (red arrow). B) The brecciated layer. C) Close up of pyritiferous breccia showing the upward decrease in grainsize.

5.1.1.13 Stromatolite Stratigraphic unit

The two stromatolite stratigraphic unit present at the Current River outcrop area have different compositions and structures (Figure 75). The first, at the mouth of the Current River, has stromatolite colonies present within the ferroan dolomite (Figure 75A and B). These stromatolites are up to 10 cm in diameter and composed of chert. Laminations are rarely preserved, but when visible they are highlighted by blocky quartz or open fractures (Figure

75C). The stromatolites sit directly above the ferroan dolomite (Figure 75D), with stromatolite
fragments in the ferroan dolomite.
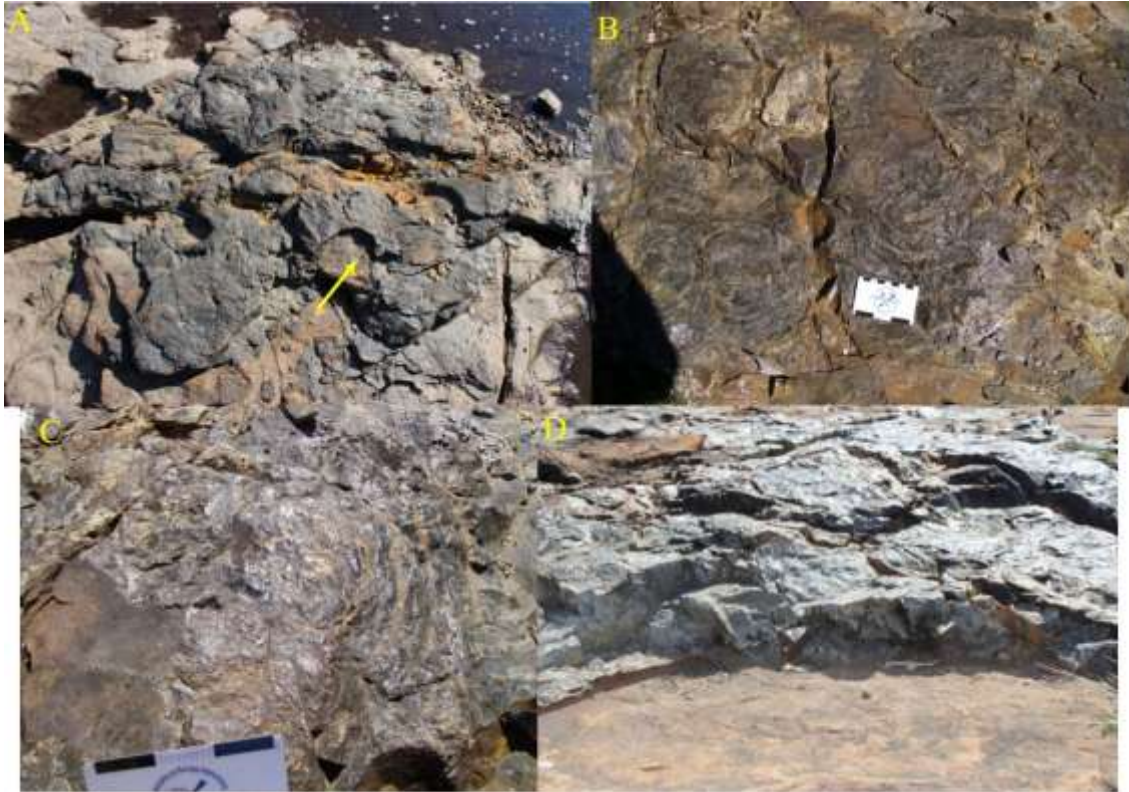
Figure 75: Stromatolites from the edge of Boulevard Lake at the mouth of Current River. A) B) Two examples of the domal stromatolites found at the Current River outcrop (yellow arrow indicates toonie for scale). C) Layering preserved by quartz replacement. D) Contact with the ferroan dolomite grainstone below.

The second site below the Arundel Street Bridge, contains microbiolites with a different composition and structure compared to those found at the edge of Boulevard Lake. The stromatolites are composed of both carbonate and chert and are associated with areas resembling thrombolites. The thrombolites show the lack of layering inconsistent with stromatolites, but instead they have clotted structure that is similar to throbolites (Figure 76C). The thrombolites

overly the brecciated layer. The stromatolites overlying the throbolitic area are covered by highly

pyriferous volcanogenic shales (Fralick, 1988) (Figure 76D).
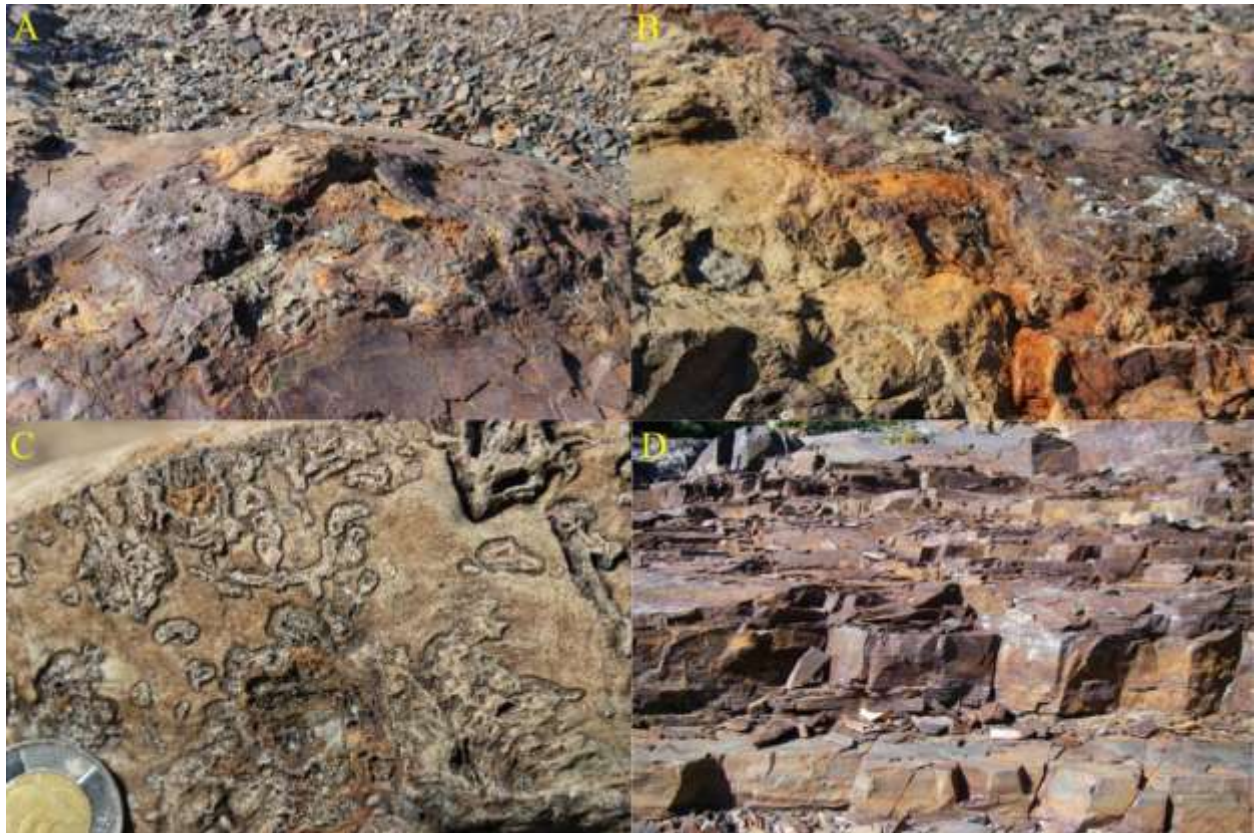
Figure 76: The microbiolites present at the Arundel Street Bridge site. A) The domal stromatolites with pyiteiferous shales coating the domes. B) Pyritiferous coating on top of the stromatolite domes. C) Clotted structure of the thrombolite showing no defined layering or stromatolitic structures. D) The shales above the stromatolites at the Arundel Street Bridge location.

Thin sections show that there is a sharp contact between the chert and ferroan dolomite in

the samples from the Current River outcrops (Figure 77). The thin sections show that the

silicified grainstones are comprised of rounded granules of mosaic chert. The grains are

cemented by a microcrystallie quartz with blocky quartz filling the open spaces between the

grains (Figure 77A). Ferroan dolomite shows neomorphic textures within the samples (Figure

77B). The thin sections show the contact with ferroan dolomite that is being replaced by the

chert (Figure 77C). The contact is very sharp between the two and shows that there is a lack of

crystal habit, which shows that replacement was rather quick. The reason that the grains are

visible in the chert but not in the ferroan dolomite is that the quartz is a stable mineral but

carbonates are not. Early silicification replacing the carbonate preserved the grains, whereas the

ferroan dolomite grains that were not silicified were destroyed by neomorphic crystal growth.

Pyrite grains are seen present within the ferroan dolomite and chert grainstone (Figure 77D).
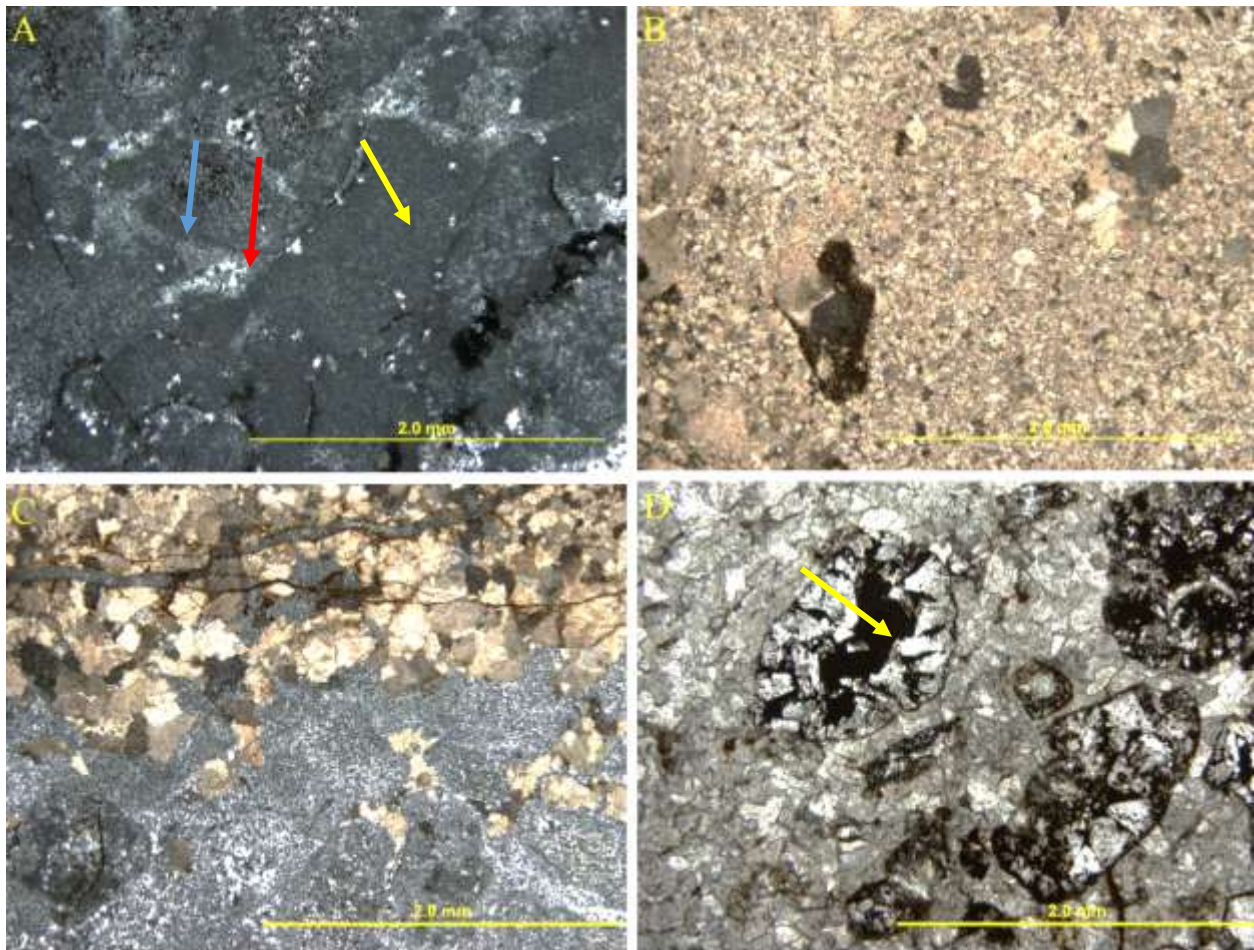
Figure 77: Photomicrographs of thin sections of samples taken from Current River. A) The cherts grainstone composed of mosaic chert grains (yellow arrow) cemented by mosaic chert (blue arrow) with blocky quartz filling the open spaces (red arrow). B) Neomorphic ferroan dolomite. C) Chert replacing the ferroan dolomite, which has been neomorphically recrystallized. D) Pyrite crystals (yellow arrow) within the ferroan dolomite.

5.1.5   DH 87-3

Drill Hole DH 87-3 was drilled south-west of Kakabeka Falls, through approximately 100m

of the Gunflint Formation and a few meters of the underlying Archean granite. This drill hole

intersects the thickening upward sequence below the regression surface upon which the middle

stromatolite unit was deposited. Much like outcrops of this cycle the rocks can be split into four

distinct stratigraphic unit. The cycle starts off with a medium-to-coarse grainstone layer,

followed by a brecciated layer upon which the stromatolites formed. This is overlain by chemical

mudstone and grainstone layers.

5.1.1.14 Grainstone Stratigraphic unit

The grainstone stratigraphic unit underlying the stromatolites in DH 87-3 is different than the

grainstone stratigraphic unit from the other study sites (Figure 78A). The grainstones is a

combination of medium-to coarse-grainstone interlayered with both carbonaceous and non-

carbonaceous shale layers (Figure 78B). The medium- to coarse- grainstone is comprised of dark

green grains that are hosted in white cement, which is likely a combination of chert and calcite

(Figure 78C). Both of these layers are cut by calcite and quartz veins from 1-10cm thick (Figure

78D) which were formed and filled post lithification. Moving up the stratigraphic unit there is a

distinct grain size change from medium grains in beds at the bottom of the core box to coarse

grains directly below the contact with the brecciated stratigraphic unit. The shale layers are either

brown carbonaceous-rich layers or black chemical mudstone layers, which are mostly

interlayered between the grainstone.

Figure 78: Photos of drill core showing the grainstone stratigraphic unit of drill hole DH 87-3. A) Medium sized grains with white chert and calcite cement. B) Carbonaceous and non-carbonaceous chemical sediments interlayered with grainstone. C) Coarse grains present in the grainstone stratigraphic unit. D) Calcite veins crosscutting the shales and the grainstone.

5.1.1.15 Brecciated Stratigraphic unit

This 295cm thick stratigraphic unit within the core box is comprised of layers of brecciated grainstone with minor amounts of allochthonous clasts near the top of the stratigraphic unit (Figure 79A). This stratigraphic unit also includes carbonaceous and non-carbonaceous shales similar to those underlying it (Figure 79B). Unlike the previous study sites, in which the grainstones were brecciated by jasper intruding into fractures, the grainstone layer from the DH 87-3 is brecciated by white calcite and chert veins (Figure 79C). Some of the brecciated

grainstones have been entirely replaced by calcite. Post lithification some of the calcite

developed vugs, which became quartz filled (Figure 79D).
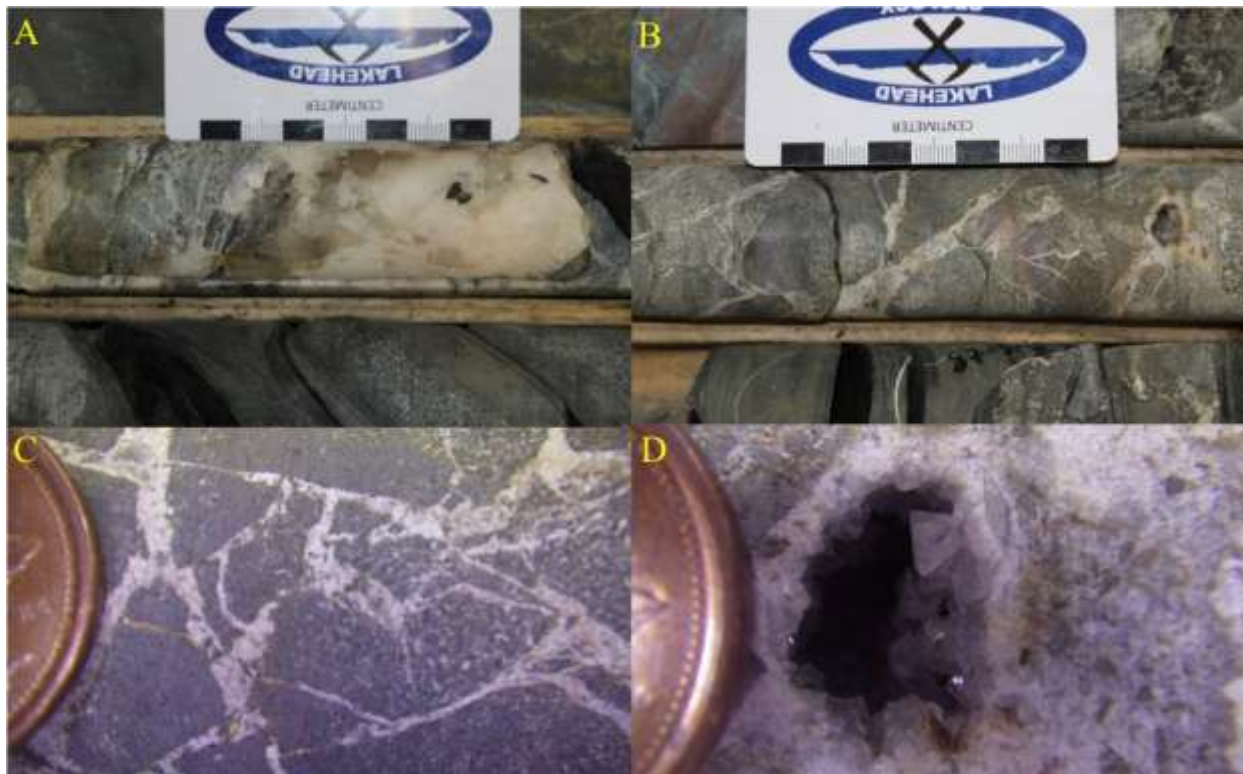
Figure 79: Photographs of the drill core showing the brecciated stratigraphic unit. A) A thick calcite vein at the base of the brecciated stratigraphic unit. B) The brecciated grainstone. C) Close up of the brecciated grainstones showing the brecciated clasts and calcite fracture fills. D) Quartz crystal in a vug within a fracture fill.

5.1.1.16 Stromatolite Stratigraphic unit

The 59 cm thick stromatolite stratigraphic unit present with in drill hole DH87-3 is

comprised of red to brown chert stromatolites (Figure 80A and B). Thin sections of the

stromatolites, show that they are comprised of fine-grained mosaic cherts (Figure 81A). The

stromatolitic layering is defined by changes in primary hematite content and thin, carbon-rich

layers (Figure 81B). The fractures present in the stromatolites are filled by spherulitic fans of

chalcedony which was probably formed post-lithification. (Figure 81C and D).

Figure 80: Core photos of the stromatolites from drill hole 87-3. A) The contact between the grainstone and stromatolites. B) The red stromatolites
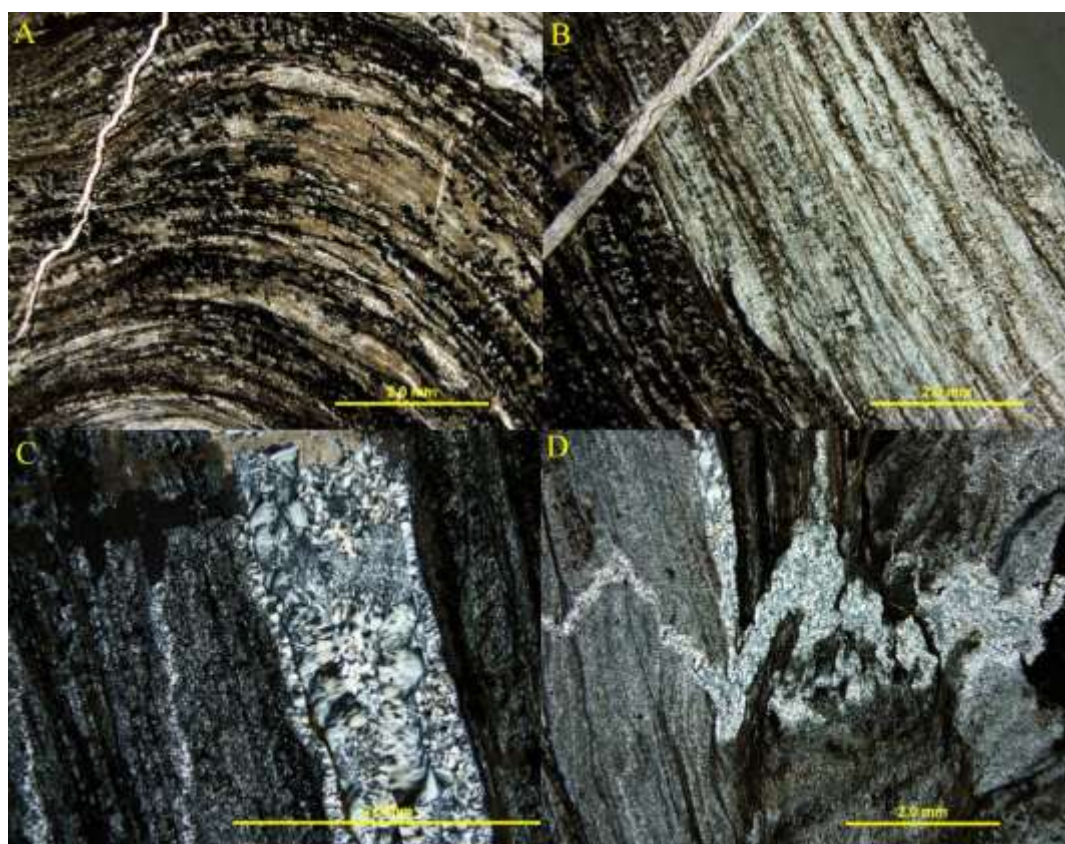
Figure 81: Photomicrographs of stromatolites from DH 87-3. A) Well-defined layering of a stromatolite showing carbon-rich layering and replacement of chert layers. B) Fine-grained mosaic cherts. C) First generation of quartz crystals can be seen forming along the margins of a fracture fill. Remaining space in the fracture is filled by chalcedony D) Post-lithification chalcedony filled fractures cross-cutting the stromatolitic layering.

5.1.1.17 *Chemical sediments stratigraphic unit*

Unlike the outcrop behind Mink Mountain and Old School Road, the unit overlying stromatolites on the regression surface in DH 87-3 is not comprised of an oolitic grainstone but composed of a 58 cm thick layer of chemical sediments. A 13cm mudstone layer sits directly on top of the stromatolites. This is then overlain by a 33cm thick grainstone with replacement patches of green silicates. This is overlain by the deposition of medium- to coarse- grained grainstone.

5.1.6 *Drill Hole MC-89-1*

Drill hole MC-89-1 was drilled outside of Thunder Bay, Ontario just off Highway 61 approximately 15km north of the U.S .border. This drill hole intercepts two of the three stromatolite layers present in the Gunflint Formation. The drill hole contains medium to coarse stromatolites are then overlain by fine-grained chemical sediments before the reappearance of the grainstone. The altered grainstone stratigraphic unit of the MC-89 drill-hole is unlike the altered layer beneath the Mink Mountain and Old School Road stromatolites which appear as brecciated grainstones (Figure 82A). The MC-89 drill hole altered grainstone stratigraphic unit is comprised of medium-to coarse- grained chert grainstone that has been partially replaced by magnetite and hematite (Figure 82B and C). The unaltered grainstones are comprised of medium- to coarse-grained chert cemented by quartz (Figure 82D). The magnetite content decreases up through the altered grainstone, whereas hematite is consistent.

In thin section the altered layer is composed of medium- to coarse-grained mosaic chert granules (Figure 83A), with the granules cemented by blocky quartz. Magnetite replaces the granules and varies from replacement of edges and rims to the complete replacement of the

grains (Figure 83B). Oxide layers are composed of rhombs of magnetite as well as recyrstallized

hematite grains (Figure 83C). Calcite replaces both the cement and grains in the altered

grainstone (Figure 83D).
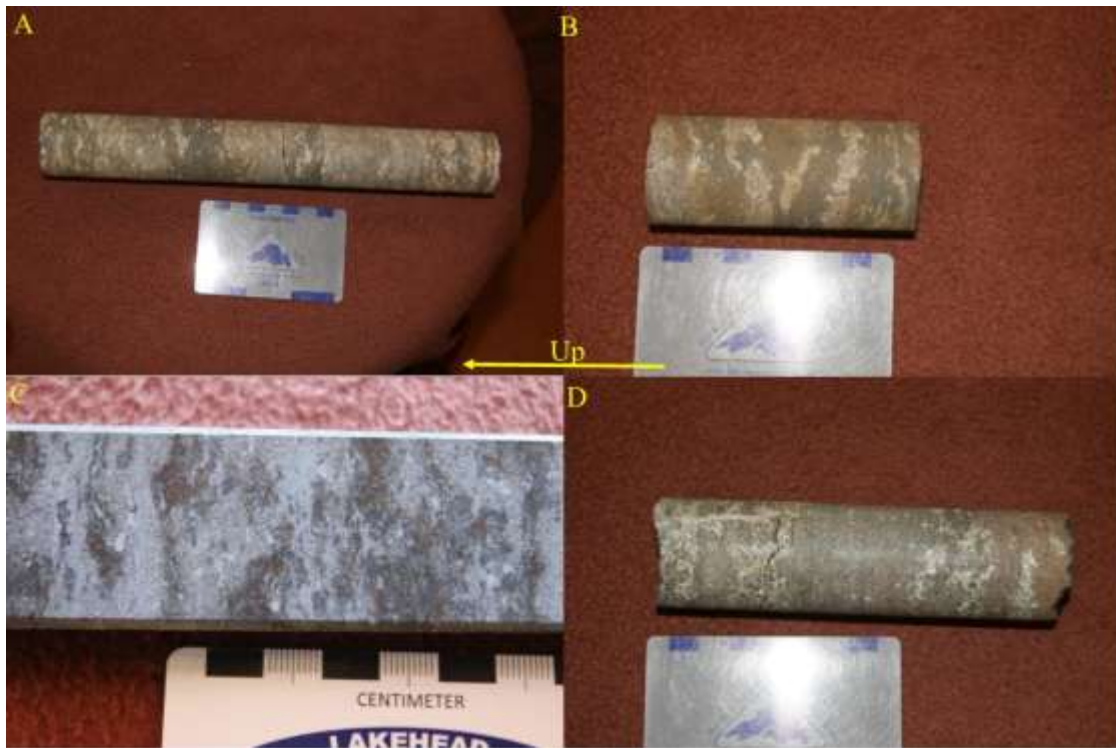
Figure 82: Photographs of the mottled altered drill core section from drill hole MC-89-1. A) Section of the mottled grainstone layer from MC-89 drill hole. B) Close up of the mottled section showing magnetite and grainstone lenses. C) Polished section of the mottled layer showing the replacement of the grainstone by magnetite and minor hematite. D) Medium-to coarse-grainstone directly below the stromatolite unit.
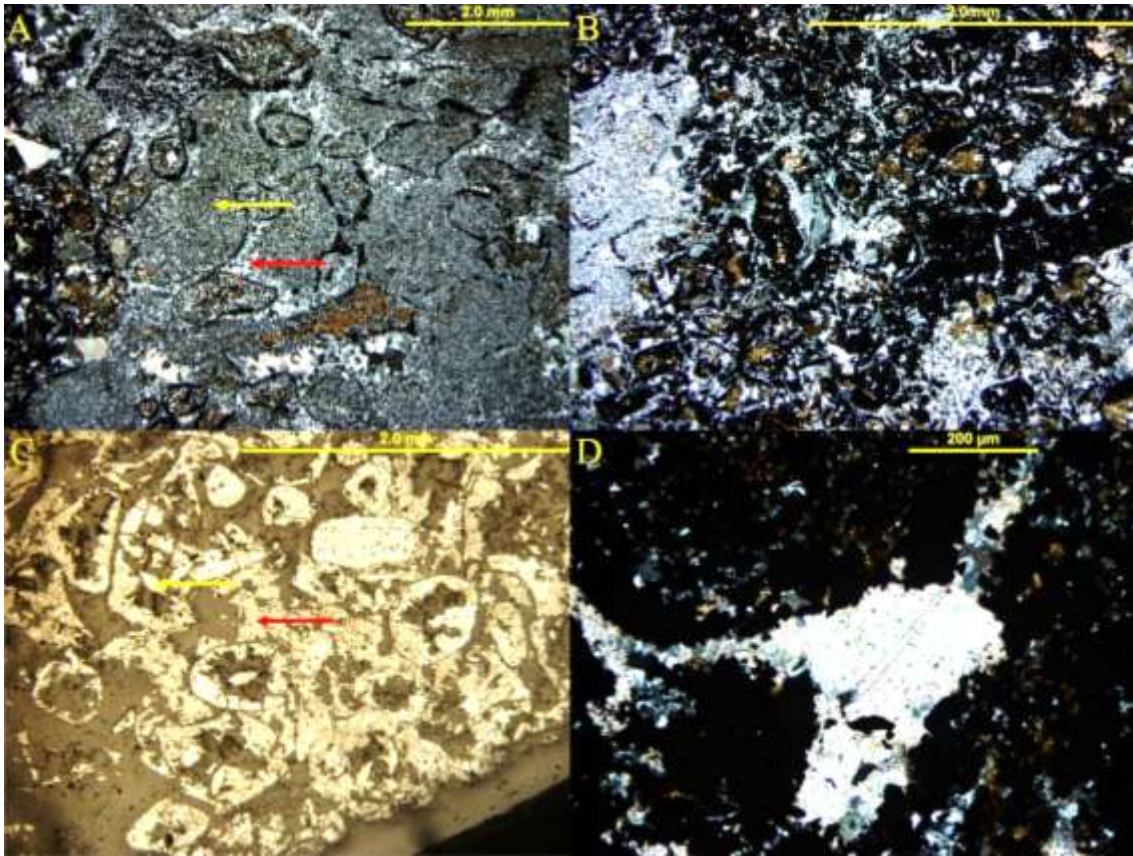
Figure 83: Photomicrographs of the MC-89-1 drill-hole mottled, altered layer. A) In the grainstone, the chert mosaic grains (yellow arrow) are cemented with blocky quartz (red arrow). B) The mottling caused by iron oxide replacing the grainstone. C) Reflected light photomicrograph of the mottled section showing the magnetite rhombs (yellow arrow) and massive hematite (red arrow), the darkest portion represents the chert and calcite. D) Calcite present within the mottled altered layer.

5.2 Whole Rock Geochemistry
5.2.1 Mink Mountain

Twenty two samples were selected from the Mink Mountain outcrop, and analysed for major oxide and trace element concentrations. Analysis of these samples occurred in two stages; half the samples were analysed for major oxides and trace element concentrations at Lakehead University, the other half of the samples were sent to the O.G.S. Geolab in Sudbury for ICP-MS analysis for rare earth elements concentrations (Table 5).

Figure 84 contains the plots of the redox sensitive oxides and elements plotted against the siliciclastic component of the samples, represented by Al_2O_3 values. The plot of Fe_2O_3 vs. Al_2O_3 shows no distinct trend forming between the two oxides (Figure 84A). The plot of MnO vs. Al_2O_3 shows no distinct tends forming between the two oxides (Figure 84B). The last plot is of V vs. Al_2O_3 also shows no trend forming between the two (Figure 84C).

The plots of the redox sensitive oxides plotted against each other are seen in Figure 85. The plot of Fe_2O_3 vs. MnO shows a positive trend forming between the two oxides (Figure 85A). The other two plots within in the figure are the redox sensitive oxides plotted against V. The plot of Fe_2O_3 vs. V shows a possible positive trend, with MnO vs. V showing no trends (Figure 85B and C).

Table 5: The samples selected from the Mink Mountain Outcrop.

Sample	Description	AES or MS	Up section

- 133 -

CY-67	Oolitic grainstone	AES/MS
CY-62	Oolitic grainstone	AES/MS
CY-61	Oolitic grainstone	AES
CY-77	Stromatolite	MS
CY-73B	Stromatolite	AES
CY-73A	Stromatolite	AES/MS
CY-72	Stromatolite	AES
CY-71	Stromatolite	AES/MS
CY-70	Stromatolite	AES
CY-16	Rubbly grainstone	AES
CY-15	Rubbly grainstone	AES
CY-13	Rubbly grainstone	AES
CY-12	Rubbly grainstone	AES/MS
CY-11	Rubbly grainstone	AES/MS
CY-9	Medium to coarse grainstone	AES
CY-17	Oolitic grainstone	AES
CY-8	Medium to coarse grainstone	MS
CY-7	Medium to coarse grainstone	AES
CY-6	Fine grained jasperlite	MS
CY-3	Medium to coarse grainstone	AES
CY-1	Medium to coarse grainstone	AES/MS
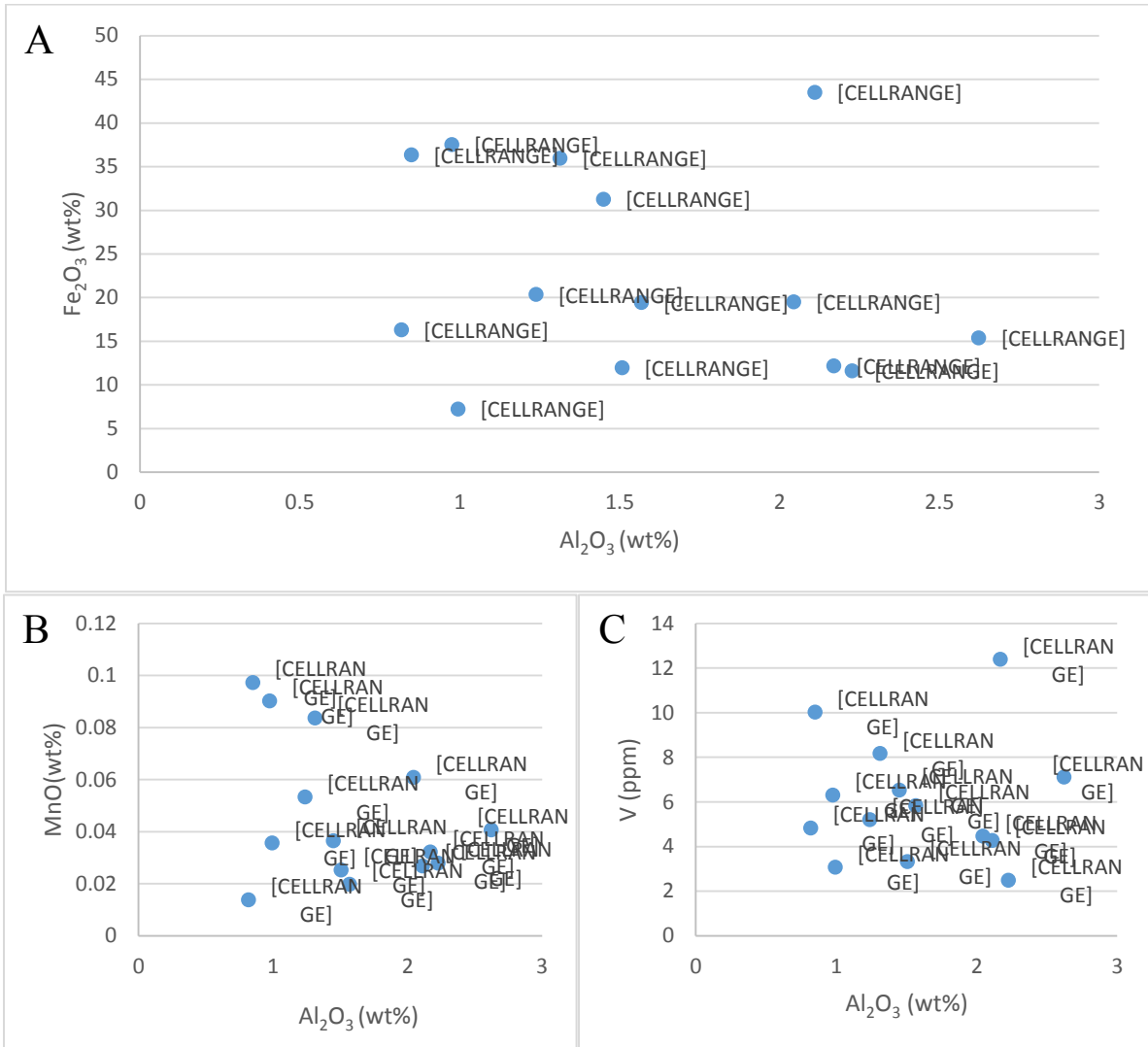
Figure 84: Redox oxides and elements plotted against the siliciclastic content represented by Al_2O_3. A) The plot of Fe_2O_3 vs. Al_2O_3 showing no trend forming between the two oxides. B) MnO vs. Al_2O_3 showing no trend forming between the two oxides. C) V vs. Al_2O_3 showing no trend forming between the two.
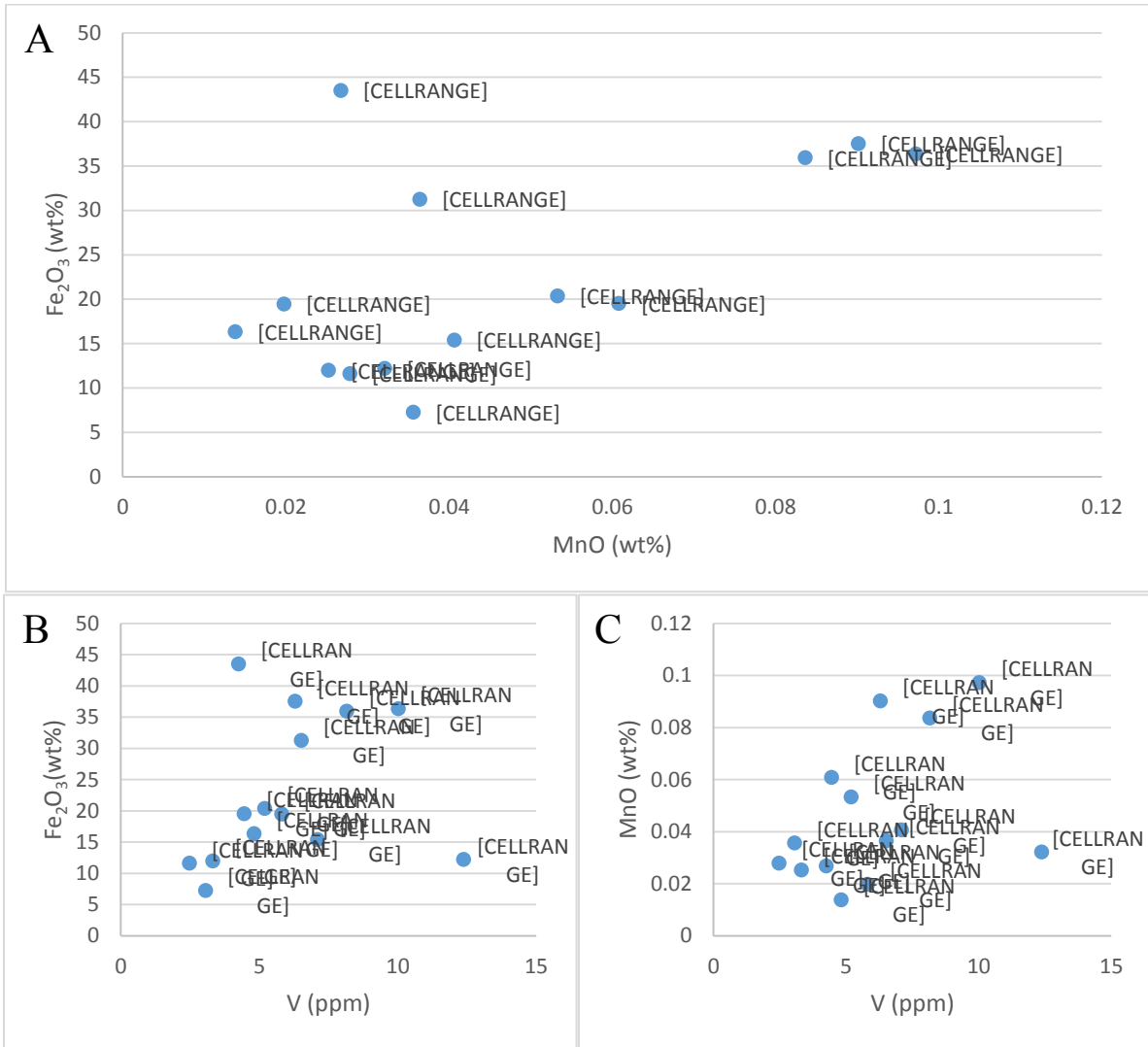
Figure 85: Redox sensitive elements plotted against each other. A) A possible positive trend is visible in the plot of Fe₂O₃ vs. MnO. B) Fe₂O₃ vs. V plot shows a possible trend between the two. C) MnO vs. V showing no trend between the two.

5.2.2 Old School Road Outcrop

Five samples were taken from the two large samples collected from the Old School Road outcrop. Table *6* show the sample numbers and descriptions of the samples collected for analysis.

Table 6: Sample number and brief description of the samples chosen for analysis.

Sample Number	Sample Description	
OSR-22	Ooilitc grainstone interlayered with stromatolites	
OSR-13	Broken up stromatolites	
OSR-12	Red chert stromatolites	Up Section
OSR 5	Brecciated grainstone from below stromatolites	
OSR-2	Unaltered grainstone from below stromatolites	

Figure 86 contains the plots of the major REDOX elements, Fe_2O_3, MnO, V, and U plotted against the siliclastic content represented by Al_2O_3. The plot of Fe_2O_3 vs. Al_2O_3 shows a positive trend forming between the two major oxides (Figure 86 A). The samples collected from the red stromatolites show the highest values. The plot of Al_2O_3 vs. MnO, shows no trend forming between the two oxides. Figure 86 C and D are the plots of V vs. Al_2O_3 and U vs. Al_2O_3 both of which show no trends between the two components.

Figure 87 contains the plots of the major redox oxides and elements Fe_2O_3, MnO and V plotted against each other. The plot of Fe_2O_3 vs. MnO shows no distinct trend forming between the two oxides (Figure 87A). The plot of Fe_2O_3 vs. V shows no trend between the two (Figure 87C). The last plot is of MnO vs. V; it shows a possible trend forming between the two (Figure 87D).

Figure 86: Redox sensitive oxides and elements vs. siliciclastic input. A) Fe_2O_3 vs. Al_2O_3 showing a positive trend forming between the samples. B) MnO vs. Al_2O_3 plot showing no trend forming between the two. C) The plot of V vs. Al_2O_3 showing no visible trend and D) U vs. Al_2O_3 showing no visible trend.
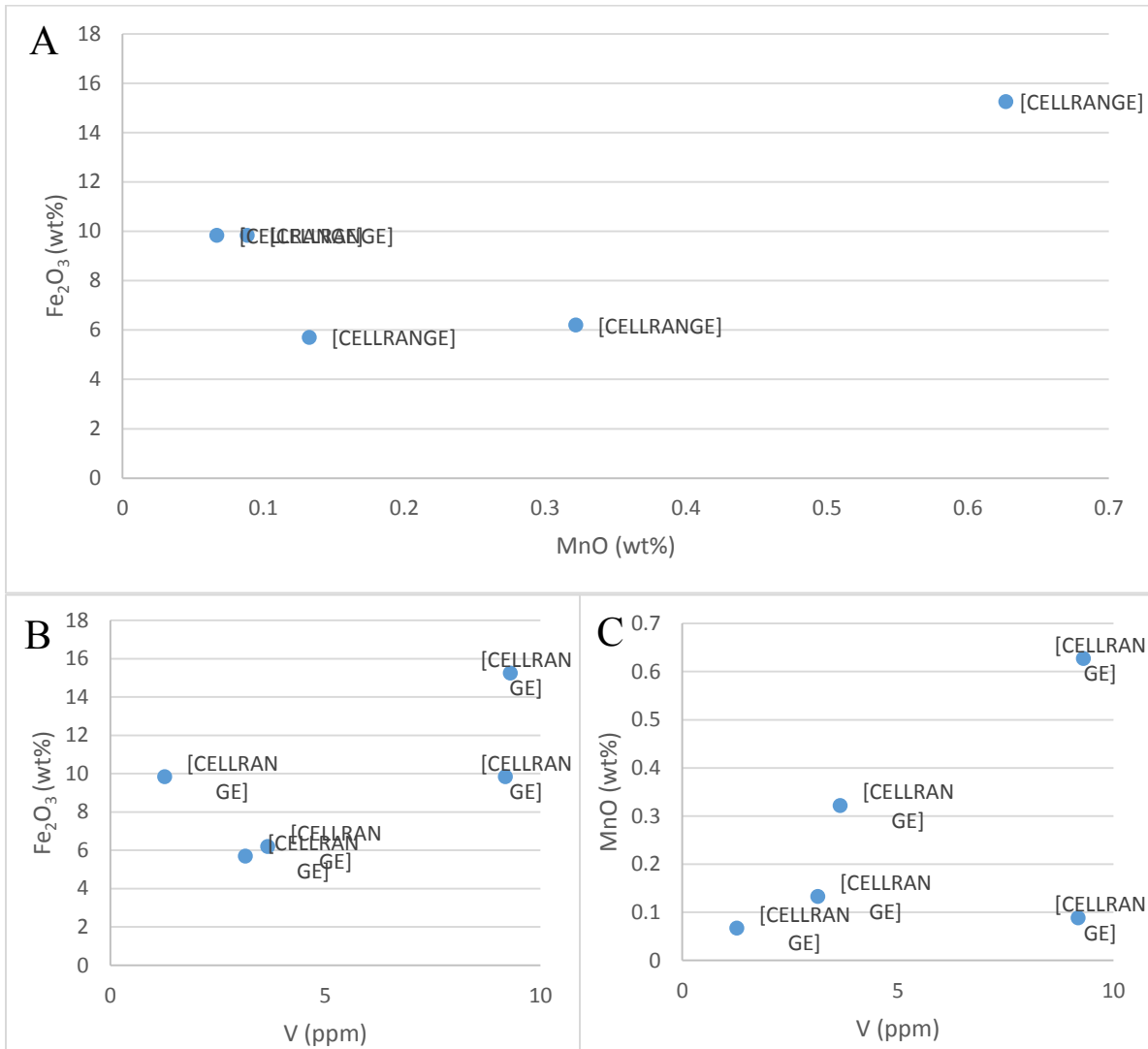
Figure 87: Redox sensitive oxides and elements. A) Fe_2O_3 vs. MnO shows no distinct trend forming between the two oxides. B) Fe_2O_3 vs. V with no trend visible. C) MnO vs V showing a possible positive trend forming between the two.

The plots of the redox sensitive elements Cr, U, Mo vs. V and U are shown in Figure 88. Samples 2 and 13 had Cr values below the detection limit, thus the samples plotted with zero Cr values. The plot of Cr vs. V shows no trend forms between the two elements. No trends are visible in the plots of U vs. V and Mo vs. V (Figure 88B and C). The samples that plotted above Cr detection levels do show a possible positive trend forming between the two elements (Figure 88D).
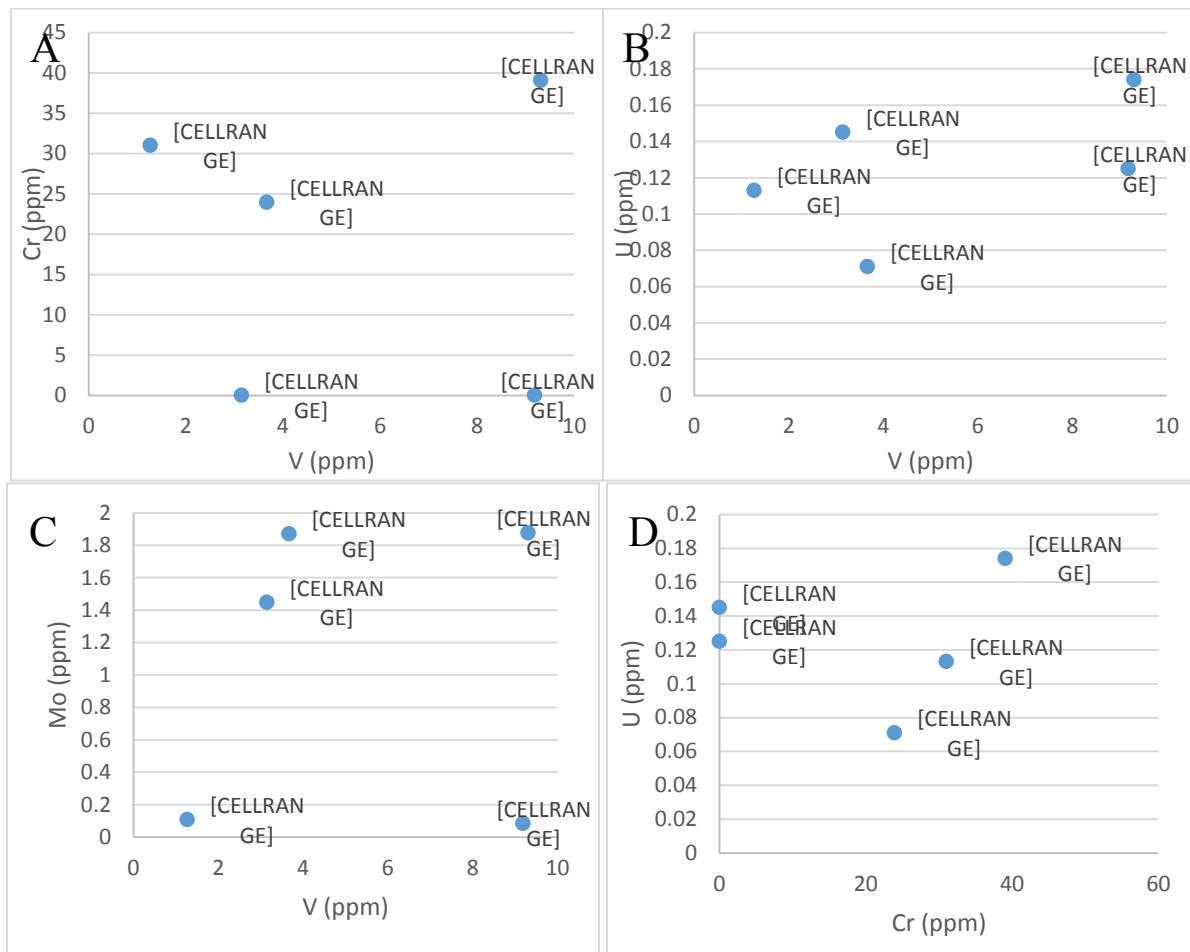
Figure 88: REDOX sensitive elements plotted against V and U. A) Cr vs. V, B) U vs. V, C) Mo vs V showing no visible trends forming between any of the elements. D) A possible trend is visible in U vs. Cr.

5.2.3 *Magnetic Rock Trail*

Twenty-three samples were collected from the Magnetic Rock Trail outcrop. The samples again were cut and digested for analysis for both major and trace elements and REEs at LUIL. The samples selected for analysis are listed in Table *7*.

Table 7: Samples selected for analysis from the Magnetic Rock Trail outcrop. The lowest samples were taken from the base on up.

Sample	Description	Distance from stromatolite (cm)
CY-117B	Grainstone interlayed with lapilli	
CY-117A	Grainstone interlayed with lapilli	
CY-116C	Grainstone interlayer with lapilli	187
CY-116B	Grainstone interlayer with lapilli	
CY-116A	Grainstone interlayer with lapilli	
CY-115	Grainstone with lapilli layer	
CY-114	Coarse grainstone	57
CY-113	Massive magnetite layer	
CY-112	Coarse grainstone	
CY-111	Coarse to fine grainstone	45
CY-110	Coarse to fine grainstone	
CY-81	Stromatolite	
CY-80		
CY-109	Grainstone	
CY-108	Grainstone	
CY-107	Massive material	96
CY-102	Medium to coarse grainstone with mud flaser	
CY-106		
CY-105	Medium to coarse grainstone with chemical muds	183
CY-104	Coarse grainstone	402
CY-103	Medium to coarse grainstone	
CY-101	Medium to coarse grainstone	410
CY-100	Medium to coarse grainstone	444

Up Section

The plots in Figure 89 are of the major redox components Fe_2O_3, MnO, V, U plotted against the siliciclastic component represented by Al_2O_3. The plot of Fe_2O_3 vs. Al_2O_3 shows no trend forming between the two major oxides (Figure 89A). Figure 89B is the plot of MnO vs. Al_2O_3; this plot shows no trend forming between the two oxides. A lack of a trend can also be seen in the plot of V vs. Al_2O_3 (Figure 89C). The measured U values were 2 orders of magnitude larger than expected.

The next three plots are of the major redox components (Fe_2O_3, MnO and V) plotted against each other (Figure 90) The plot of MnO vs. Fe_2O_3 shows a distinct positive trend forming between the two major oxides (Figure 90A). The next two plots are of Fe_2O_3 and MnO plotted against V (Figure 90B, C); these two plots do show a very distinct positive trend forming between the major oxides and V.
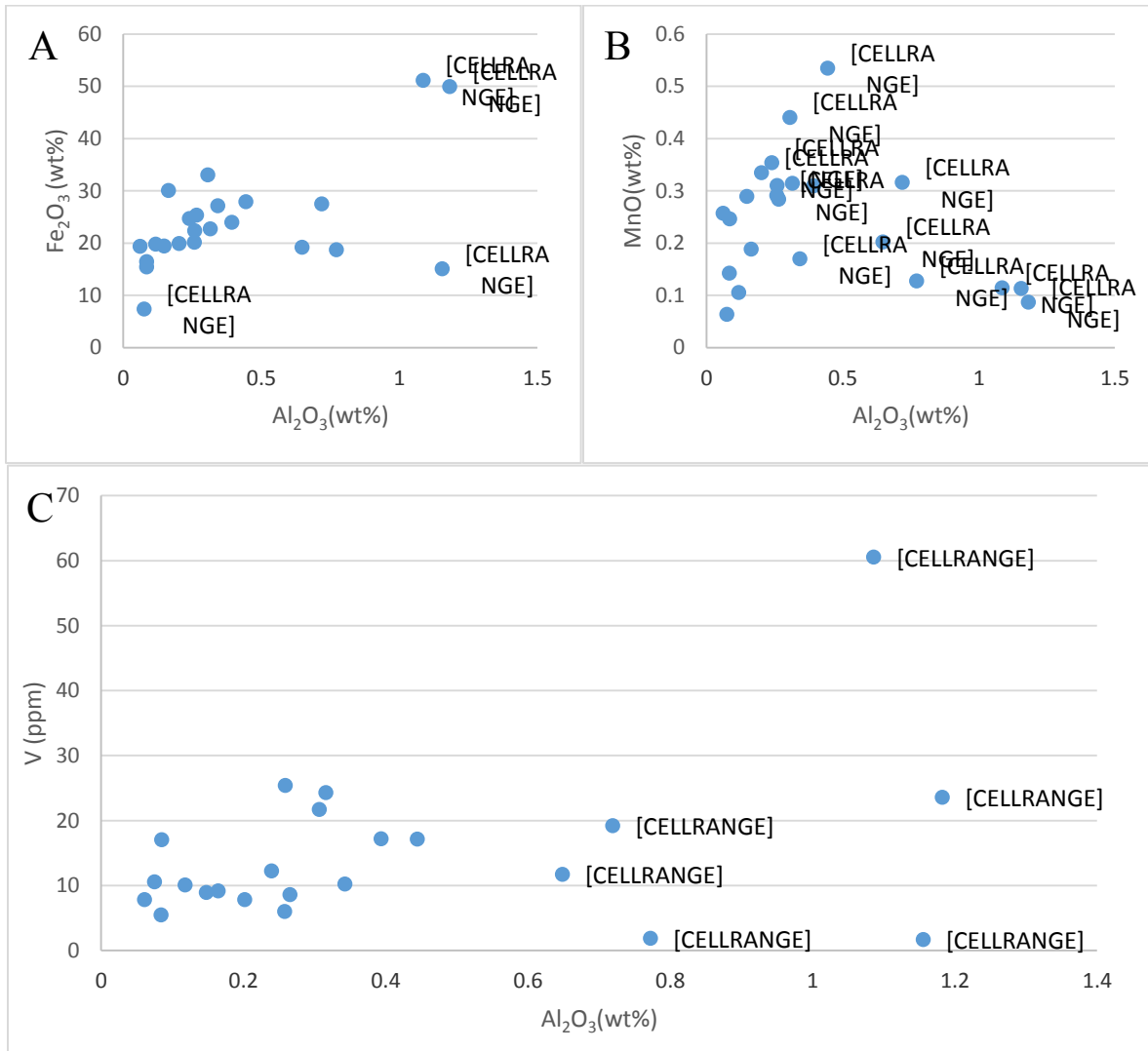
Figure 89: Main redox components plotted against the siliciclastic component represented by Al₂O₃. A) Fe₂O₃ vs. Al₂O₃ plot showing no trend forming between the two oxides. B) MnO vs Al₂O₃ plot showing no distinct trend. C) The plot of V vs. Al₂O₃ showing no visible trend as well.
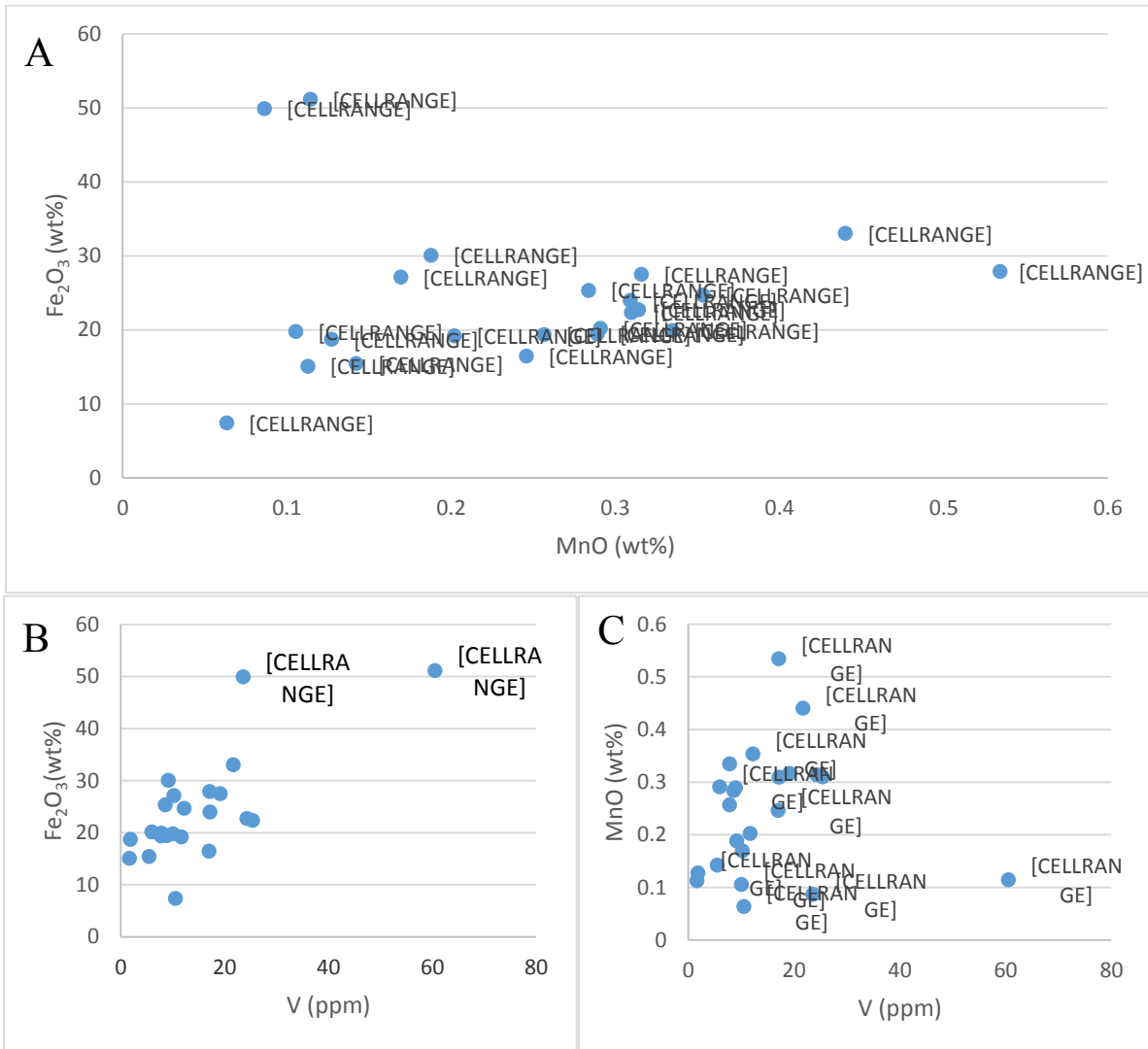
Figure 90: The major redox components for the Magnetic Rock samples. A) The plot of Fe_2O_3 vs. MnO showing a positive trend forming between the two major oxides. B) The plot of Fe_2O_3 vs V showing a similar positive trend. C) The plot of MnO vs. V showing no trend forming between the two components.

Figure 91 below contains the plots of the redox sensitive elements plotted against V and Cr. Again no acceptable values for Mo and U were measured.
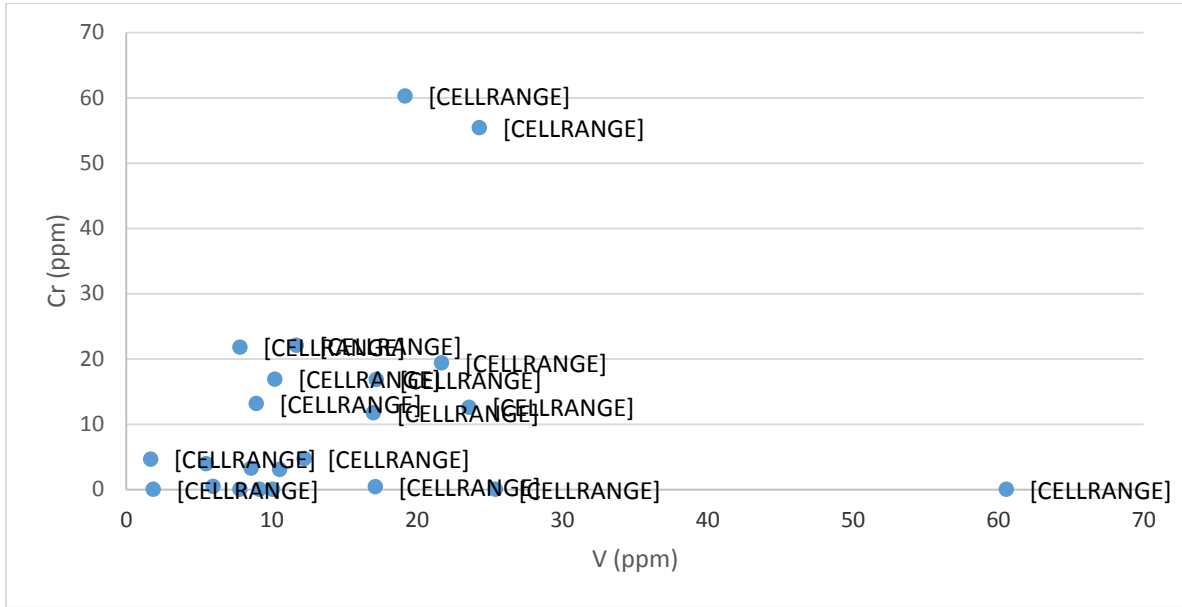
Figure 91: The redox sensitive elements V and Cr showing no positive trend.

5.2.4   Current River

A total of eight samples were collected from the two stromatolite units present on the Current River. Four were taken from the Boulevard Lake site and four others were taken from the stromatolite site below the Arundel Street Bridge. Table *8* below contains sample numbers and descriptions of the selected samples.

Table 8: The sample numbers and sample descriptions for the samples from Current River

Sample Number	Description and location		
CR-11-03 (3Aru)	Brecciated pryitiferous grainstone		
CR-11-02 (2Aru)	Pryitiferous grainstone		
CR-11-01 Wr (1Aru)	Silicified grainstone sample	Arundel Street Bridge outcrop	Up Section
CR-11-01 Mn (1Mn)	Mn carbonate present at the bottom of the silicified grainstone		
CR-8	Grainstone from further above stromatolite		
CR-7	Grainstone from directly above stromatolite	Boulevard Lake Outcrop	
CR-3	Silicififed clast from grainstone		
CR-2	Ankerite grainstone with silicicified clast		
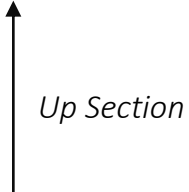
Figure 92 is of the redox sensitive oxides and elements plotted against the siliciclastic components represented by Al_2O_3. The plot of Fe_2O_3 vs, Al_2O_3 (Figure 92A) shows no trend forming between the two oxides in either sample location. The plot of MnO vs. Al_2O_3 shows a possible negative trend in which the increase in Al_2O_3 is accompanied by decreasing MnO values for the samples taken from the Arundel Street Bridge site (Figure 92B). A slight positive trend is present for the samples from the Boulevard Lake sample site. A linear positive trend is visible in

both plots of V vs. Al$_2$O$_3$ and U vs. Al$_2$O$_3$, with high values of V and U present in the 2 Arundel

samples 2 Aru (CR-11-02) and 3 Aru (CR-11-03) (Figure 92 C and D).

Figure 93 is of the major redox sensitive oxides and elements Fe$_2$O$_3$, MnO, and V plotted

against each other. The plot of Fe$_2$O$_3$ vs. MnO. Shows no trend between the two oxides (Figure

93A). No trends are seen in either plot of Fe$_2$O$_3$ vs. V and MnO vs. V (Figure 93B and C).
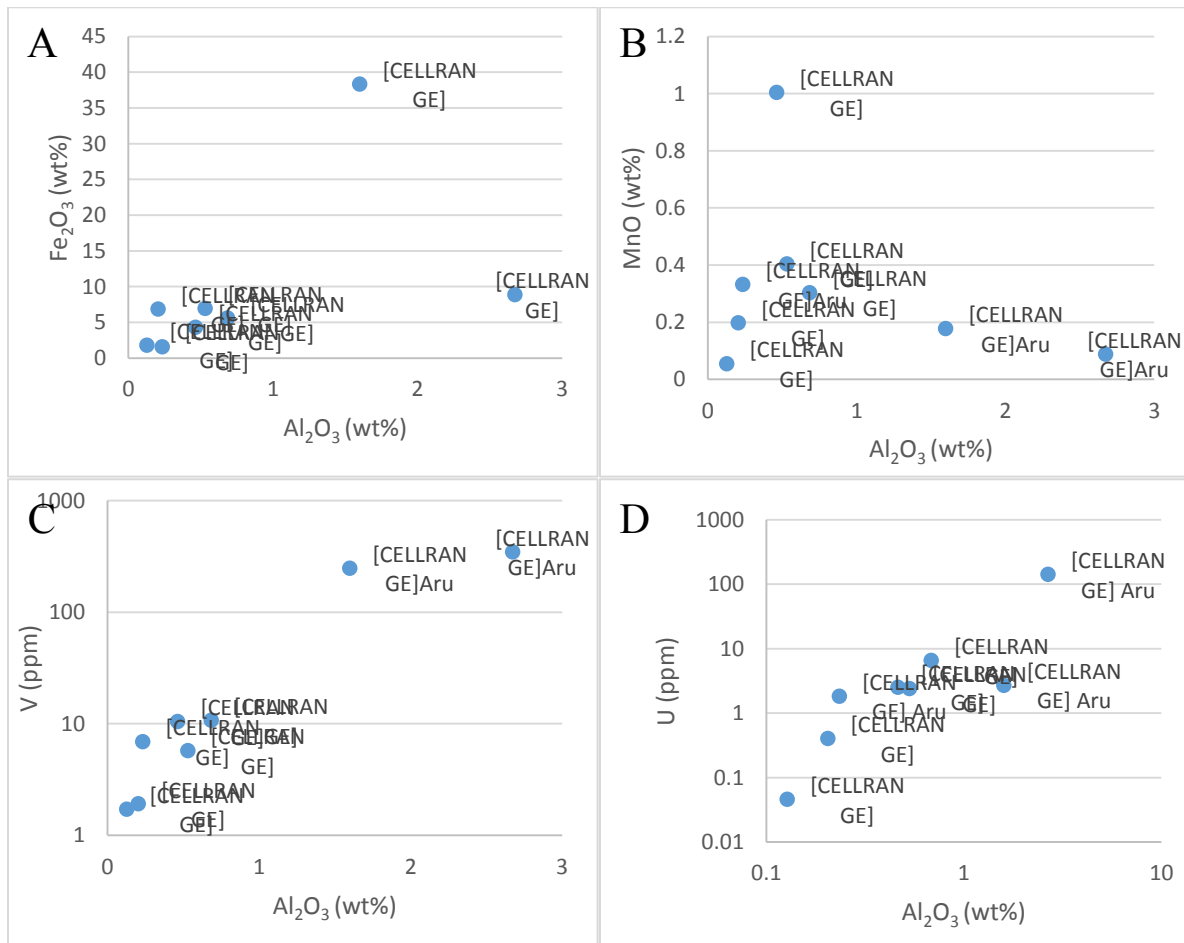
Figure 92: Major redox sensitive components plotted against the siliciclastic component of the system represented by Al$_2$O$_3$. A) Fe$_2$O$_3$ vs. Al$_2$O$_3$ plot showing no trend forming between the two oxides. B) No trend is present in the MnO vs. Al$_2$O$_3$ plot. C) V vs. Al$_2$O$_3$ showing a positive trend and D) U vs. Al$_2$O$_3$ showing a positive trend as well. Samples 2Aru and 3Aru have very high V values and sample 3Aru has an extremely high U value.
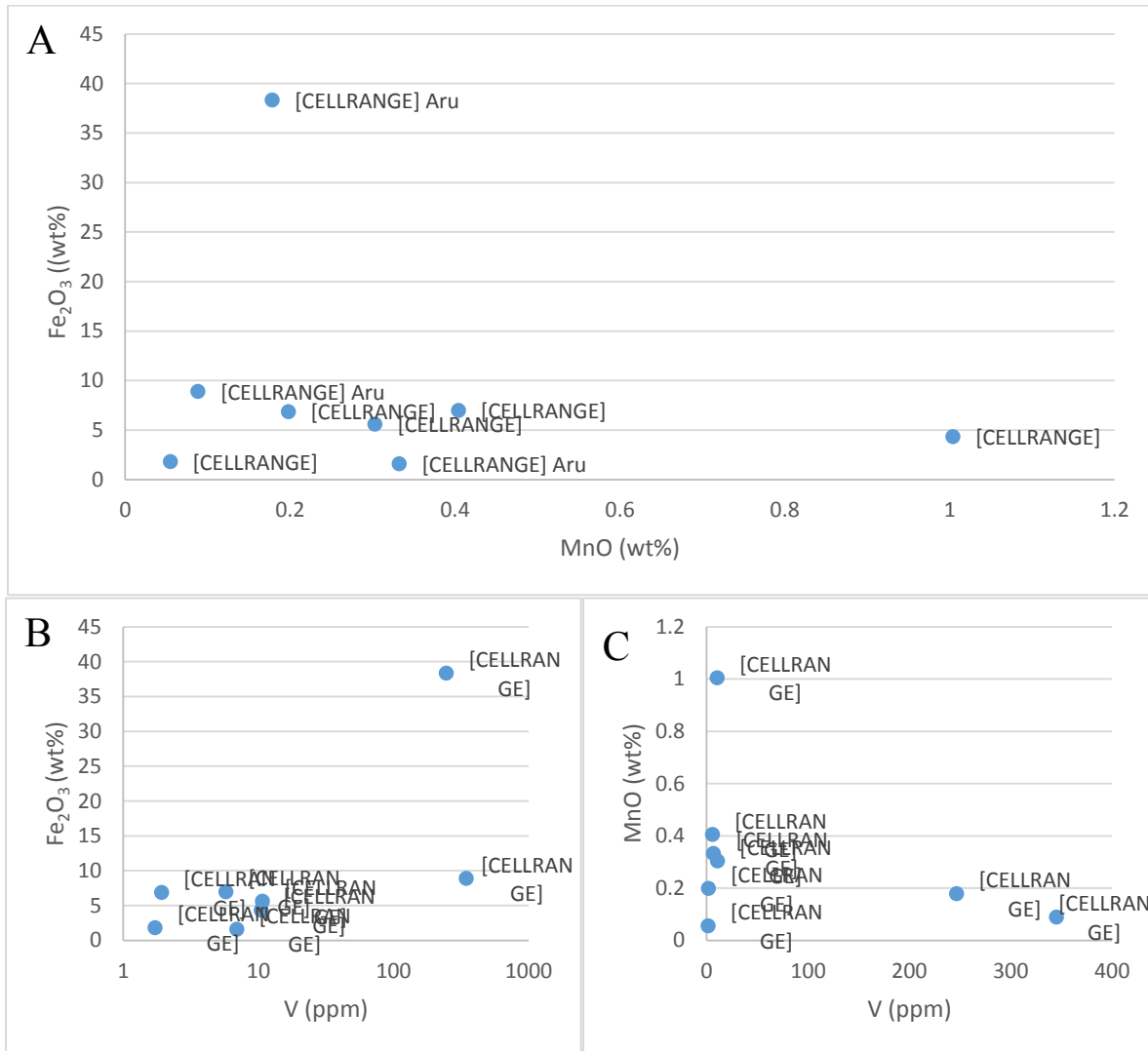
Figure 93: Redox sensitive oxides and elements for the Current River samples. A) Fe_2O_3 vs. MnO showing no trend forming between the two oxides. B) Fe_2O_3 vs. V with no trend forming between the oxide and elements. C) MnO vs. V plot showing no trend is present.

The last group of scatter plots for the Current River samples are in Figure 94 which are for the minor redox sensitive elements U, Cr and Mo plotted against V, Cr vs. V (Figure 94A) shows a positive trend forming between the two elements, with very high values in the two Arundel brecciated samples. A similar trend can be seen in the plot of U vs. V and U vs. Cr

(Figure 94B and D). A trend is visible in the plot of Mo vs. V (Figure 94C). What is of note are the very high values of V, Cr and Mo in 2Aru and 3Aru, plus the high amounts of U in 3Aru.
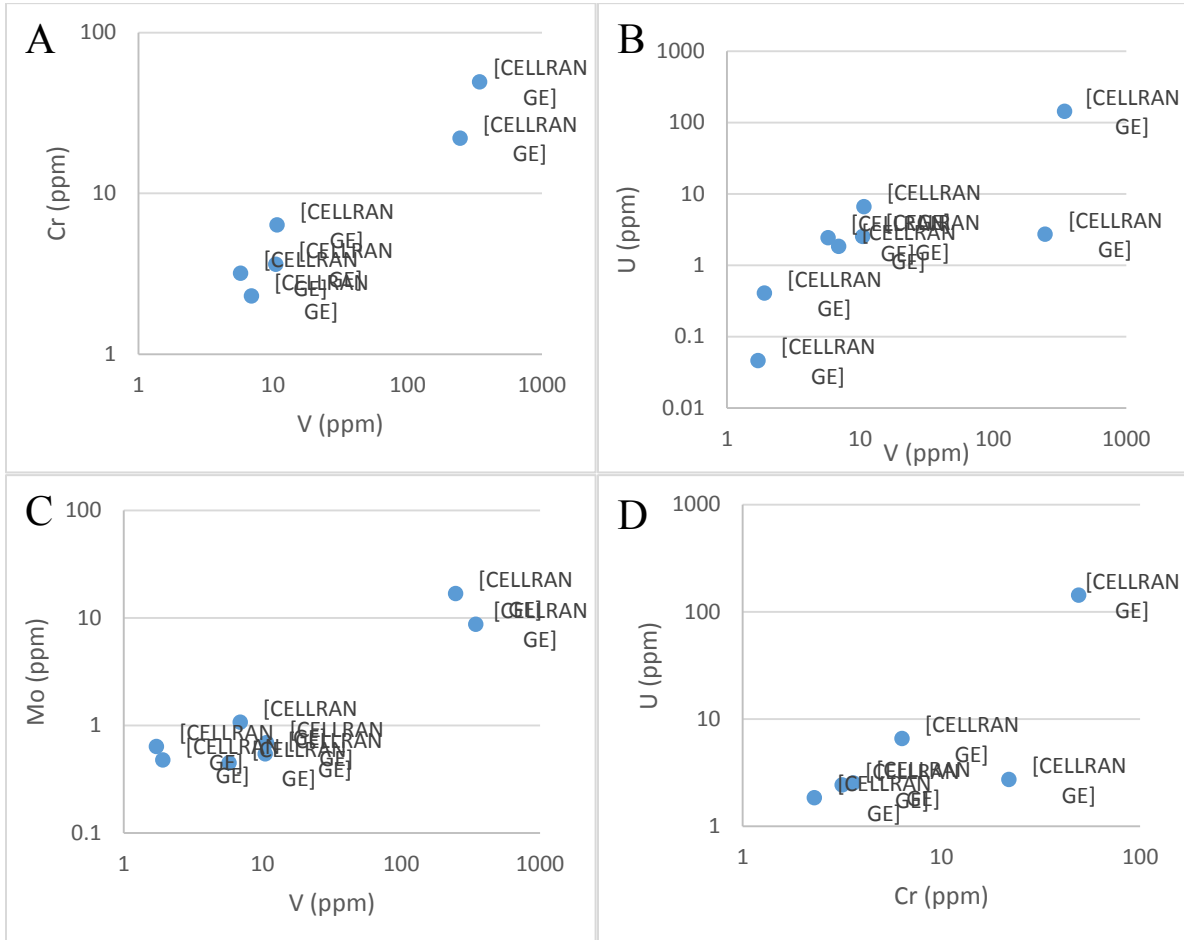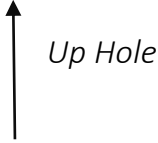
Figure 94: The plots of redox sensitive elements from the Current River sample sites. Cr vs. V (A), U vs. V (B), Mo vrs. V (C), and U vs. Cr (D) showing positive trends forming between the elements.

5.2.5 DH 87-3

Five samples were collected from the DH-3 drill core section from below the stromatolites, up through the stromatolite and up into the grainstones above the stromatolites. These five samples were analysed for primary oxide, trace elements and rare earth element concentrations (Table 9).

Table 9: Samples from the DH 87-3 drill hole selected for analysis.

Sample	Sample description	
DH-3 05	Grainstone from above stromatolite	
DH-3 04	Stromatolite	Up Hole ↑
DH-3 03	Breccia	
DH-3 02	Medium to coarse grainstone	
DH-3 01	Medium to coarse grainstone	

The first group of plots defines the siliciclastic component of the system, which again is represented by Al_2O_3; these are plotted against the principal redox sensitive components Fe_2O_3, MnO, V, and U (Figure 95). The first plot of Al_2O_3 vs. Fe_2O_3 shows a possible weak trend forming between the two major oxides (Figure 95A). The lack of any strong trends can be seen in the other three plots of MnO vs. Al_2O_3, V vs., Al_2O_3 and U vs. Al_2O_3 (Figure 95 B,C and D). However, Figure 95C and D do show weak positive trends.

When the major redox components Fe_2O_3, MnO and V are plotted against each other, one trend can be seen. The plot of Fe_2O_3 vs. MnO shows a positive linear trend that forms between the two major oxides (Figure 96A). The plots of Fe2O3 vs. V and MnO vs. V show no trend developing between these (Figure 96 B and C).
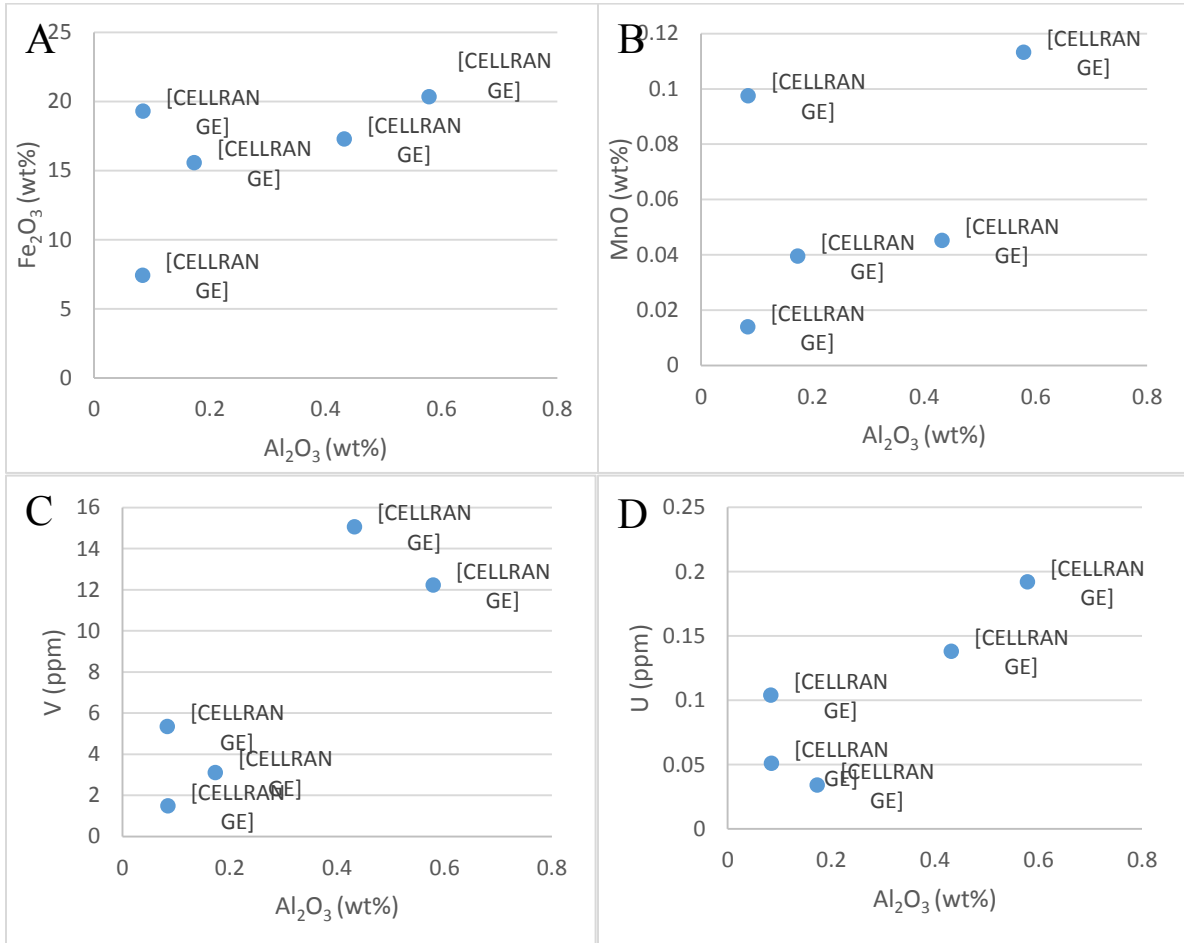
Figure 95: The plots of siliciclastic component vs. redox components. A) Al_2O_3 vs Fe_2O_3 showing a possible slight positive trend between the two. B) No strong trend forming between Al_2O_3 vs MnO. C) The plot of Al_2O_3 vs. V showing a slight positive trend. D) Al_2O_3 vs U showing a trend between the two
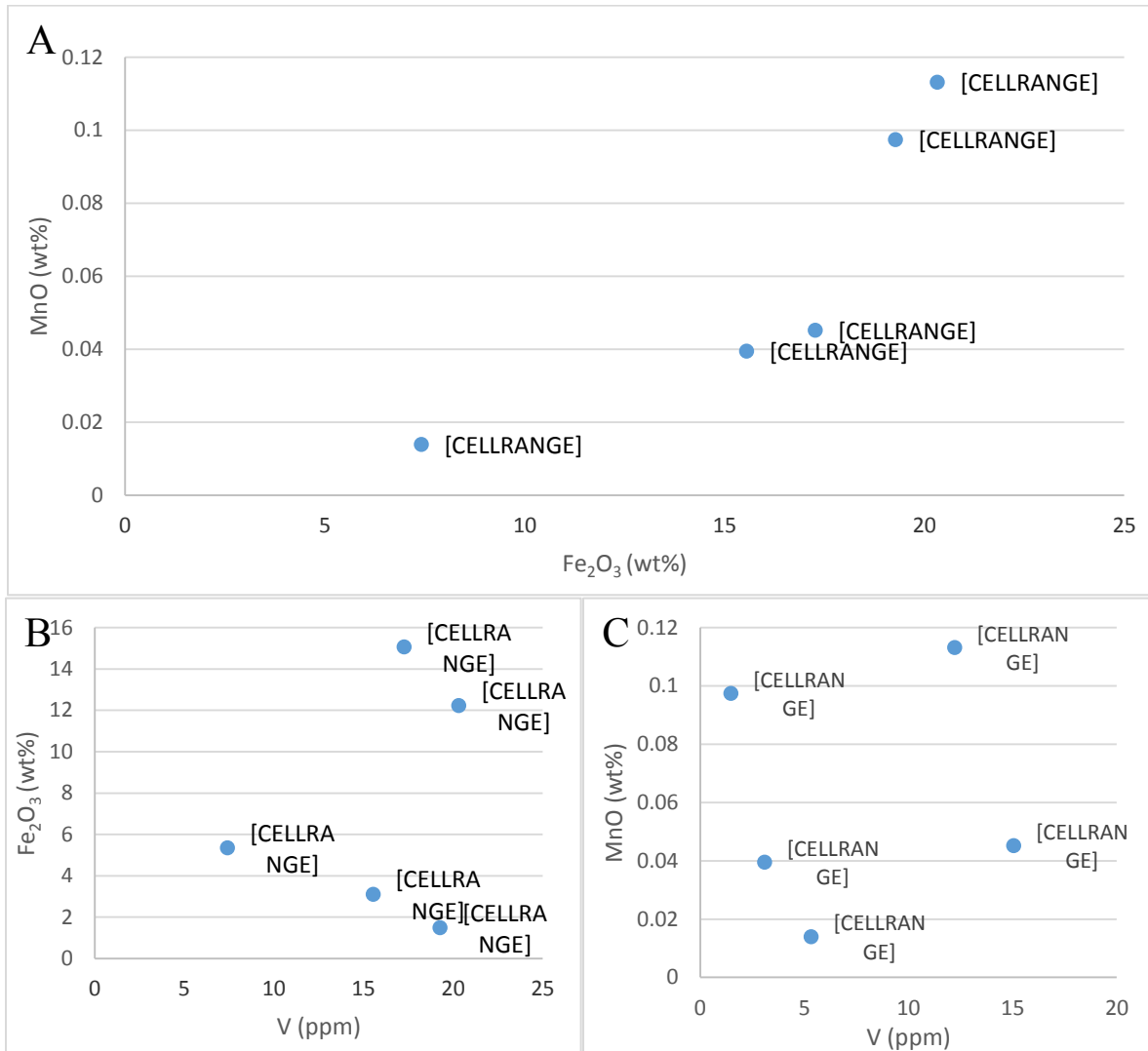
Figure 96: The plots of the major redox components. A) The plot of Fe_2O_3 vs MnO, showing a positive trend forming between the two oxides. B) The Fe_2O_3 vs V plot shows no trend forming between the two. C) The lack of any trend can be seen in the MnO vs V plot.

Figure 97 shows the plots of the minor components of the redox sensitive elements, which including Cr, U and Mo. Again most of the values for chromium plot below the detection limit. The first plot is of Cr vs. V this plot shows no trend between the two due to the lack of Cr values (Figure 97A). Strong positive trends can be seen in the plot of U vs. V (Figure 97B) and Mo vs. V (Figure 97C). No visible trend can be seen in the plot of U vs. Cr (Figure 97D).
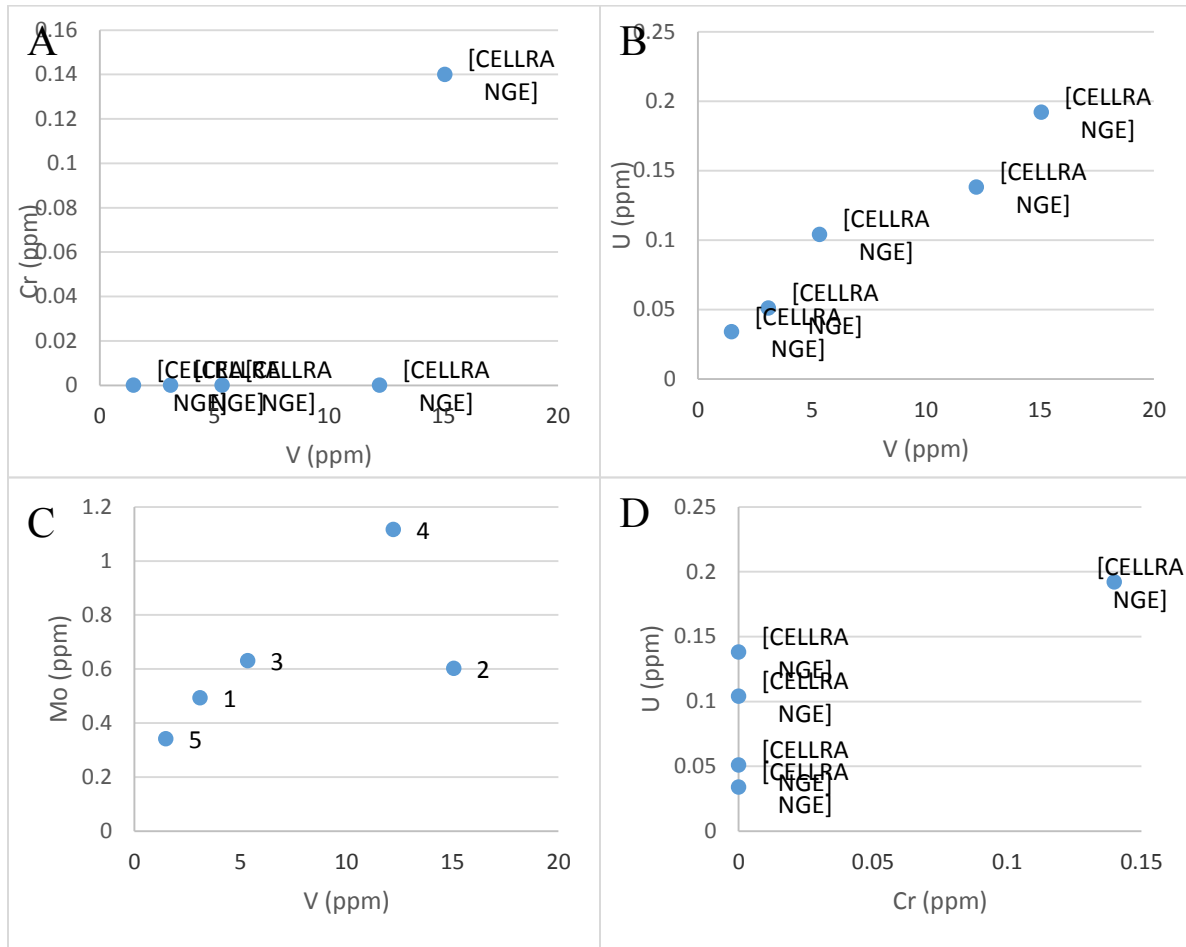
Figure 97: The minor redox sensitive components of the DH 87-3 samples. The majority of the Cr values plotted below detection. A) Cr vs. V show no trend forming between the two. B) A positive linear trend can be seen forming between V vs U. C) A similar trend can be seen with V and Mo. D) The plot of U vs. Cr showing no trend between the two.

5.2.6   MC-98-1

Nine samples were collected from the drill hole MC-89-1. The majority of the samples were taken from the grainstones below the stromatolite unit, both from the mottled grainstone and the unaltered grainstones. Two samples was taken from above the stromatolites (Table 10). shows the sample number and brief description of the samples.

Table 10: The sample number and description for each of the MC-89 samples.

Sample Number	Description	
CY-32	Grainstone sample above the stromatolite	
MC-CY-04	Medium to coarse grainstone directly above stromatolites	
CY-28	Medium to coarse grainstone with hematite	
MC-CY-03	Medium to coarse grainstone directly below stromatolite sample	Up hole
CY-26	Mottled section of grainstone layer below the stromatolite	
MC-CY-02	Medium to coarse grainstone	
MC-CY-01	Mottled section of grainstone layer below the stromatolite	
CY-25	Mottled section of grainstone layer below the stromatolite	

Figure 98 contains the plots of the redox sensitive elements Fe_2O_3, MnO, V and U plotted against Al_2O_3 which represents the siliciclastic components. The first two plots show no trends forming between these redox oxides and the siliciclastic component of the samples. V and U are slightly positively correlated with the siliciclastic content of the samples.

The plots in Figure 99 are of the redox sensitive oxides and elements Fe_2O_3, MnO and V plotted against each other. Figure 99A is Fe_2O_3 vs. MnO. This plot shows no trend forming between the two oxides. Figure 99B and C are Fe_2O_3 and MnO vs. V, which again show no distinct trend forming between the oxides and V.
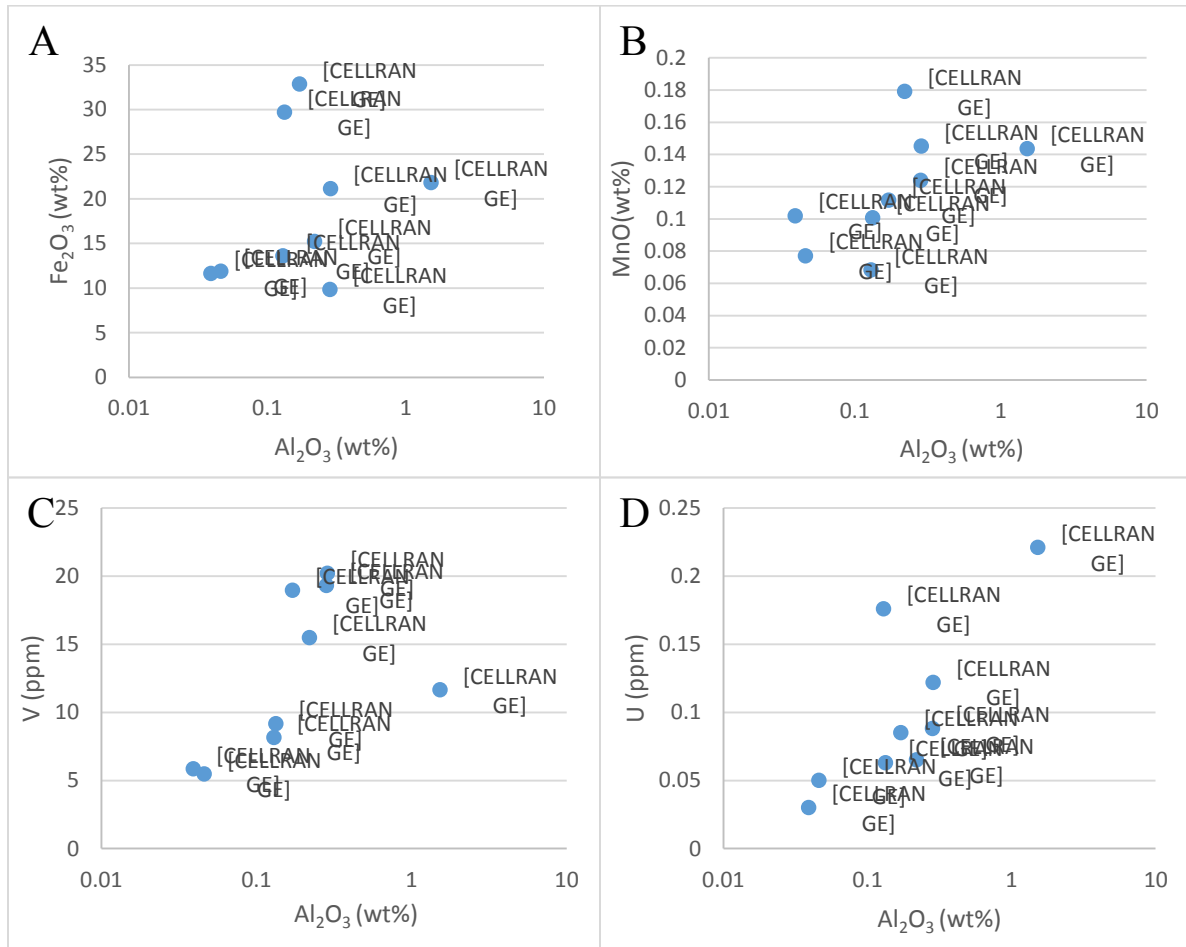
Figure 98: redox sensitive oxides and elements vs. Al_2O_3 which represents the siliciclastic component of the samples. A) Fe_2O_3 vs. Al_2O_3, B) MnO vs.Al_2O_3 C) V vs. Al_2O_3 and D) U vs. Al_2O_3 showing a possible positive trend.
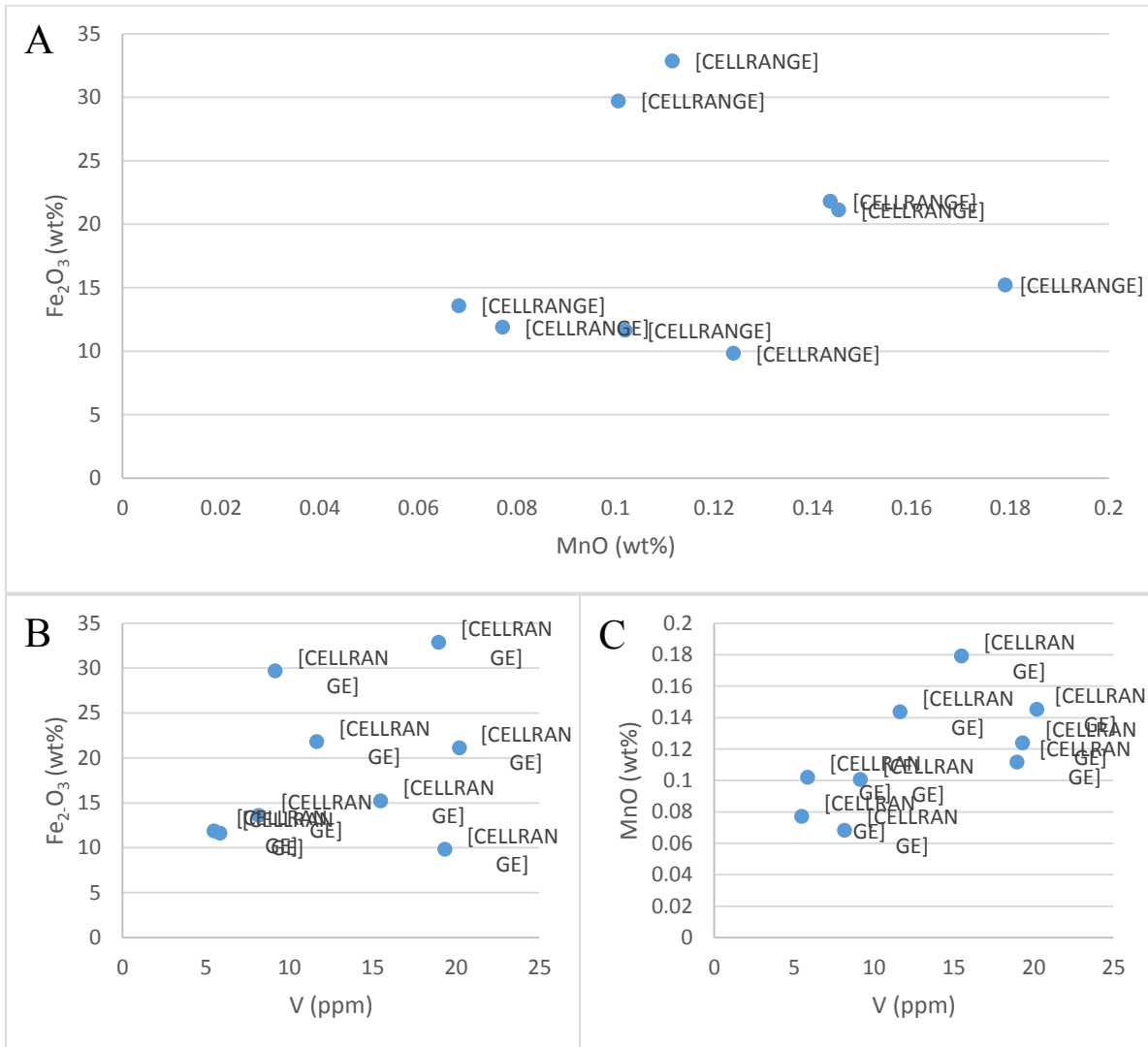
Figure 99: The plots of REDOX sensitive components Fe2O3, MnO and V plotted against each other. A) Fe_2O_3 vs. MnO showing no trend forming between the two oxides. B) Fe_2O_3 vs. V showing no trend C) MnO vs. V showing no trend.

Figure 100 contains plots of the redox sensitive components Cr, U and Mo plotted against V and Cr. The majority of the Cr values were below detection and were plotted as zero. Figure 100A is Cr vs. V showing no trend. Likewise, no trends are visible in the plots of U vs. V (Figure 98B), Mo vs. V (Figure 100C) and U vs. Cr (Figure 100D).
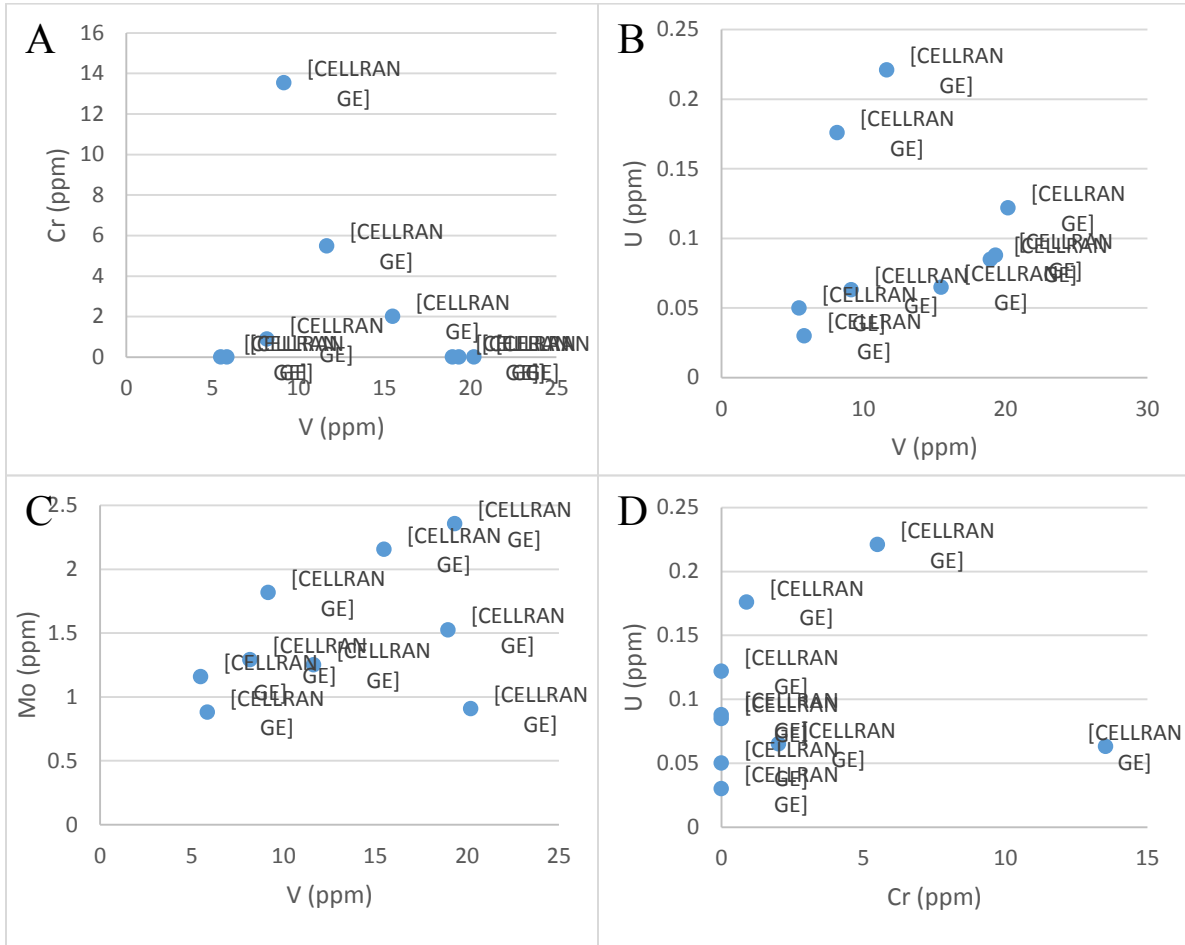
Figure 100: Redox sensitive elements Cr, U and Mo plotted against V and Cr. No distinct trend can be seen in any of the plots.

5.3   Rare Earth Element Geochemistry

5.3.1   Mink Mountain

Analysis of the rare earth elements in samples collected from the outcrop behind Mink Mountain show a pattern similar to that of the other sample sites of the regressive middle unit. The patterns from the grainstone indicate that they become enriched in light rare earth elements moving up the outcrop (Figure 101 A). The middle rare earth elements become flatter up the outcrop and HREEs have similar shapes. All the grainstone samples show a distinct positive Ce anomaly, and a very slight, possibly non-existant, to distinctive positive Eu anomaly. The stromatolites from behind Mink Mountain show a similar pattern to the other sample sites (Figure 101B). The stromatolites all appear to have similar flat patterns and concentrations. All of the stromatolites have a positive Ce anomaly and all the stromatolite samples have positive Eu anomalies. Two samples were taken from the ooidal grainstone at the top of the outcrop behind Mink Mountain (Figure 102). The samples have similar concentrations, with the same pattern showing enrichment in the HREEs compared to the LREEs, and both samples have positive Ce and Eu anomalies. The discrimination plot (Figure 103) demonstrates that, when compared to the La anomaly, all the samples collected from the outcrop behind Mink Mountain, except one, CY-73A, have a distinct positive Ce anomaly. The Eu anomaly is moderate to non-existant (Figure 103) with its highest value coming from the sample with no Ce anomaly.
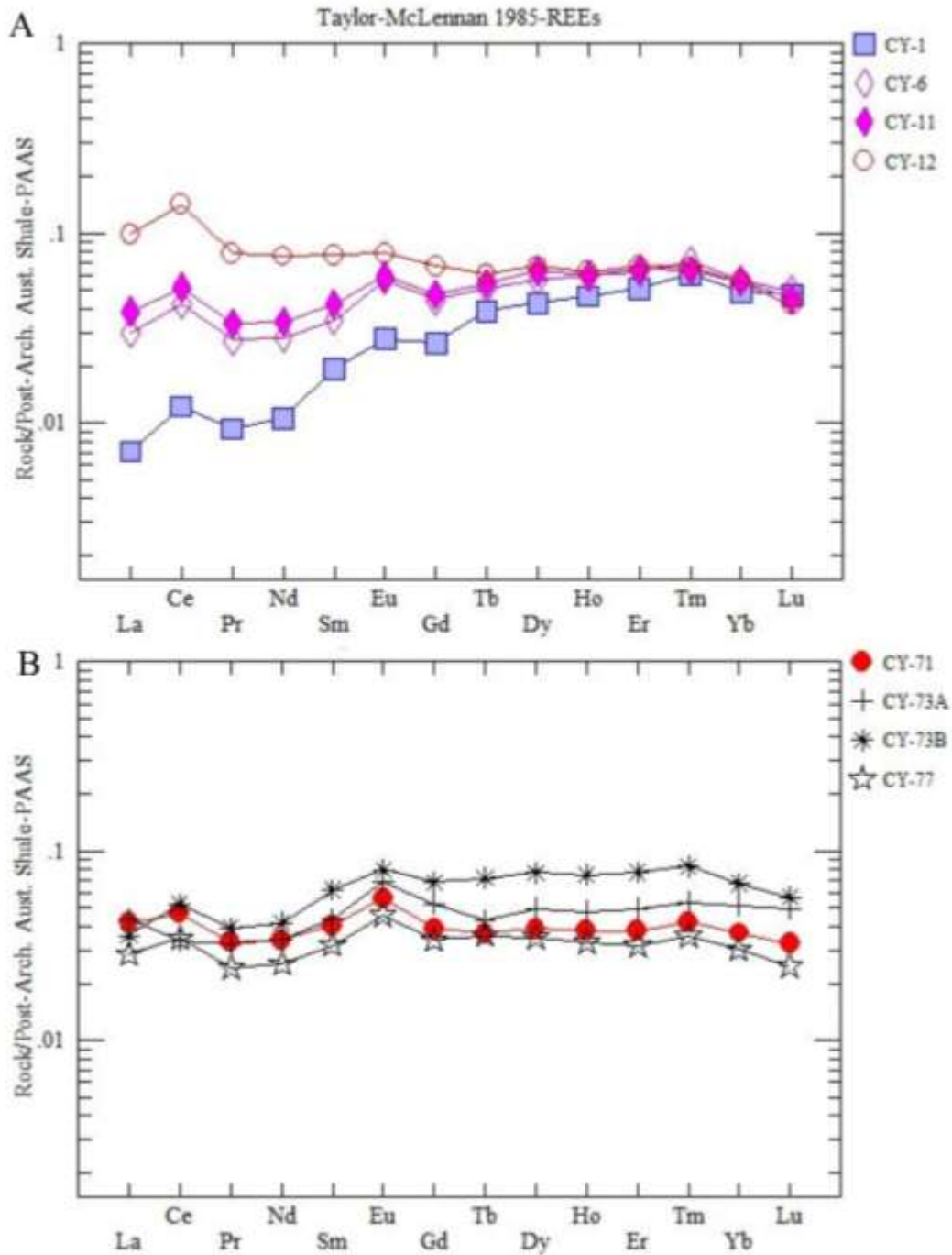
Figure 101: The PAAS normalized distribution plots for the samples from the outcrop behind Mink Mountain. A) The samples taken from the grainstone layer show a positive Ce anomaly, and slight positive Eu anomaly to no anomaly. B) Distribution plots for the samples collected from the stromatolites from Mink Mountain.
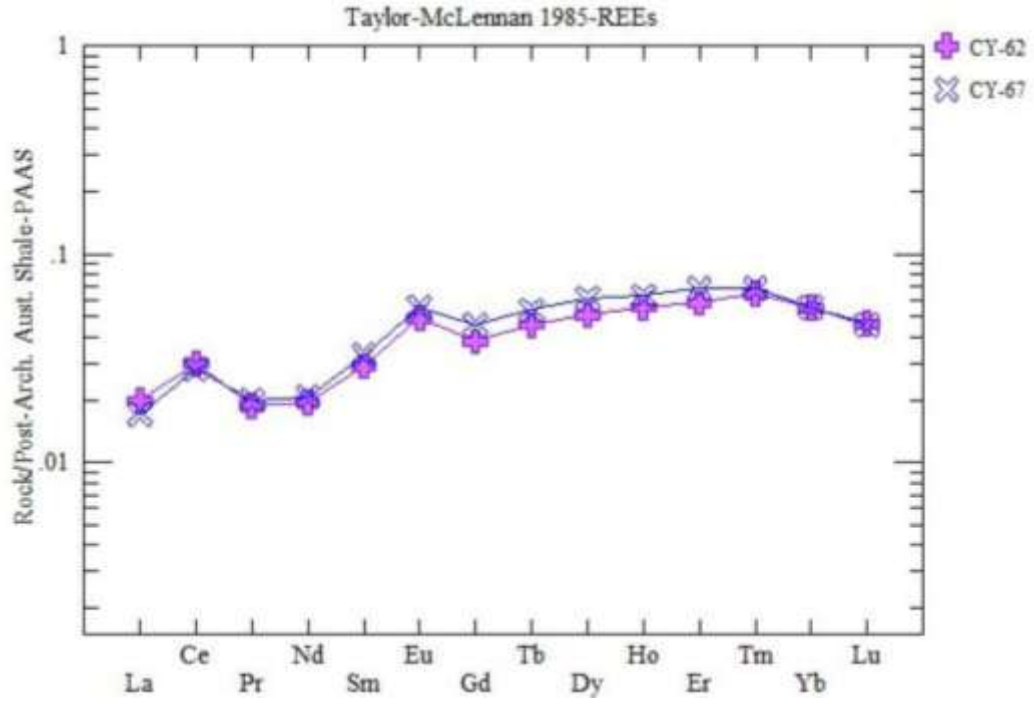
Figure 102: PAAS normalized rare earth element concentration diagram for the oolitic grainstone at the top of the outcrop behind Mink Mountain.
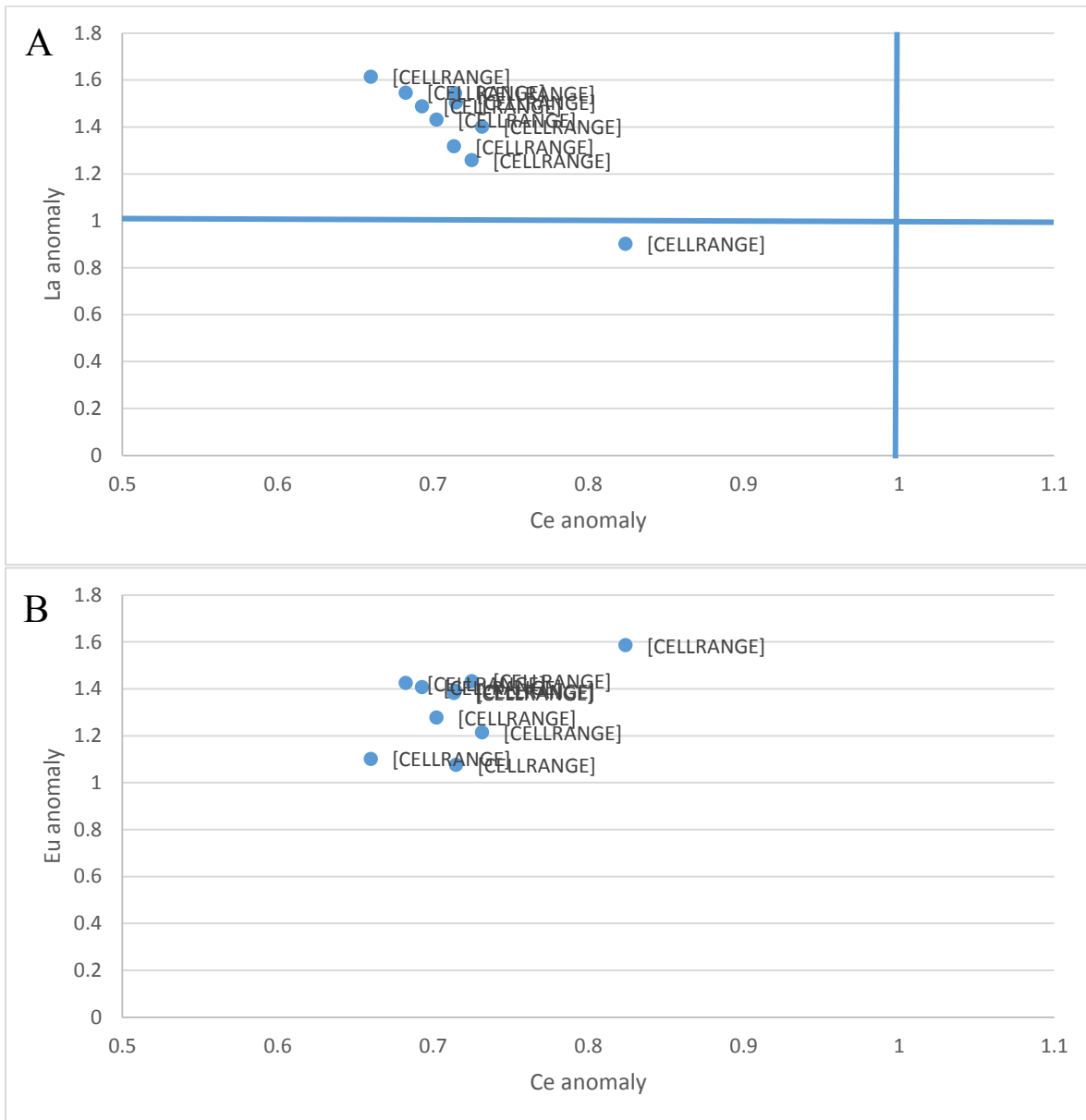
Figure 103: La anomaly and Eu anomaly vs. Ce anomaly plots. A) La vs. Ce anomaly plot showing the distinct positive Ce anomalies present in all of the samples. B) Eu anomaly vs. Ce anomaly showing no correlation between the two anomalies. The sample with the smallest positive Ce anomaly also has the greatest Eu anomaly. The other samples range from moderate Eu anomalies to no Eu anomalies.

The REDOX sensitive oxides and elements were plotted against the Ce anomaly for the samples analysed for both ICP-AES and MS. All four plots do not show a distinctive trend forming between the oxides/elements and the Ce anomalies. The four plots are A) Fe_2O_3 vs. Ce anomaly, B) MnO vs. Ce anomaly, C) V vs. Ce anomaly and D) Cr vs. Ce anomaly (Figure 104).
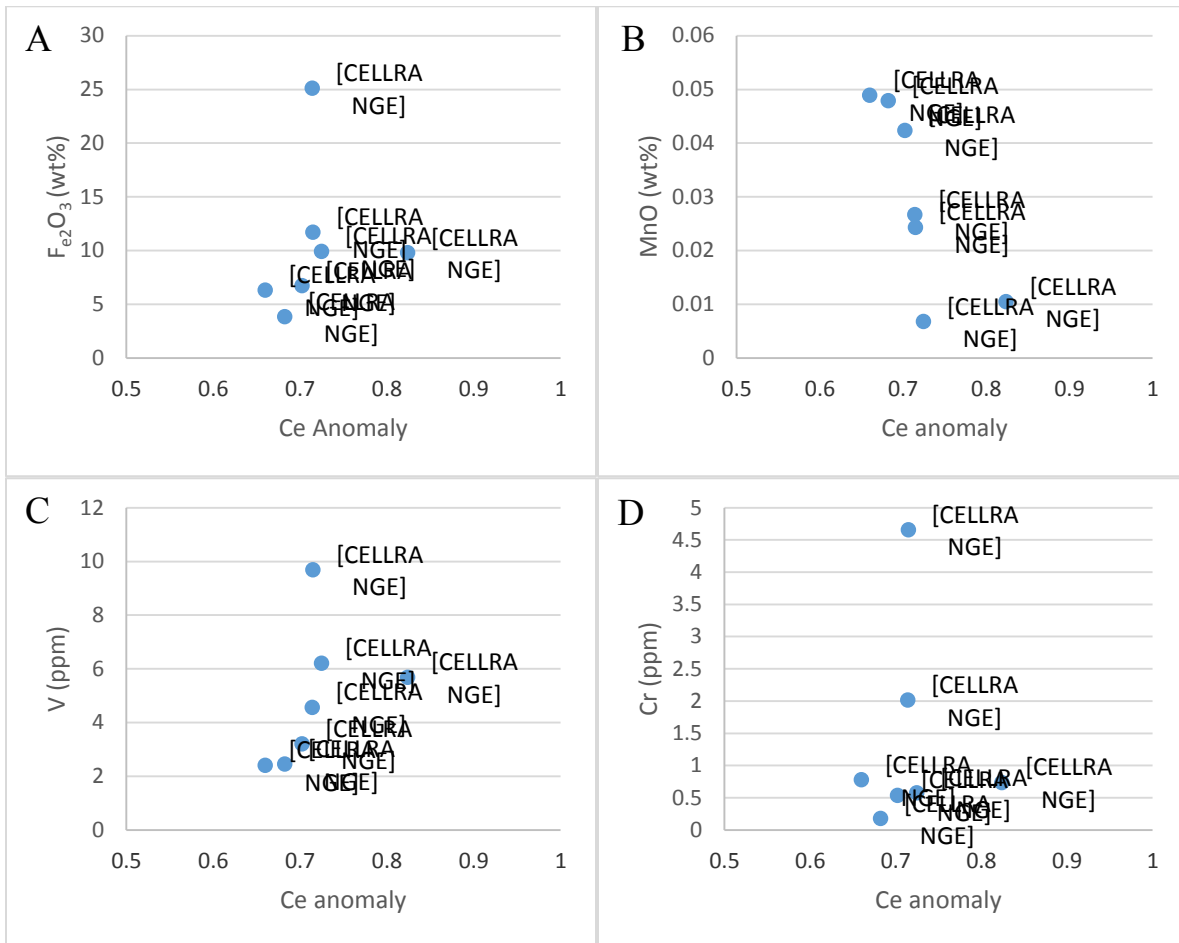
Figure 104: redox sensistive oxides and elements vs. Ce anomaly plots. No trends are visible in any of the plots. A) Fe_2O_3 vs. Ce anomaly, B) MnO vs. Ce anomaly, C) V vs. Ce anomaly, D) Cr vs. Ce anomaly.

5.3.2 *Old School Road*

The same five samples were analysed for rare earth element concentrations at LUIL as were analysed for major and trace elements. The results were normalized against PAAS values (Figure 105). The plot shows that the grainstone sample (OSR-2) is enriched in MREEs and HREEs. The sample has positive Ce and Eu anomalies. The sample collected from the brecciated grainstone (OSR-5) has a similar concentration of REEs to the grainstone sample as well as being enriched in both MREEs and HREEs. The sample have positive Ce and Eu anomalies. The red stromatolite (Sample OSR-12) has a higher concentration of REEs than the grainstones and displays the same enrichment in HREEs and MREEs with positive Ce and Eu anomalies. The sample taken from the broken up stromatolite (OSR-13) has a similar concentration and pattern to the grainstone samples, except it has only a slight positive Ce anomaly. The oolitic grainstone that tops off the outcrop shows a is enrichmed in HREEs and MREEs and also a marginally negative Ce anomaly with a possible positive Eu anomaly.

Figure 106 contains the plots of the PAAS normalized La and Eu anomaly values vs. the PAAS normalized Ce anomaly value. The La vs. Ce anomaly plot shows that the Ce anomalies present in the PAAS normalized REE distribution plots are true positive anomalies and have not been artificially suppressed by La anomalies (Figure 106A). The plot also shows nil Ce anomalies in samples 13 and 22 a linear trend forming between the two anomalies. The plot of the Eu vs. Ce anomaly shows no distinct trend forming between the two anomalies (Figure 106B).

The last four plots are of the redox sensitive oxides and elements plotted against the PAAS normalized Ce anomaly values. The plot of Fe_2O_3 vs. Ce* shows no distinct trend forming between the oxide and the Ce anomaly (Figure 107A). MnO vs. Ce* does show a strong trend

forming between the oxide and Ce* (Figure 107B). The plots of V vs. Ce* and U vs. Ce* show

no distinct trend between the elements and the Ce*, though both hint that a positive trend may

appear if more samples were analysed (Figure 107 C and D).
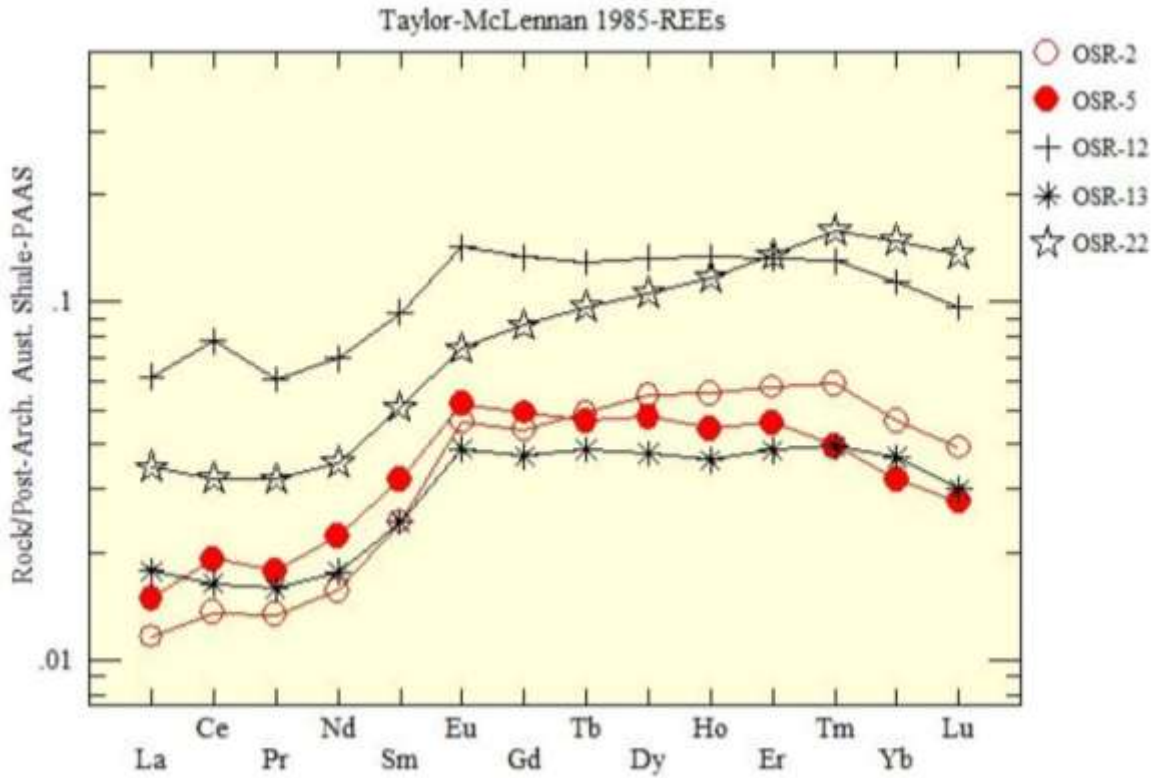
Figure 105: The PAAS normalized rare earth distribution plot for the samples from the Old School Road outcrop.
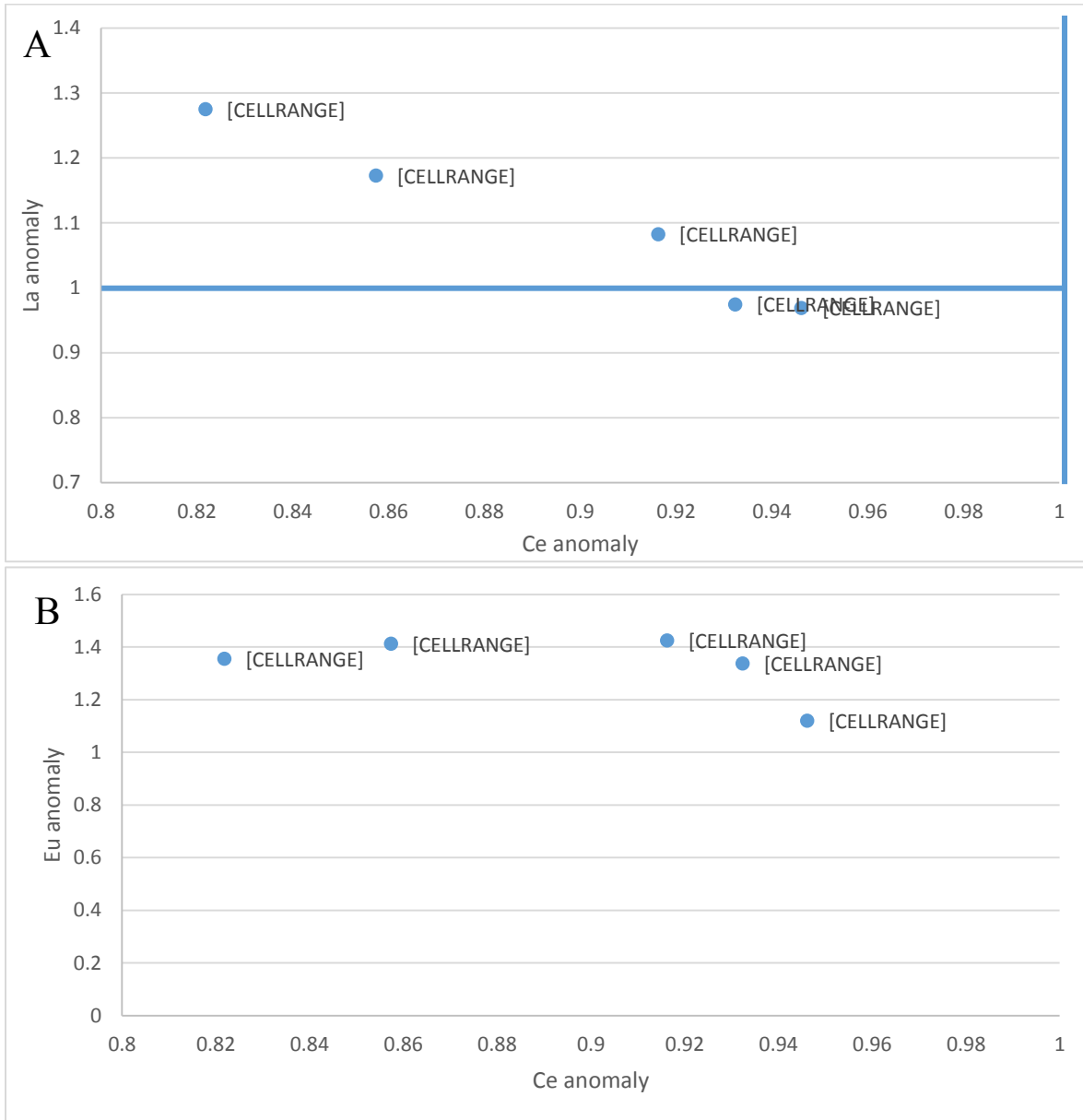
Figure 106: PAAS normalized La and Eu anomaly values vs. PAAS normalized Ce anomaly values. A) The Ce anomaly vs. La anomaly plot for the Old School Road samples. The plot shows that the grainstone, jasper and red stromatolite samples all have positive Ce anomalies. The samples with marginally present anomalies are ORS-13 and OSR-22 which are from the broken stromatolite and the overlying ooidal grainstone. B) Eu anomaly vs. Ce anomaly plot, the plot shows that there is no distinct correlation between the Eu anomaly and Ce anomaly and the positive Eu anomalies are moderate to low.
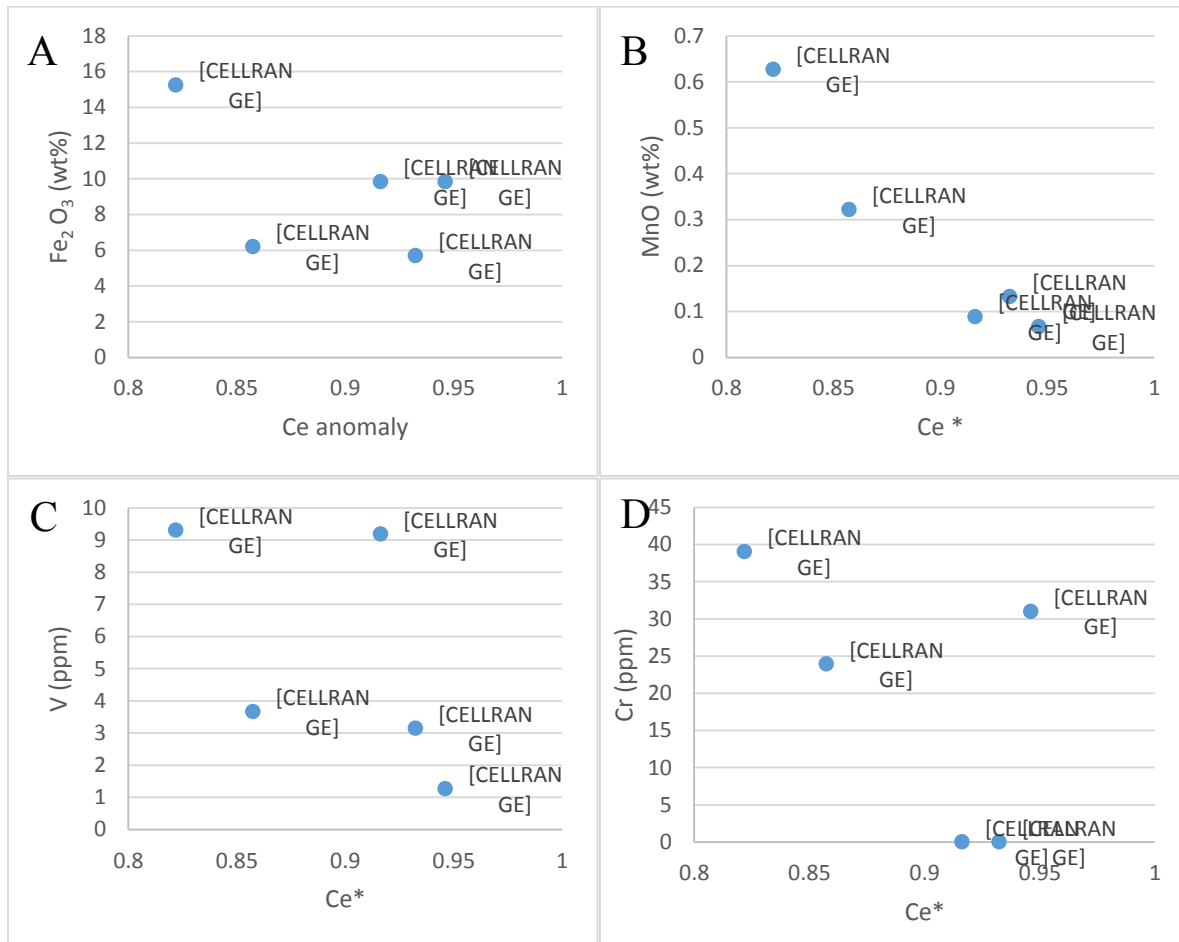
Figure 107: The main redox components plotted against the Ce anonamly (Ce*). A) Fe2O3 vs. Ce* shows no visible trend between the two. B) A positive trend can be seen in the MnO vs. Ce* where samples with larger positive Ce anomalies have more MnO. C) V vs. Ce* showing no trend forming between the two. D) Cr vs. Ce* plot showing no trend between the two.

5.3.3 Magnetic Rock Trail

ICP-MS analyses for rare earth element concentrations were carried out on the same 23 samples taken from the Magnetic Rock trail outcrops as were used for the major and trace element analyses.

The resultant analyses were normalized to Taylor and McLennan (1985) PAAS values.. Figure 108A is of the grainstone and fine-grained chemical precipitate samples taken from below the stromatolites. The samples are listed in numerical order, CY-100, 4.4 m below the stromatolites and numbers increasing upwards. Nine out of the ten samples show a similar pattern, in which the HREEs are slightly enriched compared to the LREEs. These samples have positive Ce anomalies as well as moderate to large positive Eu anomalies, especially samples CY-108 and CY-109 which show large positive Eu anomalies. Sample CY-100 exhibits a different pattern compared to the previous nine samples in that it is depleted in HREEs with a positive Ce anomaly and no Eu anomaly. The two samples taken from the stromatolites are enrichmed in HREEs with negative Ce anomalies and positive Eu anomalies (Figure 108B).

The last plot is of the samples taken from above the Magnetic Rock Trail stromatolites. The samples show two distinct groupings based on their patterns and the plots have been divided to reflect their groupings. Figure 109A is of samples 110, 111, 112, 113, 114 which are the samples taken from the grainstones directly above the stromatolites. These plots show a varying patterns ranging from a flat curve with minimal Ce and large Eu anomalies (110), to curves showing enrichment in HREEs and relatively flat Eu anomalies. Figure 109B is of the samples of the grainstones interlayered with lapilli (samples 115, 116 A, B and C, 117 A and B). These curves shows that the samples all have similar concentrations and curves with positive Ce anomalies. Eu anomalies vary from pronounced to non-existent.
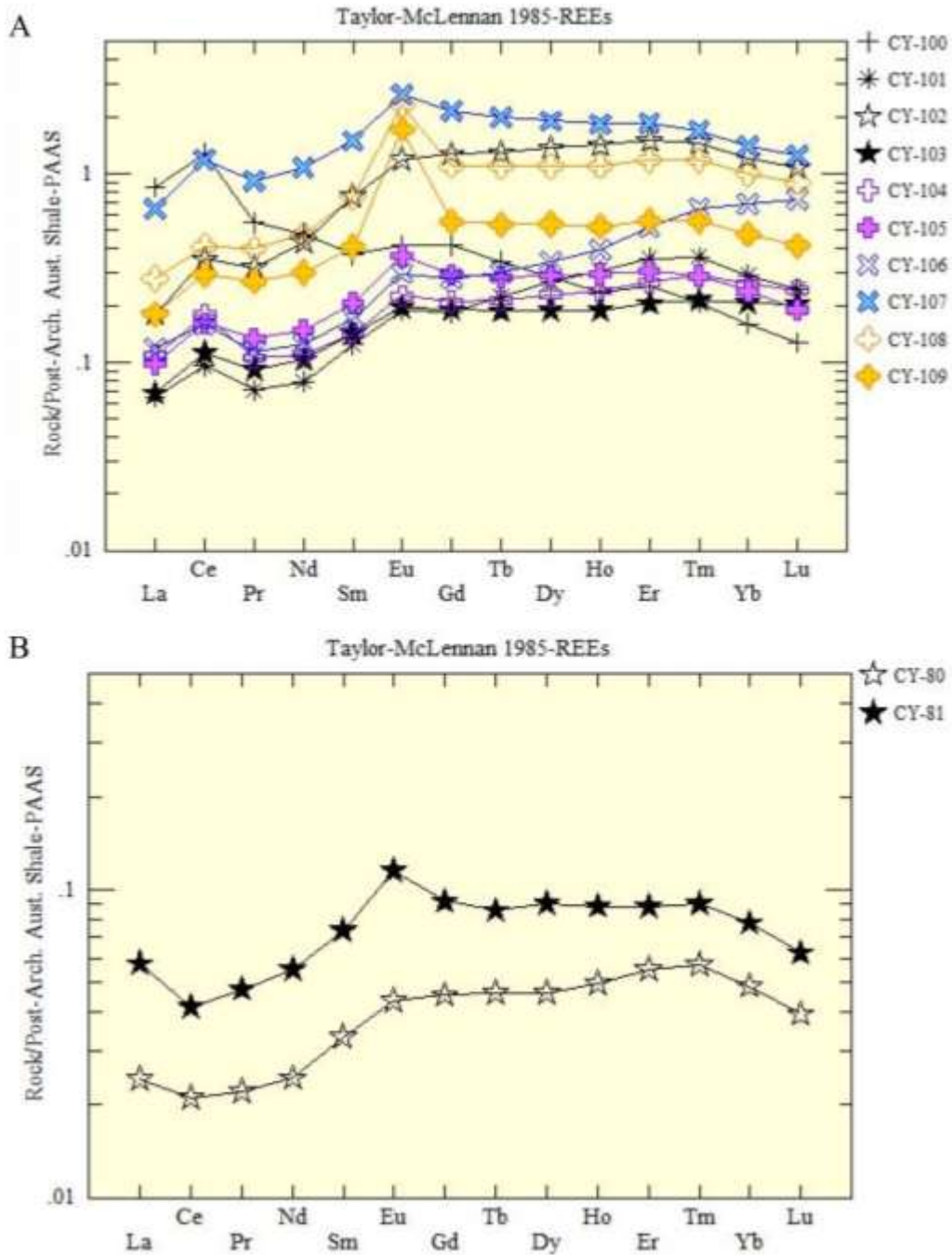
Figure 108: A) PAAS normalized rare earth element concentration plot for the Magnetic Rock Trail grainstone samples collected below the stromatolites. B) PAAS normalized plot for the stromatolites taken from the Magnetic Rock Trail outcrop.
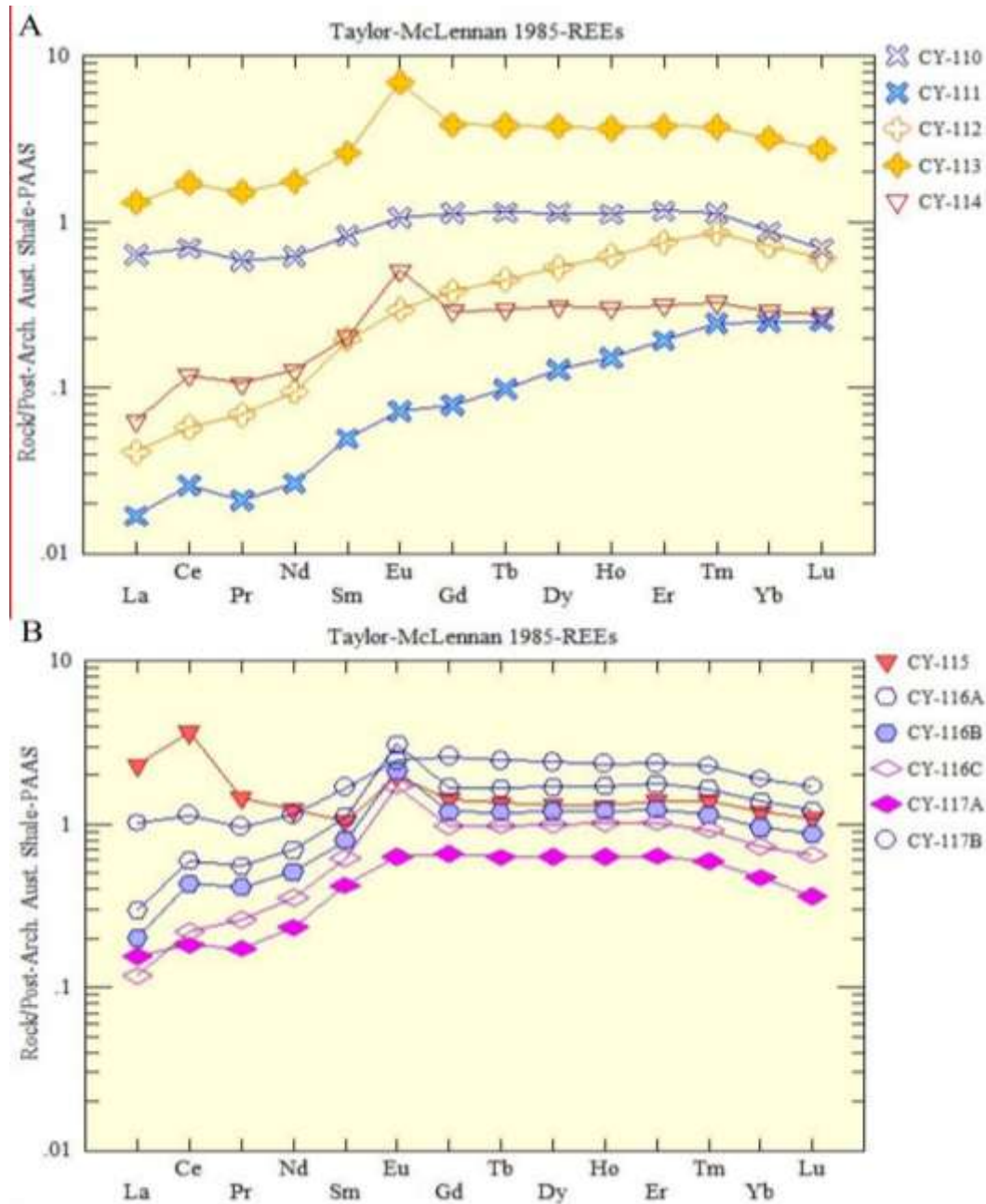
Figure 109: PAAS normalized REE distribution plots for samples taken from above the stromatolites on the Magnetic Rock Trail. A) Grainstone samples showing similar REE concentrations with positive Ce anomalies. B) The second plot is of the grainstone interlayered with the lapilli samples showing a flatter pattern with patterns similar to the two types of patterns present in A; one group having pronounced positive Eu anomalies, the other no significant Eu anomalies.

The plots of the La and Eu anomalies plotted against the values for the Ce anomalies are seen in Figure 110. Figure 110A is of the values for the La anomaly vs. Ce anomaly. This plot shows that the samples collected from the grainstones found below, and the grainstones above the stromatolite layer all have very positive Ce anomalies forming a distinct linear trend, with the highest La anomaly values having the most positive Ce values, which are found in samples CY-100 and CY-115. The stromatolite samples CY-80 and CY-81 do not have Ce anomalies. Figure 110B is of the Eu anomaly values vs. the Ce anomaly values. This plot shows no pattern forming between the two anomaly values, this shows no link between the Eu anomaly and the Ce anomaly.

Figure 111 contains the plots of the values for the major redox sensitive components (Fe_2O_3, MnO, V, Cr) plotted against the values of Ce anomalies of the samples collected from the Magnetic Rock Trail. The four plots do not show any linear trends forming, but the samples do all cluster around similar oxide values.

Figure 110: La and Eu anomalies plotted against values for Ce anomalies. A) La anomaly vs. Ce anomaly plot, showing the positive Ce anomaly found in all samples except for the two stromatolite samples. B) Eu vs. Ce anomaly plot, showing no trend forming between the two anomalies. Two groups exist. One with small to non-existent Eu anomalies (some members of this group have very significant positive Ce anomalies), and one with large Eu anomalies and small positive Ce anomalies.

Figure 111: The redox components plotted against the Ce anomaly values showing no trends forming in any of the plots. Some of the samples had Cr values below detection. A) Fe_2O_3 vs. Ce*B) MnO vs Ce* C) V vs. Ce* and D) Cr vs. Ce*. Two of the samples have high Cr values and one has a high V concentration.

5.3.4 Current River

The same eight samples were analysed for rare earth element concentrations at LUIL as were analysed for major and trace elements. The results were again normalized to Taylor and McLennan's 1985 PAAS values. Figure 112 contains the plots of the normalized rare earth elemental compositions. Figure 112A is the PAAS normalized samples collected from the Boulevard Lake outcrops. The samples are organized by their location in the stratigraphic sequence with CR-2 and 3 making up the grainstone below the stromatolites and CR-7 and 8 from above the stromatolite layer. This plot contains similar curve shapes with relatively no depletion or enrichment in LREEs vs. HREEs. All samples have positive Ce and Eu anomalies. Figure 112 B is a PAAS normalize rare earth element plot for the samples from the stromatolite layer site below the Arundel Street Bridge. This sample set can be divided into two distinct patterns. Samples 01-WR and 01-Mn are similar to the Boulevard Lake samples. However samples 2 and 3 do not have positive Eu anomalies and 02 is HREE enriched.   All the samples plot with no to negative Ce anomalies. Sample CR-11-03, which is from directly below the thrombolites, shows an enrichment in the total REE concentration.

The normalized values for the Ce anomaly were plotted against the normalized values for both La and Eu anomalies. The plot of Ce vs. La anomalies shows that the two sample sites have two distinct Ce anomaly values (Figure 113A). The samples from Arundel all have very slightly negative to nil Ce anomalies. Positive anomalies are present in the Boulevard Lake samples. The Boulevard Lake samples do show a distinct break in sample concentration in that the samples from below the stromatolites have larger positive Ce anomalies than the two samples from above the stromatolites. Figure 113B shows the values for the normalized Eu anomalies vs. Ce anomaly

values. This plot contains similar groupings to those present in the La vs. Ce anomaly plot, as well a possible positive trend.
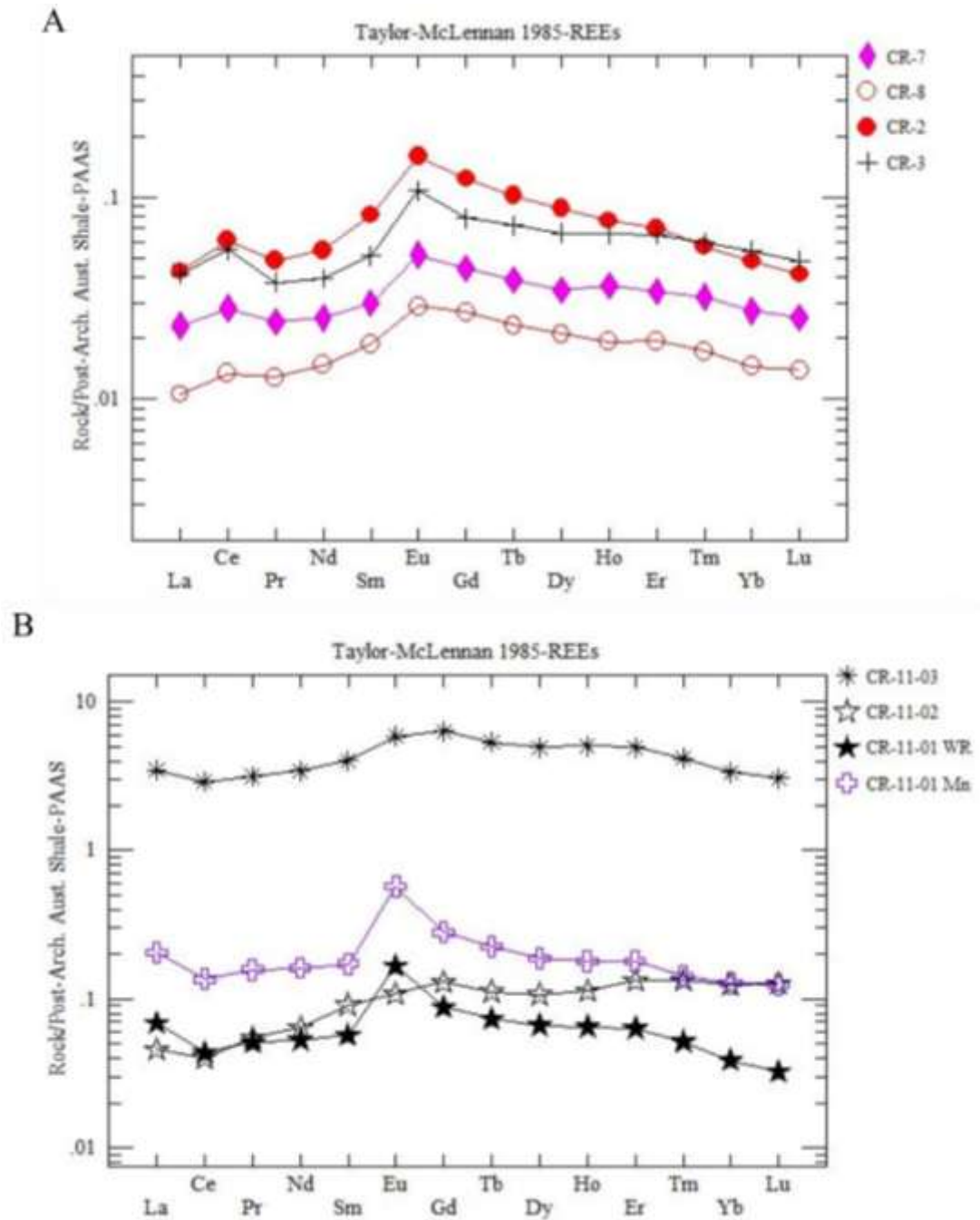
Figure 112: PAAS normalized REE distribution plots for the Current River samples. A) Samples from the Boulevard Lake site. B) Samples collected from the Arundel Street Bridge sites.
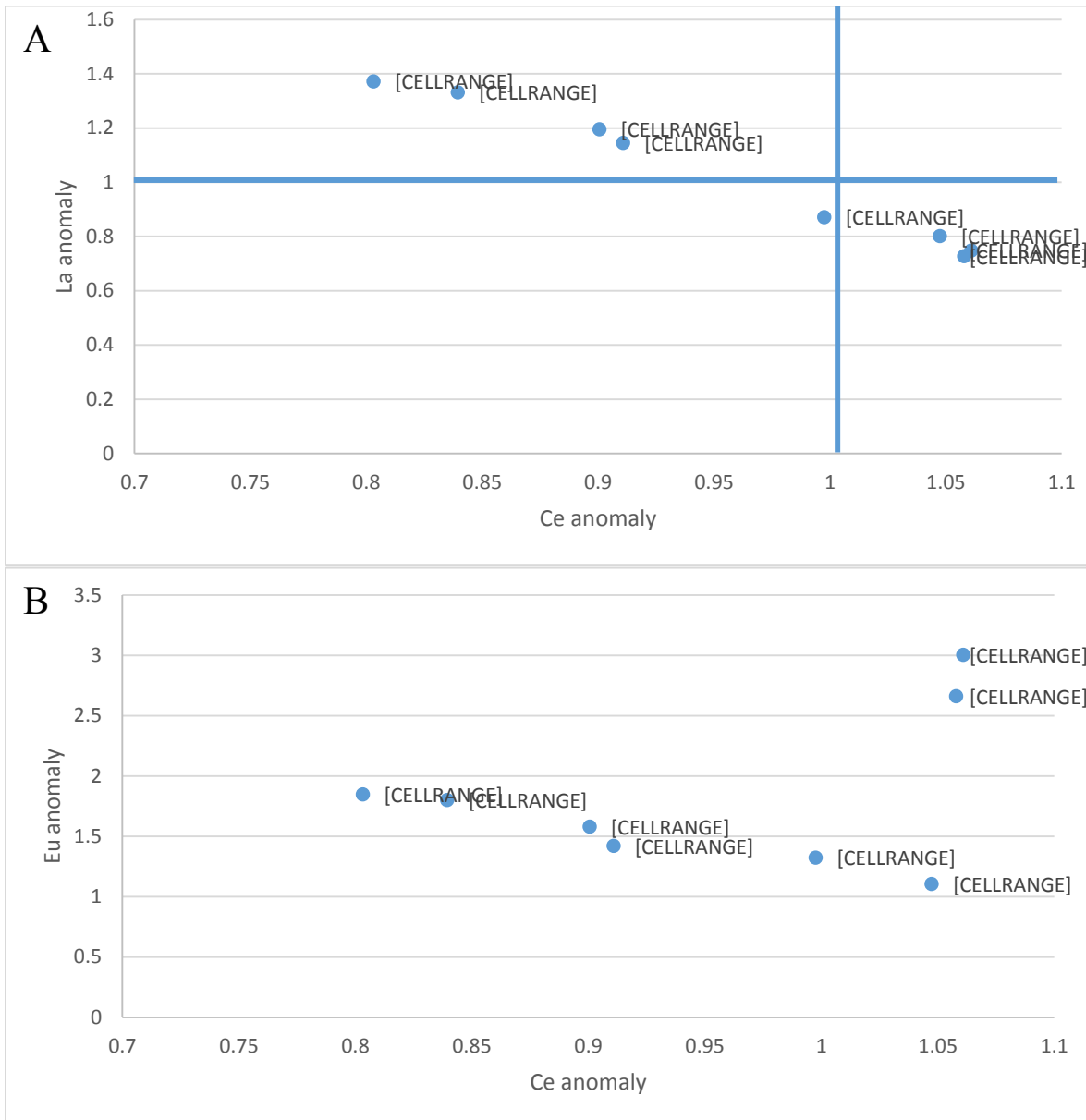
Figure 113: PAAS normalized anomalies plot for the Current River samples. A) La anomaly vs. Ce anomaly showing the two distinct groupings of the samples. The samples from below Arundel Street Bridge are plotted with nil to negative Ce anomalies and the Boulevard Lake samples plot with positive Ce anomalies. B) PAAS normalized Eu anomaly vs. Ce anomaly.

The PAAS normalized Ce anomaly values were plotted against the redox sensitive oxides and elements; Fe_2O_3, MnO, V and Cr (Figure 114A, B, C and D). No trends can be seen in any of the plots. However, two of the samples plot with very high V and Cr values.
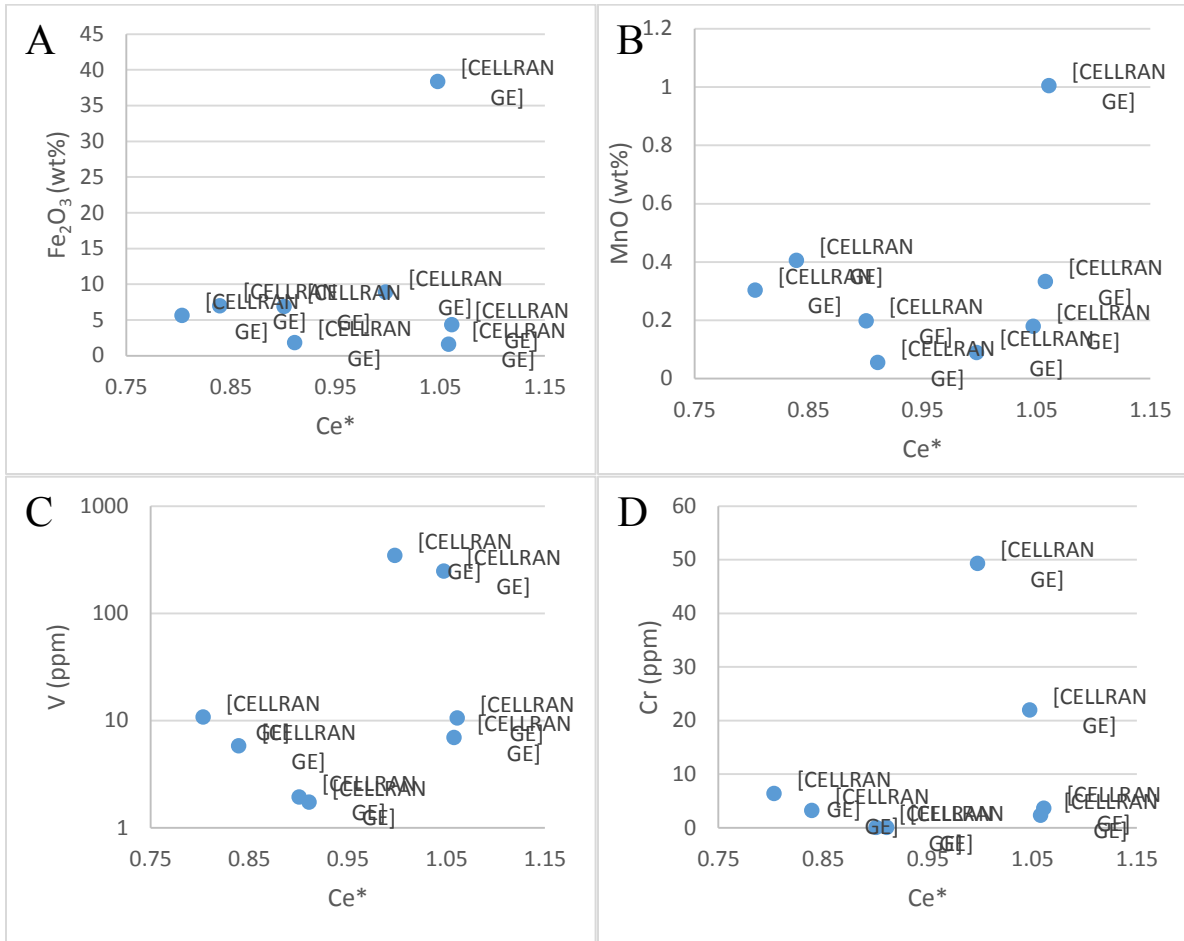
Figure 114: Redox sensitive elements vs. Ce anomalies showing no trend forming in any of the plots. A) Fe_2O_3 vs. Ce*. B) MnO vs. Ce*, C) V vs. Ce* and D) Cr vs. Ce*. Two of the samples have very high V and Cr values and have no Ce anomaly or a slight positive one.

5.3.5 DH 87-3

The PAAS normalized distribution plots for the samples taken from DH 87-3 were plotted (Figure 115). The plot shows that all the samples have a fairly flat pattern with a positive Eu anomaly and only slightly positive Ce anomalies. The stromatolites have the highest concentration of REEs and the lowest concentration is present in the grainstone layer at the base of the cycle. The samples taken from the chemical sediments layer at the top and the fine-grained chemical sediment layer at the bottom show the same concentration and pattern.

Anomaly values were calculated for the La, Ce and Eu concentrations in the samples. The La and Eu anomaly values were plotted against Ce anomaly values (Figure 116). The first plot is of the Ce vs. La anomalies and shows a flat pattern forming between the two anomalies. All the samples plot with slightly positive Ce anomalies (Figure 116A). The next plot is of the Eu anomalies vs. Ce anomalies. This plot shows no trend forming between the two anomalies (Figure 116B).

The last plots are of the redox sensitive oxides and elements plotted against the Ce anomalies. The plots are of Fe_2O_3, MnO, V and Cr. The plot of Fe_2O_3 vs. Ce anomaly shows a slight positive trend forming between the oxide and the anomaly (Figure 117A). The plot of MnO vs. Ce* shows a distinct positive trend (Figure 117B). The plots of V vs. Ce* and Cr vs. Ce* do not show any trend (Figure 117C and D).
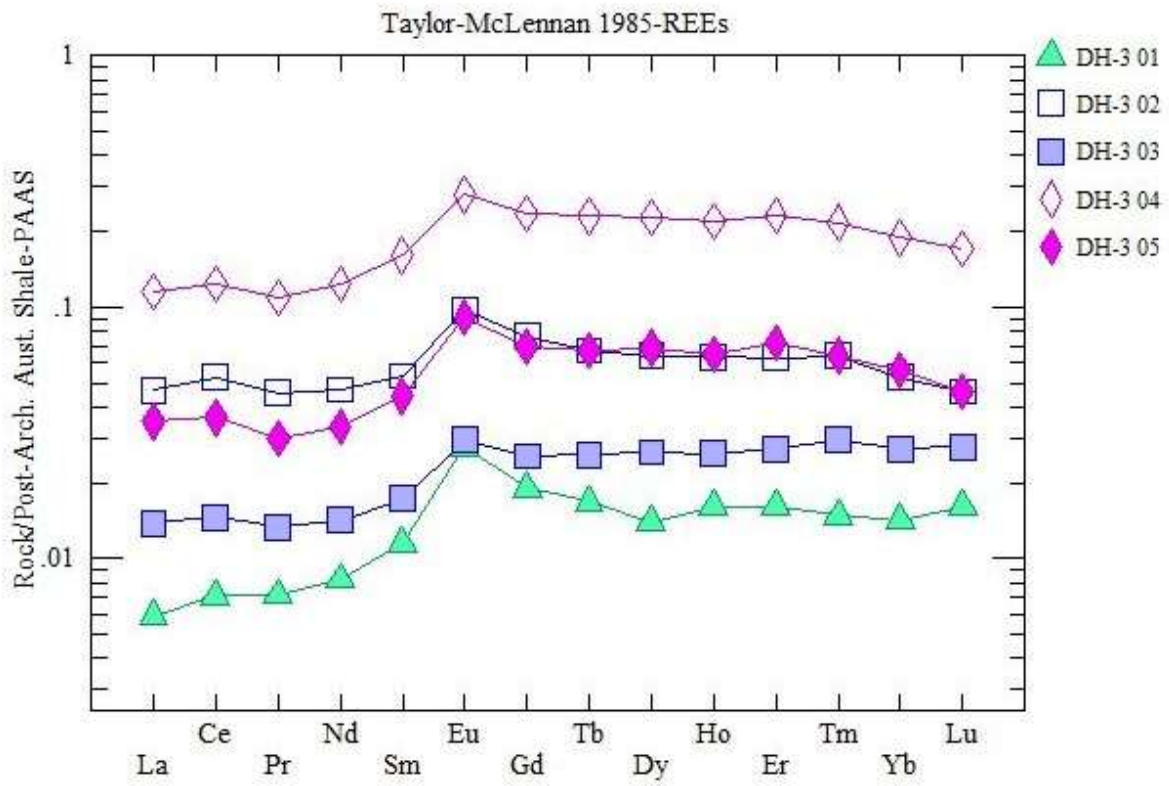
Figure 115: Rare earth element concentration diagram for the DH-3 samples. The samples show a slight positive Ce anomaly with a positive Eu anomaly.
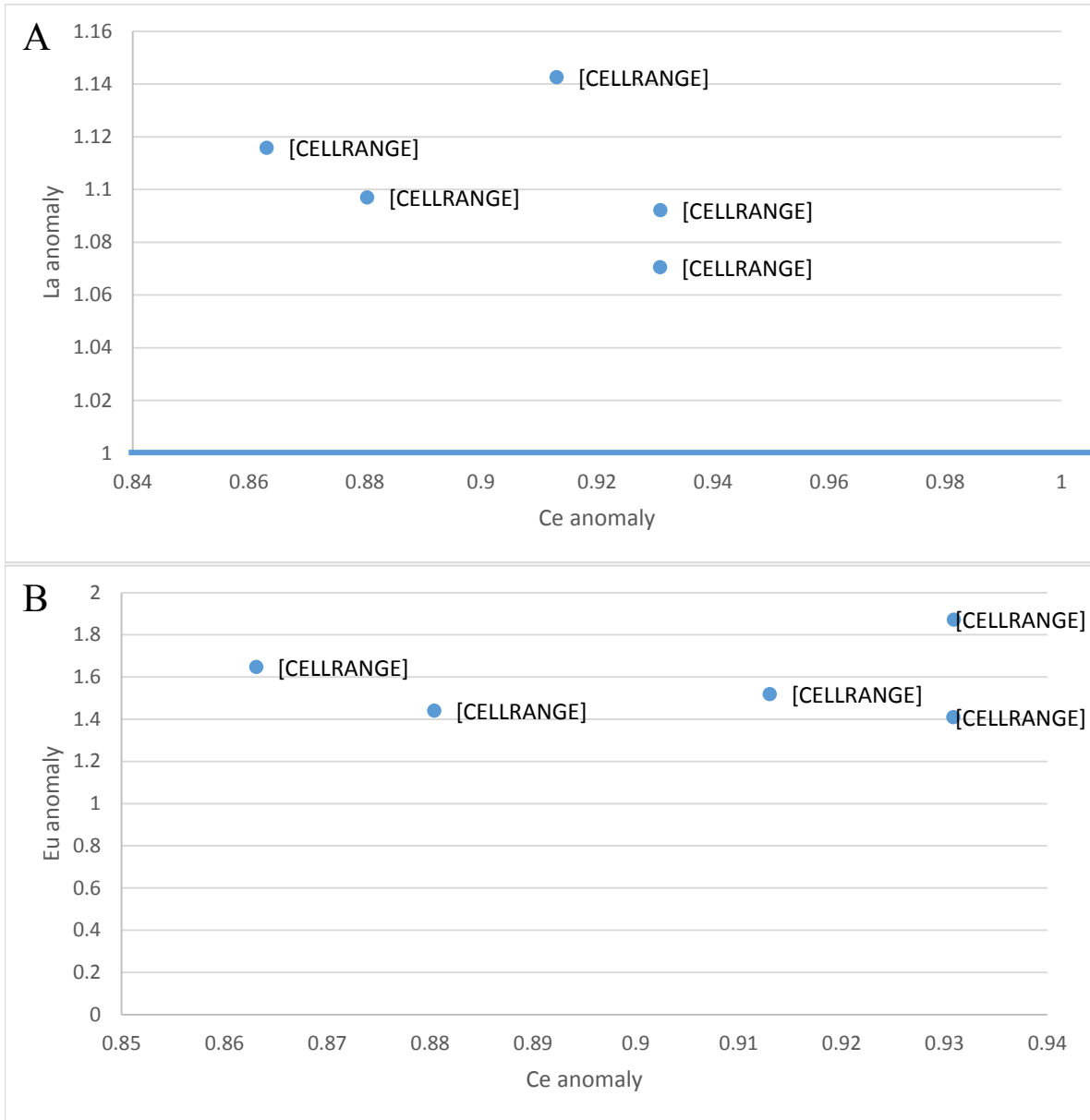
Figure 116: Calculated values of the La and Eu anomalies plotted against the calculated values for the Ce anomaly. A) La vs. Ce anomaly plot showing the slightly positive Ce anomaly found in all the samples. B) Eu vs. Ce anomaly plot showing no trend forming between the two anomalies. The values for the Eu anomaly are moderate to moderately high.
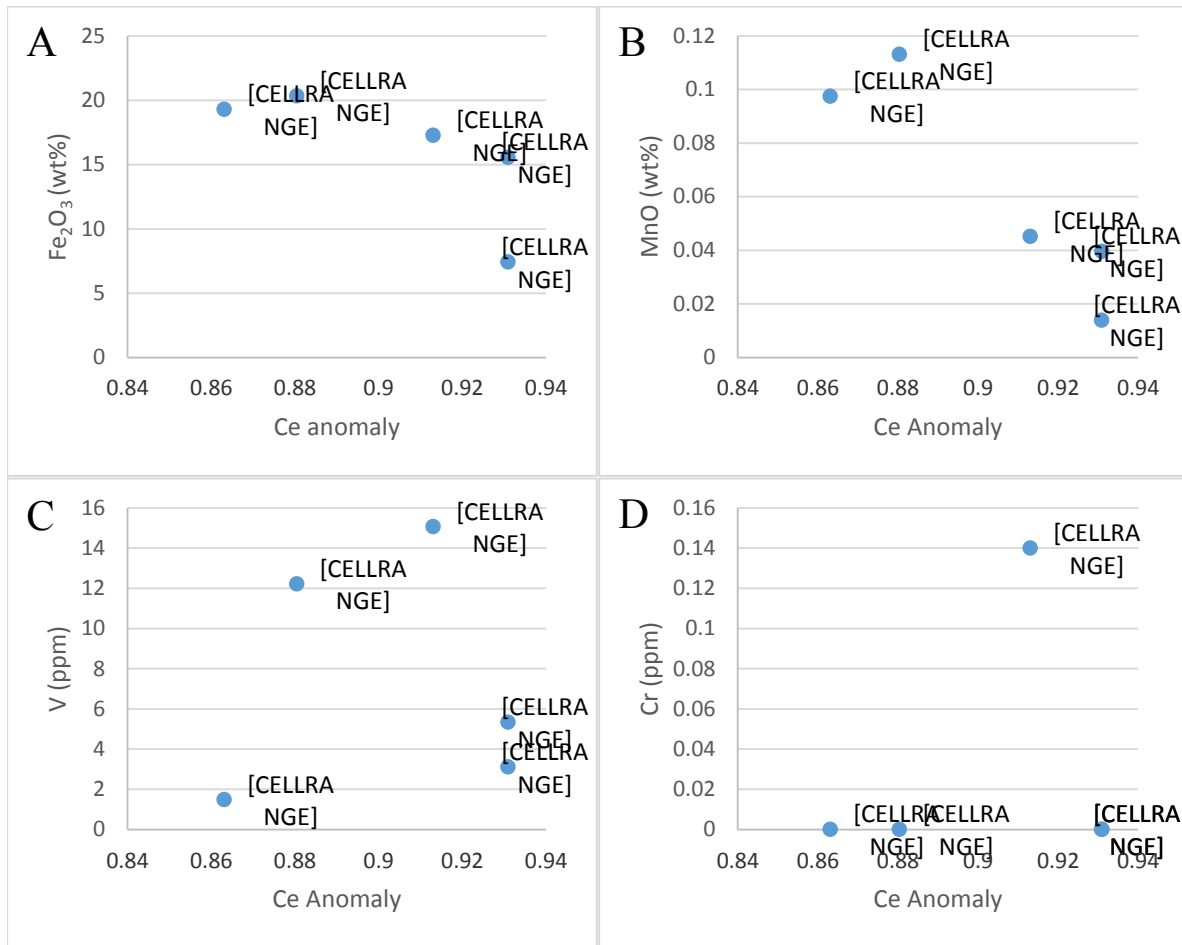
Figure 117: Plots of the Ce anomaly plotted against redox sensitive components. A and B exhibit a positive trend between increasing positive Ce anomaly and Fe_2O_3 and MnO. No trend can be seen in the other plots.

5.3.6 MC-89-1

The same nine samples were analysed for their rare earth element concentrations as were used for the major and trace elements, and the values were normalized to Taylor and McLennan (1985) Post Archean Australian Shale (Figure 118). The samples are separated into those taken from the mottled grainstone (Figure 118A) and those from the underlying unmottled grainstones (Figure 118B). The samples taken from the mottled grainstone show similar patterns, with enrichment of the HREEs and positive Ce anomalies. The enrichment of the HREEs seems to have hidden the Eu anomaly. The plot of the unmottled grainstone samples show similar patterns in which there is an enrichment in the HREEs with positive Ce and more distinctive positive Eu anomalies.

The calculated values of the Ce anomaly were plotted against the calculated values of the La and Eu anomalies (Figure 119). The plot of La anomaly vs. Ce anomaly shows that the samples from the MC-89-01 drill- core all have positive Ce anomalies which appear to form a positive trend with sample CY-32, which is from above the stromatolite, having the largest positive Ce anomaly. Figure 119B is of the Eu anomaly vs. Ce anomaly showing no trend forming in between the two anomalies.

The Ce anomalies were plotted against the major redox sensitive components Fe_2O_3, MnO, V and U (Figure 120). These plots do not show any trends forming between the elements and the Ce anomaly.
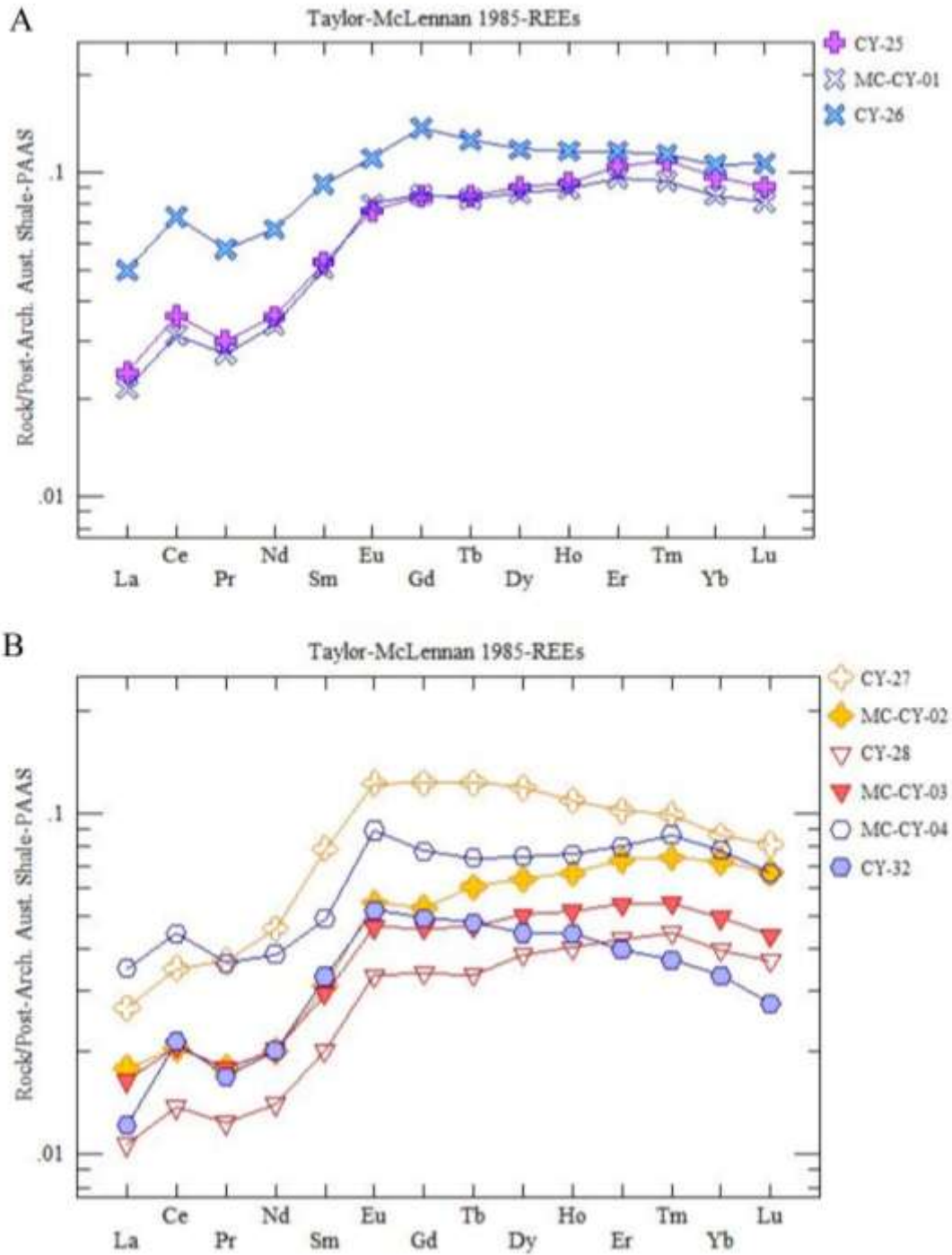
Figure 118: PAAS normalized rare earth element concentration plots. A) Samples from the mottled grainstone layer. The plot shows that the samples are enriched in HREEs with positive Ce anomalies and no Eu anomalies. B) Un-mottled grainstone samples; the plot shows enrichment of HREEs with positive Ce and possible positive Eu anomalies present.
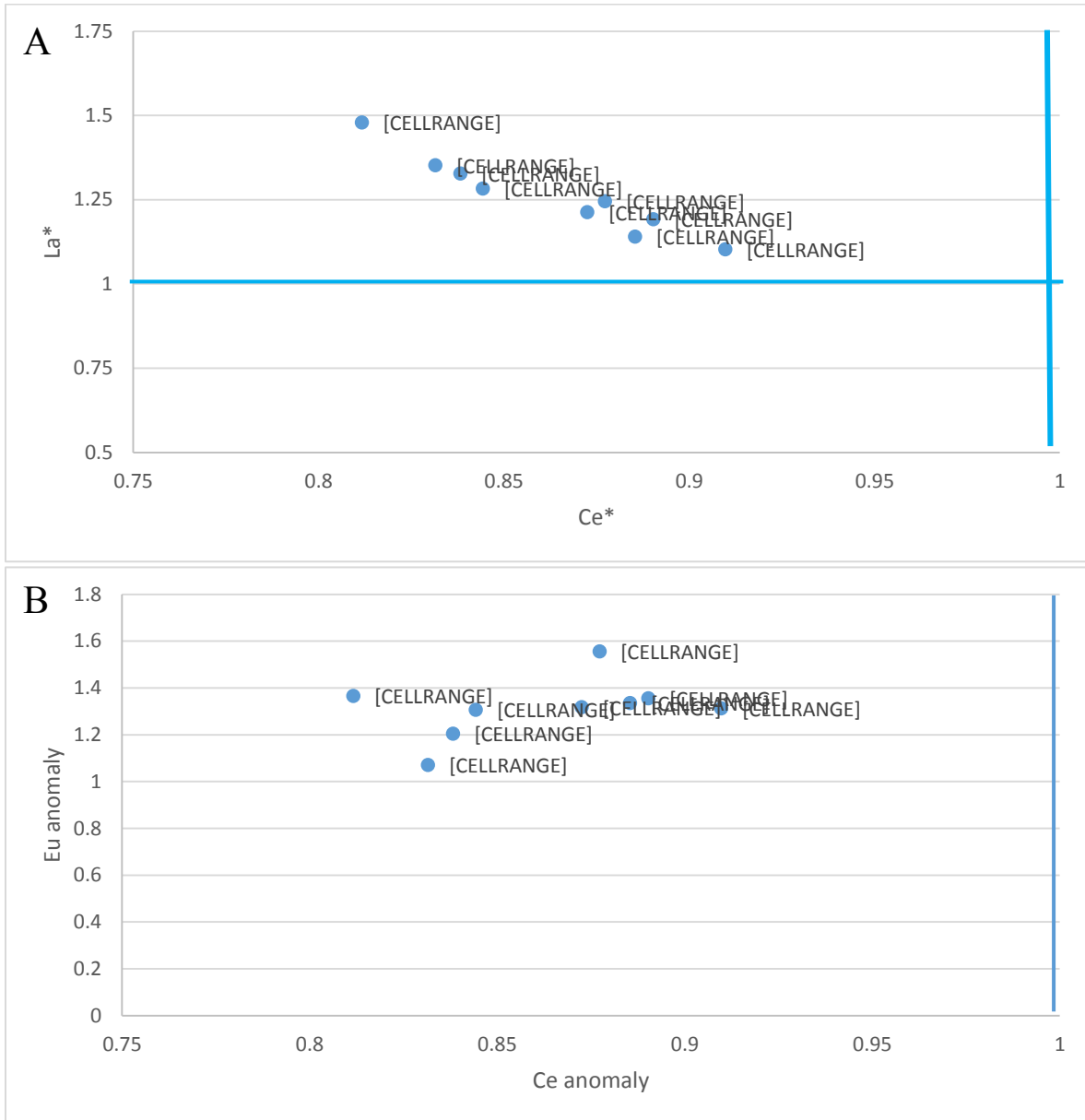
Figure 119: REE anomaly plots for the MC-89 samples. A) La anomaly vs. Ce anomaly showing distinct positive Ce anomalies in all samples, as well as a positive linear trend. B) The Eu anomaly vs. Ce anomaly showing no distinct pattern forming between the two anomalies. The Eu anomalies are low to non-existent.
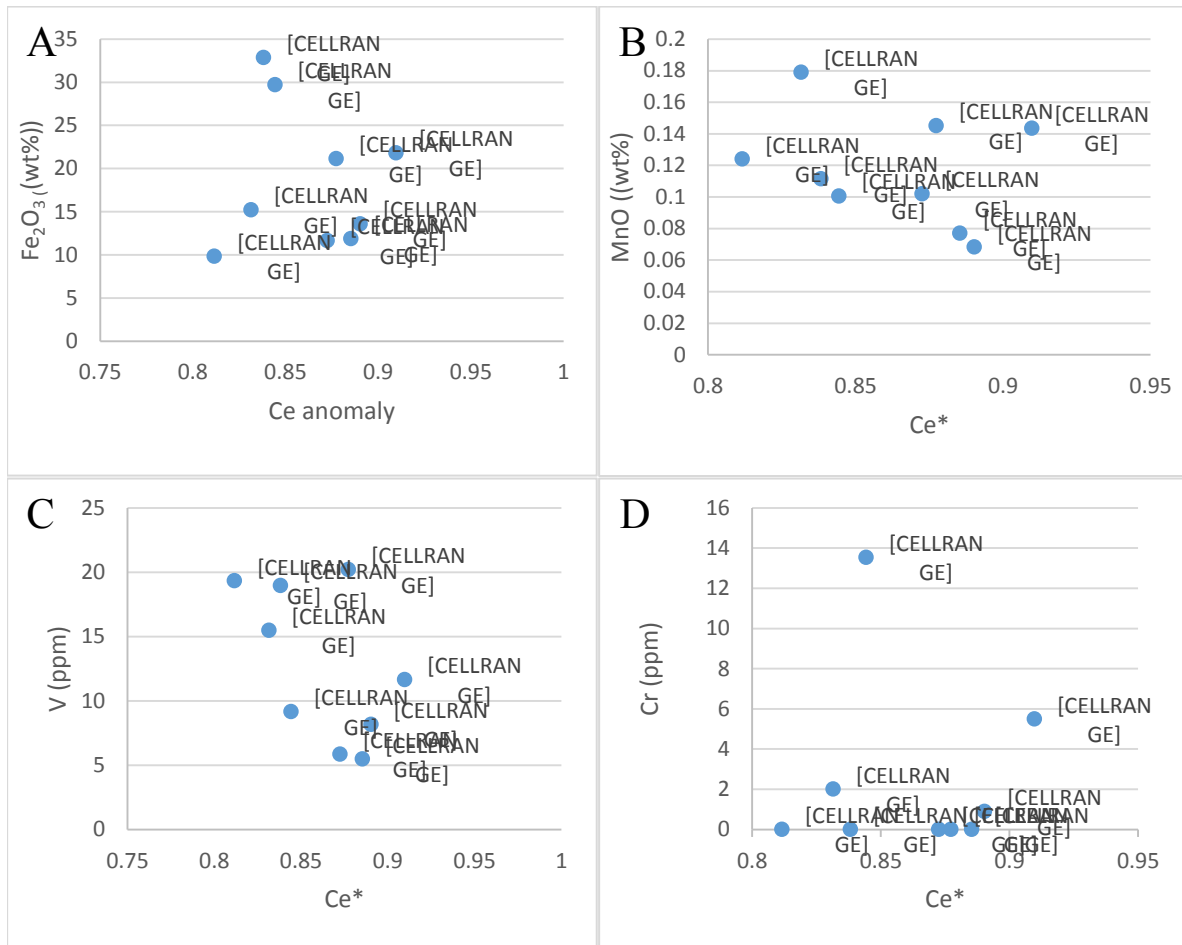
Figure 120: Redox components vs. Ce anomaly. A) Fe$_2$O$_3$ vs. Ce*. B) MnO vs. Ce* C) V vs. Ce* and D) Cr vs. Ce*. None of these plots show any trend forming between the two. One of the samples is enriched in Cr.

6 UPPER EXPOSURE SURFACE

6.1 Sample Sites
6.1.1 Mount Whittlesey outcrop

This outcrop mentioned by Hensal et al., at the 1998 ILSG conference in Minneapolis and was later studied by Pufhal and Fralick (2004), who described the presence of contorted layers within the outcrop. Nick Beukes and Bruce Simonson (personal communications, 2011) thought there were oncolites and stromatolites present in the contorted layers, in agreement with Hensal et al. (1998). This outcrop is present at the top of Mount Whittlesey near Mellen, Wisconsin, in the westernmost portion of the Gogebic iron range, a Gunflint equivalent. The large outcrop is representative of the upward coarsening, transgressive sequences that are present in the upper 120 meters of the Gunflint Formation and equivalents. The lower portion of the outcrop is comprised of an asymmetrical sequence approximately 50m thick with a section of slaty iron formation overlain by a section of cherty iron formation. The coarsening-upward cycles that make up the outcrop start with parallel laminated slaty iron formation containing occasional small grainstone lenses. The slaty iron formation coarsens up into medium- to large-scale, trough cross-stratified grainstone lenses. This is all capped off by a convoluted bed comprised of a brecciated grainstone layer with stromatolites and oncoliths which bookend the cycles (Pufahl and Fralick, 2004). The samples selected from the outcrop best represent the composition of the three individual layer types that make up the Mount Whittlesey outcrop.
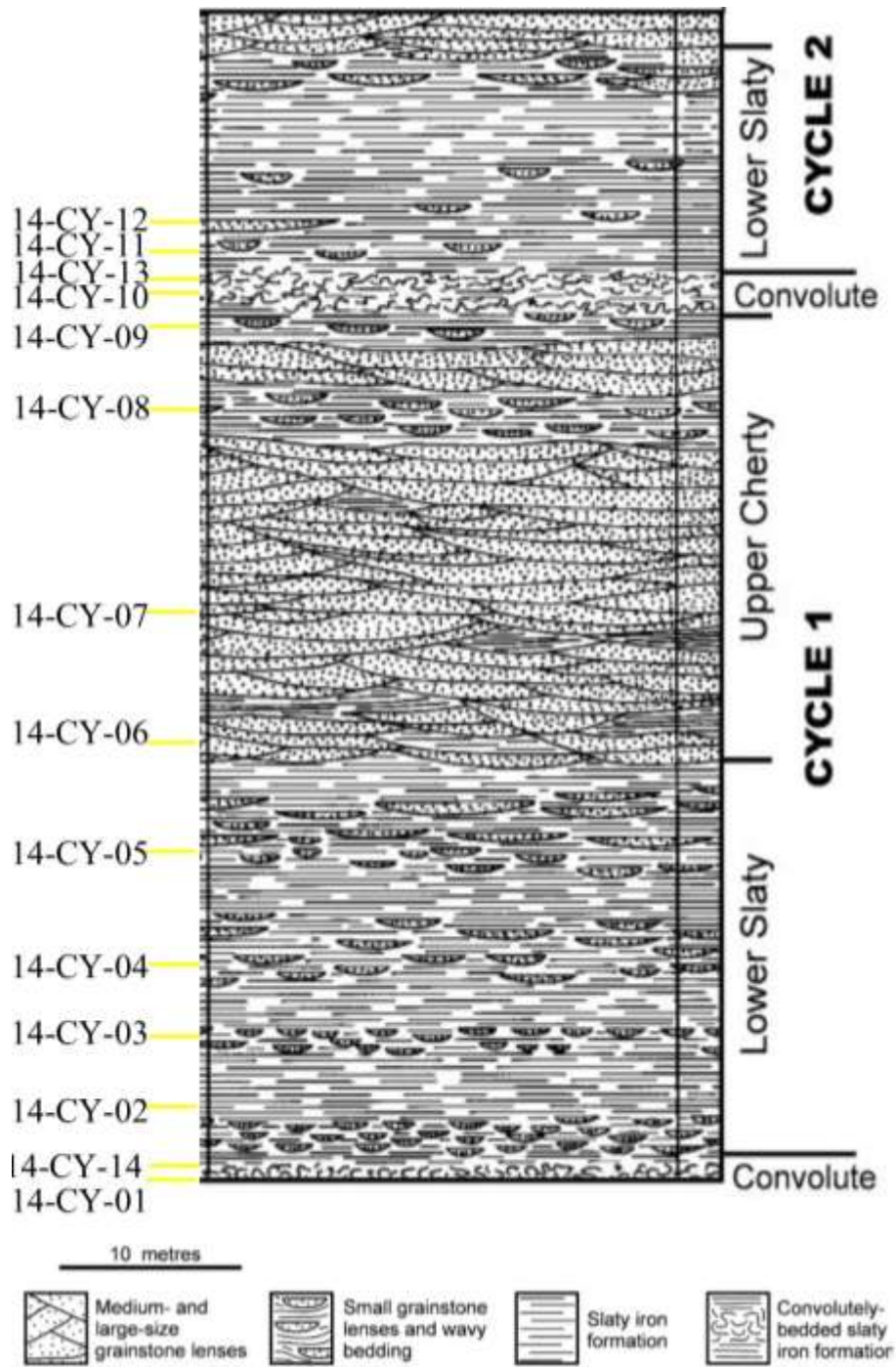
Figure 121: The stratigraphy of the Mount Whittlesey outcrop showing the composition of the cycles that make up the lower portion of the outcrop. The approximate location of the samples taken from the outcrop are shown on the left. Modified from Pufhal and Fralick (2004). Samples 14-CY-01 and 14 are from the lower convoluted layer, whereas 14-CY-10, 11, 12 and 13 are from the upper convoluted layer. The Lower and Upper designations do not refer to the informal stratigraphic names in the Mesabi iron range.

5.3.6.1   *The slaty iron formation*

The slaty iron formation forms the base of the cycle and represents the finest grained sediments that were deposited in the cycle (Figure 122A). Samples 14-CY-02 and 03 are from the parallel laminated slaty iron formation, and sample 14-CY-04 and 05 are from the small scale grainstone lenses found within the slaty iron formation. There is a repetition of very fine-grained black and grey layers in the samples from the slaty iron formation (Figure 122B). These are both graded and ungraded. The graded layers are commonly the grey layers and are comprised of silt-sized light material.Whereas, the dark layers are mostly ungraded and made up of fine-grained magnetite. In thin section, there is a sharp contact between the graded layers and the dark magnetite layers of the slaty iron formation (Figure 123A). The graded grey layers present are composed of a combination of Fe-chlorite and greenalite as identified by Pufhal and Fralick (2004) (Figure 123B). The dark layers are comprised mostly of the Fe-chlorite and greenalite with magnetite grains throughout (Figure 123C). This repetition of Fe-chlorites and greenalite rich layers and magnetite-rich layers is also visible in the slaty iron formation below the convolute layer (Figure 123 D).
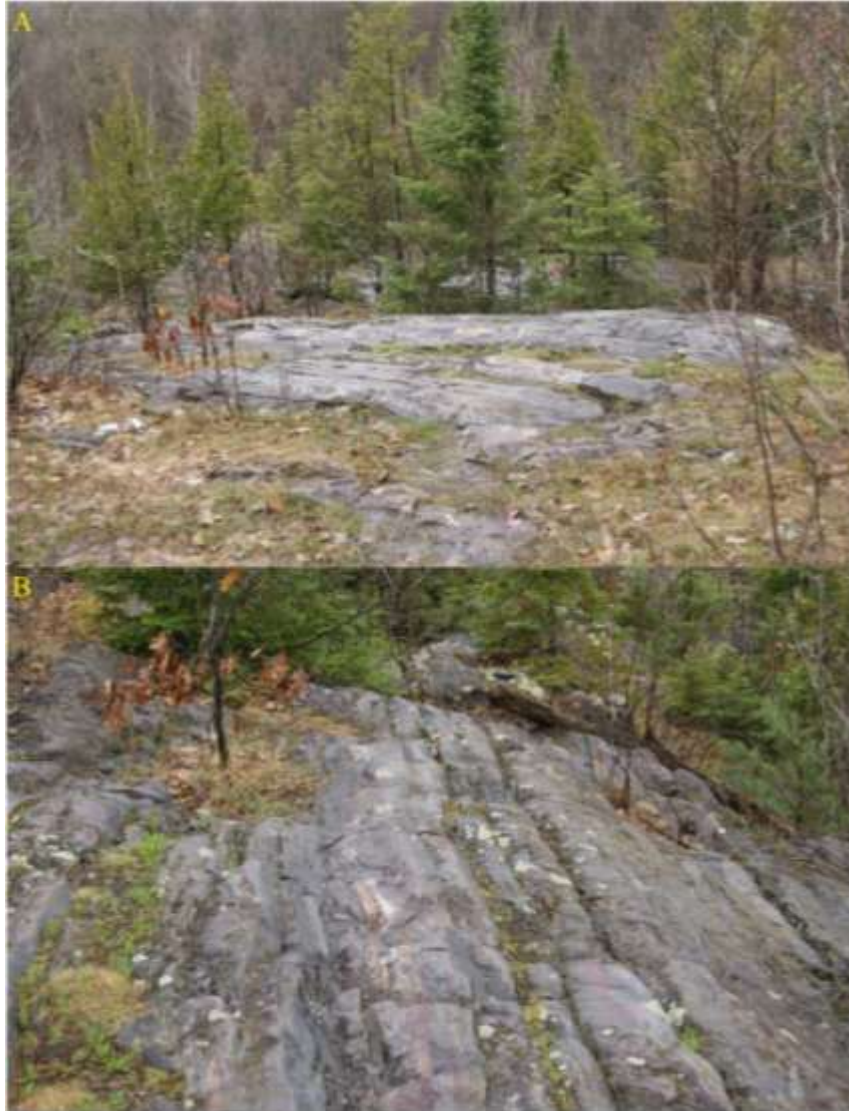
Figure 122: The outcrop at Mount Whittlesey. A) Overview of the outcrop at the top of the mountain. B) A portion of the asymmetrical cycles that make up the Mount Whittlesey outcrop stratigraphic top is to the left.
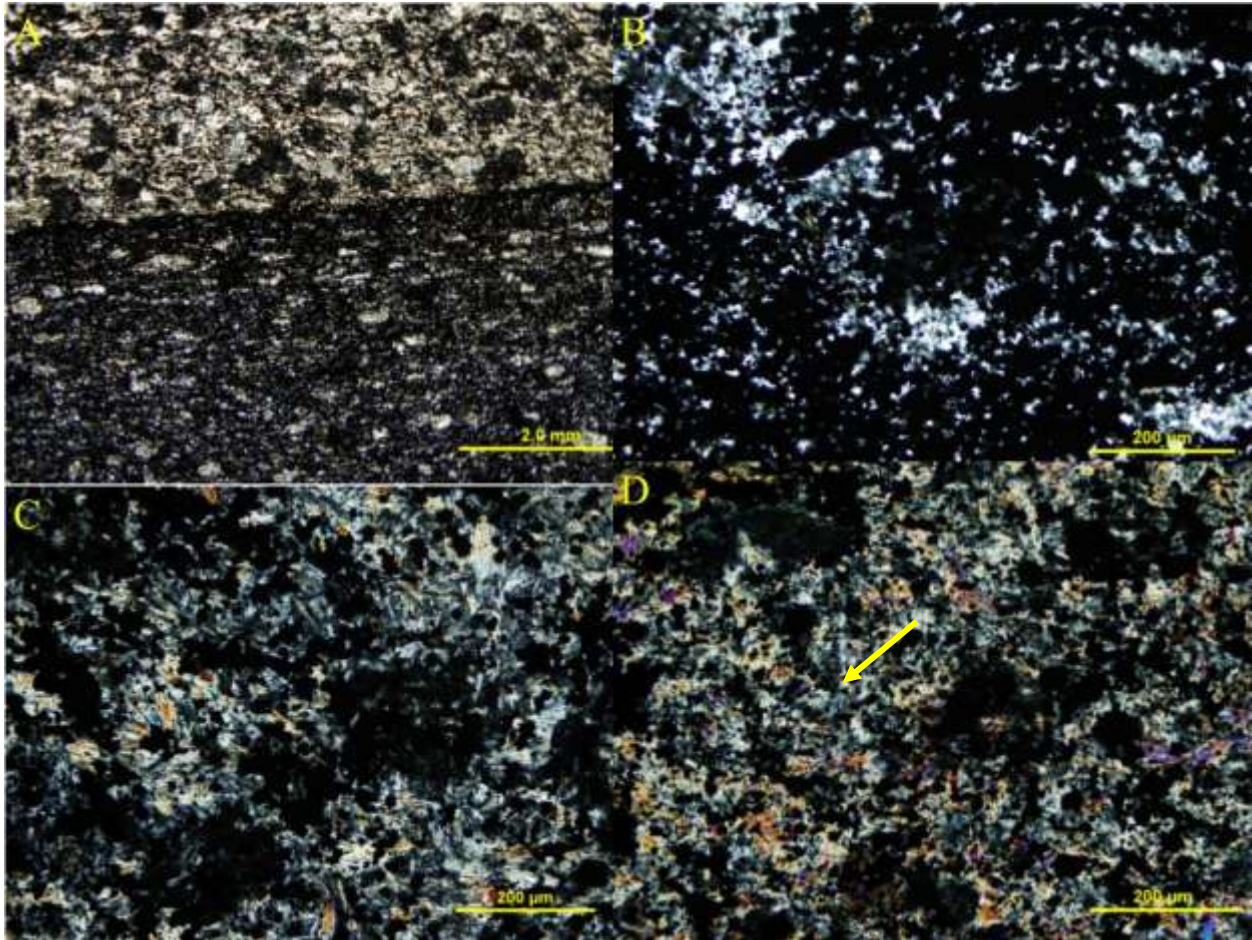
Figure 123: Photomicrographs of slaty iron formation layers in the Mount Whittlesey outcrop. A) Light and dark layers; the dark layers are comprised of opaques with silicate grains throughout the layers. The lighter layers are comprised of silicates with minor amounts of opaque grains. B) Sample 14-CY-02 is showing a close up of a dark layer in the sample. They are composed of a combination of mostly chert and iron silicates. C) The light layers are mostly composed of the greenalites and Fe-rich chlorites mentioned in Pufahl and Fralick (2004). D) The Fe-rich chlorites (yellow arrow) are present in the lighter layer from sample 14-CY-09 near the top of the cycle.

5.3.6.2   Grainstones stratigraphic unit

The grainstones present in the Mount Whittlesey outcrop are both present as small lenses in the slaty iron formation and as medium to large-scale, trough cross-stratified lenses in the upper portion of the cycle (Figure 124A). Sample 14-CY-04 is from the grainstones found in the

small lenses in the parallel laminated slaty iron formation. This sample is composed of very fine to fine grains hosted in a white chert cement. The grains are either comprised of red hematite or magnetite. Near the contact with underlying parallel laminated slaty iron formation beds, there are occasional small rip-ups of the slaty material in the grainstone layers (Figure 124B). In thin section, the grainstones range from rounded to angular grains composed of mosaic cherts. The majority of the grains show some level of coating, which varies from either completely coating the grain to surrounding and defining the edge of the grains. The coating is mostly a combination of both hematite and magnetite with minor silicates presents within the iron oxides. The grains are cemented by coarse-grained mosaic cherts.

Samples 14-CY-05 and 06 were taken from large, trough cross-stratified grainstone lenses. The grainstones from the upper portion of the slaty succession are coarser grained than the grainstones from the lower slaty iron formation (Figure 125). The grains are mostly medium-grained and are more hematite-rich, all of which is hosted in a white chert cement. Thin sections of the samples were taken from both the large and small grainstone lenses present in the upper portion of the Mount Whittlesey outcrop. The samples show that the grainstones are composed of medium to coarse, sub-angular to sub-rounded grains (Figure 125A). The grains are comprised of either; quartz, chert or hematite and are cemented by mosaic cherts cements (Figure 125 B). Minor amounts of magnetite is present within the hematite grains, with some of them being coarse enough to form their own grains. (Figure 125 C and D).

Figure 124: The small grainstone lenses found within the slaty iron formation of the Mount Whittlesey outcrop. A) Repeated small scale grainstone lenses found between the parallel laminated slaty iron formation layers at the base of the stratigraphy. B) Close up of a grainstone lens with small rip-up clast of the slaty iron formation near the contact with the slaty iron formation.
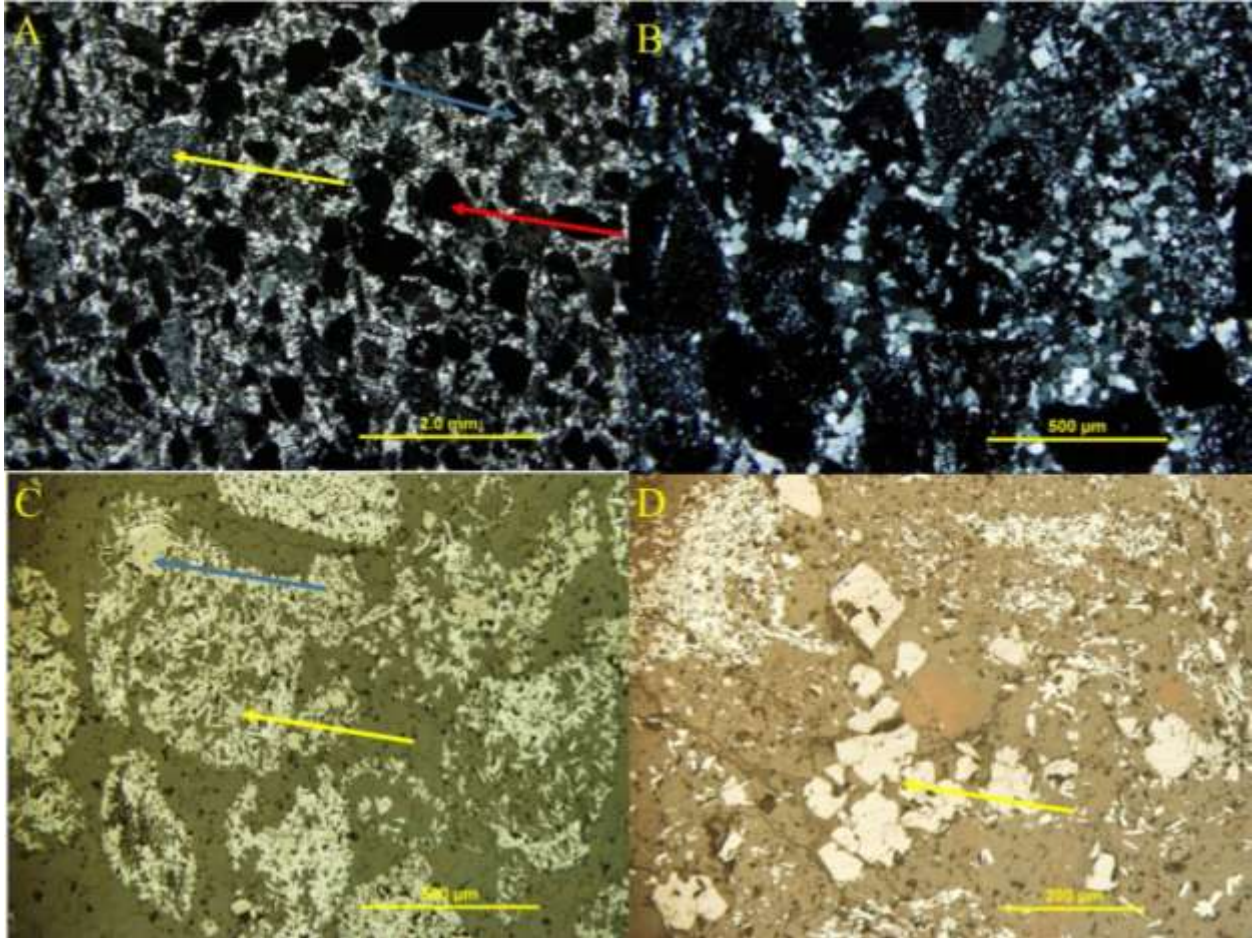
Figure 125: Photomicrographs of samples taken from the small grainstone lenses within the slaty iron formation. A) The grainstone population is composed of rounded to angular chert (yellow arrow), hematite grains (red arrow) and magnetite grains (blue arrow). B) Close up of the grains, showing the cement and grain compositions. The grains show the range of hematite coatings from complete to just rimming the grains. This also shows the coarse-grained mosaic cherts cementing the grains together. C) Reflected light photomicrograph of the recrystallized hematite (yellow arrow) and the magnetite grains (blue arrow). D) Reflected light photomicrograph of a cluster of magntite grains (yellow arrow).

5.3.6.3   *Convolute stratigraphic unit*

The stratigraphy of the outcrop shows that the asymmetrical cycles that make up the Mount Whittlesey outcrop are capped off by a brecciated layer sitting above the thick grainstone layers. There are two identifiable layers of this material present in the Mount Whittlesey outcrop. The two cycles look similar in. They are recognized by the presence of a chaotic layer of broken up pieces of the slaty iron formation and cherty grainstone (Figure 126A). This stratigraphic unit exhibits a distinct change from the sliver grey magnetite-rich slaty iron formation rip-up clasts in the lower portion of the bed to the red hematite replacing the rip-up clasts in the upper portions of the this bed (Figure 126B). The visible clasts present within the convolute stratigraphic unit are rip-up clasts from the slaty iron formation and grainstone lenses. As stated before Nick Beukes and Bruce Simonson (personal communications, 2011) thought there were oncolites and stromatolites present in the contorted layers, which appears to be a possibility (Figure 126 C). Thin section analysis of the samples collected from the convolute stratigraphic unit indicates that the rip up clasts that make up the convolute stratigraphic unit are mostly derived from the slaty and cherty grainstone stratigraphic unit with possible stromatolitic material and are cemented by mosaic chert similar to the cement present in the grainstone lenses (Figure 127A and B). Some of the rip up clasts show periods of lithification in the presence of dehydration cracks filled by the mosaic cherts and quartz crystals forming the cement (Figure 127C). The possible stromatolitic material has chert pods within the layering present within the grains, possible evidence for escaping gas during rotting of the stromatolite (Figure 127D).
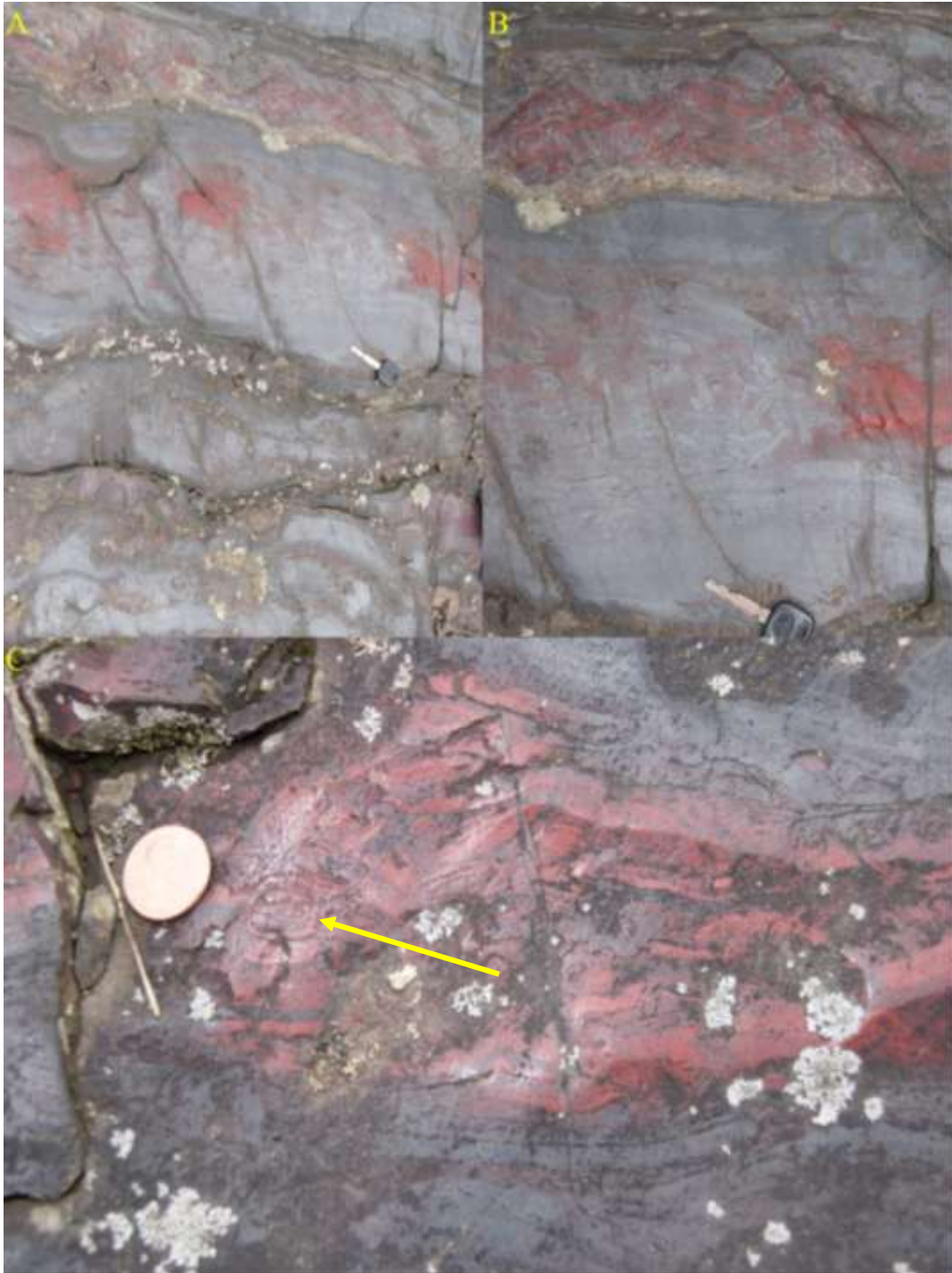
Figure 126: The convoluted layers in the Mount Whittlesey outcrop. A) The lower convoluted bed in contact with the cherty iron formation below. B) Brecciated slaty and cherty clasts that form the convoluted layer. C) A close-up of the brecciated layer showing the rip-up clasts from the slaty iron formation and some other rounded clasts. Possible oncolite present among the rip-up clasts (yellow arrow).
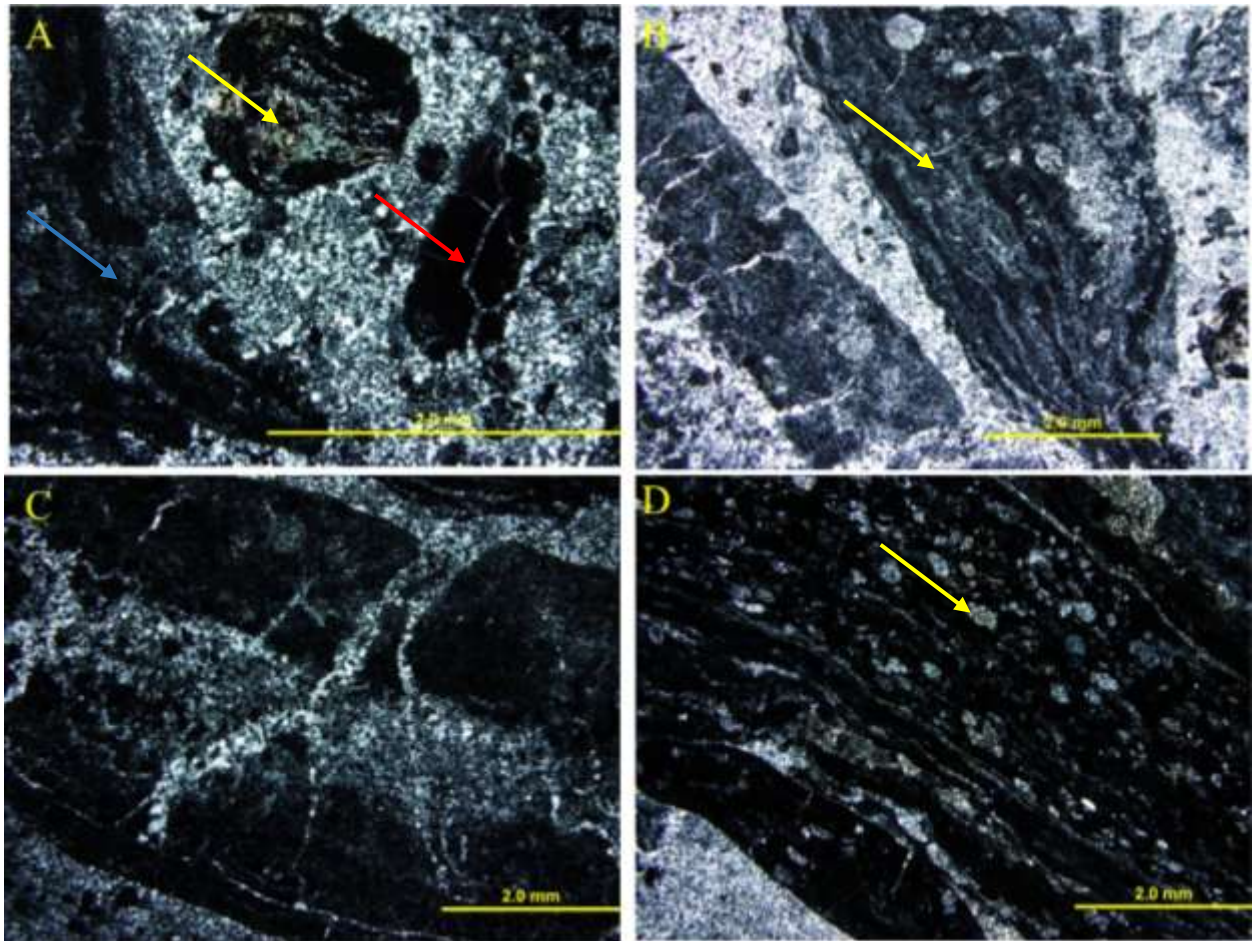
Figure 127: Photomicrographs of a sample of the convolute stratigraphic unit present in Mount Whittlesey, WI. A) The various rip up clasts that make up the convolute stratigraphic unit. Magnetite grain (yellow arrow), Fe-silicate clast (red arrow) and possible stromatolite material (blue arrow). B) Possible stromatolitic material (yellow arrow), sample 14-CY-01. C) Mosaic chert filled dehydration cracks present in a rip up clast. D) Chert pods (yellow arrow) present in the layering of possible stromatoltic material.

6.1.2 Mary Ellen Mine

The Mary Ellen Mine is located near Hibbing Minnesota (54820, 5264380 15U); the mine site is on the western edge of the Biwabik Iron Formation, on the eastern limb of the Virginia horn. The outcrops within the pit at the Mary Ellen Mine are known for the presence of very distinctive stromatolites. The stromatolites crop out in a vertical exposure 1 to 7m high. The base of the outcrop is comprised of a 100cm thick altered and brecciated layer.

5.3.6.4 Altered and Brecciated stratigraphic unit

The altered portion of this outcrop, comprising its base, is composed of alternating layers of light brown iron hydroxides and dark bands of specular hematite. The photos in Figure 128 A and B highlight the appearance of the altered and brecciated stratigraphic unit present at Mary Ellen. Slabs taken of the samples show replacement of the grainstone by brown iron hydroxides (Figure 128C) and thick specular hematite bands (Figure 128D). In thin section it is apparent that the iron hydroxides are replacing the microquartz grainstone and vise versa (Figure 129 A and B). In thin section, the thick layers of hematite are massive with no internal structure such as grains (Figure 129 C and D). The brecciated portion of the basal section overlies the altered zone and is comprised of rip-up clasts within a chert cement. The rip-up clasts range in composition from chert to hematite and range in size from sand grains to pebbles. Also present in the brecciated stratigraphic unit are large rip-up clasts of the stromatolites. Dehydration cracks can be seen forming in both the grains as well as the stromatolite fragments. This altered and brecciated portion of the Mary Ellen mine site shows a lack of finer scale stromatolite preservation due to the formation of iron hydroxides.

Figure 128: Photographs of the altered portion of the altered and brecciated stratigraphic unit at Mary Ellen Mine. A) The altered portion of the Mary Ellen outcrop. B) The altered section beneath the stomatolites showing the alternating bands of light brown iron hydroxides and hematite. C) A cut slab showing the alternating layers of iron hydroxide and hematite. D) Close-up of the hematite layering.
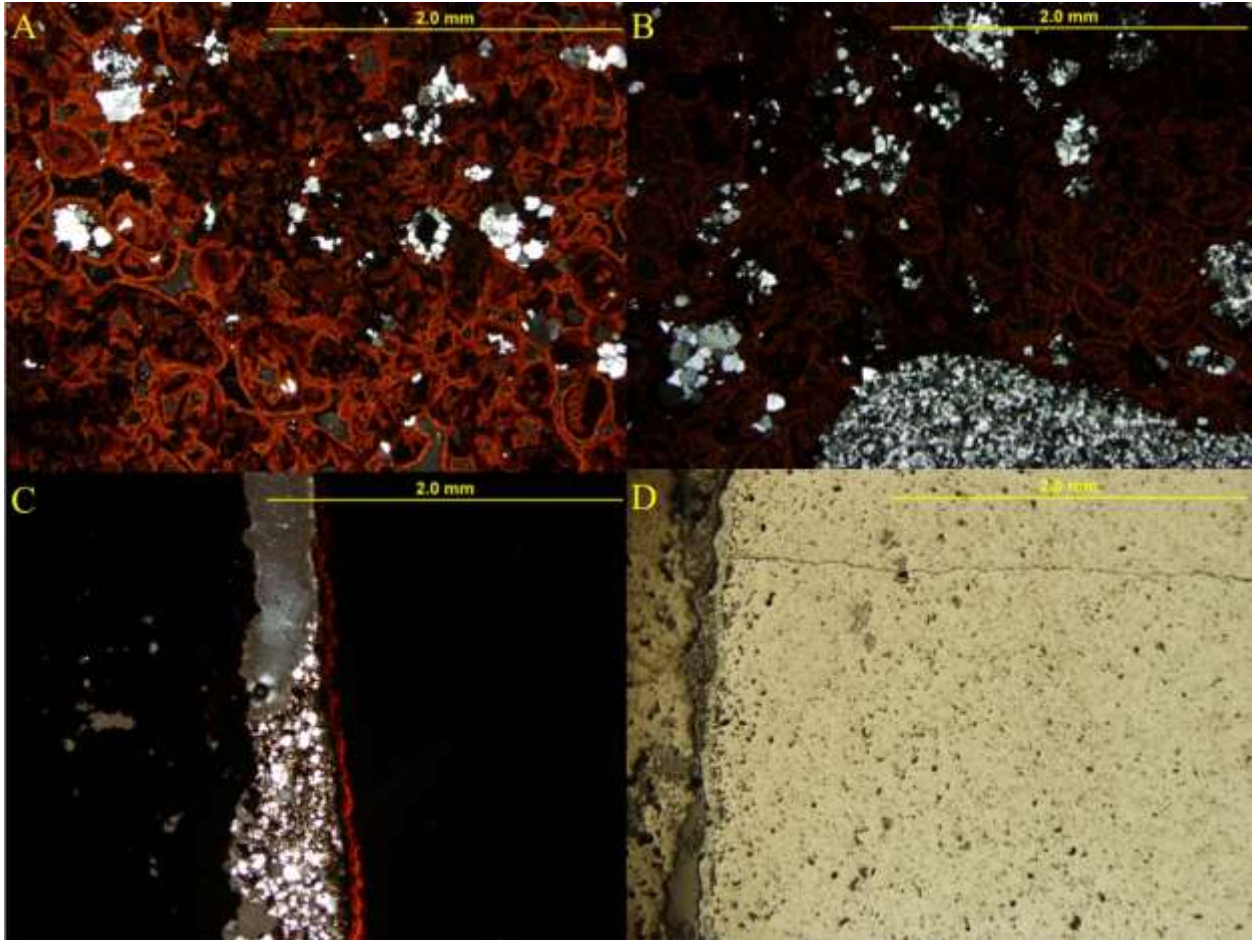
Figure 129: Photomicrographs of the altered and brecciated section form Mary Ellen Mine. A) Iron hydroxides (bright red) replacing microquartz and hematite (dark red) grains. B) Microquartz crystals replacing iron hydroxides. A primary microquartz grain at the bottom of the photomicrograph. C) Microquartz partially filled fractures in the hematite layers. D) Reflected light photomicrograph of the massive hematite showing poorly defined internal grains.

5.3.6.5   *Stromatolite Stratigraphic unit*

Located above the altered and brecciated stratigraphic unit of the Mary Ellen Mine, the

stromatolite stratigraphic unit is comprised of flat lying, columnar and domal stromatolites

(Figure 130A and B). The stromatolites are mostly composed of chert, as well as jasper, and

range in colour from white, to yellow, purple and red (Figure 130C). Thin sections show that the

stromatolites are mostly comprised of fine-grained cherts, with the layering made up of organics

(now carbon), and minor amounts of blocky quartz (Figure 131 A and B). Some of the

stromatolites show varying levels of replacement by hematite. The interspace between the

stromatolite heads are filled by pelloids and ooids. The interstitial granules and ooids are

cemented by microquartz (Figure 131D). The ooids are made up of nuclei of mircroquartz. Some

of the nuclei show replacement by mostly magnetite with minor amounts of hematite. The

concentric layering around the nuclei of the ooids is comprised of hematite. Some of the grains

show dehydration cracks forming in the chert grains (Figure *131*C).

Figure 130: Stromatolites from the Mary Ellen Mine site. A) The stromatolite section above the altered section at Mary Ellen. B) A domal stromatolite in situ at Mary Ellen. C) Varying colours of the Mary Ellen digitate stromatolites. D) Lateral cut showing a top down section of digitate stromatolites, with hematite (specularite) and chert granules between jasper stromatolite heads.
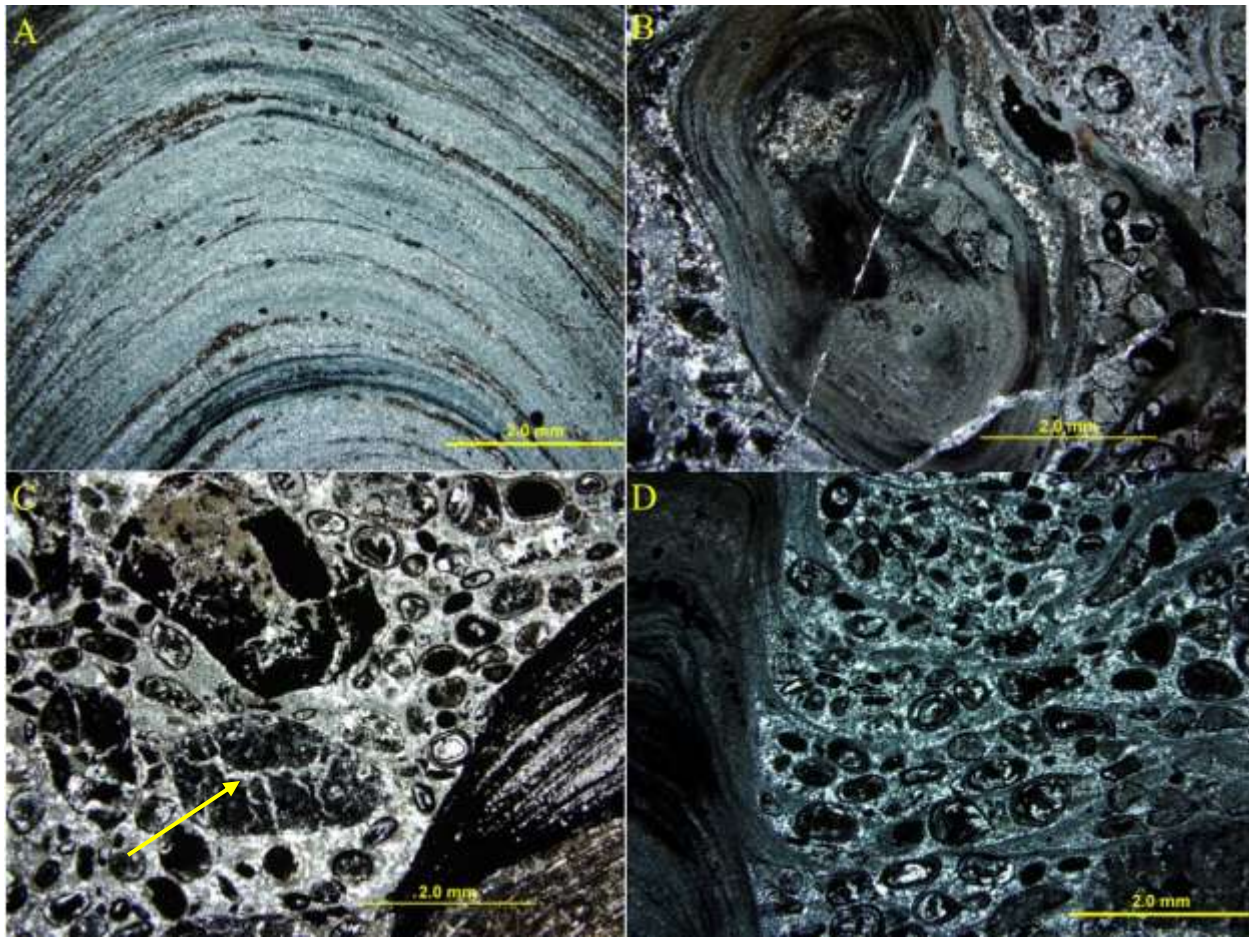
Figure 131: Photomicrographs of the stromatolites from Mary Ellen Mine. A) Columnar stromatolites comprised of microquartz, with the dark layers composed of organic material that is now carbon. B) Lateral view of the columnar stromatolites showing the interspace ooids and grains. C) The ooids and granules filling the interspace inbetween columnar stromatolites. The yellow arrow highlights the dehydration cracks forming in the chert/hematite grains. D) Ooids and coated granules present filling the negative space between columnar stromatolites and lying between connecting chert layering forming bridging lamina of the stromatolites.

6.1.3 *Drill Hole PR-98-1*

This drillhole was cored near Pine Bay and Pidgeon River. The studied zone lies approximately 40m below the Sudbury Impact layer at the top of the Gunflint Formation in this hole. This 210cm coarsening upward cycle represents a new regressive exposure surface present above the middle exposure surface (Figure 132). This area in the drill core is comprised of a series of stratigraphic unit that form a coarsening upward sequence similar to that present at the Mount Whittlesey and Mary Ellen Mine outcrops mentioned previously. The drill core is comprised of stratigraphic unit that are distinct from the Gunflint grainstones that lie above and below the section of core studied in detail. The cycle starts with a mauve grainstone layer similar to the grainstone layers beneath the Mink Mountain and Old School Road outcrops (Figure 132). This stratigraphic unit is sharply overlain by a brecciated grainstone formed by both grainstone clasts and pure chert clasts cemented by large amounts of crystals containing iron, magnesium, calcium and silicon, which is probably ferro-actinolite. The second part of the brecciated stratigraphic unit is comprised of chert-rich grainstone comprised of large grainstone clasts, which appear to be mostly rip-ups from the grainstone layer below. The oncolite stratigraphic unit sharply overlies the brecciated layer. This layer shows medium to large oncolites throughout the majority of the stratigraphic unit. The oncolites are present within a chert grainstone cemented by quartz. The oncolite stratigraphic unit has two oncolite poor layers within the oncolite stratigraphic unit. The oncolite poor areas are comprised of the same cherty grainstone as the rest of the stratigraphic unit. Gradually overlying the oncolite stratigraphic unit is the silicate stratigraphic unit. This stratigraphic unit is comprised of varying levels of replacement of the grainstone by a fine-grained green iron magnesium calcium aluminum silicate mineral, probably ferro-actinolite and fine-grained dolomite. There is a sharp contact with the Gunflint

grainstone at the top of the sequence.

Figure 132: The stratigraphy of the area of interest 40m below the top of the Gunflint in drill hole PR-98-1. This section of the drill core shows the individual layers of the brecciaed and oncolite-bearing section of the core.

5.3.6.6 Grainstone Stratigraphic unit

The grainstone layer present at the bottom of the sequence is a purple grainstone much like the grainstone present beneath the stromatolites at both the Mink Mountain outcrop as well as the boulder taken from the outcrop on the shoulder of Old School Road (Figure 133A). The grainstone stratigraphic unit is a 16 cm thick section. This stratigraphic unit sharply overlies cherty Gunflint grainstone. The section begins as parallel layers of chemical muds, upon which the grainstone was deposited (Figure 133 D). The grainstone layer is made up of predominantly medium-sized rounded chert grains as well as minor amounts of hematite. The grainstone clasts are cemented by a fine-grained white chert cement (Figure 133 C). Portions of the grainstone layer are mottled where the cement has been replaced by a fine grained bown mineral. The top

of the grainstone layer is marked by a layer of mottled rhodochrosite, which is hosted in the grainstone matrix. This layer is comprised of large amounts of rhodochrosite, and iron oxides with minor amounts of sulphides in a thin layer overlying the thicker grainstone layer described above (Figure 133B). The rhodochrosite overlying the thick grainstone layer is comprised of anhedral grains that form a massive discontinuous layer. There is also brecciation and massive replacement of the rhodochrosite by magnetite with some minor amounts of pyrite.

Thin sections of the grainstone layer show two very distinct groupings of the grainstone. The grains that comprise this stratigraphic unit are composed of rounded granules (Figure 134). The first group looks similar to the grainstone from Old School Road and the outcrop behind Mink Mountain (Figure 134A). The grains from this section of the grainstone are composed mostly of mosaic cherts (Figure 134 B). The grains show a range of recrystallization of hematite grains, from completely replacing the chert grains to just coating the edges. The cement holding the grains together is mostly mosaic chert with blocky quartz filling the larger open spaces (Figure 134 C). There are minor amounts of carbonate present throughout the grainstone, and it appears as either replacing the grains or as patches within the cement. The mottled grainstones from this layer, represent a replacement of the grains and cement in this area by a fine-grained brown mineral (Figure 134 D).
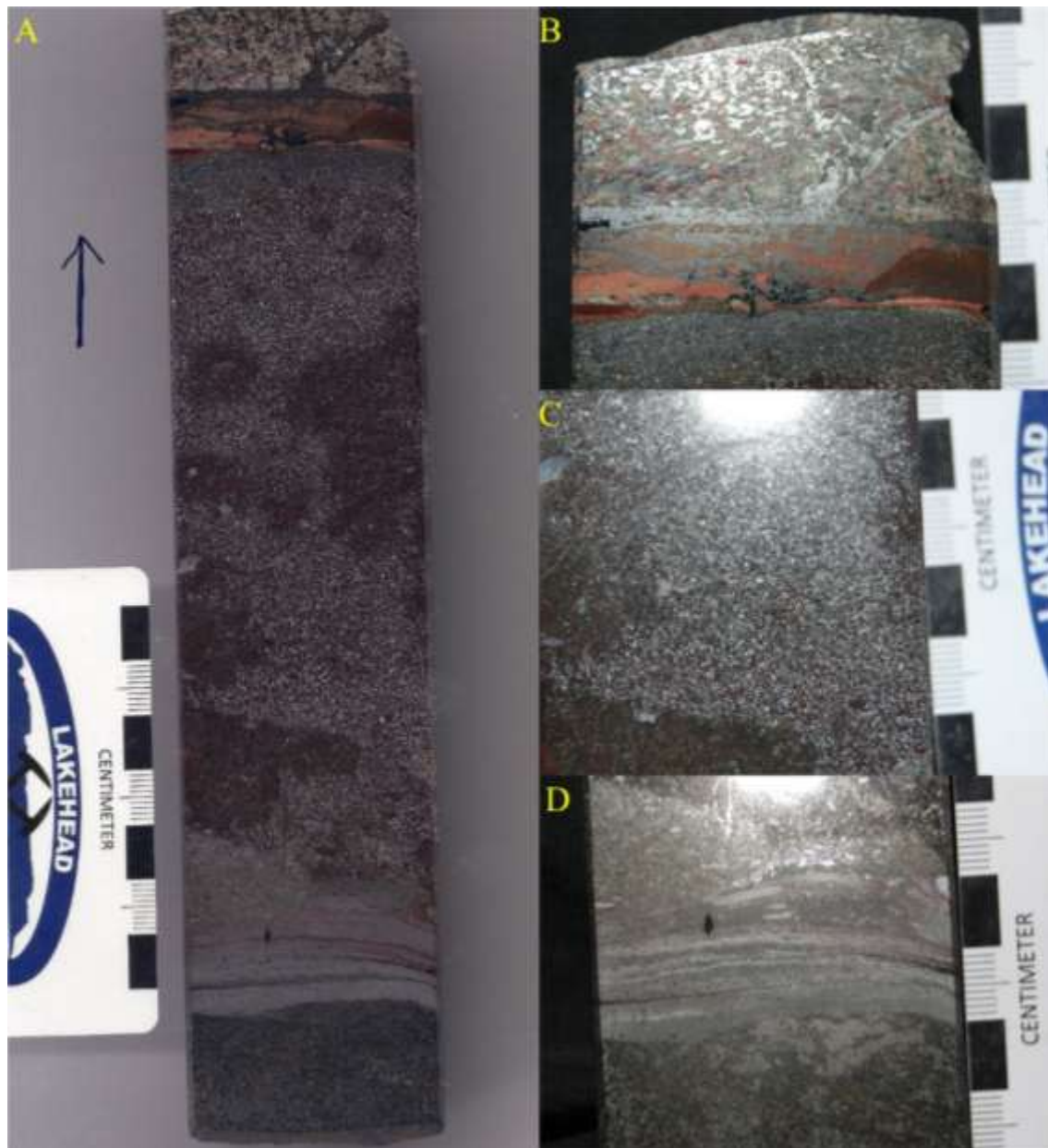
Figure 133: Polished section of the grainstone layer from drill hole PR98-1.A) The entirety of the altered grainstone section. B) The brecciated grainstone and rhodochrosite layer marking the end of the grainstone stratigraphic unit.C) The grainstone stratigraphic unit showing the rounded clasts as well as the mottling. D) The parallel laminated fine-grained hematite and jasper in contact with the slaty iron formation at the base of the grainstone.
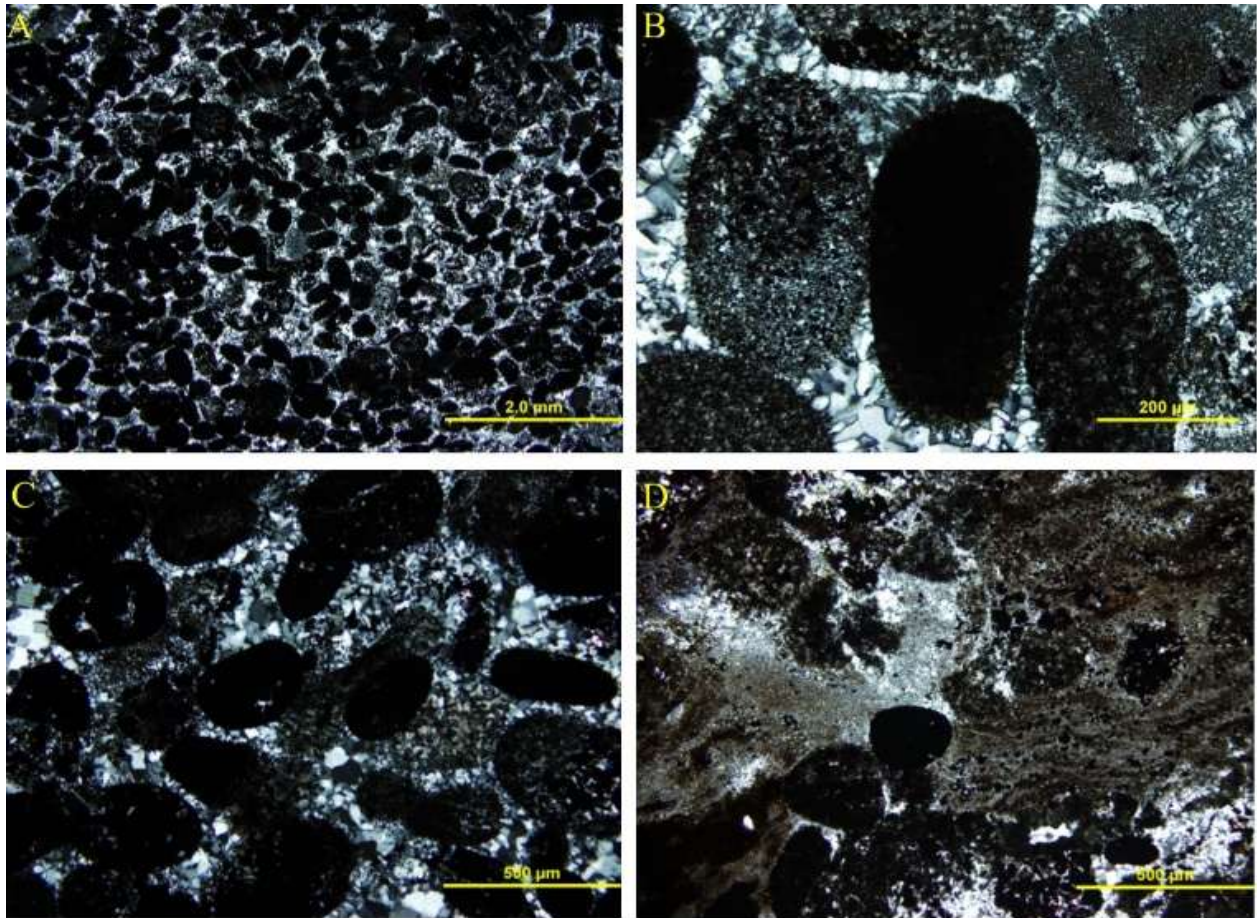
Figure 134: Thin section photomicrographs of the grainstone layer from PR98-1. A) The image shows that the grainstone is comprised of mostly rounded granuals. B) Mosaic chert cement coating the grains and filling the larger voids. C) Hematite grains along with chert grains within the mosaic chert cement. D) The mottled layer from the altered grainstone stratigraphic unit showing the fine-grained brown mineral overprinting the chert cement.

5.3.6.7   Brecciated Stratigraphic unit

The brecciated stratigraphic unit from the drill hole is a 46cm thick layer that sits sharply

over the altered grainstone stratigraphic unit (Figure 135). This stratigraphic unit can be

subdivided into two distinct sections; a red breccia and a white brecciated stratigraphic unit. The

red sub-stratigraphic unit directly overlies the grainstone stratigraphic unit. The clasts of this

brecciated stratigraphic unit are comprised of both pure white chert and jasper grainstone clasts.

Clasts are commonly broken and consitst of medium to coarse grainstone similar to the one at the

base of the brecciated stratigraphic unit. The grainstone clasts are brecciated by magnetite veins with minor replacement by the ferro-actinolite appearing as patches. The clasts are hosted in a matrix of grains and rhodochrosite cement. The second section of the conglomerate is considerably different than the one below. This 18cm thick section sits directly below the oncolite stratigraphic unit and is comprised of clasts ranging from fine grains all the way up to large rip-up clasts. The composition of these clasts are rip-ups of magnetite and cherty grainstones. At the base is a large 7cm thick clast composed of coarse grains. These clasts are all cemented by a fine-grained pure white chert cement. Three veins of purple agate can be seen in the top of the section of this stratigraphic unit. Open voids within the cement are filled by white cherts.

Thin sections of samples (Figure 136) taken from the brecciated stratigraphic unit show that the grainstone clasts are comprised of rounded non-oolitic grains comprised of mosaic cherts. The grains are cemented by spherulitic fans of chalcedony. The clasts that appear as pure chert are comprised of recrystallized chert grainstone, in which the chert in the rounded granules and rounded grains was completely recrystallized before the brecciation of the clasts. Some of the grains have been replaced by either hematite or fine-grained silicates. The open spaces between the clasts and the matrix are filled by the chalcedony fans.
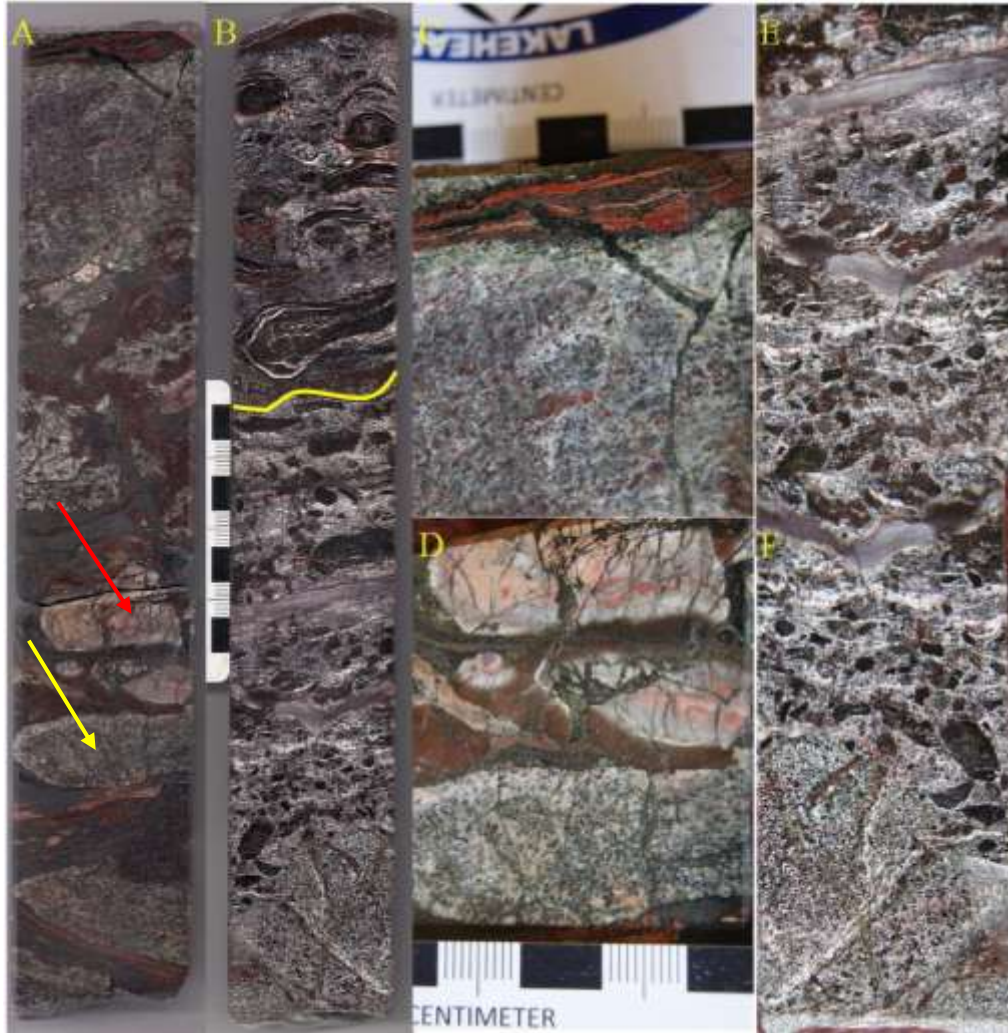
Figure 135: Images of the brecciated stratigraphic unit from PR98-1. A) The brecciated layer with grainstone clast (yellow arrow) and chert clast (red arrow). B) The white chert brecciated stratigraphic unit. The contact with the oncolite layer is highlighted in yellow. C) The brecciated grainstone with hematite filling the fractures. D) The two different clasts present near the base of the stratigraphic unit. E and F) The white grainstone sub-faices of the brecciated grainstone stratigraphic unit showing the large chert cemented grainstone clasts and three agate veins. Samples from here include PR98-4 and P98-5.
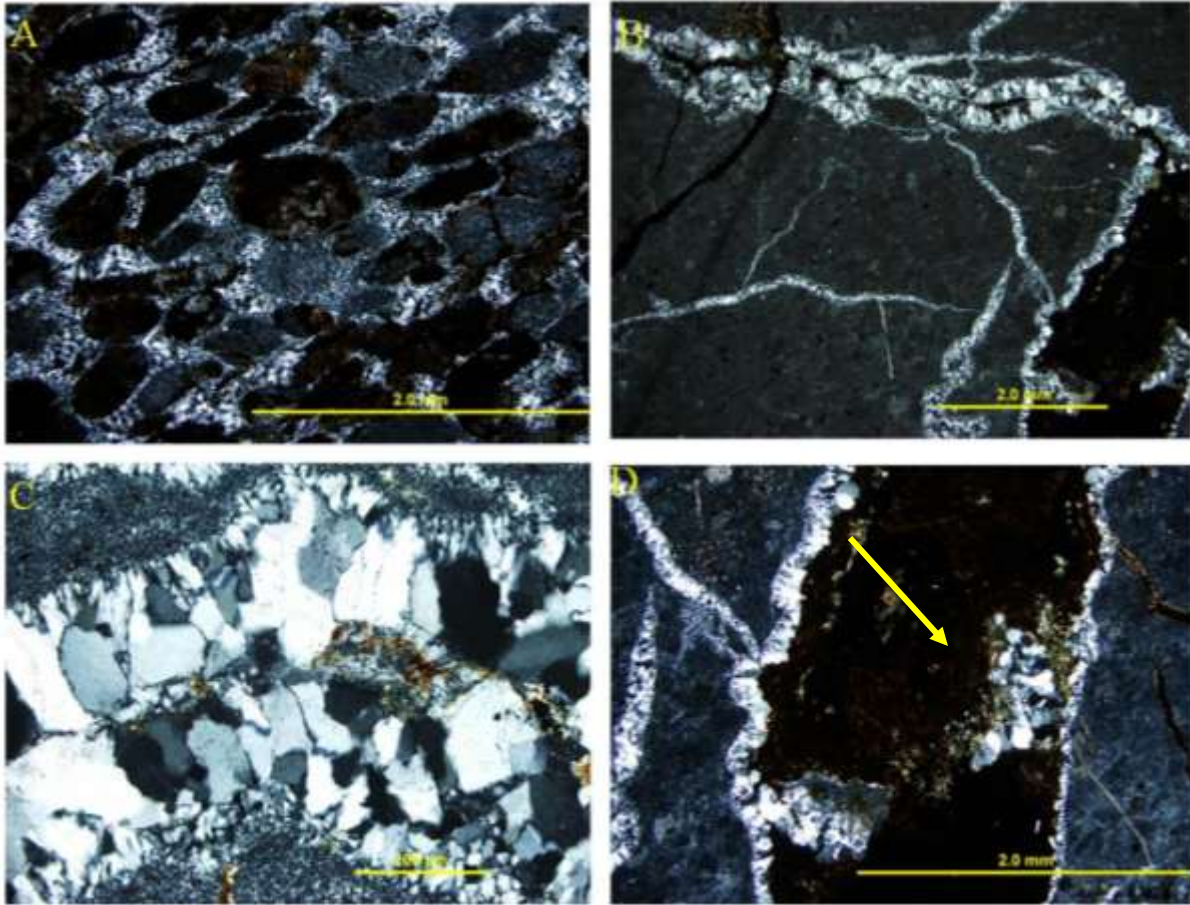
Figure 136: Photomicrographs of the brecciated grainstones in PR98-1. A) Standard grainstone from the underlying cherty grainstone. B) The brecciated recrystallized chert grainstone from the top grainstone layer. Fracturs in the grainstone are filled by radiating chalcedony fans and blocky quartz. C) Blocky quartz is cementing what were open fractures in the grainstone. D) The ferroactinolite (yellow arrow) is filling some open spaces in the brecciated chert.

5.3.6.8   Oncolite Stratigraphic unit

The oncolite-bearing section present within drill core PR98-1 is the most distinct lithostratigraphic unit in the sequence (Figure 137). This stratigraphic unit shows that there are three distinct oncolite stratigraphic unit present. The first oncolite-rich substratigraphic unit is present directly above the brecciated grainstone and is comprised of the largest oncolites (Figure 137A). The second oncolite-rich substratigraphic unit is present directly above a 4cm thick oncolite poor layer (Figure 137B). The two oncolite bearing substratigraphic unit are of similar

composition in that the chert and hematite oncolites were formed within a medium to coarse chert grainstone, with rip-up clasts and chert veins present. The green iron- silicate ferroactinolite can be seen replacing the grainstone surrounding the oncolites present in the top of the second oncolite substratigraphic unit. Above these two substratigraphic unit there is another oncolite-absent substratigraphic unit comprised of a coarsening upward sequence which changes from medium to coarse chert grainstone to magnetite- rich granules at the top (Figure 137C). The top of the oncolite stratigraphic unit is composed of the last oncolite-rich substratigraphic unit. This layer contains both oncolites and grainstone rip up-clasts throughout the medium to coarse grainstone and chert cement (Figure 137D). The top of the oncolite stratigraphic unit shows replacement by ferroactinolite marking the start of the gradational change into the green ferroactinolite stratigraphic unit above (Figure 137E).

The oncolites formed around a nucleus composed of chert grainstone (Figure 138A). The layering surrounding the nuclei of the oncolites are discontinuous and alternate in composition between hematite and white chert, with the thickest layers within most of the oncolites composed of hematite (Figure 138C). The majority of the oncolites have irregular layering surrounding the nuclei. The irregularity is caused by the incomplete formation of the layers. Dehydration cracks, formed perpendicular to the layering of the oncolites, can be seen in both the oncolites and the rip-up clast. The oncolites and rip-up clasts have fine- to coarse-grained, rounded chert grains forming their matrix. The grains are all cemented within a fine-grained white chert cement (Figure 138E). Some of the nuclei show replacement by fine-grained green iron-calcium-aluminum silicates (ferroactinolite). The veins and open spaces that can be seen in this section are composed of two different compositions of crystals with varying sizes. The larger veins are

mostly filled with translucent quartz with some minor amounts of the white chert cement and jasper, whereas the smaller, thinner veins are filled with mostly translucent quartz.

Petrographically, the oncolites are composed of a nucleus of mosaic chert, with minor amounts of blocky quartz within alternating layers of hematite and chert (Figure 138B). The chert layers are comprised of a combination of mosaic chert, blocky quartz, and chalcedony fans. Mosaic chert grains can be seen within the blocky quartz. The hematite layers are submillimeter to one millimeter thick and discontinuous around the nucleus (Figure 138D). There are replacement patches of calcite as well as ferro-actinolite. The grains that form the matrix surrounding the oncolites are comprised of rounded mosaic chert grains, the majority of them show little to no coating of the grains (Figure 138E). The grains forming the matrix between the oncolites are cemented by blocky quartz cement. Coatings on grains mostly surround one grain, but may also surround clusters of grains (Figure *138*F). Replacement patches of calcite can be seen both in the grains and the cement.

The oncolites are not continuous throughout the section. There are two layers in which there are few to no oncolites present. The first section is found 15cm above the contact with the brecciated stratigraphic unit. This 4 cm thick layer is comprised of rip-up clasts derived from the lower onocolties. The layer above the rip-up clasts is comprised of grainstone similar to that of the matrix surrounding the lower oncolites. White chert-filled fractures run parallel to the layering of the drill core (Figure 139A). This oncolite-free area is terminated by a chert and quartz filled fracture. The second area void of oncolites is found 12 cm above the previous one. This layer differs from the other oncolite poor layer. It is comprised of four distinct units. The first unit is a layer of magnetite and rhodochrosite that appears to be replacing a grainstone unit with onoclites (Figure 139B). This layer is capped off by a thin carbonate and magnetite layer.

The next layer is made up of a grainstone unit similar to the matrix of the oncolite layer; the same medium to coarse chert grains hosted in white chert cement. The fourth distinctive layer is made up of a thick layer that is comprised of a breccia of white chert and jasper clasts and a thin magnetite layer in the middle of the unit (Figure 139C). The top of the oncolite-bearing area is marked by the redeposittion of large oncolites and rip up clasts.

Figure 137: The oncolite stratigraphic unit from the PR98-1 drill hole. A) The bottom of the oncolite stratigraphic unit showing the largest oncolite (yellow) present directly above the brecciated stratigraphic unit. B) The next layer of the oncolite stratigraphic unit, showing the first of the oncolite poor layers (yellow arrows). C) The second and larger non-oncolitic layer. D) The re-emergence of oncolite deposition E) The top of the oncolite layer showing the appearance of the massive green ferroactinolite layer. Samples from here are PR98-6, PR98-7, PR98-10, PR98-11. The drill core has a diameter of 4.6 cm.
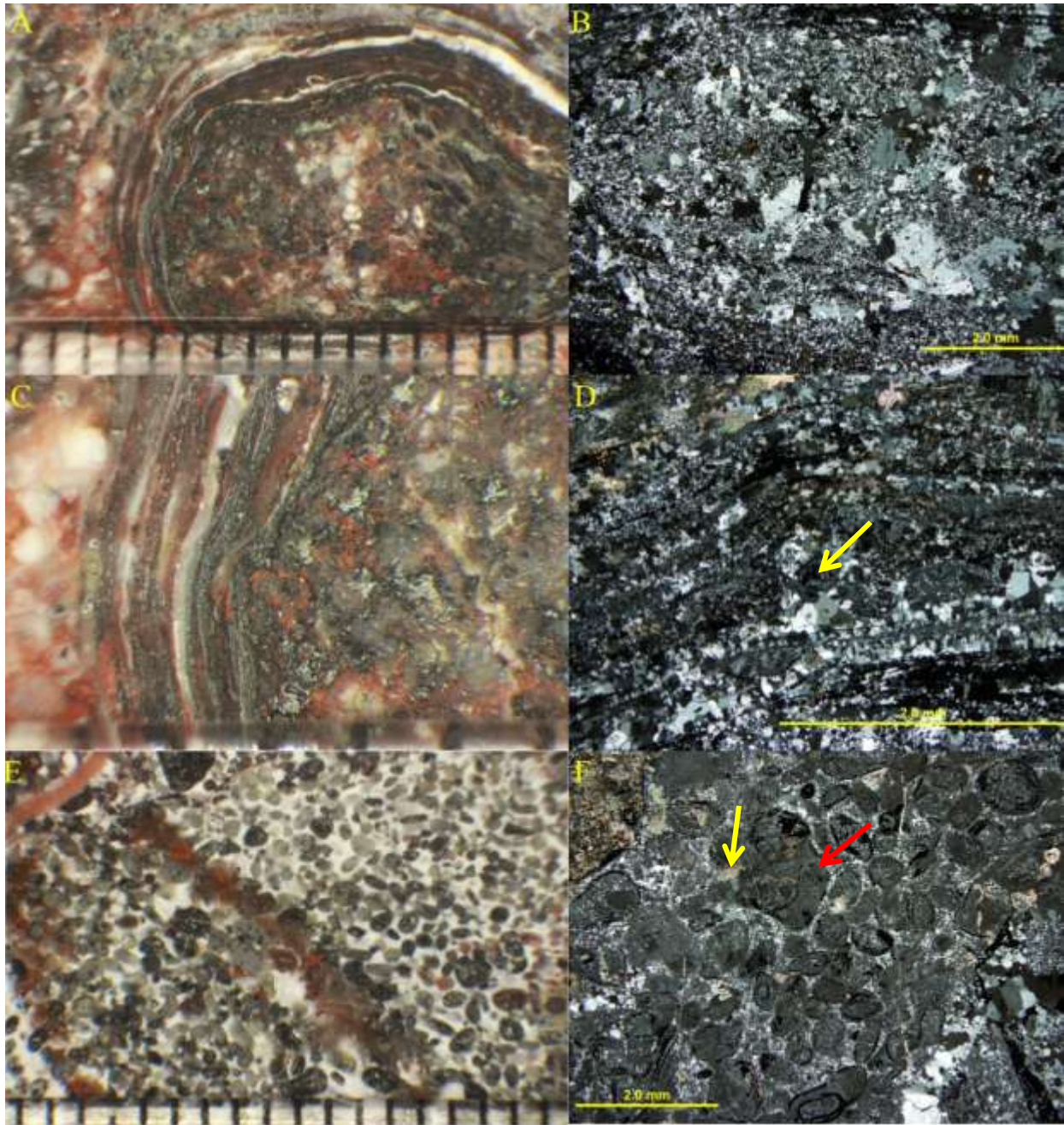
Figure 138: Binocular and thin section photomicrographs of the oncolite layer from drill hole PR98-1. A) Binocular photomicrograph of an onocolite showing the nucleus along with layering around the nucleus. B) Photomicrograph of the chert nucleus. C) The layering of the oncolite showing discontinuous hematite, magnetite, and quartz layers. D) Photomicrograph of the layering of an oncolite, showing the discontinuity of hematite and magnetite layers with blocky quartz forming the layers between them. Mosaic chert grains (arrow) can be seen within the blocky quartz layering. E) Chert grainstone from between the oncolites. F) Non-oolitic chert grains of the grainstone to the right.

Figure 139: Photographs of the non-oolitic layer present in the oolitic section of the drill core. A) The lower oncolite-poor grainstone layer featuring the horizontal chert filled fractures. B) The magnetite layer at the bottom of the second oncolite-poor sub-stratigraphic unit of the oncolite stratigraphic unit. C) The chert vein between the grainstones of the upper oncolite-poor sub-stratigraphic unit. The PR98-1 drill cores diameter is 4.6cm

5.3.6.9   Green silicate stratigraphic unit

This stratigraphic unit is 70cm thick and sits directly above the oncolite stratigraphic unit. This stratigraphic unit shows the gradational replacement of the medium to coarse grainstone by a fine-grained green mineral. This mineral has been identified by XRD as ferroactinolite. This stratigraphic unit is made up of three distinct substratigraphic unit all of which have the same green mineral grading up through the stratigraphic unit (Figure 140). The lowest substratigraphic unit is comprised of the same medium to coarse grainstone that makes up the rest of this drill core section. The substratigraphic unit has quartz filled fractures all showing the replacement by

the green silicates (Figure 140A). The second substratigraphic unit shows the increasing replacement of the grainstone as well as a distinct fine-grained calcite layer at the top of the substratigraphic unit (Figure 140B); the distinct contact between the calcite and the ferroactinolite is highlighted in yellow in the photo. The top of this stratigraphic unit shows the re-emergence of the ferroactinolite, before the grainstone reappears at the top of the stratigraphic unit (Figure 140C).

Petrographically, the only unique portion of this stratigraphic unit is the calcite and ferroactinolite layer found in the middle of the stratigraphic unit (Figure 141) Figure 142 contains photomicrographs of a thin section of sample PR98-16. These photos show that the ferroactinolite is not just replacing the grainstone (Figure 142A). The grainstones are replaced by large anhedral calcite grains (Figure 142B), which are then replaced by ferroactinolite crystal fans (Figure 142C and D).

Figure 140: Images of the green brecciated layer from the drill core PR98-1.A) The start of the stratigraphic unit comprised of mostly grainstone with quartz blobs in which the ferroactinolite is present at the bottom of each blob. B) The contact with the fine grained calcite and ferroactinolite. C) Brecciation of the grainstones. Medium to coarse grainstone is fractured by quartz filled veins. Drill core geochemistry samples from here are PR98-12, PR98-13, PR98-14, PR98-15, PR98-16, and PR98-17. PR98-1 drill core has a diameter of 4.6cm.
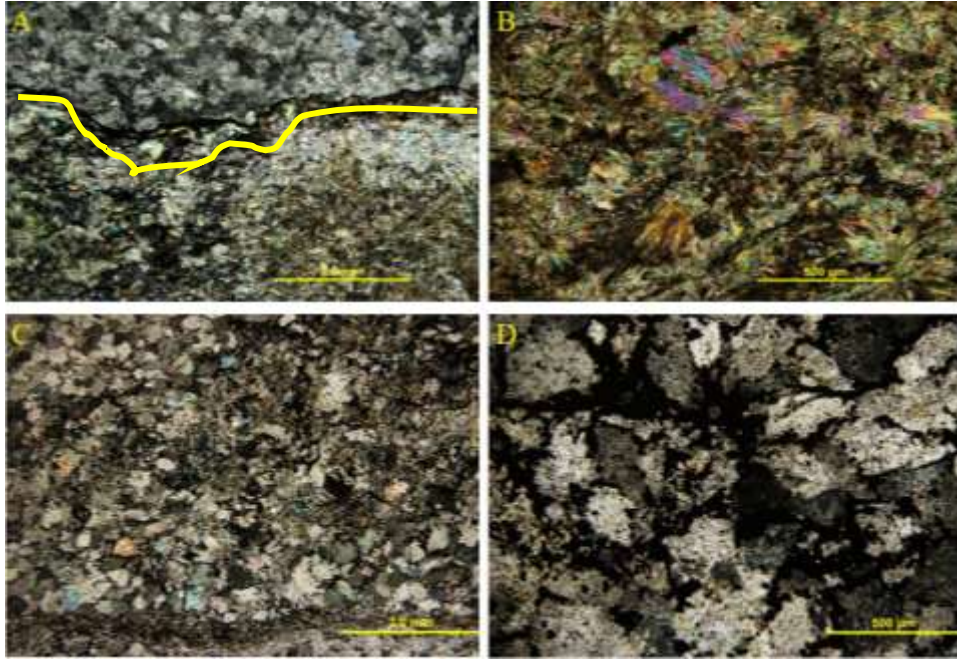
Figure 141: Photomicrographs from sample PR98-15. A) The contact between the fine-grained green mineral and the calcite. B) Crystal fans of ferroactinolite below the contact in A. C) Calcite grains above the ferroactinolite. D) Magnetite forming around the grain boundaries and replacing the calcite.
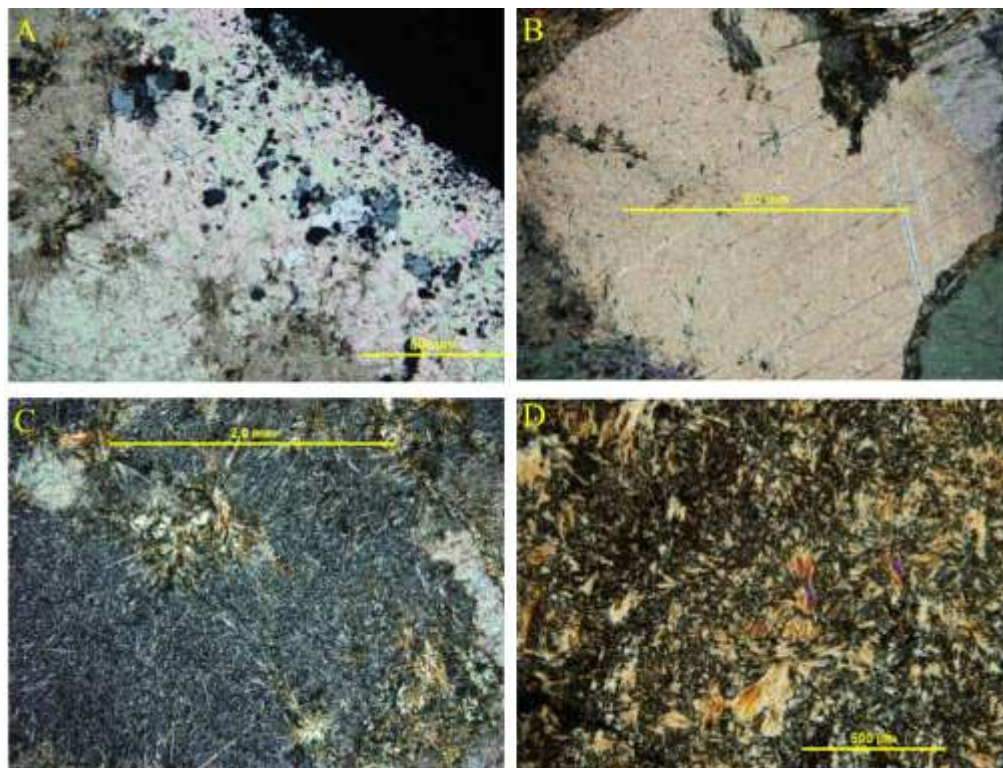
Figure 142: Photomicrographs from sample PR98-16 A) calcite replacing quartz grainstone. B) Large calcite grain. C) The ferroactinolite crystals overprinting calcite grains. D) Close up of ferroactinolite fans.

5.3.6.10 Cherty grainstone stratigraphic unit

The top of the sequence is composed of a cherty grainstone layer representative of the Gunflint grainstone. This stratigraphic unit marks the return to deposition of normal Gunflint above the PR98-1 brecciated-oncolite sequence. The stratigraphic unit is comprised of a 17 cm thick layer of slaty iron formation composed of fine-grained magnetite and chert clasts present within the magnetite. The rest of this stratigraphic unit, is made up of chert grainstone representative of typical cherty Gunflint grainstone (Figure 143).

Figure 143: The grainstone section that caps off the PR98-1 sequence. Sample PR98-23 came from this layer. The PR98-1 drill core has a diameter of 4.6 cm

6.2 WHOLE ROCK GEOCHEMISTRY

6.2.1 *Mount Whittlesey*

Fourteen samples were collected from the Mount Whittlesey outcrop. The samples were analysed at Lakehead University for major oxides and trace element concentrations. The samples selected for analysis are listed with a brief description of the sample in (Table 11).

Table 11: A brief description of the samples selected from Mount Whittlesey for analysis

Sample Number	Description	
14-CY-14	Incomplete cycle convoluted layer	
14-CY-13	Top of the convoluted layer	
14-CY-12	Grainstone from above the convoluted layer	
14-CY-11	Above convoluted layer	
14-CY-10	Upper convoluted layer (Upper convoluted layer)	
14-CY-09	Slaty layer	Up Section
14-CY-08	Slaty layer	
14-CY-07	Cherty layer	
14-CY-06	Cherty layer	
14-CY-05	Cherty layer	
14-CY-04	Cherty layer	
14-CY-03	Slaty layer	
14-CY-02	Slaty layer	
14-CY-01	(Lowest Cycle) Incomplete cycle's convoluted layer	
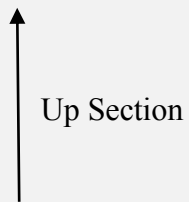
Figure 144 contains the plots of the redox sensitive elements Fe_2O_3, MnO, V and U plotted against the siliciclastic component represented by Al_2O_3. Figure 144A, the plot of Fe_2O_3 vs. Al_2O_3, shows a distinct positive trend forming between the two oxides. The plot seen in Figure 144B is of MnO vs. Al_2O_3, showing no trend forming between the two oxides. Notice the

large amount of MnO in some of the samples. The V vs. Al_2O_3 plot shows a similar positive

trend developing between the two elements (Figure 144C). Figure 144D is of U vs. Al_2O_3; this

plot shows a possible positive trend present between the oxide and element.
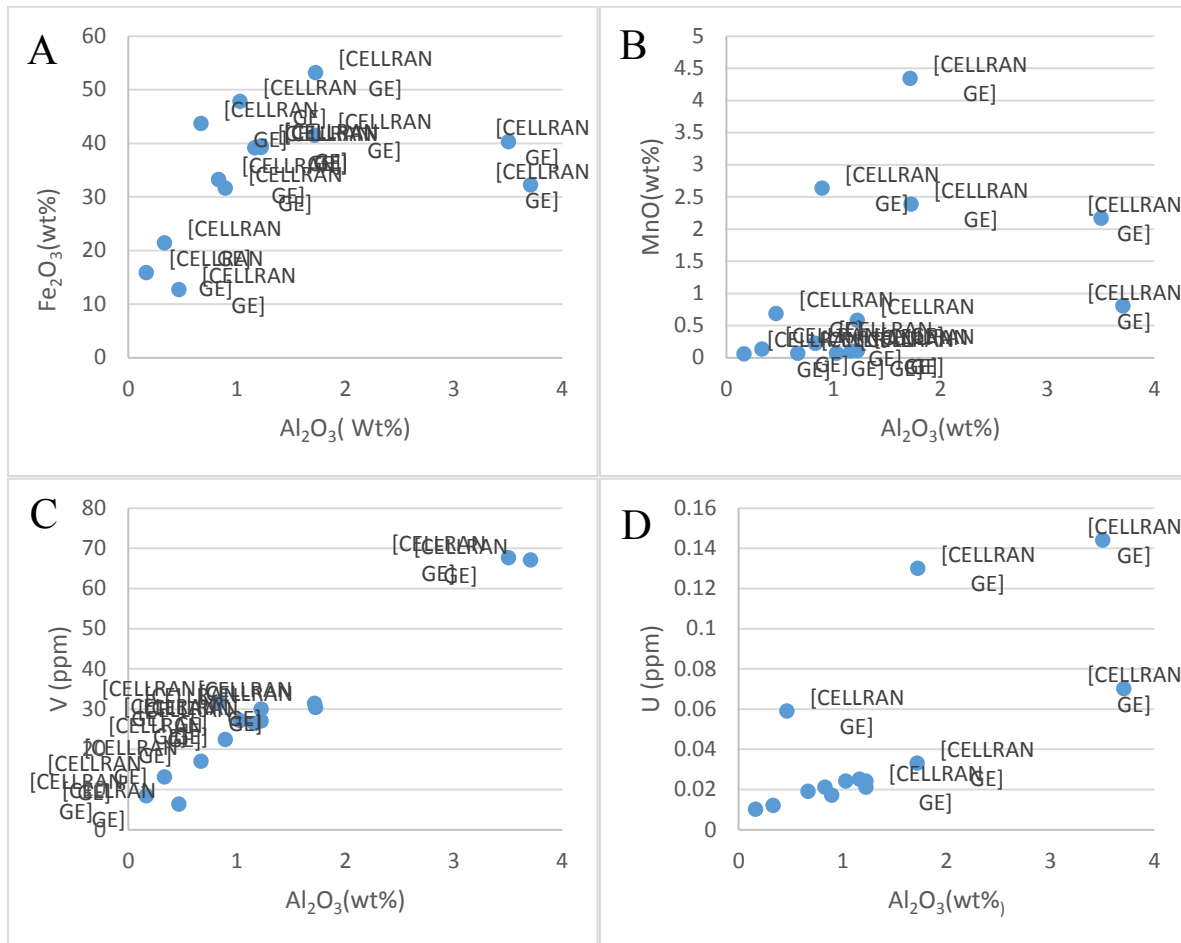
Figure 144: Redox sensitive oxides and elements vs. siliciclastic component of the sample represented by Al_2O_3. A) Fe_2O_3 vs. Al_2O_3 shows a possible positive trend forming between the two oxides. B) MnO vs. Al_2O_3 showing no trend forming between the two oxides. C) A definite positive trend can be seen in V vs. Al_2O_3. D) U vs. Al_2O_3 showing a possible positive trend forming between the two.

When the redox sensitive oxides and elements are plotted against each other, a positive

trend is present in the plot of Fe_2O_3 vs. V (Figure 145B). While there are no visible trends

present in the plots of Fe_2O_3 vs. MnO and MnO vs. V (Figure 145A and C).
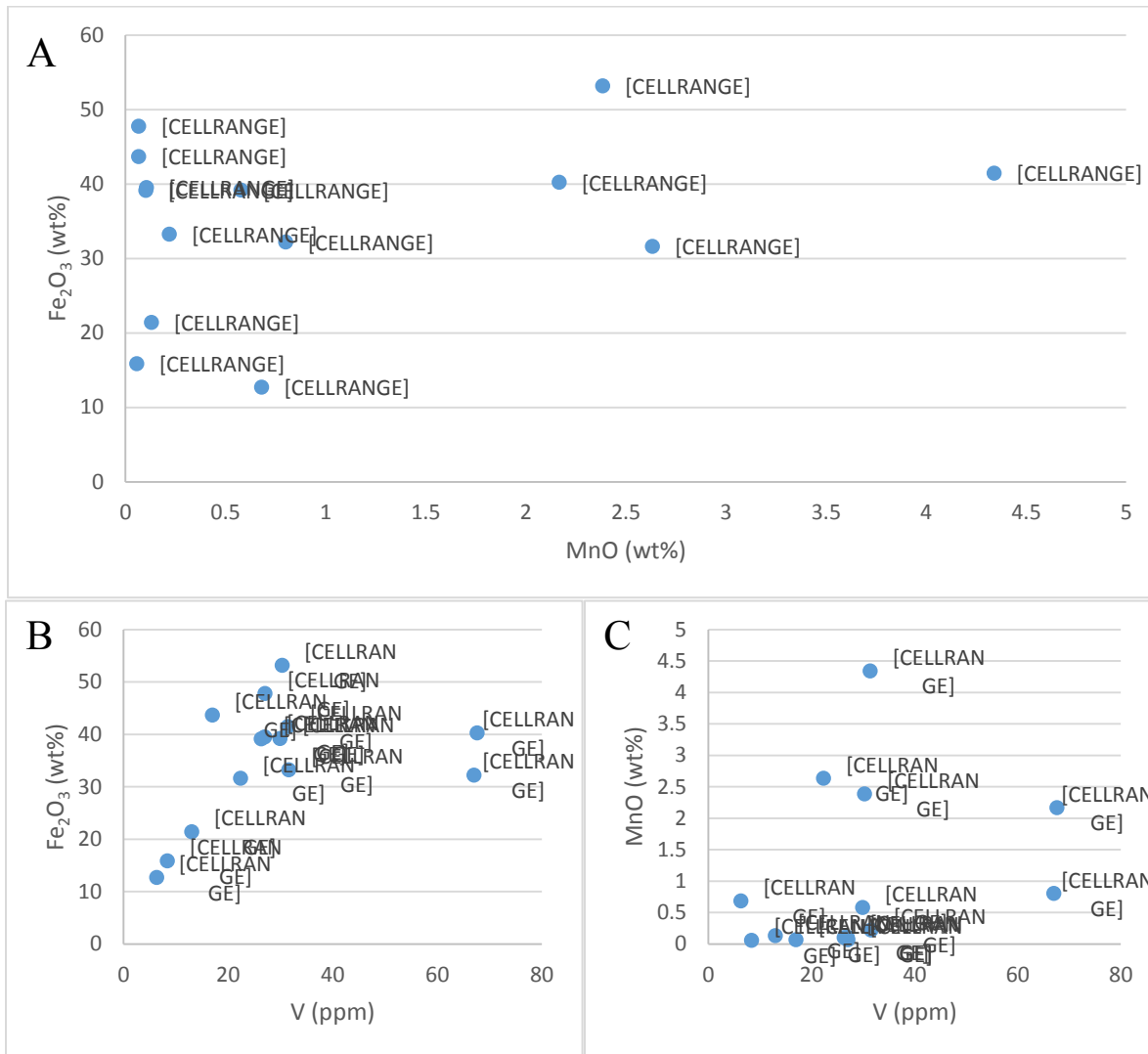
Figure 145: Redox sensitive elements plotted against each other. A) Fe_2O_3 vs. MnO showing no trend forming between the two samples. Some samples are very enriched in MnO. B) A positive trend forming in the plot of Fe_2O_3 vs. V. C) No trend seen in the plot of MnO vs. V.

The minor redox sensitive elements Cr, U, and Mo, are plotted against V and Cr. The plots of Cr vs. V and U vs. V show a possible positive trend forming between these redox sensitive elements (Figure 146A and B). Whereas, the plot of Mo vs. V shows no trend (Figure 146C). The fourth plot is of U vs. Cr; this plot shows a possible positive trend forming between the two redox sensitive elements (Figure 146D).
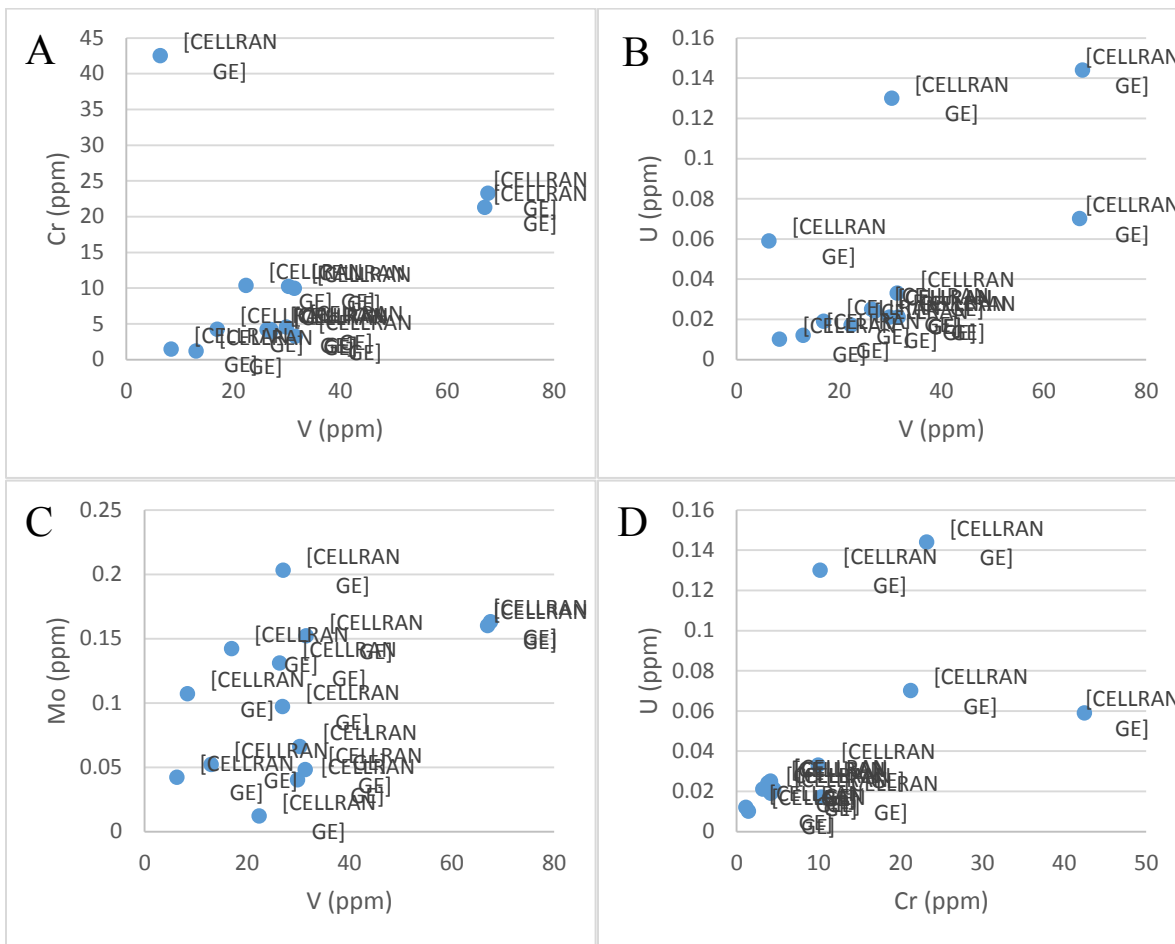
Figure 146: Redox sensitive element plots. A) A positive trend is visible in the plot of Cr vs. V. B) Possible trend forming in the plot of U vs. V. C) Mo vs. V shows no trend between the two redox sensitive elements. D) The plot of U vs. Cr shows a possible trend between the two.

6.2.2 Mary Ellen Mine

Nine samples were taken from the Mary Ellen Mine site for geochemistry. Samples ME-15 and ME-16 came from the altered grainstone underlying the breccia. Samples ME-5, ME-6 and ME-7 are from the breccia in contact with the stromatolites and samples ME-1, ME-2B, ME-3 and ME-4 are from the stromatolites. Sample numbers and a description of the samples can be seen in Table *12*.

Table 12: Sample number and description for the samples collected from the Mary Ellen mine.

Sample	Description
ME-1	Red digitate stromatolite
ME-2B	Digitate stromatolites
ME-3	Collection of stromatolites
ME-4	Collection of stromatolites
ME-5	Stromatolite
ME-6	Brecciated layer
ME-7	Brecciated layer
ME-15	Weathered layer
ME-16	Weathered layer

Up section

The first group of plots are of redox sensitive elements plotted against the siliciclastic component of the system represented by Al_2O_3 (Figure 147). Figure 147 A shows the Fe_2O_3 values plotted against the Al_2O_3 values. This plot shows no trend between the two oxides. The plot of Al_2O_3 vs. MnO shows a similar scatter of points to that found in the Fe_2O_3 plot (Figure 147 B). The highest MnO value is from the stromatolites. The plot of V vs. Al_2O_3 (Figure 147 C), shows that there is a very distinct positive trend forming between the two elements. The last plot is of U vs. Al_2O_3, which shows no distinct pattern forming between the two components (Figure 147 D).

Figure 148 shows the redox sensitive oxides and elements plotted against each other. The first plot (A) of Fe_2O_3 vs. MnO, shows no trend forming between the two oxides. The next plots are of Fe2O3 (B), and MnO(C) values plotted against V. Both of theses show no trend.
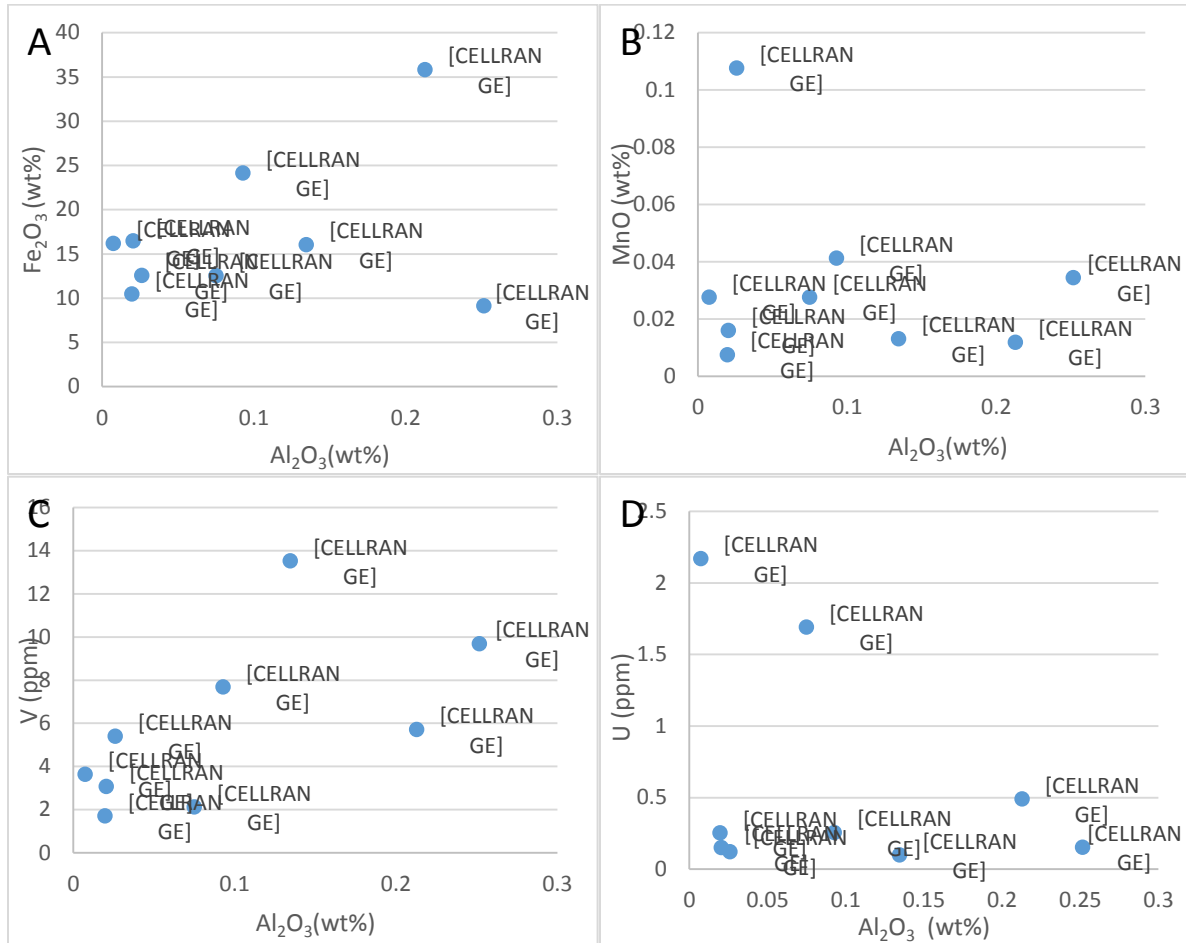
Figure 147: The Al_2O_3 vs. redox proxies. A) Fe_2O_3 vs. Al_2O_3 plot with a possible, very weak to non-existant trend forming between the two oxides. B) No trend is visible in the plot of MnO vs. Al_2O_3. C) The plot of the V vs. Al_2O_3; this plot shows a distinctive positive trend forming between the V and Al_2O_3. D) No trend forming between the U and Al_2O_3.
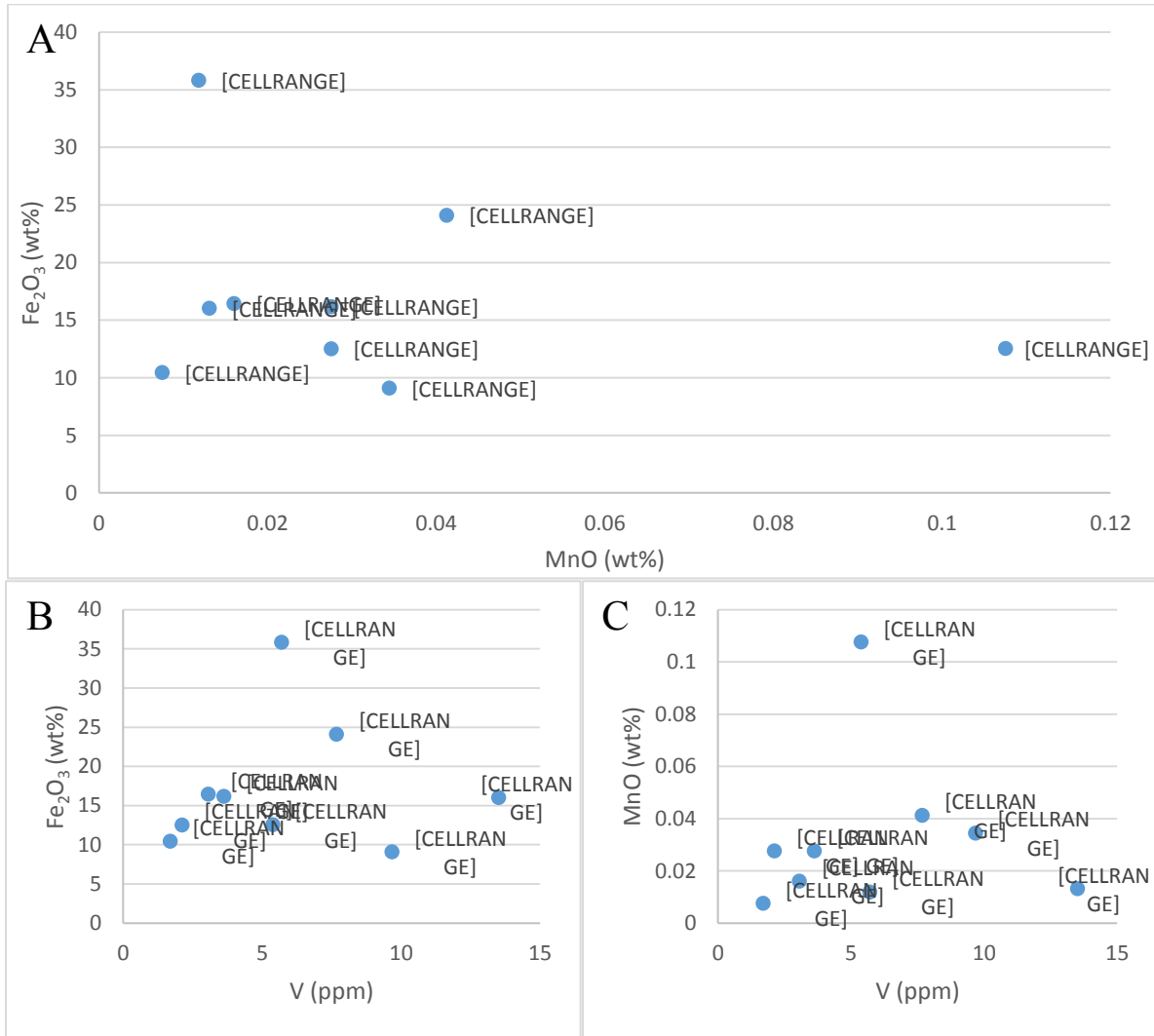
Figure 148: Fe$_2$O$_3$ vs. MnO (A), Fe$_2$O$_3$ vs. V (B), and MnO vs. V (C) plots. No trends are apparent in these plots

Redox sensitive elements, such as Cr, U, V and Mo, represent minor but relevent components of the rocks within the area. Figure 149 shows these elements plotted against each other. Unfortunately, the majority of the samples collected from the Mary Ellen Mine had Cr values below detection. All four of the plots; which are V vs. Cr, V vs. U, V vs. Mo and Cr vs. U show that there is no correlation forming between any of them.
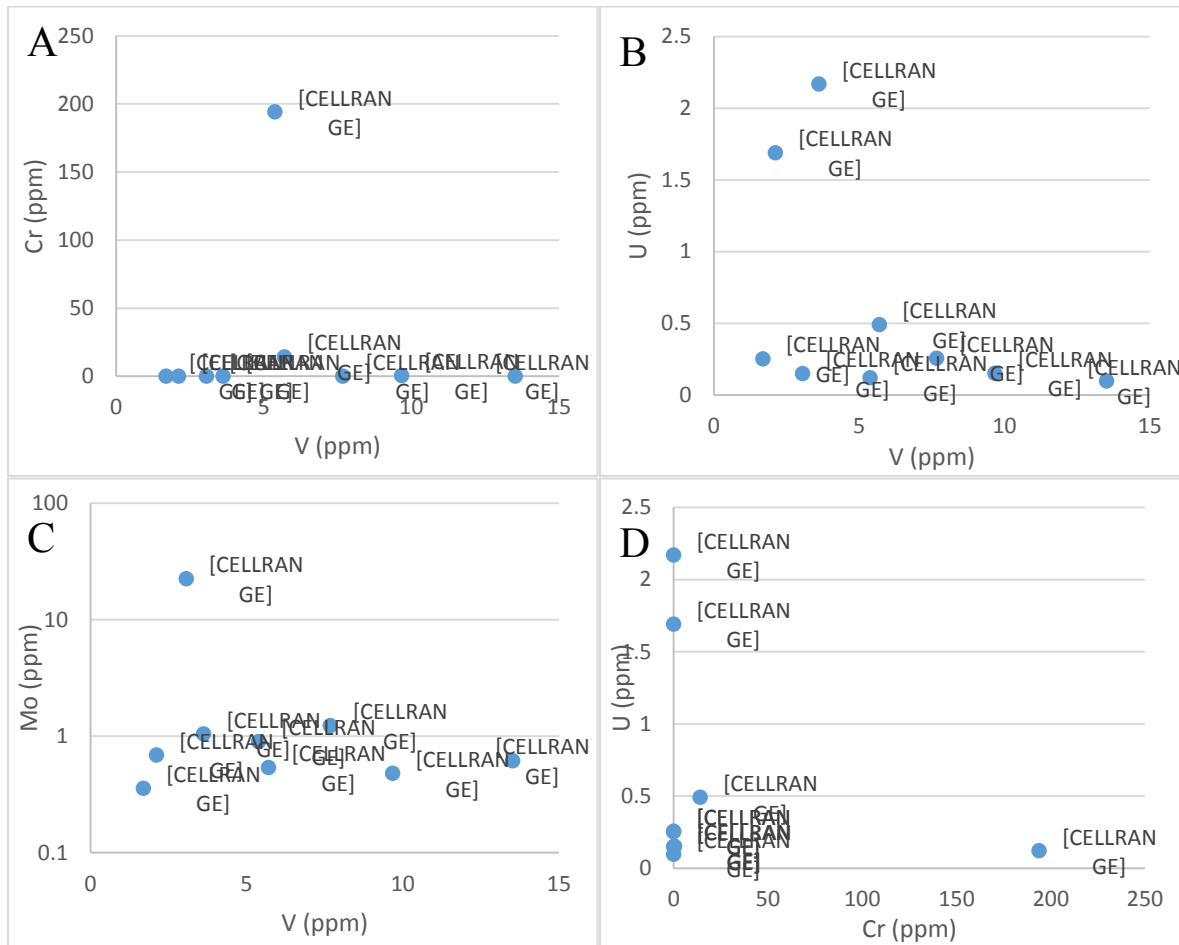
Figure 149: The plots of redox sensitive elements. A) The plot of Cr vs V. The majority of Cr values plotted below detection, though there is one very high value. B) The plot of V vs. U showing minor enrichment in two of the samples in U. C) A similar pattern can be seen in the Mo vs. V plot, with one sample with elevated Mo. D) No trend is visible in the U vs Cr plot. This is highlighted by samples with a high concentration in one of these elements having low concentrations in the other. Sample ME-5 has a high Cr value with low U, whereas samples 3 and 15 plot with high U and low Cr. Stromatolite sample ME-4 shows high Mo values as well.

6.2.3 *PR98-1*

Analysis of the PR98-1 drill hole was conducted in two distinct parts. The first part of the analysis was performed on 14 whole rock samples collected from the entire section of the drill core described previously (Table *13*). The second part was the analysis of five samples selected from the individual oncolites and the cement present in the oncolite stratigraphic unit present in the drill core. Discrimination plots are shown below to compare trends in the major and trace elements

Figure 150 contains four plots comprised of the redox sensitive elements Fe_2O_3, MnO, V and U plotted against Al_2O_3, which represents the siliciclastic component. Figure 150A is the plot of Fe_2O_3 vs. Al_2O_3. This shows a positive trend forming between the two oxides. Disregarding the oncolite samples, all other samples below PR98-16 with the exception of PR98-7, plot with low Al_2O_3. The samples taken from the oncolites and cement plot with a less obvious trend. Figure 150B is the plot of MnO vs. Al_2O_3. No trend can be seen forming between the two oxides. The plot of V vs. Al_2O_3 shows a similar positive trend forming between the elements (Figure 150C). The plot shows that the points form a less obvious trend between the two, showing that with increasing siliciclastic content there is also an increase in the vanadium. This trend implies that V is mostly located within the siliciclastic phase and is therefore in relatively low abundance. Figure 150D is the plot of U vs. Al_2O_3 with no distinct trend forming between the two elements.

Figure 151 contains plots of the redox sensitive oxides and elements Fe_2O_3, MnO and V plotted against each other. Figure 151A is the plot of Fe_2O_3 vs. MnO and shows no trend forming between the two oxides. Figure 151 B and C are the redox sensitive oxides plotted against V. A

positive trend can be seen in both whole rock samples as well as the oncolite samples in the plot of Fe_2O_3 vs. V(Figure 151B). The plot of MnO vs. V shows no distinct trend (Figure 151C).

Table 13: Samples taken from the PR98-1 drill hole for analysis.

Sample	Description
PR98-23	Cherty grainstone
PR98-19	Cherty grainstone
PR98-18	Cherty grainstone
PR98-17	Green silicate and carbonate layer
PR98-16	Green silicate and carbonate layer
PR98-15	Green silicate and carbonate layer
PR98-14	Green silicate and carbonate layer
PR98-13	Top of the oncolite layer into the green silicate layer
PR98-11 Onc	Oncolite from PR98-11 oncolite layer
PR98-11 Cem	Cement from the PR98-11 oncolite layer
PR98-10	Oncolite layer
PR98-7 Cem	Cement from around the PR98-7 oncolite
PR98-7 Onc	Oncolite from PR98-7
PR98-7	Oncolite layer
PR98-6 Lg Onc	Large oncolite from PR98-6
PR98-6 Sm Onc	Small oncolite from PR98-6
PR98-6	Brecciated grainstone and oncolite layer
PR98-5	Brecciated grainstone
PR98-3	Medium to coarse grainstone

Up hole
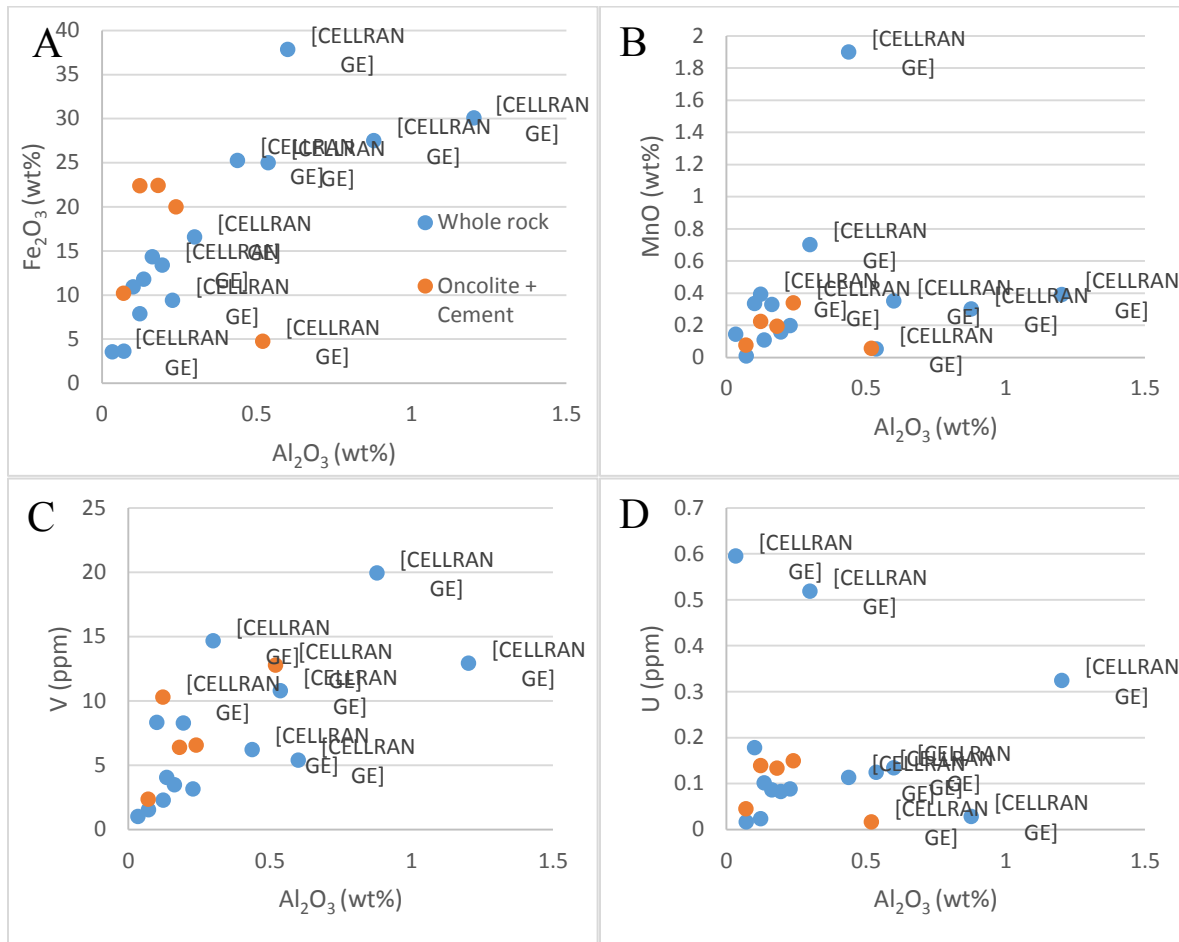
Figure 150: The redox sensitive elements plotted against Al_2O_3. A) Fe_2O_3 vs. Al_2O_3 showing the positive trend forming in in the non-oncolitic sample group, but not the oncolites. B) MnO vs. Al_2O_3 plot showing no distinct trend. C) V vs. Al_2O_3 plot showing a similar positive trend forming between the two elements. D) U vs. Al_2O_3 showing no positive trend between the two.
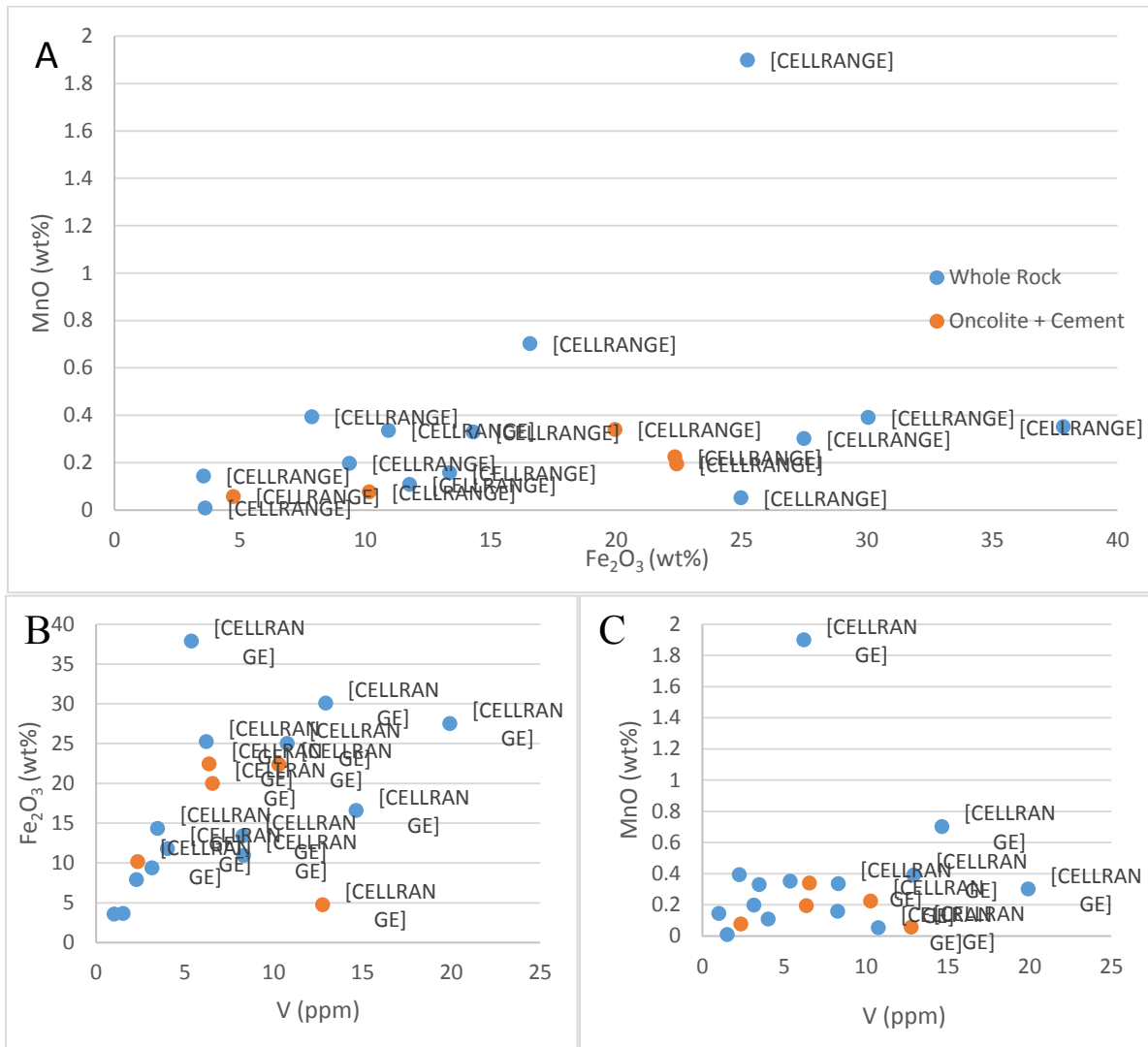
Figure 151: Plots of the redox sensitive oxides and elements. A) Fe_2O_3 vs. MnO showing no trend between the two oxides. B) Fe_2O_3 vs. V showing a positive trend between the two elements. C) No trend is present in the plot of MnO vs. V.

Figure 152 is of the minor redox sensitive elements V, Cr, Mo, and U. These elements were plotted against V and Cr. A majority of the samples had Cr values below the detection limit. The plot of Cr vs. V shows a lack of trend forming between the two elements (Figure 152A). A slight positive trend is visible in the plot of the U vs. V showing a covariance between the two elements (Figure 152B). The plot of Mo vs. V shows no distinct trend forming between

the two elements (Figure 152C). Figure 152 D is Cr vs. U which again shows no trend forming

between the two elements.
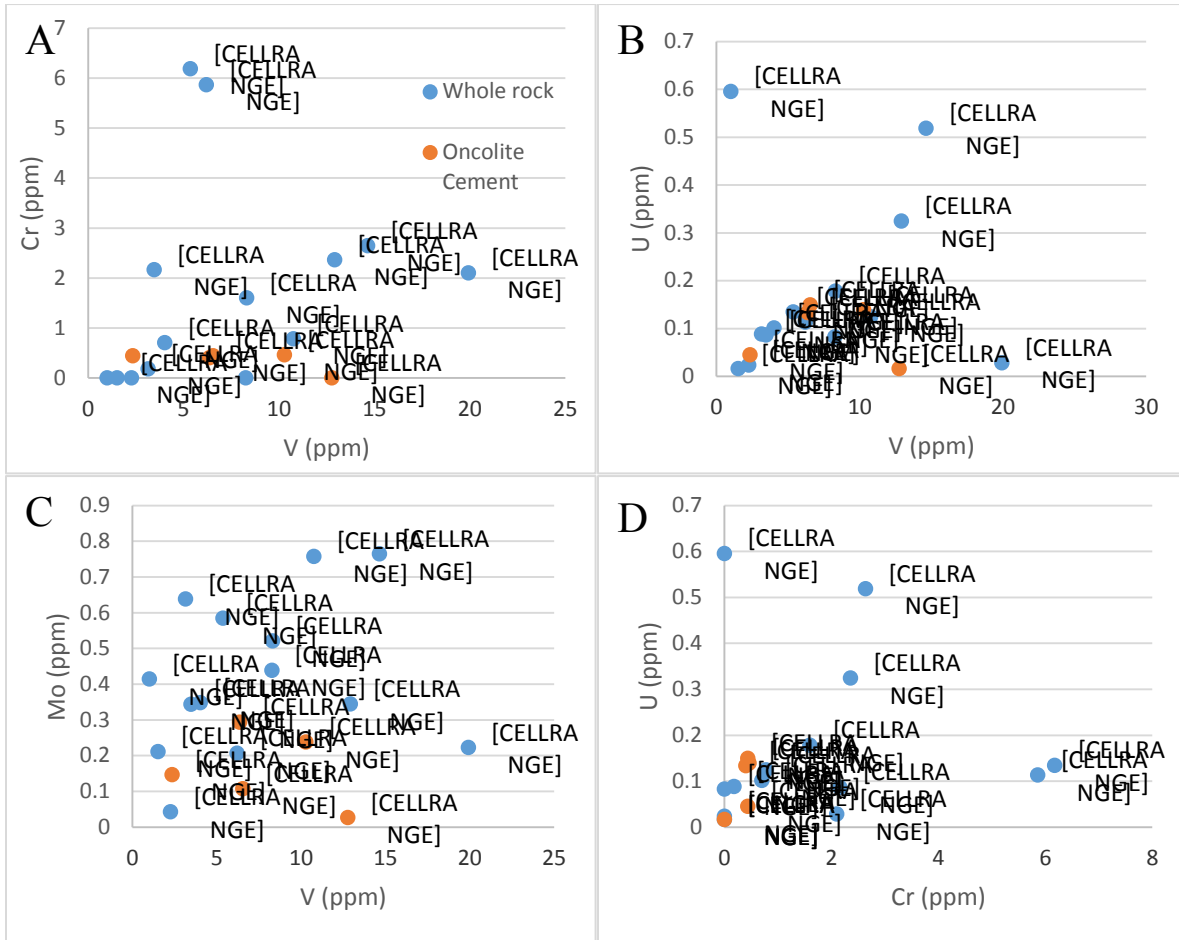
Figure 152: The plots of redox sensitive elements Cr, U and Mo plotted against V and Cr. A) Cr vs. V showing no trend between the two elements. B) A positive trend can be seen in the plot of U vs. V C) Mo vs. V showing no trend. D) No trend visible in the plot of U vs. Cr. No enrichment is seen in any of these elements.

6.3   Rare Earth Elements

6.3.1   Mount Whittlesey

The same 14 samples were analysed for rare earth element concentrations as were
analysed for major and trace elements. These values were normalized to Taylor and Mclennan
(1985) PAAS values and plotted.

Figure 153A contains the plots of the samples taken from the slaty iron formation. The
plot shows that the samples all have similar concentrations. All the samples also have a depletion
of the light rare earth elements and a positive Eu anomaly and no Ce anomaly. Figure 153B is
the PAAS normalized REE distribution plots for the samples taken from the cherty iron
formation portions of the Mount Whittlesey outcrop. These samples have a lower concentration
than the samples from the slaty IF. The cherty sedimentary rocks are enriched in MREEs and
have similar positive Eu anomalies compared to the slaty iron formation. Ce anomalies present in
the cherty samples range from nil in samples 04, 07 and 08 to negative Ce anomalies in samples
05 and possibly 06.

Figure 154 is of the PAAS normalized samples taken from the convoluted layer present
in the Mount Whittlesey outcrop. Figure 154A is of the samples taken from a convolute layer at
the base of the studied cycle. These two samples show similar concentrations to each other. The
samples also show enrichment in the MREEs, negative Ce anomalies and positive Eu anomalies.
The samples from the convolute layer at the top of the studied cycle have MREE enrichment,
positive Eu anomalies and no Ce anomalies.

PAAS normalized values for the La and Eu anomalies are plotted against PAAS
normalized Ce anomaly values in Figure 155. The majority of the plots show no Ce anomaly

(Figure 155A). The samples with negative Ce anomalies form a correlation with decreasing La

anomaly values. The plot of Eu anomaly vs. Ce anomaly is seen in Figure 155B. This plot

shows no correlation between the Ce anomaly and the Eu anomaly.

Due to the presence of the enrichment of the middle rare earth elements in the PAAS

plots, Figure 156 is of the PAAS normalized MREE values plotted vs. the PAAS normalized Ce

anomalies. The plot shows that the MREE enrichment is not connected with the formation of Ce

anomalies.
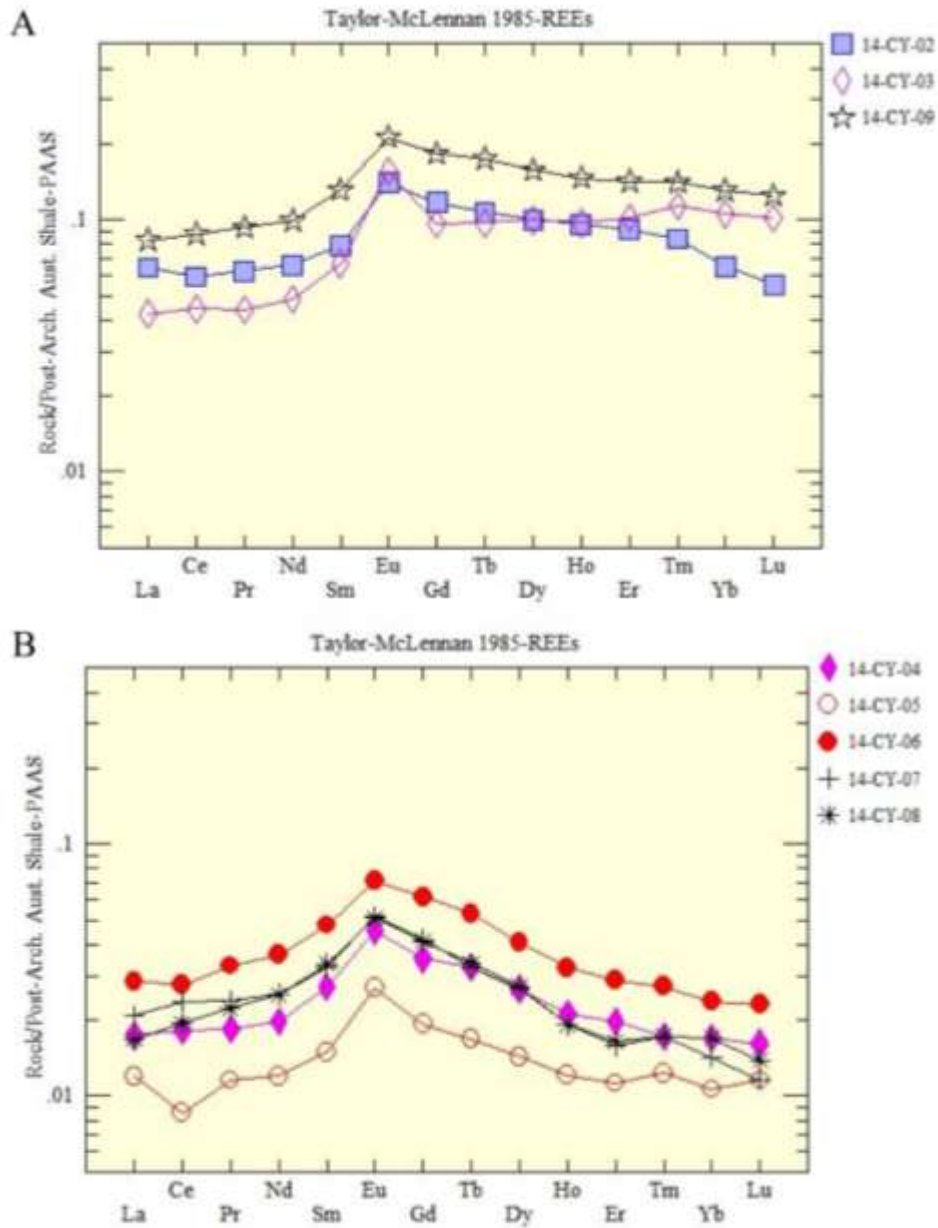
Figure 153: PAAS normalized REE distribution plots for the samples taken from Mount Whittlesey. A) Samples from the slaty stratigraphic unit. The samples are light REE depleted with nil Ce anomalies present. All samples have positive Eu anomalies. B) Samples collected from the cherty stratigraphic unit. Samples show MREE enrichment, with mostly nill Ce anomalies and positive Eu anomalies. Negative Ce anomalies are present in samples 05 and a very slight anomaly in 06.
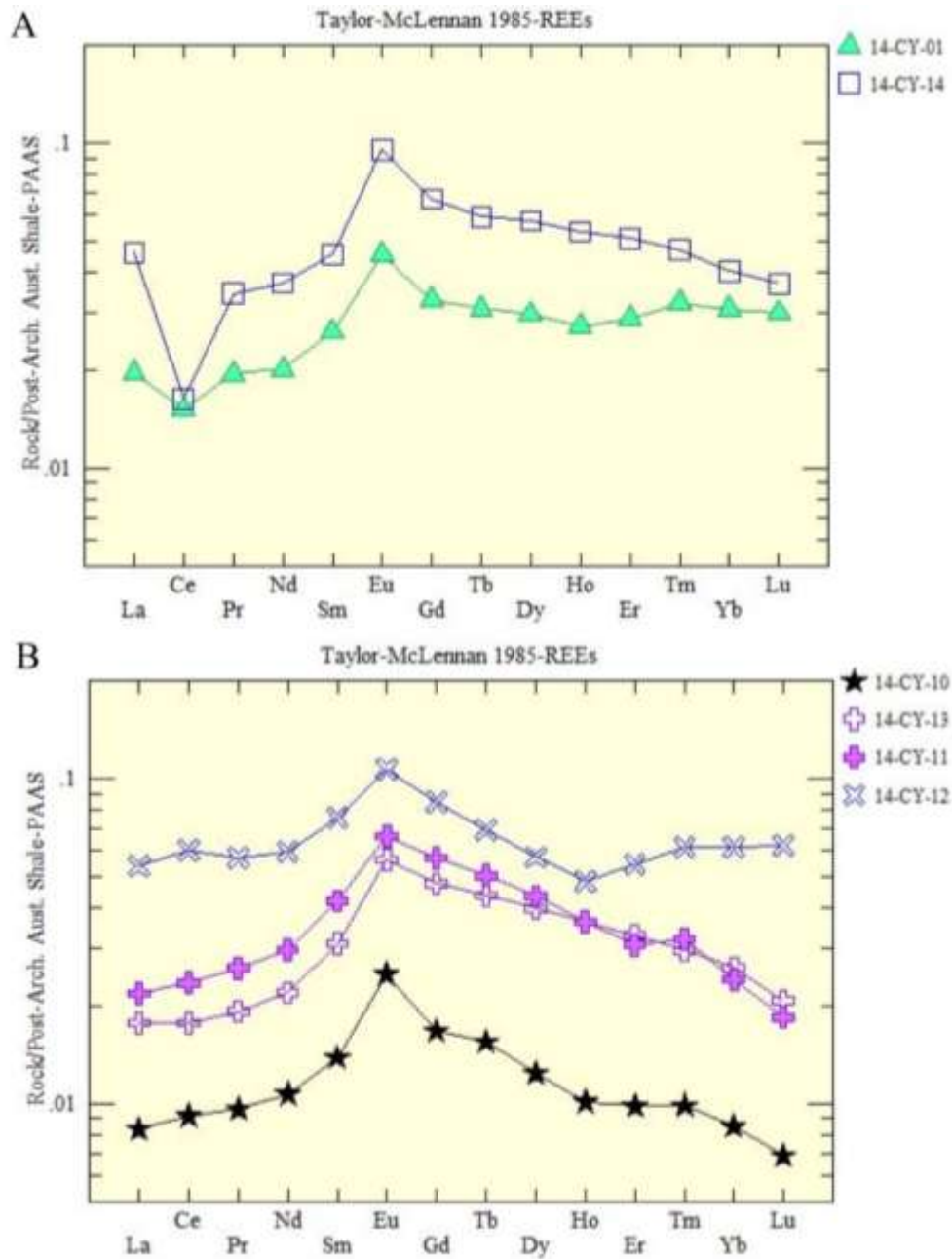
Figure 154: The PAAS normalized REE distribution plots for the samples from the convolute layers. A) Samples from the lower convoluted layer. Both samples show the MREE enrichment with negative Ce anomalies and positive Eu anomalies. B) Samples from the convoluted layer at the top of the studied cycle. The samples have the enriched MREEs with nil Ce anomalies and positive Eu anomalies.
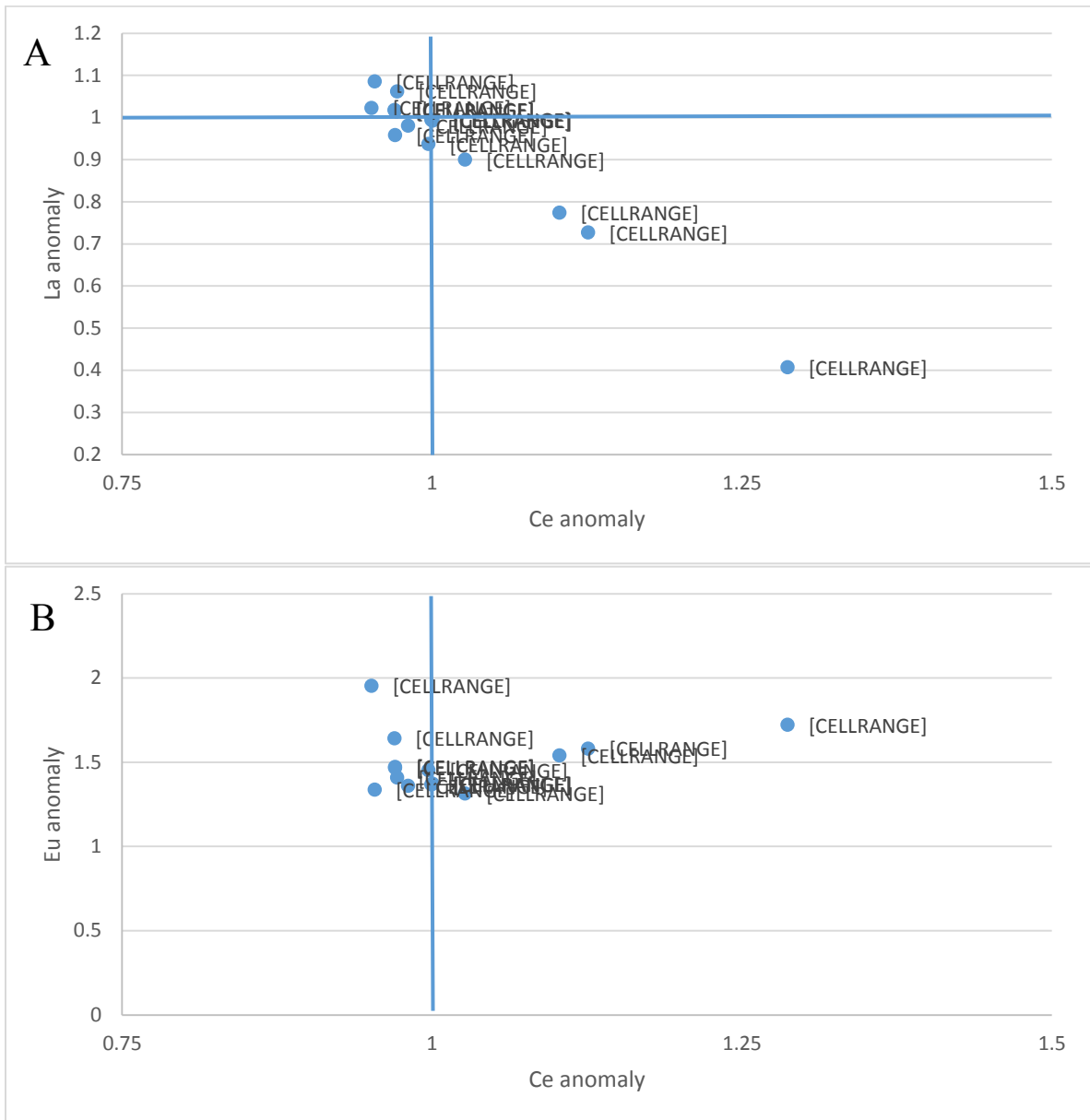
Figure 155: La and Eu anomaly values plotted against Ce anomaly values. A) La anomaly vs. Ce anomaly plot showing the cluster of samples plotting with nil Ce anomalies. The samples with negative Ce anomalies also show decreasing La anomalies, probably due to the formula for La anomalies containing the value for Ce. B) All the samples have moderate positive Eu anomalies, which do not correlate to the Ce anomalies.
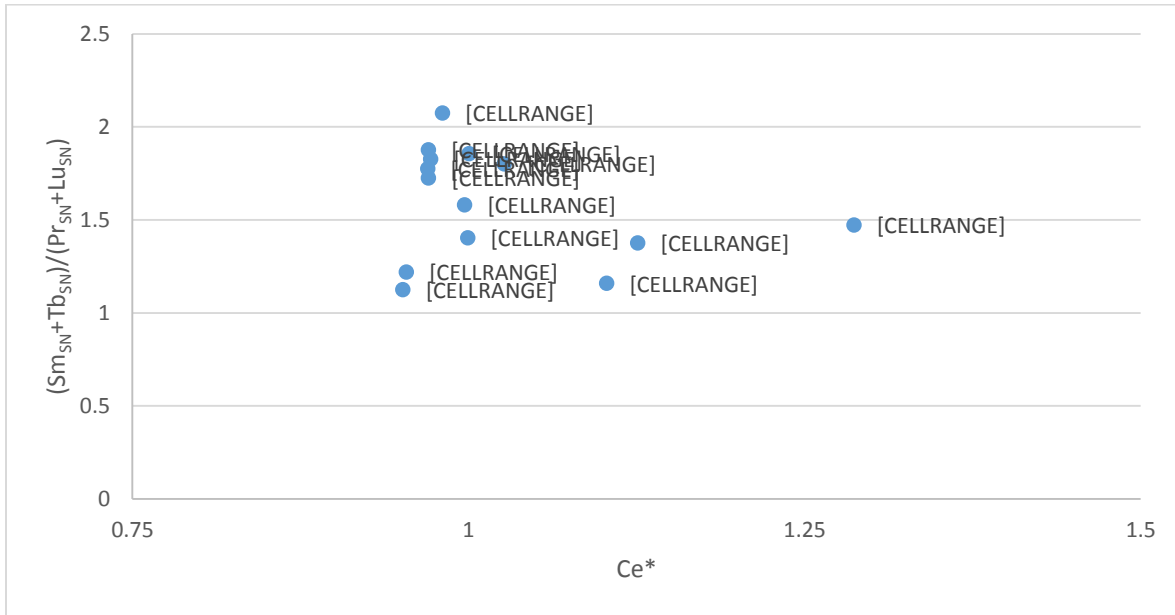
Figure 156: Enriched MREE values vs. Ce*. This plot shows no correlation between the enrichment in MREEs and the Ce anomaly, though the three samples with negative Ce anomalies do tend to have lower MREE enrichment.

The last four plots are of the redox sensitive elements plotted against the PAAS normalized Ce values (Figure 157). The plots show that there is no correlation between the redox sensitive elements and the Ce anomaly. The plots are Fe_2O_3 vs. Ce* (A), MnO vs. Ce* (B), V vs. Ce* (C) and Cr vs. Ce* (D).
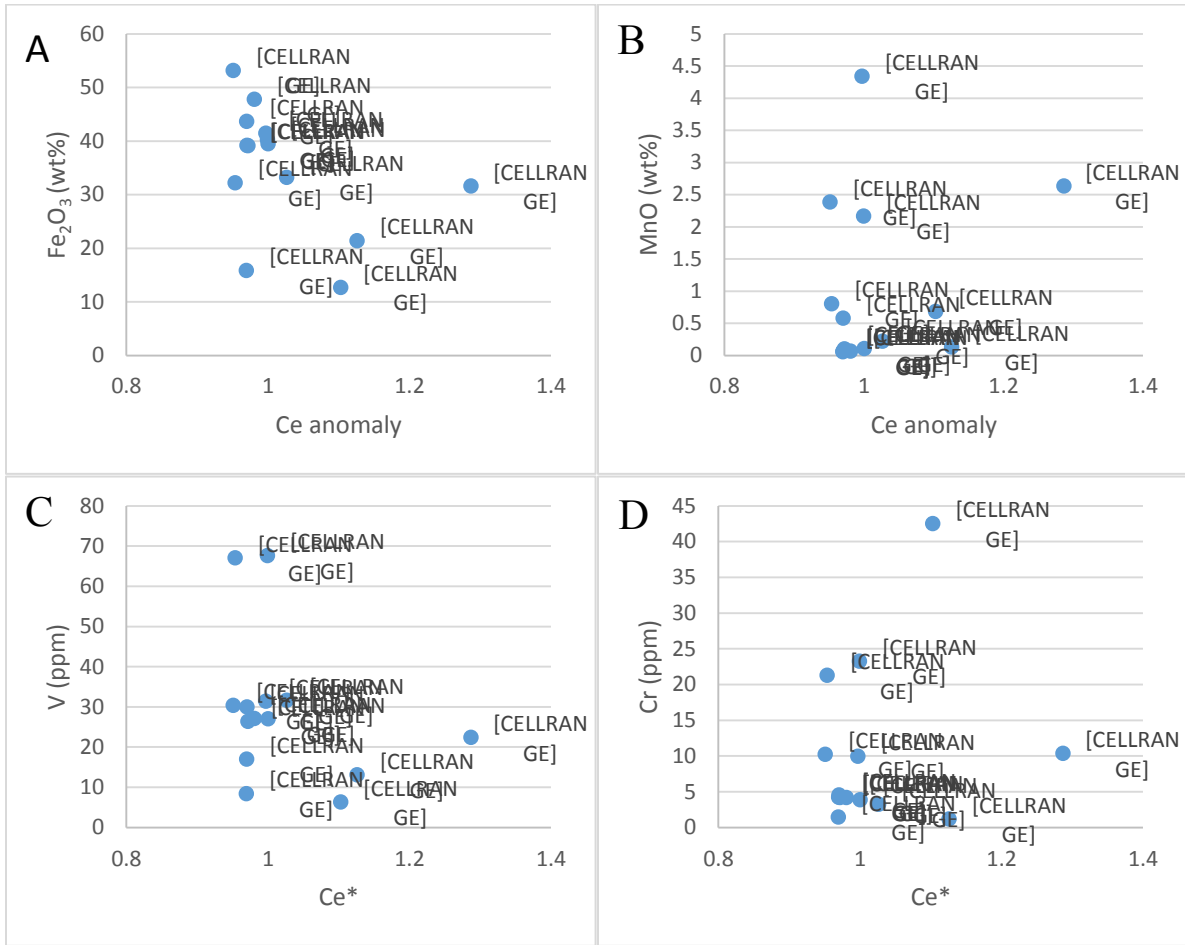
Figure 157: Redox sensitive elements vs. calculated Ce anomaly values. A) Fe_2O_3 vs. Ce*, B) MnO vs. Ce* C) V vs. Ce* and D) Cr vs. Ce*.

6.3.2 Mary Ellen Mine

The same nine samples were analysed for rare earth element concentrations as those analysed for major and trace elements. The analysed values were again normalized to Taylor and McLennan (1985) PAAS values and plotted on a concentration diagram. The plots below are divided into two groups the altered and brecciated layer including the contact with the stromatolites and the samples collected with stromatolites in them. Figure 158A reflects the samples taken from the altered (ME-15, 16) and breccia (ME-06, 07) layers. The breccia samples show a flat pattern, whereas the samples from the altered unit are LREE depleted. Four of the five samples show a positive Ce anomaly and three have Eu anomalies. The sample ME-06, one of the breccia samples, has flat Ce and Eu. The samples collected from the stromatolites either show a positive slope up into the HREEs (ME-02B) or a negative slope down into the HREEs (ME-01, 03, 04, 05). All four samples have consistent HREE concentrations (Figure 158B). Both positive and a possible slight negative Ce anomaly are present, as well as positive Gd anomalies, but no positive Eu anomalies.

Values for the Ce, La and Eu anomalies were calculated and plotted for all samples (Figure 159). The plot of Ce vs. La shows a linear trend forming between the two anomalies. The plot shows that the majority of the samples have negative Ce anomalies, with samples 3 and 6 plotting with no anomalies and 1 plotting with a positive Ce anomaly. The plot of Ce vs. Eu anomalies shows a positive corelation for the alteration samples and two of the three breccia samples.
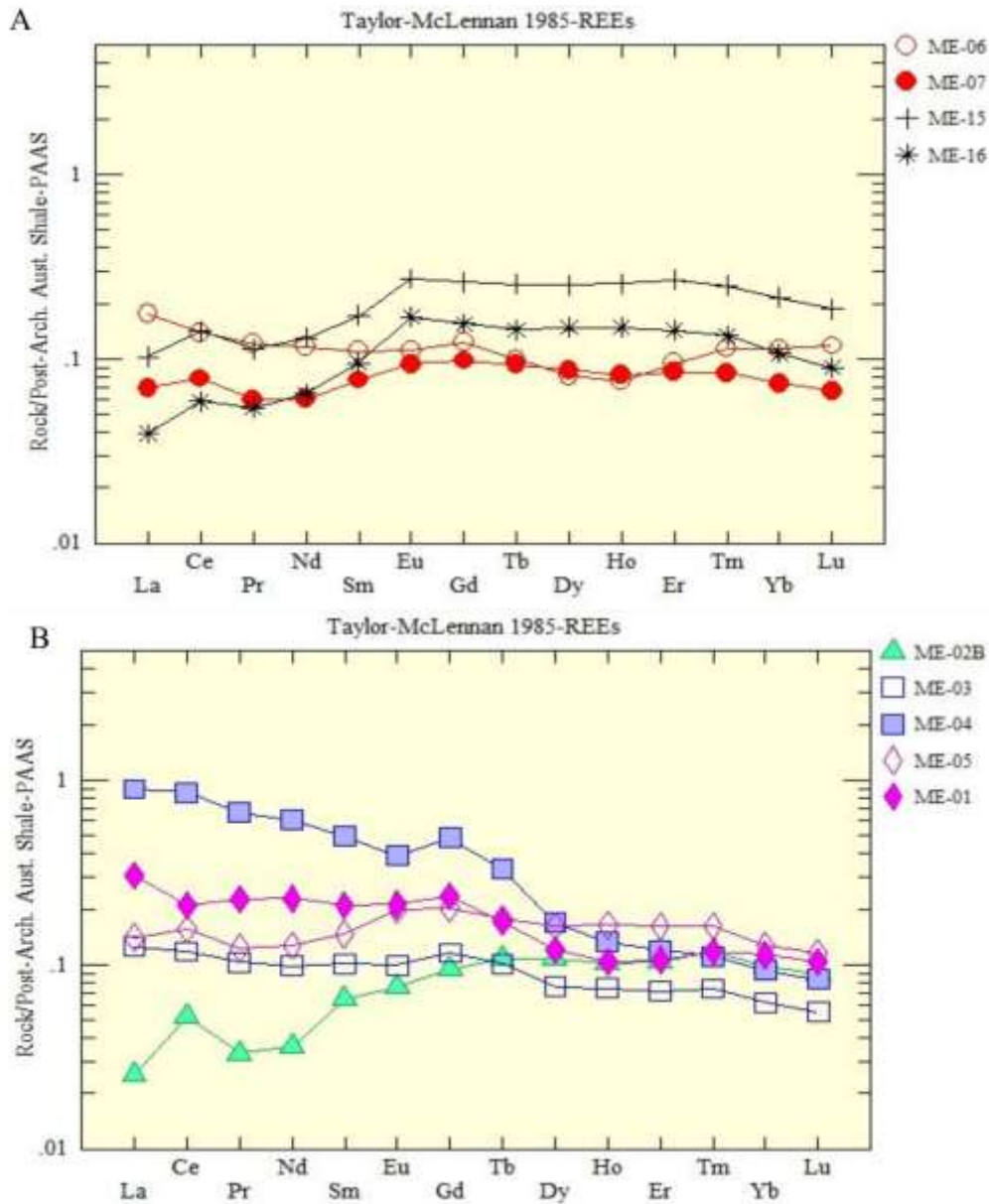
Figure 158: PAAS normalized rare earth element concentration diagram. A) The altered portion at the Mary Ellen Mine. The plot shows consistent concentration. Positive Ce anomalies can be seen in all the samples but ME-06. ME-06 also shows a null Eu anomaly. B) The stromatolite samples have either enrichment or depletion of LREE compared to the HREEs. ME-03 and ME-04 do not have Ce anomalies. ME-02B and ME-05 have positive Ce anomalies and ME-01 has a possible slight negative Ce anomaly. Positive Gd anomalies can be seen in all samples, except for ME-02B.
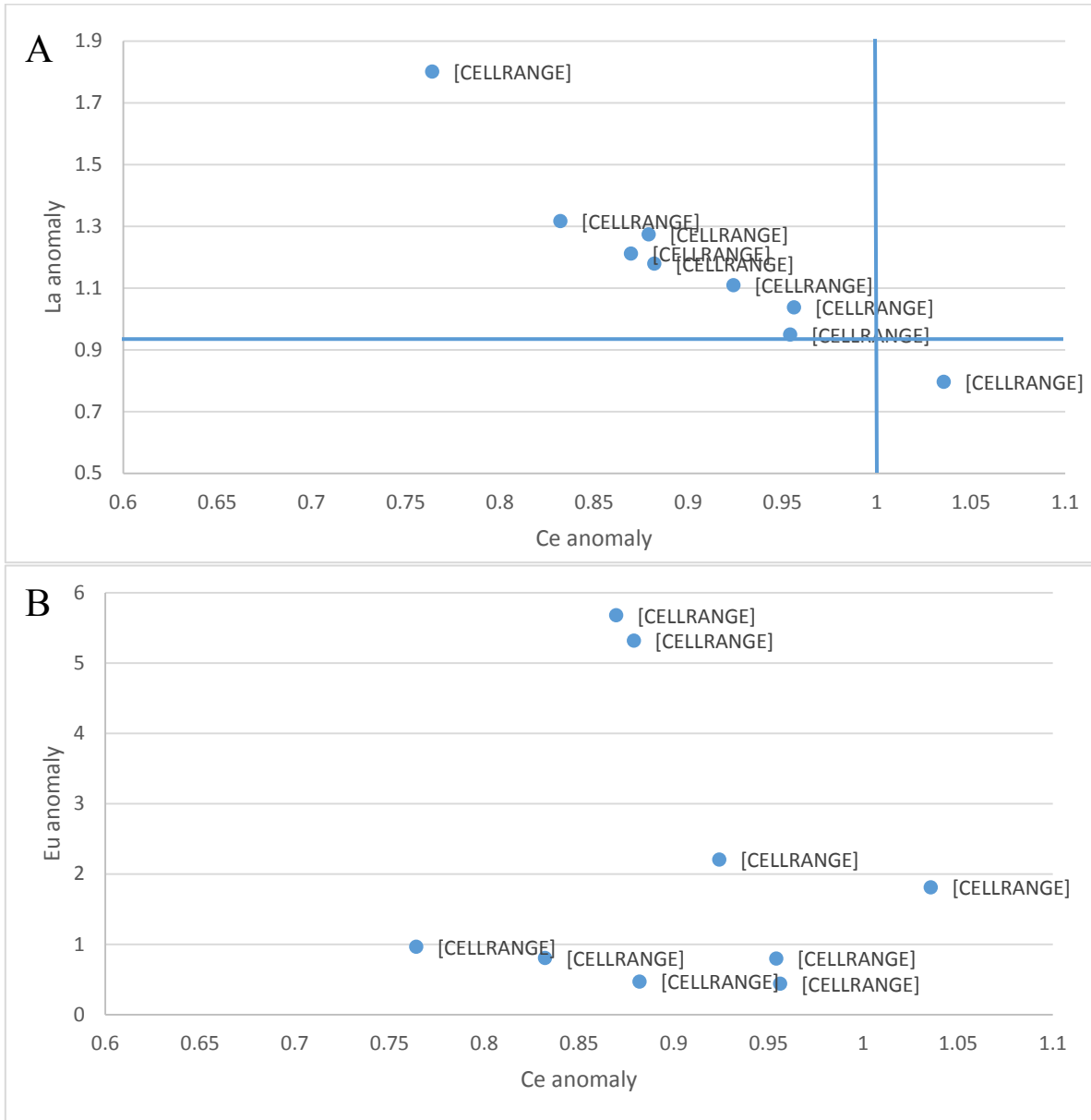
Figure 159: Ce vs. La anomaly plot, showing a distinct linear trend forming between the two. The majority of the samples show positive Ce anomalies present and a slight negative Ce anomaly present in only one sample. B) The plot of Ce vs Eu anomaly with no trend between the two.

The last four plots are of the Ce anomaly plotted against the redox sensitive oxides and elements (Figure 160). The first plot is of the Ce anomaly vs Fe_2O_3 (Figure 160A), the plot have

a cluster forming around the 1-1.1 mark. A similar trend is seen in the Ce vs. MnO plot (Figure 160B). The plot of Ce anomaly vs. V shows a distinct negative linear trend with the highest V values found in stromatolite sample and the lowest found in the altered samples (Figure 160C). Due to the lack of above detection level Cr values for the Mary Ellen samples, the plot of the Ce anomaly vs Cr shows no distinctive trend (Figure 160D).
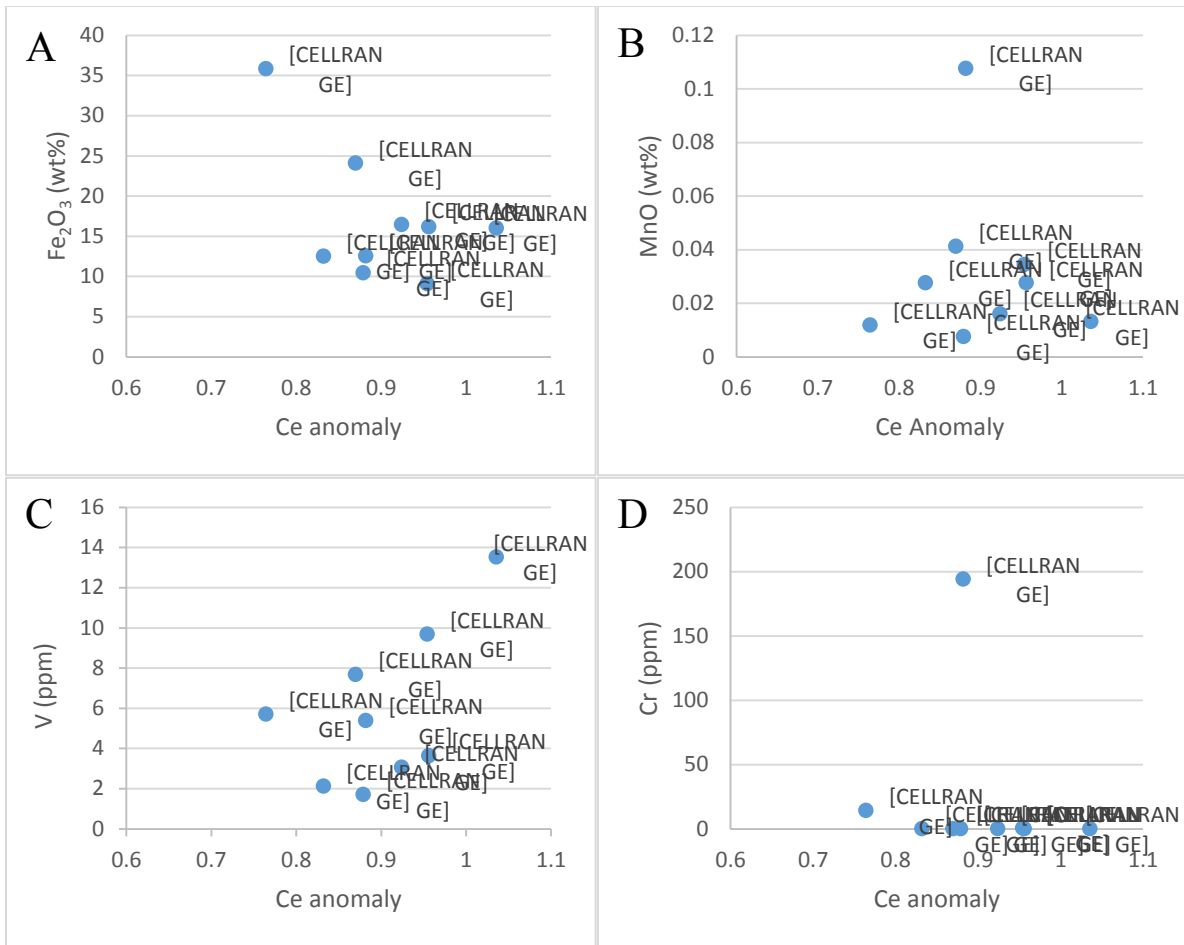
Figure 160: Redox proxies plotted against Ce anomalies. A) A cluster pattern forming between Fe_2O_3 vs Ce. B) Similar trend forming between MnO vs Ce anomaly. C) A distinct linear trend is visible between V and the Ce anomaly. D) No trend is visible with Cr and Ce anomaly.

6.3.3   PR98-1

Samples collected from the PR98-1 drill hole were also analyzed for rare earth element concentration using the ICP-MS. As in the previous sections on REE geochemistry the samples were normalized to PAAS values and plotted as distribution plots. The samples were divided into four graphs dependent on their location through the sequence. The first plot (Figure 161A) is of the purple grainstone and the brecciated layer that mark the base of the sequence. The grainstone (red circles) shows no distinct Ce anomaly, with a slightly positive Eu anomaly. The overall pattern is flat, only showing slight enrichment in the MREEs. The second plot is of the samples taken from the brecciated layer (plus sign) above the mauve coloured grainstone layer. This plot shows a higher concentration of overall REEs compared to the grainstone layer. The patterns of the plots are flat, similar to the grainstone layer below. Unlike the grainstone plots, the breccia plots have distinct positive Ce and Eu anomalies. Figure 161B represents samples of the homogenous, oncolites and cement taken from the oncolite layer. The samples from this layer all show similar patterns, although there is a distinct concentration change between samples PR98-1-7 and PR98-1-11. However, the rest have similar concentrations to PR98-11. All plotted samples show a distinct positive Ce anomaly. No Eu anomaly can be seen in the plot due to enrichment in the MREEs compared to the HREEs and LREEs in most samples.

Figure 162, shows the plots for the PAAS normalized samples taken from above the oncolite layer, This is the area comprised of silicate and carbonate layers, as well as a final brecciated layer. There is also a sample taken from the slaty iron formation at the top of the sequence. Figure 162A is of the samples collected from the green silicate layer above the oncolite layer and below the cherty grainstone. The samples plotted are PR98-13, PR98-14,

PR98-15, PR98-16 and PR98-17. The samples from the brecciated layer above the oncolites show similar patterns to each other in that there is a slight depletion in HREEs and a positive Ce anomaly, though sample PR98-13 shows a smaller anomaly than sample PR98-14. The samples from the silicate layer show a similar pattern to each other. All the samples from above the oncolite stratigraphic unit including the green-silicate stratigraphic unit as well as the brecciated stratigraphic unit show an enrichment in the HREEs with positive Ce and slighty negative Eu anomalies present in most samples. The next plot is of samples PR98-18, PR98-19, and PR98-23 (Figure 162B). These samples represent the top of the sequence from the cherty iron formation directly above the contact with the previously described units. Sample PR98-23 was taken from the grainstone 30cm above the oncolite-brecciated sequence. The PAAS normalized plot shows that these samples all have similar patterns. Sample 18, which is from directly above the sequence is enriched in the HREEs with a distinct positive Ce anomaly, and slight positive Eu and Gd anomalies. Sample 19 is from the cherty iron formation and is depleted in the HREEs, as well as having a smaller positive Ce anomaly, though its Eu and Gd anomalies are similar. The two samples taken from the grainstone stratigraphic unit show similar patterns with similar sized Ce anomalies and slightly positive Eu anomalies.

The oncolite samples were plotted together with the samples of the cement from the similar stratigraphic unit of the drill core. The oncolite samples were taken from the bottom, middle and top of the oncolite layer. The samples taken from the bottom layer included the very large oncolite in Figure 163. The cement and oncolite samples have similar flat patterns. Oncolites samples from the PR98-6 drill core section show distinct positive Ce and slightly positive Eu anomalies. The oncolite and cement sample labeled PR98-7 has a similar pattern, with the exception that the cement has an enrichment in the HREEs compared to the oncolite

sample, which has a slight depletion in the HREEs. Both samples have a positive Ce anomaly and a slightly positive Eu anomaly. The oncolites from near the top of the oncolite layer show lower overall REE concentrations compared to the ones from the base of the oncolite layer. The patterns that appear from the oncolite and cement samples are similar, except the cement is enriched in MREEs and HREEs while the oncolites are depleted in HREEs. Both sample types show positive Ce anomalies and slight positive Eu anomalies.

Values for the Ce, La, and Eu anomalies present in the PAAS REE distribution plots presented above were plotted, and the plots are present in Figure 164. Figure 164A is of the La anomaly values vs. the Ce anomaly values. This plot shows that all samples have positive Ce and La anomalies though the latter may be due to the Ce being in the La anomaly equation. This plot has a distinct linear trend forming between the two anomalies. Figure 164B is of the Eu anomaly plotted against Ce anomaly values. This plot shows no trend forming between the two.
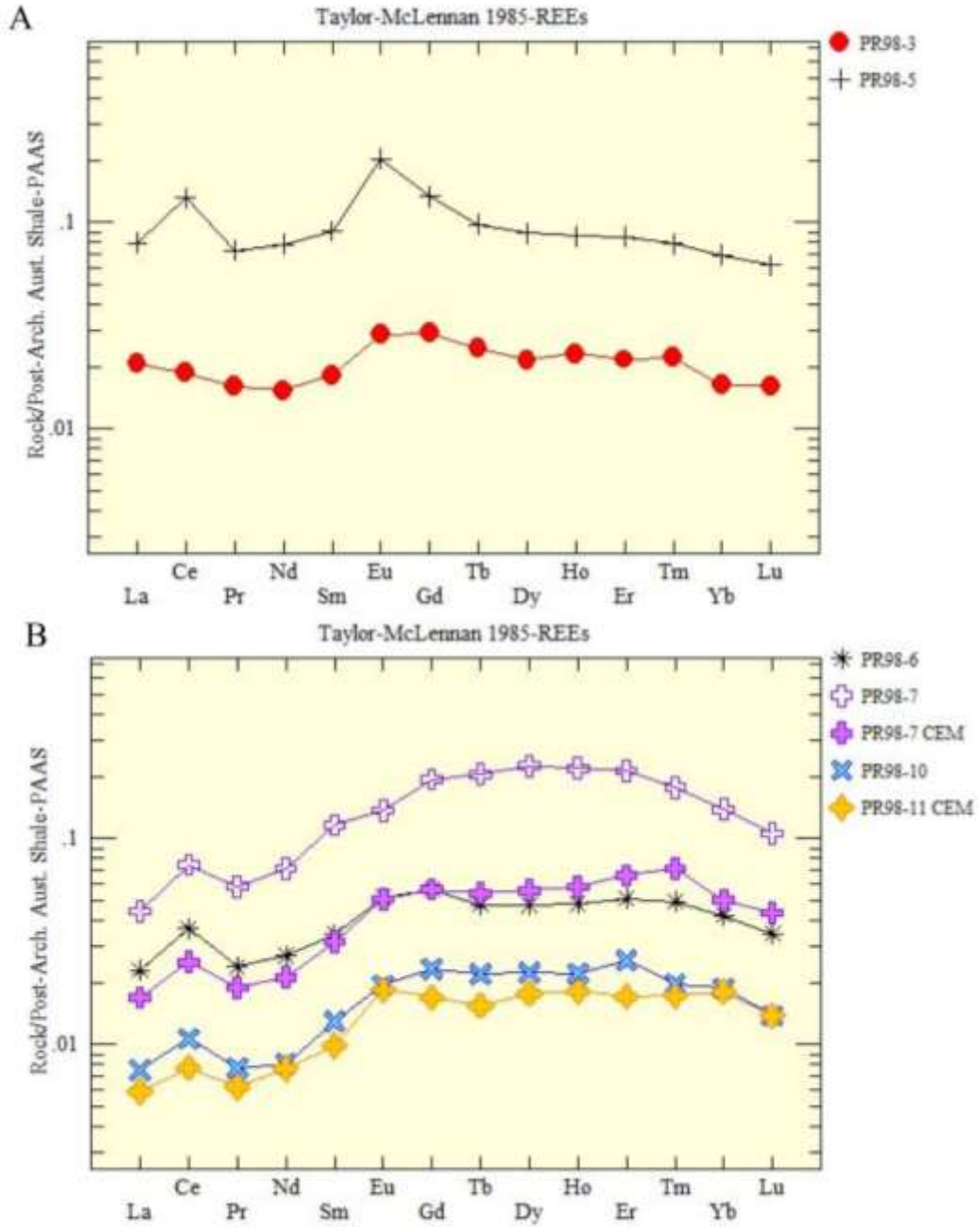
Figure 161: PAAS normalized distribution plots for selected samples from the PR98-1 hole drilled near Pidgeon River Ont. Plot A) are samples collected from the grainstone (PR98-3)and brecciated layer. (PR98-5)B) The plot of the homogenous samples from the oncolite layer.
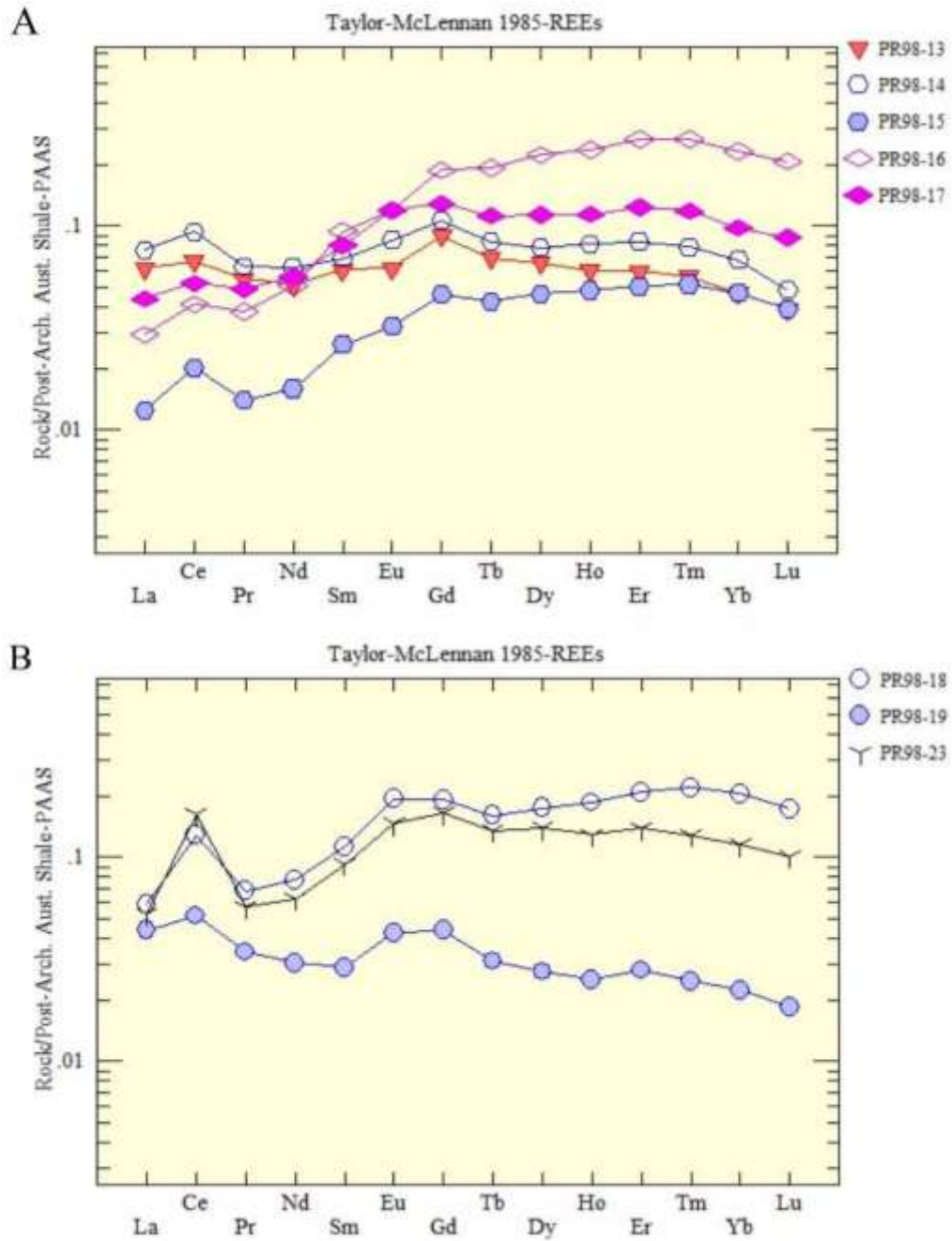
Figure 162: The PAAS normalized distribution plots for the top of the PR98-1 sequence. A) Diagram for samples from the silicate layer B) Plot for samples collected from the overlying cherty Gunflint grainstone.
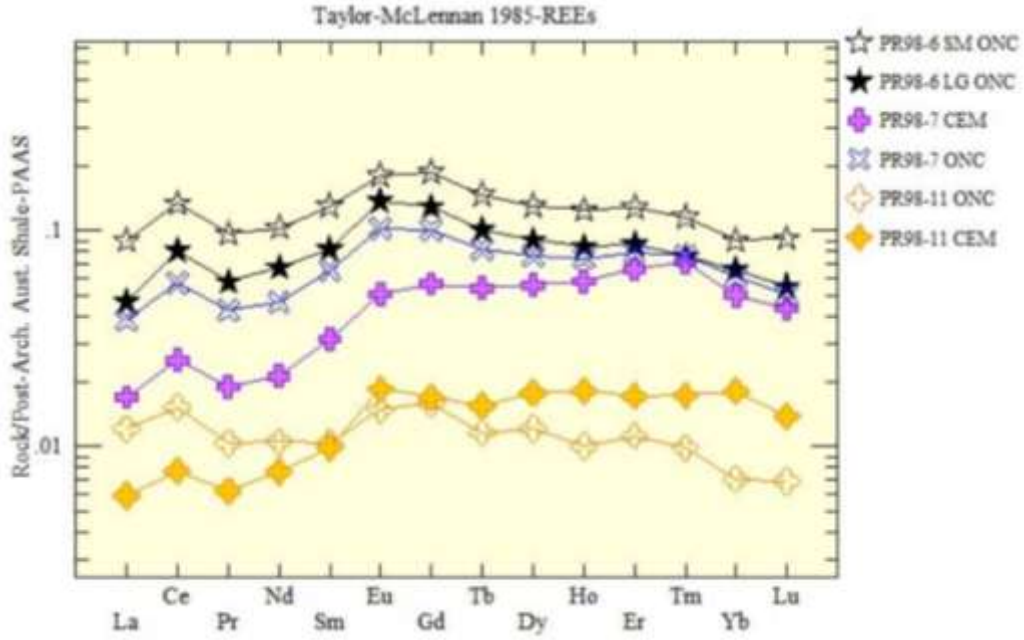
Figure 163: The PAAS normalized diagram for oncolite samples and corresponding cement samples.
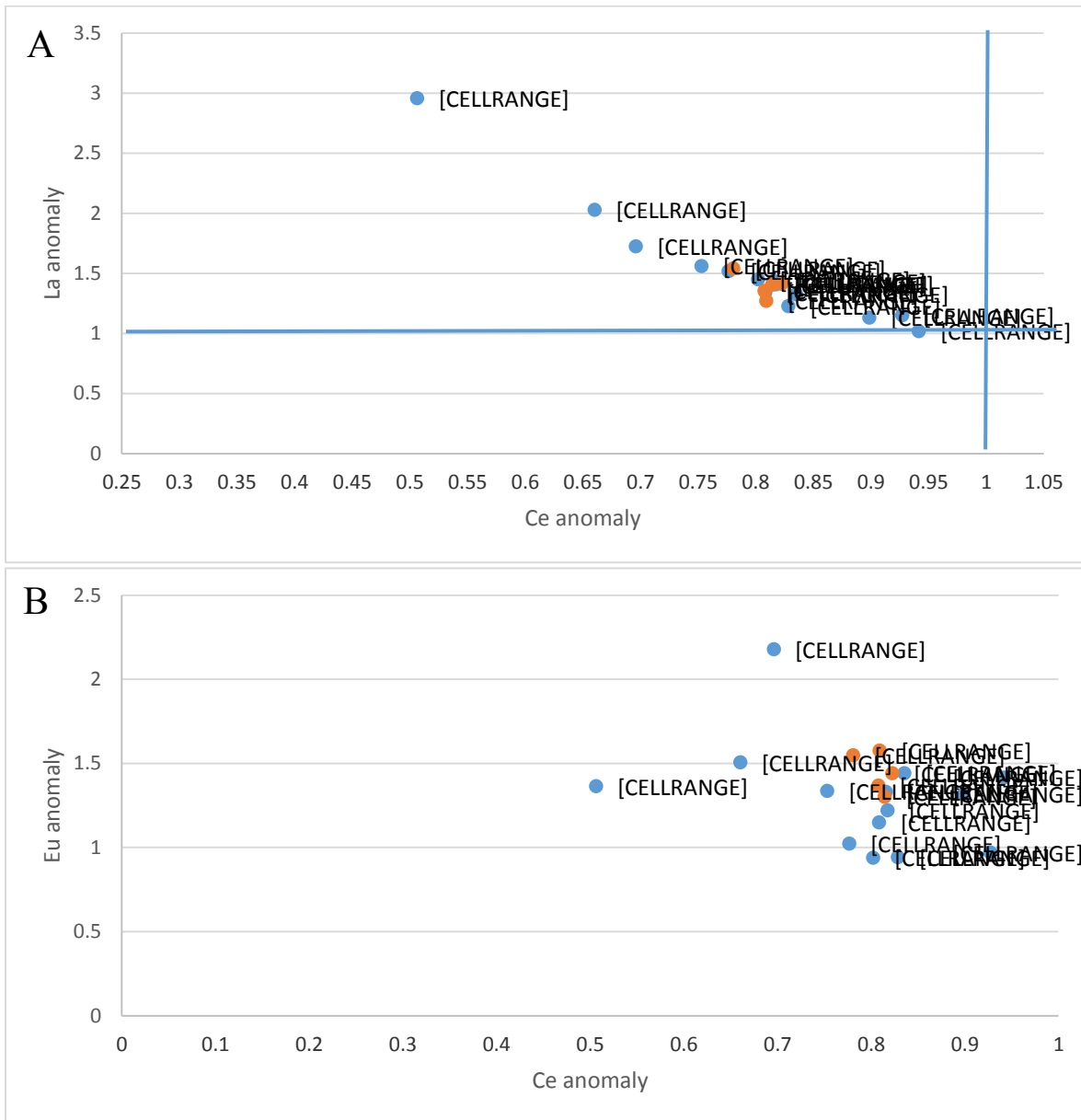
Figure 164: The plots of the calculated values for La and Eu anomalies vs. calculated values for Ce anomalies. A) La anomaly vs. Ce anomaly, showing distinct positive Ce anomalies. The positive La anomaly may be an artifactt of having Ce in the equation for calculating the La anomaly. B) Eu anomaly vs. Ce anomaly showing no trend forming between the two anomalies. The Eu anomaly exhibits a range of values from high to non-existant. Blue dots represent whole rock samples. Yellow dots represent sample taken of the oncolites and surrounding cement.

The calculated values for the Ce anomaly present in the PR98-1 sample were plotted against the redox sensitive elements Fe_2O_3, MnO, V, and Cr. These plots show that the there are no trends for the plots of Fe_2O_3 vs. Ce* (Figure 165A), MnO vs. Ce* (Figure 165B), V vs. Ce* (Figure 165C) and Cr vs. Ce* (Figure 165D).
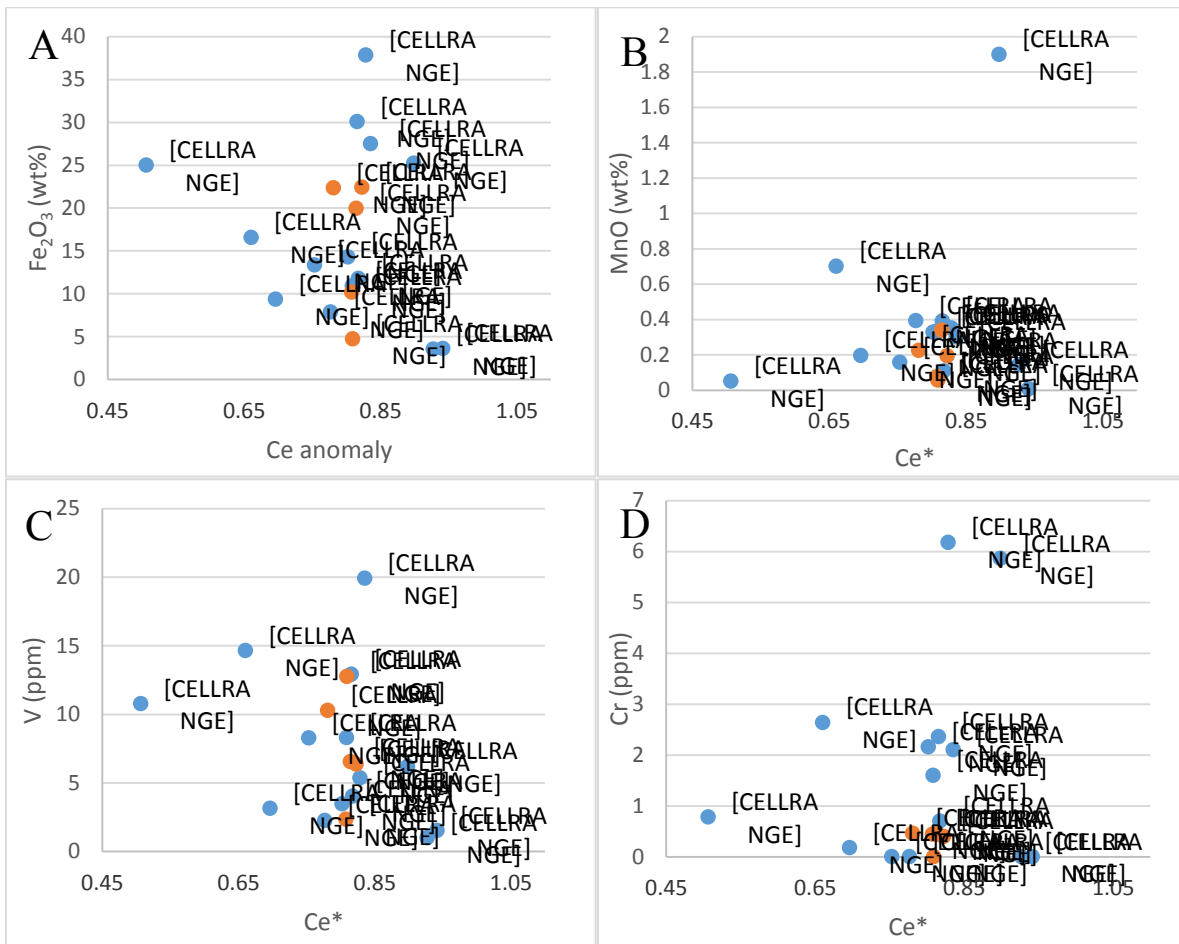
Figure 165: Redox sensitive elements vs. Ce anomaly (Ce*) plots. A) Fe_2O_3 vs. Ce* no trend between the two. B) MnO vs. Ce* showing no trend. C) V vs. Ce* showing no trend. D) Cr vs. Ce* showing no trend between the two.

7 DISCUSSION

All of the samples selected for this project are representative of one of the three known exposure surfaces present within the stratigraphy of the Gunflint and equivalent formations. The three exposure surfaces are located at: 1) the base of the Gunflint, 2) 45m above the base, and 3) 50m below the limestone member at the top of the formation. The first two exposure surfaces are well defined and described as exposure surfaces by other authors. The first exposure surface present at the base of the Gunflint reflects the exposure of the Archean crystalline basement rocks and initial grainstone and stromatolite deposition during the initial transgression of the Animikie Sea. The exposure surface present 45m above the base has been defined as an exposure surface by Barrett and Fralick (1995). The samples collected from this layer reflect the exposure of the grainstones during the regression of the Animikie Sea, with diastem forming noted within the Magnetic Rock Trail outcrop. This surface is underlain by thickening- and coarsening-upward grainstones as well as the brecciated grainstones upon which the stromatolites grew. The presence of stromatolite colonies forming on the two well-known exposure surfaces appears to be a key indicator of exposure of the grainstone. The exposure surface present 50m below the limestone member is less defined as an exposure surface but the presence of the stromatolites at Mary Ellen and oncolites in the PR98-1 drill hole suggest the formation of an exposure surface before stromatolite formation. Gunflint formation stromatolites-are formed in the foreshore of the Animike Basin. The combination of the presence of the stromatolites and the brecciated grainstones within the upper layer underlying the stromatolites heavily suggest their formation occurred on an exposure surface.

7.1 Physical Attributes of the Exposure Surfaces

The 15 outcrops and drill holes presented in this project all contain examples of exposure surfaces present in the Gunflint and equivalent formations. These exposure surfaces reflect the period during deposition in which the deposited layer was exposed to the atmosphere. During this period, the substrate developed interesting alteration patterns. Starting at the bottom of the Gunflint, the three outcrops that make up the crystalline basement rocks and overlying Gunflint stromatolites and/or grainstones show various examples of the alteration pattern formed by exposure to the atmosphere. The most noticeable are the formation of the large corestones present in the outcrop on the shoulder of Highway 11/17. It is clear through the lithology of the corestones that they are formed in situ by the spheroidal weathering of the granodiorite. The corestones are formed by percolating fluids moving through the highly fractured and jointed granodiorite, in turn, rounding the large blocks into round boulders, creating the boulder horizon seen in the outcrop. The spheroidal weathering is indicative of a wetter climate in which precipitation and surface water moved through the highly jointed granodiorite rounding the blocks. The other two outcrops studied do show some evidence of exposure, but it is not as well defined as the Highway 11/17 outcrop. Both of these outcrops are discoloured to a darker hue for approximately one meter below the Gunflint.

The grainstones that overlie the granodiorite at Kakabeka Falls also contain evidence of exposure. The fine-grained carbonate and pyrite vadose silt layer present at the bottom of quartz cement filled cavities suggests percolating waters dissolved the carbonate grainstones, with settling of fine-grained carbonate and insoluble material at the bottom of the cavity. The second piece of evidence of exposure is the chert pebble conglomerate found at the top of the outcrop,

which formed from the silicification of the carbonate grainstone and its brecciation by wave activity.

The middle exposure surface present 45m above the base of the Gunflint Formation is comprised of medium to coarse chert grainstone cemented mostly by a micro-quartz cement. The exposure alteration of the grainstone stratigraphic unit is marked by cementation and later brecciation of grainstones as well as the hematite and jasper that fill open spaces between grainstone blocks. The breakup of the grainstone into the blocks, as seen in the outcrops at Old School Road, behind Mink Mountain and in DH 87-3, is indicative of lithification before brecciation. Pre-litification of the grainstone before the formation of the stromatolites is important due to the fact that stromatolite growth is inhibited in loose sediments and the lithification during exposure would allow for the formation of lithified surface, which creates stability and resultant stromatolitic growth. The brecciated grainstone blocks appear to be formed by nearshore wave action during large storm events. The storm domination of the inner shelf is evidenced by the presence of hummocky cross-stratification within the grainstones at the Current River-Boulevard Lake area (Fralick, 1988; Fralick and Barrett, 1995). The crashing waves and rushing waters took advantage of fractures and joints formed during lithification of the grainstone to break up and rotate the grainstone blocks on which the stromatolites later grew. The hematite and jasper cement are derived from the interaction between O_2-rich meteoric waters coming off the craton and dissolved Fe^{2+} from both the grainstone, as well as being possibly transported into the area during storm events (Kato et al., 2009).

The upper layer, located 50m below the top of the Gunflint shows similar brecciation of the grainstone. The brecciation present in the PR98-1 drill hole and the Mary Ellen mine indicate that the period of exposure may have been more extensive than the period of exposure of the

middle layer. The brecciated clasts of grainstone and chert in the PR98-1 drill core are rounded compared to angular grainstone clasts present in the Mink Mountain and Old School Road outcrops. The cement present in PR98-1 breccia, Mink Mountain and Old School Road outcrops are both iron-rich, with the PR98-1 cement being mostly magnetite-rich instead of the hematite- and jasper-rich cement from the middle layer. The appearance of the grainstone is the result of a similar mechanism to that which formed the spheroidal weathering horizon present in the Highway 11/17 outcrop, in which the percolation of waters through highly fractured rocks resulted in their rounding. The top exposure surfaces' brecciated layer appears to be more like the breccia in the middle exposure surface, in that it is formed by the reworking and transportation of the grainstones and other iron formations into the area before the formation of the oncolites and ooids on top.

7.2 Geochemical attributes of the alteration of the crystalline basement

The alteration of the Archean crystalline basement present in three outcrops studied in this project is characterized by the strong enrichment in Fe_2O_3, MnO, and MgO, as well as depletion in Ca, K and Na and the presence of chlorite and sericite replacing the feldspar. Similar alteration patterns have been noted by authors at two other Gunflint unconformity sites. The first was described from the core in diamond drill hole DH 87-3 by Kronberg and Fralick (1992), which contains an unconformable contact formed between Archean granite and the Gunflint grainstones. The second outcrop was noted by Polat et al. (2012), which discussed the unconformity present in the Schreiber Channel Nature Preserve, comprised of Archean pillow basalt, hyaloclastite, and pyroclastics beneath stromatolites and chert grainstones of the Gunflint Formation. The two groups of authors have put forward vastly different reasons for the alteration patterns present in the Archean crystalline basement rocks. The alteration pattern in the granitic

core from immediately below the unconformity in the DH 87-3 drill hole noted by Kronberg and Fralick (1992) is similar to the patterns in the Highway 11/17 and Kakabeka Falls outcrops. The alteration of the outcrops and core consists of the mineralogical replacement of feldspar and ferromagnesian minerals, mostly by chamosite, with some clinochlore and minor amounts a kaolinite. Geochemically the granite studied by Kronberg and Fralick (1992) shows the addition of Fe and Mn with losses in Mg, Ca and K. The sample site at the Schreiber Channel nature preserve has chlorite, silica and/or carbonate alteration of the basaltic pillows, hyaloclastite, and pyroclastics. Geochemically, the Schreiber Channel outcrop, has undergone mobilization of elements, including Fe, Na, MgO, K and Ca, as well as Si and Ti (Polat et al., 2012). Regarding alteration mechanism, Kronberg and Fralick (1992) have attributed the alteration of the granite beneath the unconformity to the diagenetic to possibly very low-grade metamorphic conditions that contributed to the replacement of the ferromagnesian phases by chlorite group minerals, with the diffusion of iron-rich fluids down into the alteration horizon. They attribute the source of the Fe, Mn and Mg in their fluids to leaching from the Gunflint grainstone that would have been deposited previously. Whereas Polat et al. (2012) attributed the alteration of the pillows, especially the Fe-enrichment, to exposure and weathering by the humid and warm Paleoproterozoic continental climate forming a paleosol horizon. Recent lateritic deposits form in similar warm, humid environments that would have accommodated the formation of the three outcrops present in the study as well as the other two mentioned above. Exposure to a tropical climate will increase the solubility of elements such as K, Na, Mg and Ca, while the less soluble elements, such as Fe and Al, become enriched (Freyssinet et al., 2005). When compared to the three study sites my data shows extreme enrichment in only iron content and not aluminum content. The high solubility of the elements Mg and to a lesser extent Mn can allow, during

weathering, the dissolution of these elements, by percolating groundwater, and redistribution elsewhere (Golightly, 1981; Elias, 2001; Fan and Gerson, 2011). This is not the case with two of the three outcrops in this study, which clearly show that alteration of the crystalline rocks has highly enriched them in Mg and Mn. The enrichment in both Fe_2O_3 and MgO, and to a lesser extent MnO, suggest that their presence in alteration of the study site outcrops is more than just subaerial weathering. This evidence indicates that Polat et al. (2012) have made an incorrect conclusion in that these authors omit, or do not factor in, the role of basinal fluids from the overlying Gunflint Formation, as suggested by Kronberg and Fralick (1992), in the alteration of the underlying Archean pillow basalts. The solubility, mobility and resulting depletion in Ca, Na and especially K are probably due to the inevitable chemical weathering during exposure to a possibly hot, humid climate, but the weathering signature can not be distinguished from the alteration pattern that overprints the basinal fluids altered horizon. Kronberg and Fralick (1992) also found evidence of weathering in the presence of kaolinite but were unable to comment further on it due to the intense diagenetic overprinting the rocks have undergone.

7.3   Geochemical attributes of the exposure surface

The Ce anomaly is an excellent proxy for redox conditions in which positive Ce represents in situ oxidation of Ce, negative Ce represents the movement of a Ce bearing fluid through an oxidized area that precipitated Ce and later precipitates phases with negative Ce anomalies, and samples with no Ce anomalies form in anoxic environments (German and Elderfield, 1990; Winter and Knauth, 1992; Bau, 1999; and Kato, 2006). Okajangas (1983) and Planavsky et al. (2009) have suggested that the Animikie basin had a strong redoxcline that stratified the oxygenated nearshore stratigraphic unit and the suboxic to anoxic deep water stratigraphic unit. The geochemical evidence presented above can show the location of this redox

boundary during regression and the prelude to exposure and also provides insight into the atmospheric content at the same time.

Figures 165, 166, and 167 are the combined plots of the Ce anomaly vs. La anomaly and the Ce anomaly vs. Eu anomaly for the samples collected from each of the exposure surfaces present in the Gunflint stratigraphy. The plots of the La vs. Ce anomalies show that the samples from the grainstones and stromatolites of the basal Gunflint contact mostly plot with negative Ce anomalies. These anomalies suggest that the grainstones and stromatolites were deposited in oxidized shallow waters shoreward of the redox front. Moving up the Gunflint stratigraphy the samples collected from the exposure surface present 45m above the base of the Gunflint, or equivalent formations, show that there is an overall change from the negative Ce anomalies above the lower exposure surface to predominantly positive Ce anomalies in these samples. This change in the anomalies suggests that the grainstones and stromatolites associated with the middle exposure surface formed in the redox boundary where anoxic waters carrying Ce came in contact with oxygen. There are a few sample sites that show no Ce anomalies; the grainstones at the Arundel Street bridge site and the stromatolites in the Magnetic Rock Trail outcrops. The Arundel Street Bridge sample site (Figure 167 E) was deposited in shallow water prior to maximum regression and exposure. Thus, the grainstones have no Ce anomaly, which is typical of most Gunflint samples. Whereas the Boulevard Lake grainstones interlayered with stromatolites show the distinct positive Ce anomalies suggesting deposition in the redox boundary of a slightly oxygenated environment. The positive Ce anomaly is present in all three sections of the exposure surface in the other various outcrops indicating the evolution of the redox front. The best evidence of this are the samples from Magnetic Rock Trail, which shows the change from positive Ce anomalies present in lower grainstones (Figure 167 E), which move

- 258 -

to no Ce anomaly in the stromatolites (Figure 167C). The positive Ce anomaly returns in the upper grainstone layers (Figure 167 A). This is due to a changing redox environment during deposition, which was interupted by sub-aerial exposure.

The upper stromatolite layer 50m below the capping limestone member has a wide spread of Ce anomalies, these include positive and negative Ce anomalies to nil anomalies in the Mount Whittlesey slaty and grainstone IF and oolitic layers. The samples from Mount Whittlesey are unique because the Gogebic IF was deposited in deeper, further offshore waters. Pufahl and Fralick (2004) interpreted this outcrop represent a coarsening upward sequence in which the parallel laminated IF layers near the base were deposited in deeper water, which during shallowing allowed for the formation of sand dunes that became exposed. It is difficult to explain the negative Ce anomalies in three of the grainstone samples underlying the stromatolites in the Gogebic IF; however the absence of anomalies in the other parallel laminated fine-grained precipitate from here indicate insignificant oxidation in this environment. The presence of high levels of Mn convolutes this theory a bit because positive Ce anomalies can be produced by scavenging of Ce by Mn-oxides, as seen in the PR98-1 oncolites, but positive Ce anomalies are not present here. The Mary Ellen and PR98-1 samples mostly have positive Ce anomalies indicating the oxidation of Ce occurring directly in the environment they were deposited in or developing later due to sub-aerial exposure.

Ce anomalies are ubiquitous throughout all the samples collected from the three exposure surface present in this project. These Ce anomalies are atypical of the rest of the Gunflint, which commonly contains no Ce anomalies. This suggests that the Ce anomalies are associated with shore proximal water and/or exposure and the evolution of the redox boundary affecting the chemistry of the area during deposition. Starting at the bottom of the Gunflint, the lower

stromatolites are mostly comprised of white cherts with negative Ce anomalies. This is indicative

of the redox boundary being farther offshore, where the ocean waters would have passed through

the boundary oxidizing the Fe and Ce and precipitating them before they reached the

stromatolites. This gives the stromatolites and grainstones a negative Ce anomaly. The white

colour is caused by the lack of oxidized Fe which would otherwise turn the stromatolites red.

Moving up the stratigraphy to the grainstones and stromatolites of the middle exposure surface

that show positive Ce anomalies and red colouration of the stromatolites. This is indicative of the

change in the location of the redox boundary to directly at the stromatolite growth area. Here the

reduced ocean waters passing through the boundary will oxidize and precipitate the Ce and Fe

directly into the stromatolites and grainstones. Most of the samples collected from the upper

layer still show the ubiquitous Ce anomaly in terms of a positive Ce anomaly and mostly red

stromatolites which support the presence of the redox boundary directly in the stromatolites. The

majority of samples collected from Mount Whittlesey do not show any Ce anomalies suggesting

deposition further offshore in this shoaling-upward sequence limited exposure of the sandbar

crest leading to insiginifacnt interation with meteroic waters(Pufahl and Fralick, 2004).

The plots presented in Figures 168, 169 and 170 are of the siliciclastic normalized

Cr/Al_2O_3 vs. V/Al_2O_3 and the V/Al_2O_3 vs. Ce anomaly (Cr and V in ppm, Al_2O_3 in %). This

miminimizes the role of siliciclastic content in controlling Cr and V content. To obtain average

ratios for Gunflint siliciclastic material seventeen samples with Al_2O_3 values above 5% were

randomly selected from analysis of the Gunflint Formation in Lafernier (2013) and the Cr/Al_2O_3

and V/Al_2O_3 ratios calculated. It was apparent that the data formed two groups. Eleven of the

samples had ratios of Cr/Al_2O_3 =8.7σ2.3 and V/Al_2O_3=17.3σ7.8, whereas six of the samples had

much lower values for Cr and V with ratios of Cr/Al_2O_3= 2.6σ0.3 and V/Al_2O_3=4.5σ3.4. The

highest ratios were Cr/Al$_2$O$_3$=12 and V/Al$_2$O$_3$=34. The existence of two geochemically distinct groups of siliciclastics was commented on by Lefreniere (2013) who believed the members of the groups with higher Cr and V values were sourced from basaltic volcanic ash, whereas the group with lower values was sourced from erosion of the craton. The ratios for the two groups plus the highest ratio values are plotted on the figures to determine the siliciclastic field for the Gunflint Formation (red dots). The majority of the plots especially from the samples collected from the lower and middle exposure surfaces, show enriched Cr and V values over the siliciclastic fields presented in the plots. This enrichment is visible in the upper exposure surface but only in samples from Mary Ellen mine and PR98-1, The Mount Whittlesey outcrop shows no enrichment. Lafraniere (2013) notes that the rocks from the Gunflint and Biwabik sampled away from exposure surface have low values of Cr and V, with V concentrations consistently below 50 ppm. Enrichment in Cr and V associated with exposure surfaces suggest that there must have been a second source of Cr and V, in addition to siliciclastics supplied by the weathering of the craton and basaltic ash. This source must be through the redox reactions of Cr and V. Cr and V are both immobile under anoxic condition and somewhat mobile under oxic conditions (Eary and Rai, 1987; Oze et al., 2007; Frei et al., 2009,2011). This addition of Cr and V requires an oxidizing fluid leaching Cr, and V from source rock sediments and precipitating the Cr and V when it enters a reduced area. This is probably done through a combination of two causes: 1) during exposure, lateral percolation of oxidized meteoric waters, leached Cr and V from the overlying adjacent craton and precipitating them in the reduced rocks below or, 2) oxidized surface and groundwaters carrying Cr and V entered the O$_2$ deficient oceans and precipitated them the vary nearshore environments.
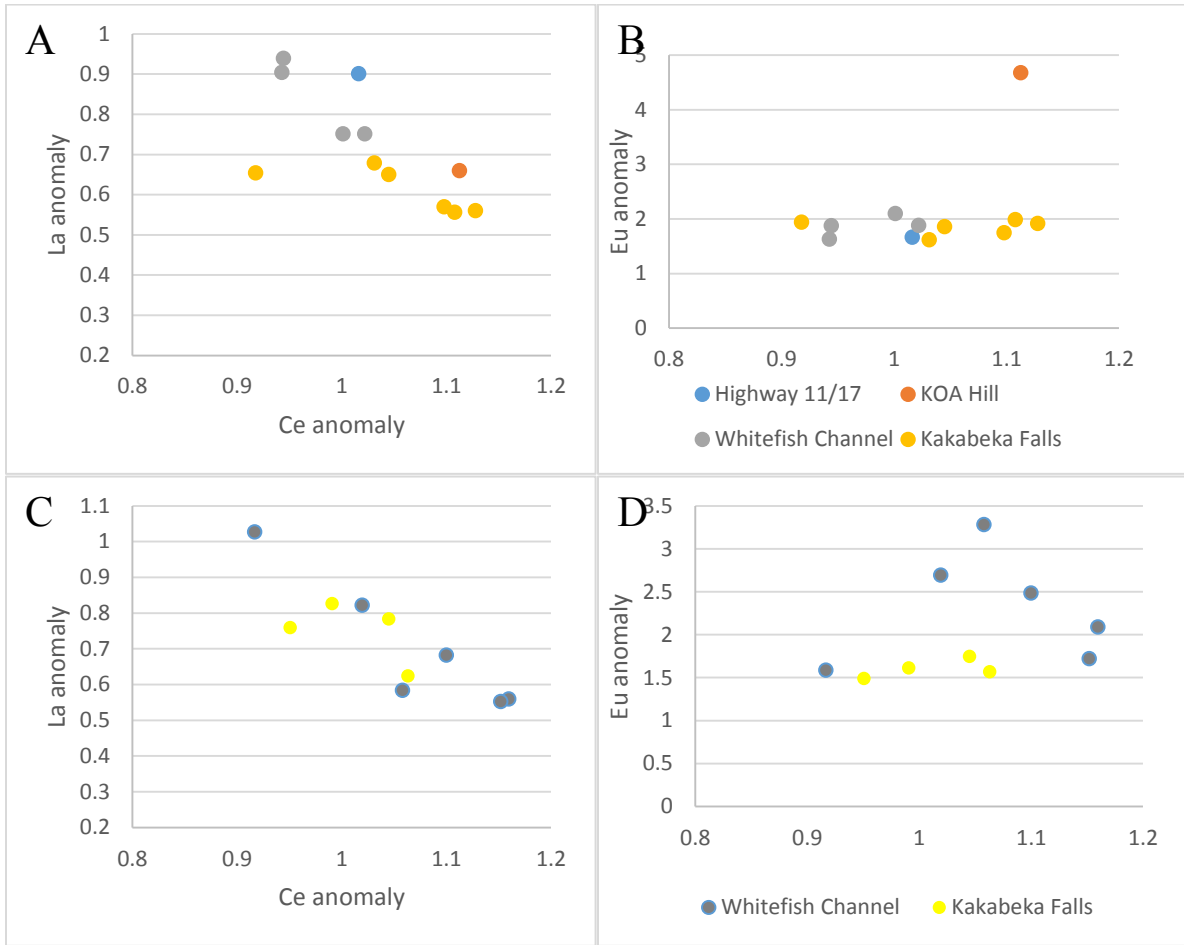
Figure 166: The La vs. Ce and Eu vs. Ce anomaly plots for the samples collected from the basal Gunflint contact. A,B) samples from grainstone overlying stromatolites; C,D) stromatolite samples.
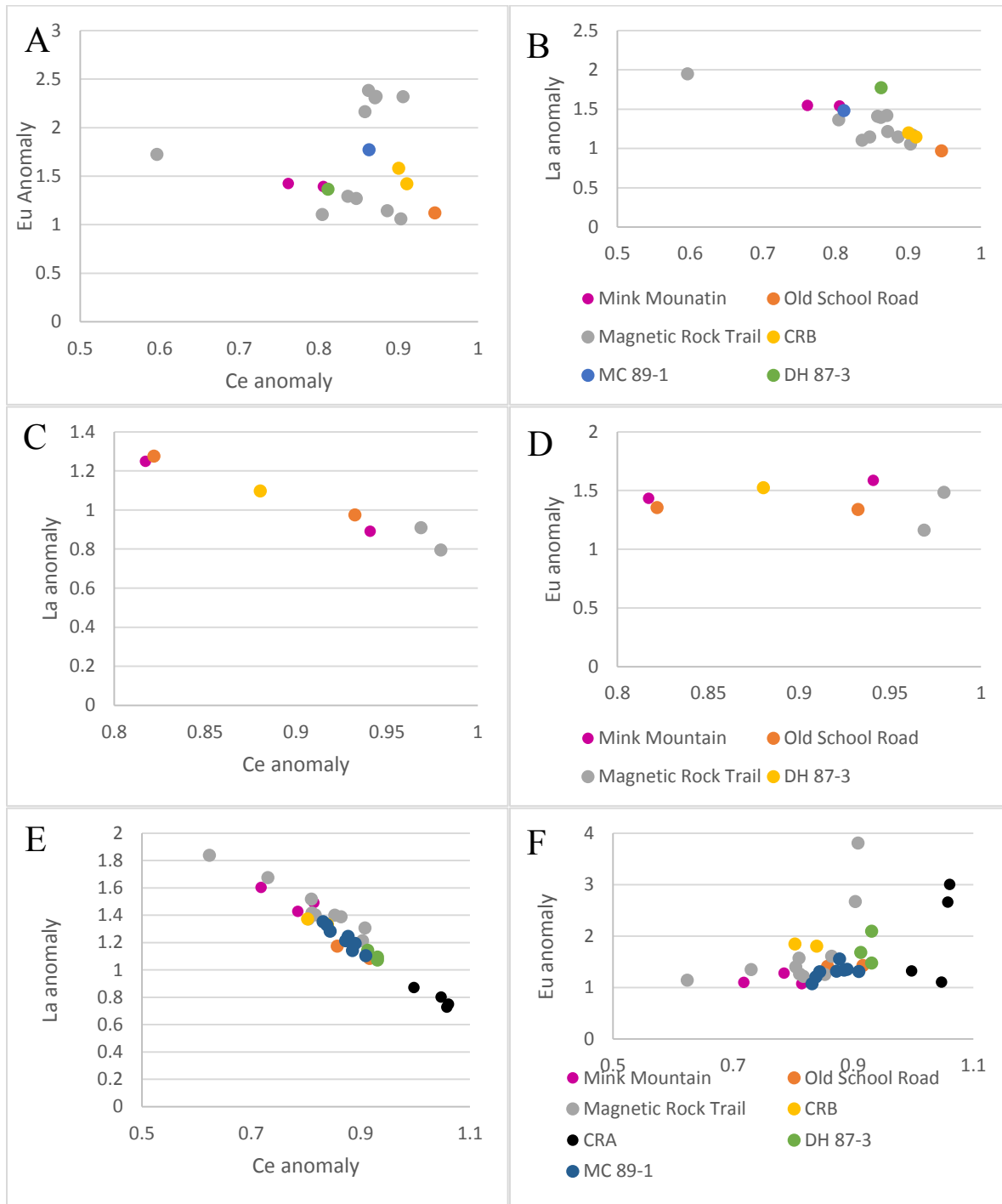
Figure 167: La vs. Ce anomaly and Eu vs. Ce anomaly plots for the middle exposure surface. A, B) upper grainstone; C, D) stromatolite stratigraphic unit; E, F) the lower grainstones and breccia.
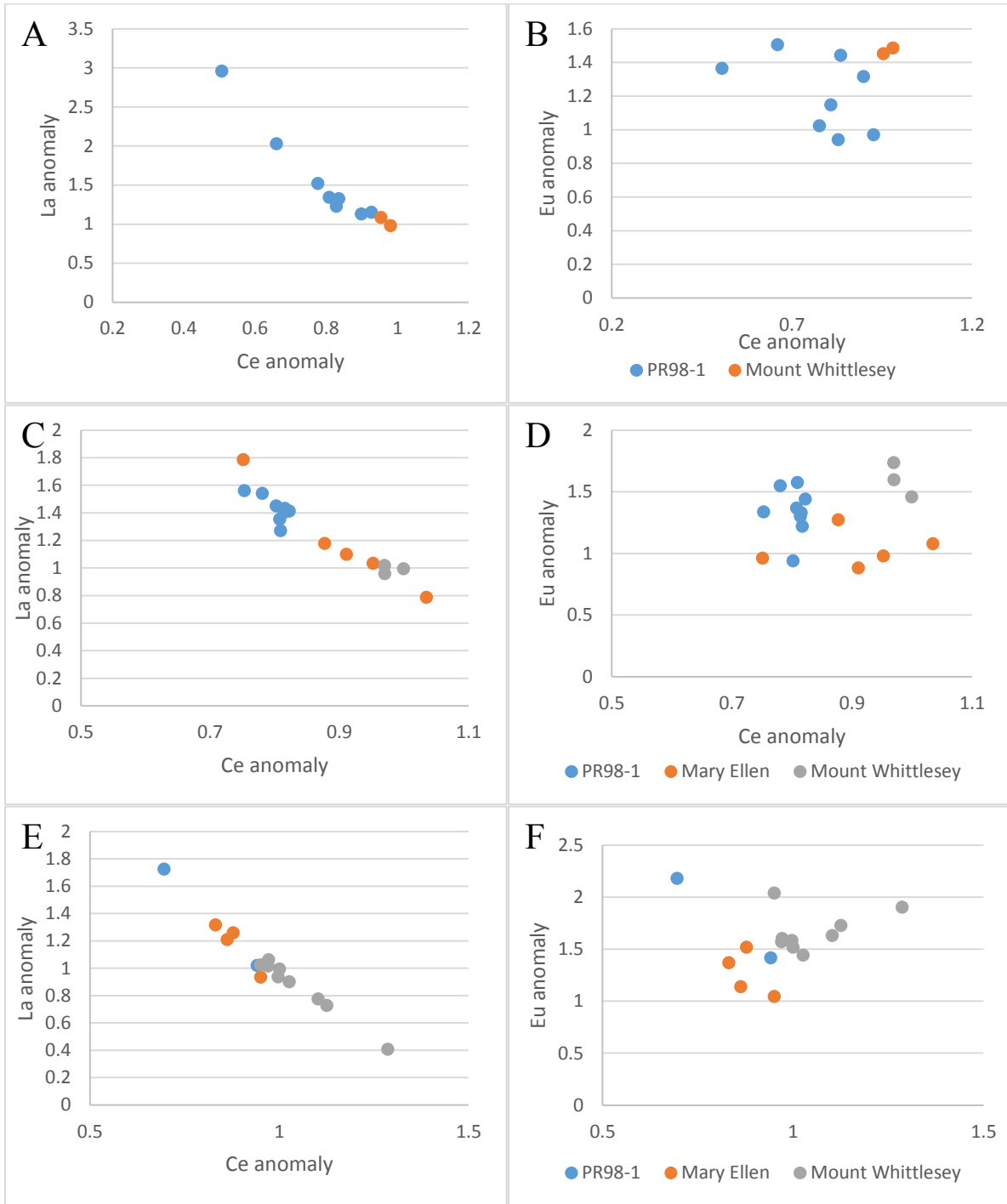
Figure 168: The Ce vs. La anomaly plots and Ce vs. Eu plots of the upper exposure surface: A, B) The upper grainstone layer. C, D) The stromatolites and E, F) The lower grainstone.

The other half of Figures 168, 169 and 170 are the plot of the V/Al_2O_3 ratio vs. Ce anomaly. The siliciclastic field is defined by plotting high and low average V/Al_2O_3 ratio as well as the highest V/Al_2O_3 ratio. These values were plotted with a Ce anomaly of 1 because it is safe to assume that these siliciclastic samples would plot with no Ce anomaly. These plots show no trend forming between the two. However, there are samples highly enriched in V and/or Cr associated with each of the exposure surfaces except Mount Whittlesey.

Eu anomalies seen in the REE curves are presented in the other half of the plots presented in Figures 165, 166, 167. These plots show that the majority of the samples collected for this project have positive Eu anomalies. A modern example of positive Eu anomalies can be found in samples taken from both metalliferous sediments and the fluids associated with modern hydrothermal vent systems (Barrett et al., 1988; German et al., 1990; Michard et al., 1993; Cocherie et al., 1994;). The positive Eu anomaly present in the Gunflint is indicative of a large component of fluids in the ocean at this time being derived from a hydrothermal vent source. This is indicative of the widespread anoxia throughout the ocean allowing for Fe and Mn to build up and concentrate in the waters (Kamber and Webb, 2001). However, a condsiderable number of samples have no Eu anomaly. It is unlikely that the majority of the chemical sediments comprising these samples were precipitated from typical seawater of the time and thus another fluid must have been involved. As the rocks associated with exposure surfaces have come into contact with, and had cements precipitates from, meteroic waters, which contain no Eu anomaly, it is resonable to assume these were responsible for the lack of Eu anomalies in some samples.
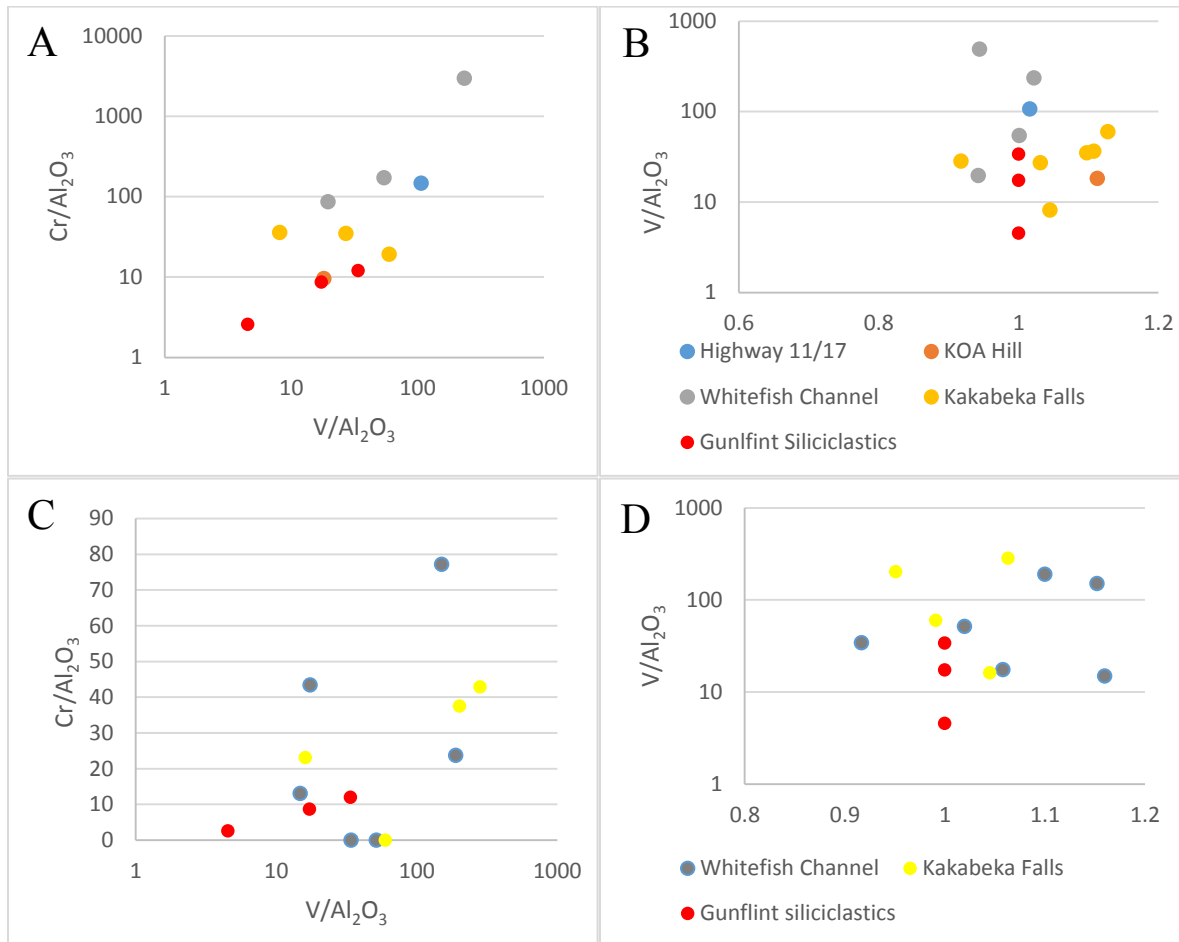
Figure 169: Cr vs. V and V vs. Ce anomaly plots of the Basal Gunflint contact. The Cr and V values (in ppm) were divided by the Al_2O_3 value (in %) of that sample to standardize for the siliciclastic component. A, B) Grainstones; C, D) stromatolites. The number of points for the various sample sites vary from A to B and C to D as samples with Cr below detection could not be plotted on A and C. See text for explanation of red dots.
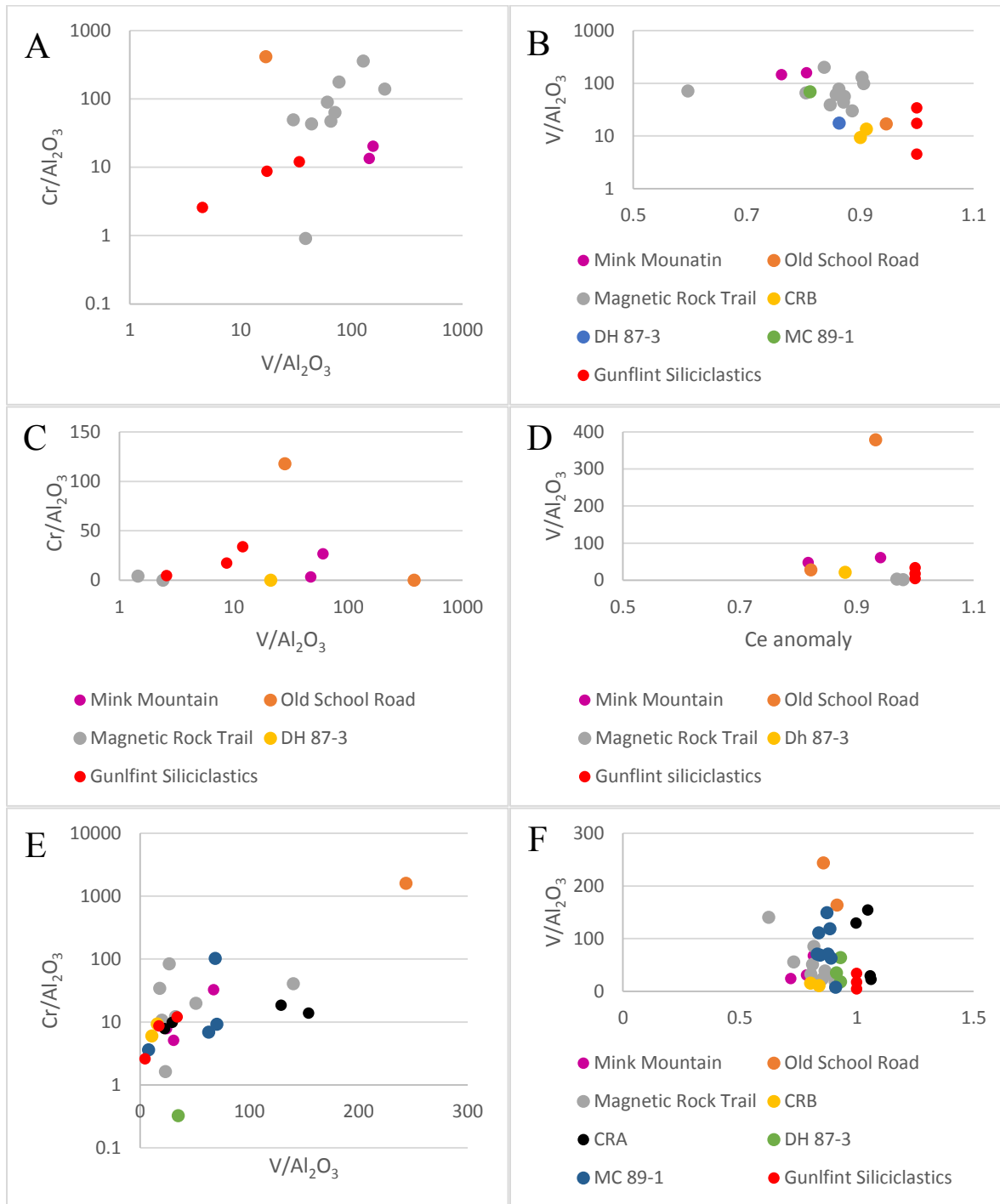
Figure 170: Siliciclastic standardized Cr vs. V and V vs. Ce anomaly plots for the middle exposure surface. A, B) the upper grainstones; C, D) the stromatolites; and E, F) the lower grainstones.
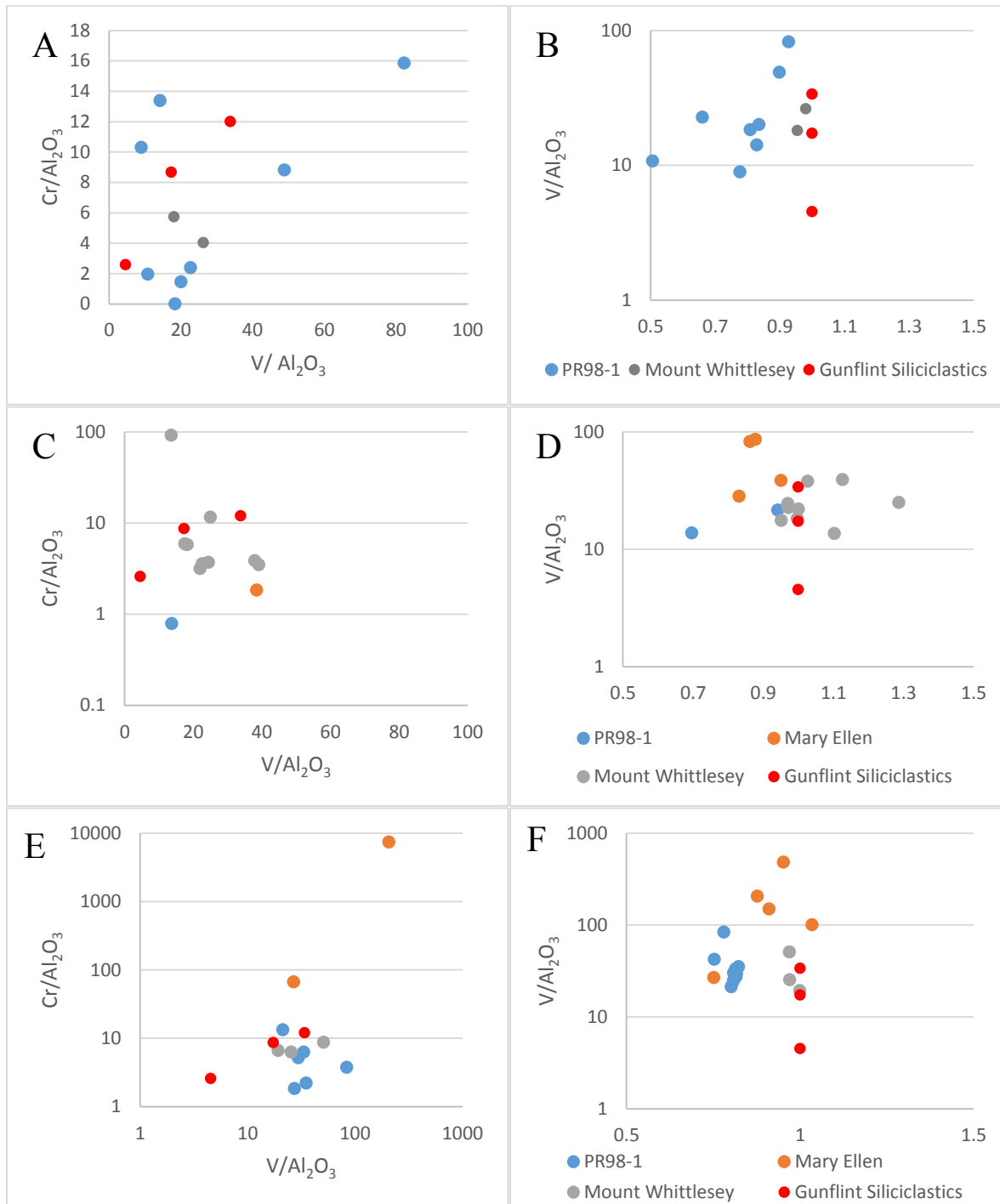
Figure 171: Siliciclastic standardized Cr vs V and V vs. Ce anomaly plots for the samples collected from the upper exposure surface. A,B) grainstones above the stromatolites C, D) Stromatolite samples and E, F) Grainstone samples from below the stromatolites.

The data collected for this project was not collected and analysed to calculate an exact value for the level of oxygen in the atmosphere, nor to give an overall characteristic of the atmosphere at the time of deposition. What this project did succeed in was identifying and describing the exposure surfaces and the subaerial alteration formed during the transgression-regression of the Animike Sea depositing the Gunflint formation. This project will hopefully help in the long run instead of the short term. This project will hopefully assist in identifying other exposure surfaces in outcrops deposited in the Proterozoic. The geochemical analysis performed on the samples can be used to prove the existence of the exposure surfaces as well as help identifying any alteration occurring within the exposure surface rocks.

8 CONCLUSIONS

Finding from this work allowed me to infer several aspects around the conditions during the deposition of the Gunflint and equivalent formations, especially during exposure to the atmosphere. A strong meteoric water component was essential in the alteration of the rocks at each exposure surface in the Gunflint. The spheroidal weathering of the crystalline basement rocks demonstrated that, even before the deposition of the Gunflint, meteoric water flowed through the area. The evidence of the flow of oxic meteoric water is evident throughout the exposure surfaces in the Gunflint formation. Starting at the base, there is dissolution of carbonate grainstone with deposition of vadose silt and subsequent precipitation of quartz within the open cavities. Progressing up the Gunflint stratigraphy, the grainstones exposured 45m above the base of the formation developed a quartz cement during exposure and were subsiquently brecciated.

Geochemically, the contrast between the oxic freshwaters coming off the craton and the anoxic seawaters filling the Animikie basin at the time is even more compelling. The Eu anomaly, which is present in most of the samples, is commonly much smaller than expected. This is probably representative of mixing of seawater with a positive Eu anomaly with oxic freshwaters with no Eu anomaly. Continuing with the Cr and V data presented previously, this data shows that the majority of the sample sites have some Cr and V values above the determined siliciclastic field. This enrichment in Cr and V is again representative of a system in which the oxic meteoric waters dissolve and transport Cr and V until they reached anoxic seawaters or sediments which causes precipitation. The Ce anomalies present throughout the samples collected for this project, are also indicative of the mixing of seawater with oxic freshwater. The samples with negative Ce anomalies present in the basal Gunflint layer denote a redox boundary offshore from the oxidizing nearshore waters. The positive Ce anomalies present

in the samples collected from directly above the Middle and Upper exposure surfaces indicates that oxygen supply to the nearshore during these times was not as robust and the redox boundary was directly in the environment of deposition.

The Mount Whittlesey outcrop represents a further offshore depositional environment with only a small, isolated area exposed to the atmosphere during maximum regression. Deposition of the iron formation in this coarsening- and thickening-upward sequence was driven by storm events delivering more oxygenated water from the nearshore (Pufahl and Fralick, 2004). Geochemically the samples collected from the outcrop at Mount Whittlesey show no Ce anomalies and Cr and V values within the siliciclastic field indicating the lack of significant amount of oxidized fresh water entering the depositional area during maximum regression.

9 REFERENCES

Abbey, S. (1983). Studies in "Standard Samples" of Silicate Rocks and Minerals 1969-1982. *Canadian Geological Survey paper 83-15*, 114.

Addison, W. D., Brumpton, G. R., Vallini, D. A., McNaughton, N. J., Davis , D. W., Kissin, S. A., . . . Hammond, A. L. (2005). Discovery of distal ejecta from the 1850 Ma Sudbury impact event. *Geology (Boulder), 33*, 193-196.

Aldrich , H. H. (1929). Geology of the Gogebic Iron Range of Wisconsin. *Wisconsing Geological and Natural History Survey Bulletin, 71*, 279 p.

Arthur, M. A., Dean, W. E., & Schlanger, S. O. (1985). Variations in global carbon cycle during Cretaceous related to climate volcanism, and changes in atmopheric CO2. In E. T. Sundquist, & W. S. Broecker (Eds.), *The carbon cycle and atmospheric CO2: natural variations Archean to present* (pp. 504-529). Washington D.C.: American Geophysical Union.

Arts, A. (2015). *Macro- and Micro-Structure Comparison of Ancient and Modern Iron-Rich Stromatolites.* Lakehead University, Ontario, Canada.

Barrett, T. J., Fralick, P. W., & Jarvis, I. (1988). Rare-earth-element geochemistry of some Archean iron formations north of Lake Superior, Ontario. *Canadian Journal of Earth Science, 25*, 270-580.

Bau, M. (1999). Scavenging of dissovled yttrium and rare earths by precipitating iron oxyhydroxides: experimental evidence for Ce oxidation, Y-Ho fractionation, and lanthanide tetrad effect. *Geochimica et Cosmochimica Acta, 63*, 67-77.

Bau, M., & Dulski, P. (1996). Distribution of yttrium and rare-earth elements in the Penge and Kuruman iron-formation, Transvaal Supergroup, South Africa. *Precambrian Research, 79*, 37-55.

Bekker, A., Holland, H. D., Wang, P. -L., Rumble III, D., Stein, H. J., Hanna, J. L., . . . Beukes, N. J. (2004). Dating the rise of atmospheric oxygen. *Nature, 427*, 117-120.

Bekker, A., Slack, J. F., Planavsky, N., Krapez, B., Hofman, A., Konhauser, K. O., & Pouxel, O. J. (2010). Iron Formation: The Sedimentary Product of a Complex Interplay among Mantle, Tectoic, Oceanic, and Biospheric Processes. *Economic Geology*, 467-508.

Bertine, K. K., & Turekian, K. K. (1973). Molybdenum in marine deposits. *Geochimica et Cosmochimica acta, 37*, 1415-1434.

Beukes, N., & Simonson, B. (2011). *Personal communication* .

Borchert , H. (1960). Genesis of marine sedimentary iron ores. *Inst Min. Met. Trans.,, 69*, 261-279.

Borchert, H. (1952). Die Bildungsbedingungen mariner Eisen-erzlagerstatten. *Chemie der Erde, 16*, 49-74.

Brancazio, P. J., & Cameron, A. G. (1964). The origin and evolution of atmosphere and oceans . *Proceedings of a Confrence, held at Goddard Institute for Space Studies, NASA, New York April 8-9.* New York: Wiley .

Braun, J. -J., Viers, J., Dupre, B., Polve, M., Ndam, J., & Muller, J. -P. (1998). Solid/liquid REE fractionation in the lateritic system of Goyoum, East Cameroon: The implication for the present dynamics of the soil covers of the humid tropical regions. *Geochimica et Comochimica Acta, 62*, 273-299.

Broderick , T. M. (1920). Economic Geology and stratigraphy of the Gunflint Iron District, Minnesota. *Economic Geology*, 422-452.

Brown, A. C. (2003). Redbeds: source of metals for sediments-hosted stratiform copper, sandstone copper, sandstone lead, and sandstone uranium-vanadium deposits. In D. R. Lentz (Ed.), *Geochemistry of Sediments and Sedimentary Rocks:Evolutionary Considerations to Mineral Deposits-Forming Environments* (pp. 121-132). St. John's: Geological Association of Canada.

Burton, J., & Fralick, P. W. (2007). Deposition and Cementation of Paleoproterozoic Gunflint Formation carbonate: implication for early hydrosphere chemistry. *Procedings and Abstracts- Insitiue on Lake Superior Geology. Meeting 53* (pp. 18-19). Institute on Lake Superior Geology.

Button , A., Brock, T. D., Cook, P. J., Eugster, H. P., Goodwin, A. M., James, H. L., . . . Walter, M. R. (1982). Sedimentary iron deposits, evaporites and phosphorites. State of the Art Report. In H. D. Holland, & M. Schidlowski (Eds.), *Mineral Deposits and Evolution of the Biosphere* (pp. 259-273). Berlin: Spriger-Verlag.

Canfield, D. E. (1998). A new model for Proterozoic ocean chemistry. *Nature, 396*, 450-453.

Canfield, D. E. (2005). The early history of atmospheric oxygen. *Annual Review of Earth Planetrary Science, 33*, 1-36.

Canfield, D. E., & Raiswell, R. (1999). The evolution of the sulphur cycle. *American Jorunal of Science, 299*, 697-723.

Cannon, W. F., & Addison, W. D. (2007). Distal ejecta from the 1850 Ma Sudbury impact in the Lake Superior Iron Ranges. *Geological Society of America Abstracts with Programs, 39*, p. 220.

Cannon, W. F., & Fralick, P. W. (2010). Field Trip 1: Western Gogebic Iron Ranges in Wisconsin,. In *Field Guide to the Geology of Precambrian Iron Formations in the Western Lake Superior Region, Minnesota and Michigan* (Vols. 10-01, pp. 1-14). Precambrian Research Center Guidebook.

Cloud , P. E. (1968). Atmospheric and hydrospheric evolution on the primitive Earth. *Science, 160*, 729-736.

Cloud, P. E. (1973). Paleoecological significance of the banded iron-formation. *Economic Geology, 68*, 1135-1143.

Cocherie, A., Calvez, J. Y., & Oudin-Dunlop, E. (1994). Hydrothermal activity by Red Sea sediments; Sr-Nd isotopes and REE signatures. *Marine Geology, 118*, 291-302.

Condie, K. C., Des Marais , D. J., & Abbott, D. (2001). Precambrian superplume and supercontinents: a record in black shales, carbon isotopes and paleoclimates? *Precambrian Research, 106*, 239-260.

Conway Morris, S. (2006). Darwin's dilemma: the realitites of the Cambrian 'explosion'. *Philosophical transactions of the Royal Society, 361*, 903-915.

Decho, A. W. (1990). Microbial exopolymer secretions in ocean envrionments: their role(s) in food webs and marine processes. *Oceanographic MArine Biology Annual Review, 28*, 73-153.

Dimroth , E. (1968). Sedimentary textures, diagenesis, and sedimentary environments of certain Precambrian ironstones. *Neues Jahrbuch fuer Geologie und Palaeontologie. Abhandlungen, 130*, 247-274.

Dimroth, E. (1976). Aspects of the sedimetary petrology of cherty iron formation. In K. H. Wolf (Ed.), *Handbook of Strata-Bound and stratiform Ore Deposits* (Vol. 7, pp. 203-254). Amsterdam: Elsevier.

Dimroth, E., & Chauvel, J. -J. (1973). Petrography of the Sokoman Iron Formation in part of the central Labrador trough. *Geological Society of America Bulletin, 84*, 111-134.

Dolence, J. D. (1961). The Pokegama quartzite in the Mesabi Range. 72.

Drever, J. I. (1974). Geochemical model for the origin of Precambrian banded iron formations. *Geological Society of America Bulletin, 85*, 1099-1106.

Eary, L. E., & Rai, D. (1987). Kinetics of chromium (III) oxidation to chromium (VI) by reaction with mangeses dioxide. *Environmental Science and Technonlgy, 21*, 1187-1193.

El Tabakh, M., Grey, C., Pirajoo, F., & Schreiber, B. C. (1999). Pseudomorphs after evaporite minerals interbedded with 2.2 Ga stromatolites of Yerrida Basin, Western Australia: origins and signifigance. *Geology, 27*, 871-874.

Elias, M. (2001). Nickel Laterite deposits-geological overview, resources and explotation . In *Giant Ore Deposits: Characteristics, genesis and exploration* (pp. 205-220).

Eugster, H. P., & Chou, I. -M. (1973). Depositional envrionemts of Precambrian banded iron formations. *Economic Geology, 68*, 1144-1168.

Ewers, W. E. (1983). Chemical factors in the deposition and diagensis of banded iron formations. In A. F. Trendall, & R. C. Morris (Eds.), *Iron-Formations:facts and problems* (pp. 491-512). Amsterdam: Elsevier.

Ewers, W. E., & Morris, R. C. (1981). Studies on the Dales Gorge Member of the Brockman Iron Formation. *Economic Geology, 76*, 1929-1953.

Fan, R., & Gerson, A. (2011). Nickel geochemistry of a Philippine laterite examined by bulk and microprobe synchtron analyses. *Geochimica et Comochimica Acta, 75*, 6400-6415.

Farquhar, J., Bao, H., & Thiemens, M. (2000). Atmospheric influence of Earth's earliest sulphur cycle. *Science, 289*, 756-758.

Flanagan, F. J. (1976). Description and Analzyes of Eight New USGS Rock Standards. *U.S. Geological Survey Professional Paper 840*, p 192.

Folk, R. L. (1968). *Petrology of Sedimentary Rocks.* Austin: Hemphill's.

Fralick , P. W., & Barrett, T. J. (1995). Depositional controls on iron formations associations in Canada. In A. G. Plint (Ed.), *Sediment Facies Analysis: International Association of Sedimentologist Special Publication 22* (Vol. 22, pp. 137-156). Oxford, U.K.: Blackwell Scientific Publications .

Fralick, P. W. (1988). Microbial Bioherms, Lower Proterozoic Gunflint Formation, Thunder Bay, Ontario. In H. H. Geldsetzer, N. P. James, & G. E. Tebbutt (Eds.), *Reefs: Canada and adjacent areas* (pp. 24-29). Canadian Society of Petroleum Geologist.

Fralick, P. W., & Riding, R. (2015). Steep Rock Lake: Sedimentology and geochemistry of an Archean carbonate platform. *Earth-Science Reviews, 151*, 132-175.

Fralick, P. W., Davis, D. W., & Kissin , S. A. (2002). The age of the Gunflint Formation, Ontario, Canada: Single Zircon U-Pb age determination from reworked volcanic ash. *Canadian Journal of Earth Sciences, 39*, 1089-1091.

Fralick, P., & Barrett, T. J. (1995). Depositional controls on iron formation associations in Canada. In S. F. Analysis.

Frankel, R. B., & Bazylinski, D. A. (2003). Biologically induced mineralization by bacteria. In P. M. Dove, S. Weiner, & J. J. De Yoreo (Eds.), *Biomineralization* (Vol. 54, pp. 94-114). Mineralogical Society of America, Reviews in Mineralogy and Geochemistry.

Frei, R., Gaucher, C., Dossing, L. N., & Sial, A. N. (2011). Chromium isotopes in carbonates- A tracer for cliamate change and for reconstructing the REDOX state of ancient seawater. *Earth and Planetary Science Letters, 312*, 114-125.

Frei, R., Gaucher, C., Poulton , S., & Canfield, D. (2009). Fluctuations in Precambiran atmospheric oxygenation recorded by chromium isotopes. *Nature, 461*, 250-253.

Freyssinet, P., Butt, C. R., Morris, R. C., & Piantone, P. (2005). Ore-Forming Process Related to Lateritic Weathering. In J. W. Hedenquis, J. F. Thompson, R. J. Goldfarb, & J. P. Richards (Eds.), *Economic Geology: One Hundreth Anniversary Volume 1905-2005* (pp. 681-722). Society of Economic Geology.

Garrels, R. A. (1987). A model for the deposition of the microbanded Precambrian iron formations. *American Journal of Science, 287*, 81-106.

Gellatly, A. M., & Lyons, T. W. (2005). Trace sulphate in mid-Proterozoic carbonates and the sulphur isotope record of biosphere evolution. *Geochimica et Cosmochimica Acta, 69*, 3813-3829.

German, C. R., & Elderfield, H. (1990). Application of the Ce anomaly as a paleoredox indicator; The ground rules. *Paleoceanography, 5*, 823-833.

German, C. R., Klinkhammer, G. P., Edmond, J. M., Mitra, A., & Elderfield, H. (1990). Hydrothermal scavenging of rare-earth elements in the ocean. *Nature, 345*, 516-518.

Gill, J. E. (1926). *Gunflint iron-bearing formation, Ontario.* Geological Survey of Canada, 1924 Part C.

Gill, J. E. (1927). Origin of the Gunflint iron-bearing formation. *Economic Geology, 22*, 687-728.

Gladney, E. S., & Roelandts, I. (1988). 1987 Compliation of Elemental Concentration Data for USGS BHVO-1, MAG-1, QLO-1, RGM-1 SCo-1, SDC-1, SGR-1 and STM-1. *Geostandard Newsletter, 12*, 253-362.

Glenn , C. R., Follmi, K. B., Riggs, S. R., Baturin, G. N., Grimm, K. A., Trappe, J., . . . Siegmund, H. (1994). P and phosporites: sedimentology and environments of formation. *Eclogae Geologicae Helveticae, 87*, 747-788.

Golightly, J. P. (1981). Nickeliferous laterite deposits . *Economic Geology* , 710-735.

Goodwin, A. M. (1956). Facies relations in the Gunflint Iron Formation. *Economic Geology, 51*, 565-595.

Goodwin, A. M. (1982). Distribution and origin of Precambrian banded iron formation. *Review of Brasilian Geoscience, 3*, 1-3.

Goodwin, A. M., Thode, H. G., Chou, C. -L., & Karkhansis, S. N. (1985). Chemostratigraphy and origin of the Late Archean siderite-pyrite-rich Helen Iron Formation, Michipicoten belt, Canada. *Canadian Journal of Earth Sciences, 22*, 72-84.

Govindaraju, K. (1994). 1994 Compilation of Working Values and Descriptions for 383 Geostandards. *Geostandards Newsletter, 18*, 1-158.

Gruner, J. W. (1946). *The mineralogy and geology of the taconites and iron ores of the Mesabi Range, Minnesota.* Office of the Commissioner Iron Range Resources and Rehabilitation. St. Paul: Minnesota Geological Survey.

Hazen, R. M., Papineau , D., Bleeker, W., Downs , R. T., Ferry , J. M., McCoy, T. J., . . . Yang , H. (2008). Mineral Evolution. *American Mineralogist, 93*, 1693-1720.

Helz, G. R., Miller, C. V., Charnock, J. M., Mosselmans, J., Pattrick , R., Garner, C., & Vaughan, D. (1996). Mechanism of molybdenum removal from the sea and its concentration in black shales; EXAFS evidence. *Geochimica et Cosmochimica Acta, 60*, 3631-3642.

Hemming , S. R., McLennan, S. M., & Hanson, G. N. (1995). Geochemical and Nd/Pb isotopic evidence of the Early Proterozoic Virginia Formation, Minnesota: Implication for tectonic setting of the Animikie Basin. *Journal of Geology, 103*, 147-168.

Hendrix, T. E. (1960). *Structural History of the East Gogebic iron range.* PhD Thesis, University of Wisonsin, Madison.

Hensel, E., Joslin, R., & Lehrmann, D. (1998). Early Proterozoic Ironwood Iron Formation, Mt. Whittlesey, Wisconsin. *Institute of Lake Superior Geology*, *44*, pp. 71-72. Minneapolis.

Hoffman, P. F. (in press). On the glacial history of snowball Earth 'exercising the imaginative muscle". *South Afircan journal of Geology* .

Hoffman, P. F., & Schrag, D. P. (2002). The snowball Earth hpothesis: testing the limits of global change. *Terra Nova, 14*, 129-155.

Hoffmann, P. (1987). Early Proterozoic foredeeps, foredeep magmatism and Superior-type iron-formations of the Canadian Shield. In A. Kroner (Ed.), *Proterozic Lithosphere Evolution Geodynamics Series* (Vol. 17, pp. 85-98).

Holland, H. D. (1984). *The chemical evolution of the atmosphere and oceans.* Princeton: Princeton University Press.

Holland, H. D. (2002). Volcanic gases, black smokers, and the Great Oxidation Event. *Geochemica et Cosmochimica Acta*, 3811-3826.

Holland, H. D. (2006). The oxygenation of the atmosphere and oceans. *Philosophical transactions of the Royal Society, 361*, 903-915.

Horwitz, R. C., & Smith, R. E. (1978). Bridging the Yilgarn and Pilbara Blocks, Western Australia. *Precambrian Research, 6*, 293-322.

Hotchkiss. (1919). Geology of the Gogebic range and its relation to recent mining. *Engineering and Mining Journal, 108*, 443-582.

Hough, J. L. (1958). Fresh-water environments of deposition of Precambrian banded iron formations. *Journal of Sedimentary Petrology, 28*, 414-430.

Huber, N. K. (1959). Some aspects of the Ironwood Formation of Michigan and Wisconsin. *Economic Geology, 54*, 82-118.

Ingall, E. D. (1888). *Mines and mining on Lake Superior. Part I.* Geological and Natural History Survey of Canada.

James , H. L. (1966). Chemistry of the iron-rich sedimentary rocks. *U.S. Geological Survey Professional Paper 440 W*, 61p.

James, H. L. (1954). Sedimentary facies of iron-formations. *Economic Geology, 49*, 235-293.

Ji, H., Wang, S., Ouyang , Z., Sun , C., Liu, X., & Zhou , D. (2004). Geochemistry of Red residua underlying dolomites in karst terrains of Yunnan-Guizhou Plateau II: The mobility of rare earth elements during weathering. *Chemical Geology, 203*, 29-50.

Kamber, B. S., & Webb, G. E. (2001). The geochemistry of late Archaen microbial carbonate: Implication for ocean chemistry and contiental erosion history. *Geochimica et Cosmochimica Acta, 65*, 2509-2525.

Kasting, J. F., & Walker , J. C. (1981). Limits on oxygen concentrations in the prebiological atmosphere and rate of abiotic fixation of nitrogen. *Journal of Geophysical Research, 86*, 1147-1158.

Kasting, J. F., Pavlov, A. A., & Siefert, J. L. (2001). A coupled ecosystem-climate model for predicting the methane concetration in the Archean atmosphere. *Origins of Life and Evolution of Biospheres, 31*, 271-285.

Kato, Y., Suzuki, K., Nakamura, K., Hickman, A. H., Nedachi, M., Kusakabe, M., . . . Ohmoto, H. (2009). Hematite formation by oxygenated groundwater more than 2.76 billion years ago. *Earth and Planetary Science Letters, 278*, 40-49.

Kato, Y., Yamaguchi, K. E., & Ohmoto, H. (2006). Rare earth elements in Precambrian banded iron formation: Secular changes of Ce and Eu anomalies and evolution of atmopheric oxygen. In S. E. Kesler , & H. Ohmoto (Eds.), *Evolution of Early Earth's Atmophere, Hydropshere and Bioshpere- Constraints from Ore Deposits* (pp. 269-291). Geological Society of America.

Kendall, B., Gordon, G. W., Poulton, S. W., & Anbar, A. D. (2011). Molybdenum isotope constraints on the extent of Late Paleoproterozoic ocean euxinia. *Earth and Planetary Science Letters, 307*, 450-460.

Kholodov, V. N., & Butuzova, G. Y. (2004). Problems of siderite formation and iron ore epochs: communication 1. Types of siderite being iron ore deposits. *Lithology and Mineral Resources, 39*, 389-411.

Kimberley, M. M. (1974). Origin of iron ore by diagenetic replacement of calcareous oolite. *Nature, 250*, 319-320.

Klein, C. (2005). Some Precambrian banded iron-formations from around the world: Their age, geologic setting, mineralogy, metamorphism, geochemistry, and origin. *American Mineralogist, 90*, 1473-1499.

Knoll, A. H., Javaux, E. J., Hewitt, D., & Cohen, P. (2006). Geological perspectives on the early diversification of eukaryotic organisims. *Philiosophical Transactions of the Royal Society B, 361*, 1023-1038.

Konhauser, K. O., Lalonde, S. V., Planavsky, N. J., Pecoits, E., Lyons, T. W., Mojzsis, S. J., . . . Bekker, A. (2011). Aerobic bacterial pyrite oxidation and acid rock drainage during the Great Oxidation Event. *Nature, 478*, 369-373.

Konhauser, K. O., Pecoits, E., Lalonde, S. V., Papineau , D., Nisbet, E. G., Barley, M. E., . . . Kamber, B. S. (2009). Oceanic nickel depletion and methoangen famine before the Great Oxidation Event. *Nature, 458*, 750-753.

Koppi, A. J., Edis, R., Field, D. J., Geering, H. R., Klessa, D. A., & Cockayne, J. H. (1996). Rare earth element trends and cerium-uranium-manganese association in weathered rock from Koongarra, Northern Territory, Austraila. *Geochimica et Cosmochimica Acta, 52*, 1695-1707.

Kronberg, B., & Fralick, P. (1992). Geochemical alteration of felsic Archean rocks by Gunflint Formation-derived fluids, Quetico-Superior region, northwest Ontario. *Canadian Journal of Earth Science, 29*, 2610-2616.

LaBerge, G. L., Robbins, E. J., & Han, T. -M. (1987). A model for the biological precipitation of Precambrian iron-formations, A Geological evidence. In P. W. Appel, & G. L. LaBerge (Eds.), *Precambrian iron-formations* (pp. 69-96). Athens: Theophrastus Publication.

Lafreniere, D. (2013). *A regional geochemical study of the Gunflint Formation.* Lakehead University.

Lei, W., Linsalata, P., Franca, E. P., & Eisenbud, M. (1986). Distribution and mobilization of cerium, lanthanum and neodymium in the Morro do Ferro basin, Brazil. *Cheimcal Geology, 55*, 313-322.

Liu, Y. -G., Miah, M., & Schmitt, R. a. (1988). Cerium: a chemical tracer for paleo-oceanic redox conditions. *Geochimica et Cosmochimica Acta, 52*, 1361-1371.

Lowenstam, H. A. (1981). Minerals formed by organisms. *Science, 211*, 1126-1131.

Lougheed, M. S. (1983). Origin of Precambrian iron formations in the Lake Superior region. *Geological Society of America Bulletin, 94*, 325-340.

Lowenstam, H. A., & Weiner, S. (1983). Mineralization by organisms and the evolution of biomineralization. In P. Westbrook, & E. W. de Jong (Eds.), *Biomineralization and Biological Metal Accumulation* (pp. 191-203).

Maliva, R. G., Knoll, A. H., & Siever, R. (1989). Secular change in chert distribution: A reflection of evolving biological participation in the silica cycle. *PALAIOS, 4*, 519-532.

Maric, M. (2006). *Sedimentology and sequence stratigrphy of the Paleoporoterzoic Rove and Virginia Formations, southwest Superior Province. MSc Thesis.* Lakehead University.

Marseden, R. (1978). Iron Ore reserves of Wisconsin: A minerals availability system report. *Proceedings, American Insttutes of Mining Engineers, 51st Annual Meeting, Minnesota Section.* Duluth, MN.

Marsh, J. S. (1991). REE fractionation and Ce anomalies in weathered Karoo dolorite. *Chemical Geology, 90*, 189-194.

Melezhik, V. A., Fallick, A. E., Rychanchik, D. V., & Kuznetsov, A. B. (2005). Mass-independent isotope effects in Archean (2.5 to 3.8 Ga) sedimentary sulphides determined by ion microporbe analysis. *Terra Nova, 17*, 141-148.

Micahrd , A., Michard , G., Suben, D., Stoffers, P., Cheminee, J.-L., & Binard , N. (1993). Submarine thermal springs associated with young volcanoes: The Teahitia vents, Society Islands, Pacififc Ocean. *Geochimica et Cosmochimica Acta, 57*, 4977-4986.

Moorhouse, W. W., & Goodwin, A. M. (1960). Neebing Area, Gunflint Iron Range, District of Thunder Bay. *Map*. Ontario Geological Survey.

Morey , G. B. (1983). Animikie Basin, Lake Superior Region, U.S.A. In A. F. Trendall, & R. C. Morriss (Eds.), *Iron Formation Facts and Problems* (pp. 13-67). Amsterdam: Elsevier.

Morris, R. C. (1993). Genetic modeling for banded iron-formation of the Hamersley Group, Pilbara and Kaapvaal cratons. *Precambiran Research, 60*, 243-286.

Nesbitt, W. H. (2003). Petrogenesis of siliciclastic sediment and sedimentary rocks. In D. R. Lentz (Ed.), *Geochemistry of Sediments and Sedimentary Rocks: Evolutionary Consideration to Mineral Deposits-Forming Environments GEOtext 4* (pp. 39-51). St. John's: Geological Association of Canada.

Nesbitt, W. H., & Young, G. M. (1982). Early Proterozoic climates and plate motion inferred from major element chemistry of luities. *Nature*, 715-717.

Nisbet, E. G., Grassineau, N. V., Howe, C. J., Abell, P. I., Regelous, M., & Nisbet, R. E. (2007). The age of Rubisco: The evolution of oxygenic photosynthesis. *Geobiology, 5*, 311-335.

Ohmoto, H. (2002). Banded iron formations as guides for the history of the lithosphere, atmosphere, and hydrosphere. *Abstracts with Programs - Geological Society of America, Geological Society of America, 2002 Annual Meeting,*, *34*, pp. 283-284. Denver.

Ohta, A., & Kawabe, I. (2001). REE (III) adsorption onto Mn dioxide and Fe oxyhydroxide: Ce (III) oxidation by Mn dioxide. *Geochimica et Cosomochimica Acta, 65*, 695-703.

Ojakangas, R. W. (1983). Tidal deposits in the Early Proterozoic basin of the Lake Superior Region- The Palms and Pokegama Formations: Evidence for subtidal-shelf deposition of Superior-type banded iron formations. In L. G. Medaris (Ed.), *Early Proterozoic Geology of the Great Lakes Region: Geological Society of America Memoir 160* (pp. 49-66). Geological Society of America.

Ojakangas, R. W., Morey, G. B., & Southwick, D. L. (2001). Paleoproterozoic basin development and sedimentation in the Lake Superior region, North America. *Sedimentary Geology, 141*, 319-341.

Oze, C., Bird, D. K., & Fendorf, S. (2007). Genesis fo hexavalent chromium from natural sources in soil and groundwater. *Proceedings of the Natural Academy of Science, 104*, 6544-6549.

Pavlov, A. A., & Kastings, J. F. (2002). Mass-independent fractionation of sulphur isotopes in Archean sediments: strong evidence for an anoxic Archean atmosphere. *Astrobiology, 2*, 27-41.

Peter, J. M. (2003). Ancient Iron Formations: their genesis and use in the exporation for stratiform base metal sulphide deposits, with examples from the Bathurst Mining Camp. In D. R. Lentz (Ed.), *Geochemistry of Sediments and Sedimentary Rocks: Evolutionary Consideration to Mineral Deposit-Forming Environments GEOText 4* (pp. 145-173). Geological Association of Canada.

Polat, A., Longstaffe, F., Weisener, C., Fryer, B., Frei, R., & Kerrich, R. (2012). Extreme element mobility during transformation of Neoarchean (ca 2.7 Ga) pillow basalts to a Paleproterozoic (ca. 1.9 Ga) paleosol, Schreiber Beach, Ontario, Canada. *Chemical Geology, 326-327*, 145-173.

Poulton, S. W., Fralick, P. W., & Canfield, D. E. (2004). The transition to a sulphidic ocean ~1.84 billion years ago. *Nature, 43*, 173-177.

Poulton, S. W., Fralick, P. W., & Canfield, D. E. (2010). Spatial variability in ocean redox structure 1.8 billion years ago. *Nature Geoscience, 3*, 486-490.

Pufahl, P. K. (2010). Bioelemental sediments. In N. P. James , & R. W. Dalrymple (Eds.), *Facies Models* (4th ed., pp. 477-503). Geological Association of Canada.

Pufahl, P. K., & Fralick , P. W. (2004). Depostional controls on Palaeoproterozoic iron formation accumulation, Gogebic Range, Lake Superior region, USA. *Sedimentology*, 791-808.

Pufahl, P. K., & Hiatt, E. E. (2011). Oxygenation of the Earth's atmosphere-ocean systems: A review of physical and chemical sedimentological responses. *Marine and Petroleum Geology, 32*, 1-20.

Pufahl, P. W., Fralick, P. W., & Scott, J. (2000). Field trip 4: Geology of the Paleoproterozoic Gunflint Iron Formation. *Institute on Lake Superior Geology Procedings, 46th Annual Meeting, Thunder Bay, Onatrio, 46th* . Thunder Bay.

Rankin , P. C., & Childs, C. W. (1976). Rare-earth elements in iron-maganese concretion from some New Zealand soils. *Chemical Geology, 18*, 55-64.

Rasmussen, B., & Buick, R. (1999). Redox state of the Archean Atmosphere: Evidence from detrital minerals in ca. 3250-2750Ma sandstones from the Pilbara Craton, Australia. *Geology, 27*, 115-118.

Reddy, S. M., & Evans, D. A. (2009). Paleoproterozoic supercontinents and global evolution: correlations from core to atmosphere. In S. M. Reddy , R. Mazumder, D. A. Evans, & A.

S. Collins (Eds.), *Paleoproterozoic Supercontinents and Global Evolution* (Vol. 323, pp. 1-26). London: Geological Society, Special Publication .

Riding, R. (1991). *Classification of microbial carbonates.* (R. Riding , Ed.) Berlin: Springer.

Riding, R. (2000). Microbial Carbonates: the geological record of calcified bacterial-algal mats and biofilms. *Sedimentology, 47 (Suppl. 1)*, 179-214.

Roscoe, S. M. (1969). Huronian Rocks and Uraniferous Conglomerates in the Canadian Shield. *Geological Survey of Canada Paper*, 68-40.

Roscoe, S. M., & Minter, W. E. (1993). Pyritic paleoplacer gold and uranium deposits. *Mineral Deposit Modeling, Geological Association of Canada special paper 40*, pp. 103-124.

Roy, S. (1997). Genetic diversity of manganese deposition in the terrestrial geological record. In K. Nicholson, J. R. Hein, B. Buhn, & S. Dasgupta (Eds.), *Manganese mineralization:geochemistry and mineralogy of terrestrial and marine deposits* (Vol. 119, pp. 5-27). Geological Society Special Publications.

Schmidt, R. (1976). Geolgogy od the Precambrian W (lower Precambrian) rocks in western Gogebic County Michigan. *US Geological Survey Bulletin, 1407*.

Schneider , D. A., Bickford , M. E., Cannon, W. F., Schulz, K. J., & Hamilton , M. A. (2002). Age of volcanic rocks and syndepositional iron formations, Marquette Range Supergroup: implications for the tectonic setting of Paleoproterozoic, iron formations of the Lake Superior region. *Canadian Journal of Earth Sciences, 39*, 999-1012.

Scott, C., Lyons, T. W., Bekker, A., Shen, Y., Poulton, S. W., Chu, X., & Anbar, A. D. (2008). Tracing the stepwise oxygenation of the Proterozic ocean. *Nature, 425*, 456-459.

Severson, M. J., Heine, J. J., & Patelke, M. M. (2009). *Geologic and stratigraphic controls of the Biwabik Iron Formation and the aggregate potential of the Mesabi Iron Range, Minnesota.* University of Minnesota, Duluth. National Resources Research Institute,.

Shapiro, R. S., & Konhauser, K. O. (2015). Hematite-coated microfossils: Primary ecological fingerprint of taphonomic oddity of the Paleoproterozoic? *Geobiology, 13*, 209-224.

Shiller, A. M., & Mao, L. (1999). Dissolved vanadium on the Louisiana shelf: effect of oxygen depletion. *Continental Shelf Research, 19*, 1007-1020.

Shiller, A. M., & Mao, L. (2000). Dissolved vanadium in rivers: effects of silicate weathering. *Chemical Geology, 165*, 13-22.

Siever, R. (1992). The silica cycle in the Precambrian. *Geochimica et Comochimica Acta*, 3265-3272.

Silver, L. P. (1906). *The Animikie iron range.* Ontario Bureau of Mines.

Simonson, B. M. (1987). Early silica cementation and subsequent diagensis in arenites from four Early Proterozoic iron formations of North America. *Journal of Sedimentary Petrology, 57*, 494-511.

Smith, W. N. (1905). *Loon Lake iron bearing district.* Annual Report, Ontario Bureau of Mines.

Sommers, M. G., Awramik, S. M., & Woo, K. S. (2000). Evidence for initial calcite-aragonite composition of Lower Algal Chert member ooids and stromatolites, Paleoproterozoic Gunflint Formation, Ontario, Canada. *Canadian Journal of Earth Sciences, 37*, 1229-1243.

Southwick, D. L., & Morey , G. B. (1991). Tectonic imbrication and foredeep development in the Penokean orogeny, east-central Minnesota. An Interpretation based on regional geophysical and the results of test drilling. *United States Geological Survey Bulletin, 1904-C*, 17.

Sugiyama, M. (1989). Seasonal variation of vanadium concentration in Lake Biwa, Japan. *Geochemistry Journal, 23*, 111-116.

Tanton, T. L. (1923). *Iron Formation at Gravel Lakes, Thunder Bay District, Ontario.* Summary Report, Geologcal Survey of Canada, Part C.

Taylor, S. R., & McLennan, S. M. (1985). *The continental crust: it composition and evolution; an examination of the geochemical record preserved in sedimentary rocks.* Blackwell,Oxford.

Taylor , S. R., & McLennan, S. M. (1995). The Geochemical evolution of the continental crust. *Reviews of Geophysics, 33*, 241-265.

Trendall, A. F. (2002). The Significance of iron-formation in the Precambrian stratigraphic record. In W. Altermann, & P. L. Corcoran (Eds.), *Precambrian Sedimentary Environments: A Modern Appproach to Ancient Depositional Systems* (Vol. Special Publication Number 33, pp. 33-67). Blackwell Science.

Wanty , R. B., & Goldhaber, M. B. (1992). Thermodynamics and kinematics of reactions involving vanadium in natural systems:accumulation of vanadium in sedimentary rocks. *Geochimica et Cosmochimica Acta*, 1471-1483.

Wehrli, B., & Stumm, W. (1989). Vanadyl in natural waters: adsorption and hydrolysis promote oxygenation. *Geochimica et Cosmochimica Acta, 53*, 69-77.

Wilson, S. A. (2000). Data Compilation for USGS reference material BHVO-2, Hawaiian Basalt. U.S.G.S Open File Report.

Winter, B. L., & Knauth, L. P. (1992). Stable isotope geochemistry of cherts and carbonates from the 2.0 Ga Gunflint Iron Formation: implications for the depositional setting, and the effects of diagenesis and metamorphis. *Precambrian Research, 59*, 283-313.

Wolff, J. F. (1917). Recent geologic developments on the Mesabi Iron Range, Minnesota. *Transactions of the American Institue of Mining and Metallurgical Engineers, 56*, 229-257.

Yang, W., & Holland, H. D. (2003). The Hekpoort paleosol profile in Strata 1 at Gaborone, Botswana: soil formation during the Great Oxidation Event. *American Journal of Science, 303*, 187-220.

Zahnie, K., Claire, M., & Catlin, D. (2006). The loss of mass-independent fractionation in sulpher due to Paleoproterozic collaspe of atmospheric methane. *Geobiology, 4*, 271-283.

10 APPENDIX

10.1 Appendix A

10.1.1 Basal Exposure Surface

Highway 11/17 outcrop

Sample	Above the base (cm)	Lithology
17C		Core of the altered granodiorite boulder
17B	All above	Inbetween the edge and the core
17A	the	Edge of the altered granodiorite boulder
16	alteration	Large scale planar cross-stratified sandstone
15	horizon	Immature clay-rich sandstone
14		Immature pebbly congomerate
13	250	Outer edge of the spheroidal weathering boulder
13A	245	
12	246	Altered material from between the altered boulders
11	226	Altered material that the boulder sit on
10	218	
9	211	Completely altered granodiorite
8	205	
7	183	
6	173	Slighly altered granodiorite
5	160	
4	120	
3	105	Fresh granodiorite
2	60	
1	10	

Major Oxide (wt%)

	Al_2O_3	CaO	Fe_2O_3	K_2O	MgO	MnO	Na_2O	P_2O_5
17C	12.812	0.476	30.343	0.043	4.354	0.126	1.365	0.268
17B	11.674	0.355	28.599	0.025	3.969	0.141	1.397	0.301
17A	12.464	0.302	30.143	0.030	4.267	0.135	1.749	0.263
16	0.351	15.173	0.912	0.014	0.209	0.184	0.493	0.002
15	4.233	0.041	9.964	0.040	1.682	0.061	0.649	0.025
14	6.433	0.065	14.985	0.031	2.735	0.053	0.539	0.036
13	11.829	0.459	30.086	0.023	4.039	0.189	1.657	0.259
13A	9.652	0.368	25.182	0.021	3.229	0.152	1.118	0.218
12	3.671	12.425	11.683	0.032	5.322	0.965	1.535	0.163
11	10.949	0.309	27.604	0.040	3.886	0.179	1.435	0.233
10	9.755	0.202	24.596	0.058	3.285	0.207	0.869	0.179
9	10.503	0.233	25.216	0.645	3.594	0.184	1.103	0.169
8	11.568	0.229	24.544	1.689	3.976	0.231	1.093	0.207
7	12.876	1.110	2.710	7.877	1.421	0.030	9.500	0.174
6	12.540	2.259	2.682	7.366	1.759	0.048	9.301	0.192
5	12.646	2.043	2.526	8.113	1.965	0.045	9.284	0.206
4	12.782	2.246	2.734	7.342	2.180	0.049	10.185	0.215
3	12.687	2.170	2.652	7.829	2.174	0.047	9.387	0.215
2	13.144	2.155	3.156	7.303	2.222	0.051	10.519	0.226
1	12.453	1.963	2.987	7.751	2.160	0.051	9.193	0.203

Major Oxide and Trace Elements (wt% and ppm)

	TiO2	Ba	Cr	Sr	V	Zr	Y
17C	0.294	1232.100	47.473	644.680	36.440	171.940	1.340
17B	0.328	1234.100	54.693	681.480	40.420	198.820	1.600
17A	0.313	1282.700	51.073	729.480	37.360	177.580	1.480
16	0.320	1331.900	51.153	696.680	37.480	157.520	0.440
15	0.291	1472.300	46.993	713.880	34.540	157.740	0.200
14	0.287	1366.300	53.233	701.280	34.800	152.980	0.320
13	0.250	1384.700	43.413	641.880	31.780	165.260	1.620
13A	0.184	223.100	44.073	32.040	28.380	166.240	1.280
12	0.110	74.860	31.293	9.800	21.340	145.060	1.080
11	0.149	150.320	35.613	8.860	26.960	135.840	1.260
10	0.183	169.880	54.533	9.420	31.020	172.120	0.900
9	0.011	111.480	4.893	27.480	2.120	73.100	1.040
8	0.180	84.160	45.473	6.160	25.700	191.420	1.120
7	0.312	70.580	62.513	8.700	25.500	233.620	0.840
6	0.029	37.820	8.533	3.120	18.080	40.100	0.920
5	0.017	7.640	4.793	2.820	5.420	63.840	0.900
4	0.002	12.540	0.453	17.580	6.180	24.100	0.980
3	0.307	18.580	54.913	20.540	31.360	198.020	1.000
2	0.279	12.240	54.993	8.020	36.720	207.820	1.100
1	0.324	13.980	63.293	8.320	49.420	260.820	0.960

Rare Earth Elements (ppm)

Sample	La	Ce	Pr	Nd	Sm	Eu	Gd	Tb
17C	127.748	367.709	28.36	100.942	15.008	3.119	11.408	1.537
17A	13.842	41.167	5.888	27.006	6.908	1.839	7.445	1.363
16	33.207	62.005	7.602	31.024	5.974	2.155	6.041	0.819
15	5.113	11.234	1.348	5.37	1.207	0.313	1.201	0.207
14	13.1	27.767	3.203	11.93	2.286	0.562	1.955	0.319
13	25.589	60.573	7.968	35.068	8.467	2.268	8.783	1.549
13A	16.882	40.137	5.35	23.683	5.541	1.439	5.527	0.967
12	66.139	123.559	16.543	70.57	16.127	5.147	16.915	2.498
11	124.939	314.373	24.92	93.199	14.607	3.294	12.282	1.593
10	74.103	137.854	15.647	59.69	9.821	2.074	7.928	1.058
9	90.005	166.286	18.987	70.194	11.385	2.158	9.011	1.211
8	240.289	455.252	35.977	133.913	20.572	4.078	15.583	1.853
7	274.909	585.221	47.461	182.936	30.133	10.08	25.148	3.118
6	258.538	559.55	45.337	172.34	28.758	9.809	24.234	3.036
5	279.727	605.337	49.893	193.049	32.583	11.185	27.763	3.448
4	342.95	727.367	60.195	230.148	37.993	11.976	32.078	4.034
3	291.275	631.527	52.552	201.691	33.789	10.741	29.119	3.582
2	294.022	631.572	52.355	204.617	34.316	10.631	29.181	3.698
1	328.358	706.017	58.582	226.734	37.442	11.91	32.194	4.021

	Dy	Ho	Er	Tm	Yb	Lu
17C	7.898	1.385	4.373	0.659	4.231	0.66
17A	8.83	1.881	6.13	0.923	5.828	0.891
16	4.27	0.767	2.147	0.312	2.019	0.295
15	1.255	0.257	0.817	0.124	0.824	0.126
14	1.864	0.363	1.121	0.171	1.094	0.167
13	9.838	2.067	6.706	0.986	6.27	0.941
13A	6.396	1.376	4.504	0.691	4.381	0.676
12	13.206	2.394	6.108	0.766	4.469	0.606
11	8.13	1.377	4.074	0.588	3.725	0.559
10	5.508	0.96	2.93	0.424	2.703	0.41
9	6.259	1.086	3.233	0.458	2.949	0.464
8	8.612	1.345	3.822	0.544	3.538	0.532
7	14.133	2.135	5.814	0.824	5.622	0.875
6	13.9	2.096	5.646	0.801	5.388	0.844
5	15.633	2.374	6.373	0.906	6.157	0.958
4	18.524	2.854	7.735	1.107	7.447	1.166
3	16.685	2.593	7.018	1.013	6.821	1.045
2	16.987	2.642	7.251	1.036	6.968	1.084
1	18.636	2.862	7.676	1.108	7.405	1.153

Kakabeka Falls Outcrop

	Distance below exposure surface (cm)	Lithology
KF-11-03	10	Completely altered granodiorite directly below exposure
KF-11-02	60	Slightly altered granodiorite at the middle of the unit
KF-11-01	130	Fresh granodiorite at the base of the unit

Major Oxides (wt%)

Sample	Al_2O_3	CaO	Fe_2O_3	K_2O	MgO	MnO	Na_2O
KF-11-01	11.898	2.535	1.857	1.741	0.709	0.073	4.139
KF-11-02	11.255	1.155	2.711	2.345	0.932	0.028	2.837
KF-11-03	12.174	0.161	18.734	1.588	2.989	0.053	0.418
	P_2O_5	TiO_2					
KF-11-01	0.073	0.177					
KF-11-02	0.067	0.186					
KF-11-03	0.057	0.165					

Trace Elements (ppm)

	Ba	Cr	Ni	Sr	V	Y
KF-11-01	337.073	2.753	3.387	361.500	16.007	4.687
KF-11-02	309.473	13.353	6.207	104.840	19.047	3.767
KF-11-03	171.873	2.793	10.447	16.220	17.327	4.087

Rare Earth Elements (ppm)

	La	Ce	Pr	Nd	Sm	Eu
KF-11-01	3.971	7.713	0.819	3.167	0.578	0.184
KF-11-02	6.291	12.568	1.406	5.324	0.991	0.329
KF-11-03	5.697	10.605	1.169	4.458	0.871	0.382
	Gd	Tb	Dy	Ho	Er	Tm
KF-11-03	0.699	0.118	0.749	0.14	0.396	0.051
KF-11-02	1.103	0.174	0.997	0.184	0.505	0.067
KF-11-01	0.936	0.157	0.879	0.146	0.341	0.042
	Yb	Lu	Mo	U		
KF-11-03	0.308	0.048	0.292	0.466		
KF-11-02	0.459	0.071	0.308	0.586		
KF-11-01	0.257	0.038	0.325	0.557		

KOA Hill Outcrop

	Distance from the exposure surface (cm)	Lithology
KOA-10	175	Silicious grainstone with minor manganese carbonates and hemaite
KOA-09	155	Massive hematite
KOA-08	130	Conglomerate layer; clasts comprised of quartz, feldspar and shale within a matrix of clays
KOA-07	75	
KOA-06		Altered zone of metasediments, which appears more flakey and without a distinct foliation direction
KOA-05	0	
KOA-04		
KOA-03		Unaltered metasedimentary rocks comprised of fine grained quartz and micas. Schistosity at 070/90
KOA-02	15	
KOA-01	80	

Major Oxides (wt%)

Sample	Al_2O_3	CaO	Fe_2O_3	K_2O	MgO	MnO
KOA-01	10.526	0.431	6.647	2.818	2.702	0.068
KOA-02	12.034	0.657	11.108	3.230	3.728	0.103
KOA-03	11.036	0.252	12.821	3.223	3.334	0.084
KOA-04	10.318	0.256	12.809	4.413	2.303	0.098
KOA-05	8.342	0.227	13.538	2.809	2.231	0.098
KOA-06	10.208	0.256	17.101	2.150	3.061	0.132
KOA-07	5.398	0.705	9.589	1.044	1.612	0.174
KOA-08	5.942	0.373	14.493	0.066	2.124	0.124
KOA-09	0.671	4.408	41.627	0.026	1.300	2.239
KOA-10	0.435	22.995	7.345	0.010	11.379	1.625
	Na_2O	P_2O_5	TiO_2			
KOA-01	1.438	0.119	0.657			
KOA-02	1.108	0.150	0.731			
KOA-03	0.218	0.142	0.737			
KOA-04	0.160	0.144	0.533			
KOA-05	0.130	0.130	0.616			
KOA-06	0.159	0.167	0.745			
KOA-07	0.187	0.041	0.230			
KOA-08	0.192	0.053	0.186			
KOA-09	0.460	0.030	0.014			
KOA-10	0.752	0.005	0.004			

Trace Elements (ppm)

	Ba	Cr	Ni	Sr	V	Y
KOA-01	549.273	52.173	43.727	57.280	82.127	4.767
KOA-02	620.073	61.353	48.327	29.960	106.107	4.807
KOA-03	980.873	62.313	49.187	27.760	79.667	7.067
KOA-04	343.673	37.093	18.807	9.620	44.887	4.387
KOA-05	171.093	46.933	22.487	5.580	53.807	4.407
KOA-06	197.213	60.453	27.847	6.680	97.427	8.747
KOA-07	235.273	40.313	13.047	31.200	34.447	6.767
KOA-08	25.013	27.453	23.547	5.160	54.547	4.907
KOA-09	19.913	10.733	5.307	26.800	21.247	5.447
KOA-10	9.993	4.153	1.667	21.340	7.887	17.747

Rare Earth Elements (ppm)

Sample	La	Ce	Pr	Nd	Sm	Eu	Gd	Tb
KOA-10	5.956	7.802	1.249	5.297	1.106	0.643	1.568	0.228
KOA-09	4.061	6.739	0.677	3.014	0.609	0.231	0.846	0.11
KOA-08	2.801	5.343	0.723	3.317	0.785	0.232	0.969	0.146
KOA-07	5.617	6.456	1.407	6.122	1.241	0.355	1.38	0.201
KOA-06	13.254	26.265	2.761	10.218	1.557	0.472	1.588	0.235
KOA-05	20.619	40.666	4.378	15.63	2.067	0.533	1.57	0.194
KOA-04	14.977	30.215	3.194	11.673	1.588	0.522	1.289	0.159
KOA-03	2.799	5.96	0.69	2.656	0.619	0.54	0.88	0.177
KOA-02	5.377	11.485	1.339	5.045	0.948	0.476	0.99	0.153
KOA-01	8.603	19.027	2.26	8.882	1.566	0.606	1.476	0.221
	Dy	Ho	Er	Tm	Yb	Lu	Mo	U
KOA-10	1.368	0.284	0.822	0.113	0.62	0.085	0.107	0.546
KOA-09	0.606	0.121	0.349	0.049	0.289	0.039	4.492	0.357
KOA-08	0.834	0.178	0.526	0.081	0.499	0.077	2.789	0.339
KOA-07	1.039	0.199	0.536	0.074	0.489	0.075	5.08	0.253
KOA-06	1.343	0.287	0.883	0.134	0.857	0.132	1.374	1.285
KOA-05	0.928	0.151	0.48	0.077	0.528	0.083	0.686	0.418
KOA-04	0.748	0.123	0.364	0.056	0.393	0.061	1.234	0.417
KOA-03	1.245	0.282	0.849	0.113	0.748	0.117	2.013	0.786
KOA-02	0.899	0.175	0.519	0.08	0.558	0.089	1.379	0.903
KOA-01	1.185	0.223	0.609	0.091	0.577	0.094	1.638	0.779

Kakabeka Falls Grainstone

Sample	Lithology
KF-A	Domal Stromatolite (light laminae)
KF-B	Domal Stromatolite (dark laminae)
KF-C	Basal Microbiolite (light laminiae)
KF-S	Basal Microbiolite (dark Laminiae
SH-2	Stromatolitic Cherts
SH-3	Ankerite Grainstone
SH-4	Ankerite Grainstone
SH-5	Silicicfied carbonate grainstone
SH-6	Layered Chert
SH-10	Layered microbolite

Major Oxides and trace elements (wt% and ppm)

	Al_2O_3	CaO	Fe_2O_3	K_2O	MgO	MnO	Na_2O	P_2O_5
KF-A	0.0231	1.3328	0.6520	0.0115	0.2739	0.1378	0.0104	0.0000
KF-B	0.0315	2.6055	1.4057	0.0107	0.8649	0.2129	0.0273	0.0000
KF-C	0.0368	3.5659	0.3565	0.0098	0.1409	0.0821	0.0158	0.0000
KF-S	0.0492	2.2412	0.6039	0.0124	0.2546	0.1189	0.0140	0.0000
SH-2	0.0600	1.8900	0.4800	0.0200	0.1900	0.1000	<0.01	<0.01
SH-3	0.0800	30.1800	11.0300	<0.01	11.4300	2.6700	0.1100	0.0100
SH-4	0.0700	22.4400	9.1900	0.0100	7.8200	2.7000	<0.01	<0.01
SH-5	0.0600	0.1600	2.9800	0.0300	0.1000	0.0600	<0.01	0.0200
SH-6	0.1300	0.9400	0.1800	0.0200	0.0600	0.0200	<0.01	<0.01
SH-10	0.0600	0.2500	0.4300	0.0200	0.0900	0.0500	<0.01	<0.01

	TiO_2	Cr	V
KF-A	0.000454	0	0.84
KF-B	0.002322	0.6	1.88
KF-C	0.000794	1.28	1
KF-S	0.000561	1.76	0.4
SH-2	<0.01	0	1.7
SH-3	0.01	3	16.2
SH-4	0.01	3	19.8
SH-5	0.01	0	3.6
SH-6	0.01	3	2.1
SH-10	<0.01	0	2.1

Rare Earth Elements (ppm)

Sample	La	Ce	Pr	Nd	Sm	Eu	Gd	Tb
KF-A	0.913	0.89	0.144	0.619	0.116	0.052	0.164	0.024
KF-B	1.212	1.253	0.216	0.937	0.179	0.073	0.239	0.032
KF-C	1.768	2.112	0.282	1.2	0.237	0.082	0.307	0.043
KF-S	1.27	1.478	0.211	0.921	0.186	0.074	0.23	0.034
SH-2	0.15	0.17	0.023	0.12	0.025	0.009	0.022	0.003
SH-3	12.58	15.86	1.727	7.19	1.359	0.435	1.729	0.25
SH-4	14.25	14.92	2.014	8.19	1.419	0.475	1.732	0.257
SH-5	0.68	1.11	0.141	0.62	0.139	0.047	0.15	0.024
SH-6	0.55	0.83	0.108	0.44	0.113	0.041	0.133	0.019
SH-10	1.23	1.23	0.195	0.84	0.156	0.054	0.181	0.023

	Dy	Ho	Er	Tm	Yb	Lu	U	Mo
KF-A	0.125	0.032	0.086	0.012	0.075	0.01	0.087	0.207
KF-B	0.185	0.04	0.124	0.016	0.102	0.014	0.066	0.101
KF-C	0.214	0.046	0.131	0.019	0.12	0.02	0.07	0.3
KF-S	0.168	0.037	0.103	0.014	0.084	0.011	0.1	0.293
SH-2	0.018	0.004	0.014	0.003	0.013	0.002	0	0.09
SH-3	1.67	0.367	1.077	0.141	0.853	0.116	0.536	0.3
SH-4	1.72	0.381	1.101	0.153	0.881	0.115	0.203	0.47
SH-5	0.156	0.036	0.11	0.013	0.085	0.01	0.051	0.29
SH-6	0.126	0.028	0.075	0.01	0.063	0.008	0.115	0
SH-10	0.146	0.034	0.087	0.012	0.078	0.01	0.113	0.18

Whitefish Channel Outcrop

Samples	Lithology
WF-CY-1	Grainstone from inbetween strmatolites
WF-CY-2	Chert from stromatolite bioherm
WF-CY-3	Material draping the bioherms
WF-CY-4	Material draping the bioherms
WF-CY-5	Red chert stromatolites
WF-CY-6	Material draping the bioherms
WF-A	Red Jasperlitic Stromatolites
WF-B	Red Jasperlitic Stromatolites
WF-3	White Chert Stromatolites
WF-10	White Chert Stromatolites

Major Oxides (wt%)

Samples	Al_2O_3	Fe_2O_3	CaO	K_2O	MgO	MnO	Na_2O	P_2O_5
WF-CY-1	0.0074	5.7887	4.4070	0.0328	0.0160	0.0441	0.0147	0.0089
WF-CY-2	0.0688	0.7847	1.5735	0.0191	-0.0162	0.0226	0.0301	0.0000
WF-CY-3	0.2995	25.1185	14.1980	0.0506	0.4422	0.1461	0.0420	0.0175
WF-CY-4	0.3132	4.7845	62.9142	0.0953	0.1554	0.3105	0.0772	0.0248
WF-CY-5	0.3189	32.5531	18.6048	0.1584	0.4899	0.2468	0.0382	0.0633
WF-CY-6	0.0107	8.7053	0.7358	0.0095	0.0163	0.0970	0.0176	0.0045
WF-A	0.0109	4.2308	0.0372	0.0082	0.0085	0.0364	0.0212	0.0000
WF-B	0.0135	4.5437	0.0449	0.0065	0.0127	0.0177	0.0078	0.0000
WF-3	0.0709	0.2535	0.0529	0.0146	0.0139	0.0151	0.0134	0.0000
WF-10	0.0675	0.2996	0.0215	0.0106	0.0159	0.0147	0.0116	0.0000

Major Oxides and Trace Elements (wt% and ppm)

	TiO_2	Cr	V	Mo	U
WF-CY-1	0.0028	0.0000	3.6267	0.0750	0.5570
WF-CY-2	0.0046	0.0000	3.5467	1.3690	0.1640
WF-CY-3	0.0075	25.8133	5.8667	2.6900	0.2700
WF-CY-4	0.0112	53.6933	17.0267	0.1420	0.5630
WF-CY-5	0.0037	0.0000	10.8667	3.1680	0.7650
WF-CY-6	0.0010	31.7333	2.5067	3.4970	0.2680
WF-A	0.0014	0.8400	1.6400	0.3650	0.1010
WF-B	0.0014	0.3200	2.5600	0.3310	0.1290
WF-3	0.0040	3.0800	1.2400	1.1270	0.1620
WF-10	0.0020	0.8800	1.0000	1.4430	0.3810

Rare Earth Elements (ppm)

Sample	La	Ce	Pr	Nd	Sm	Eu	Gd	Tb
WF-CY-1	1.591	2.865	49.417	0.081	0.309	1.292	0.119	0.383
WF-CY-2	0.728	1.142	28.515	0.195	0.14	0.568	0.072	0.15
WF-CY-3	3.739	6.42	13.804	0.135	0.711	3.057	0.242	0.89
WF-CY-4	8.189	11.371	1030.528	0.237	1.465	6.393	0.661	2.009
WF-CY-5	8.931	18.436	39.043	0.164	1.919	8.219	0.553	1.998
WF-CY-6	1.103	1.543	74.267	0.159	0.201	0.853	0.071	0.217
WF-A	0.952	0.945	0.16	0.664	0.144	0.056	0.185	0.03
WF-B	0.677	0.884	0.131	0.538	0.112	0.066	0.15	0.026
WF-3	0.3	0.293	0.042	0.18	0.036	0.029	0.051	0.009
WF-10	0.281	0.277	0.045	0.18	0.034	0.016	0.046	0.007

Sample	Dy	Ho	Er	Tm	Yb	Lu
WF-CY-1	0.059	0.364	0.073	0.219	0.028	0.177
WF-CY-2	0.023	0.158	0.034	0.096	0.014	0.077
WF-CY-3	0.134	0.814	0.179	0.529	0.076	0.453
WF-CY-4	0.28	1.596	0.332	0.863	0.1	0.564
WF-CY-5	0.292	1.66	0.34	0.958	0.124	0.73
WF-CY-6	0.033	0.177	0.039	0.115	0.017	0.101
WF-A	0.174	0.037	0.109	0.014	0.084	0.012
WF-B	0.14	0.029	0.082	0.012	0.077	0.008
WF-3	0.064	0.015	0.052	0.007	0.037	0.005
WF-10	0.038	0.01	0.025	0.004	0.022	0.004

10.1.2 Middle Exposure Surface

Mink Mountain (DFES- distance from exposure surface)

	DFES *(cm)	Lithology
CY-1	104	Medium to coarse grainstone
CY-3		Medium to coarse grainstone
CY-5		Jasper within the grainstone
CY-7	58	Rubbly grainstone with laths of japser throughout
CY-8		Rubbly grainstone with laths of japser throughout
CY-9		Rubbly grainstone with laths of japser throughout
CY-11		Rubbly grainstone with laths of jasper throughout
CY-12		Rubbly grainstone with laths of jasper throughout
CY-13		Rubbly grainstone with laths of jasper throughout
CY-70	0	Stromatolite sample
CY-71		Digitate stromatolites
CY-73		Thin digitate stromatolites coalescing into domal stromatolites
CY-72		Domal stromatolite
CY-73		Domal stromatolite
CY-15	22	Coarse grained ooidal grainstone
CY-16		Coarse grained ooidal grainstone
CY-67	55	Medium to coarse ooidal grainstone
CY-17		Ooidal grainstone
CY-60		Medium to coarse ooidal grainstone
CY-61		Medium to coarse ooidal grainstone
CY-62		Medium to coarse ooidal grainstone

Major Oxides and trace elements (wt%, ppm)

	Al_2O_3	CaO	Fe_2O_3	K_2O	Na_2O	MgO	MnO	P_2O_5
CY-3	1.568	0.016	19.440	0.030	0.050	0.026	0.020	0.003
CY-5	2.227	0.005	11.588	0.025	-0.004	0.018	0.028	0.009
CY-7	1.239	0.014	20.338	0.031	-0.003	0.031	0.053	0.018
CY-8	2.045	0.115	19.515	0.031	0.081	0.112	0.061	0.032
CY-9	1.508	0.007	11.966	0.027	0.001	0.013	0.025	0.018
CY-13	0.819	0.010	16.307	0.019	-0.001	0.022	0.014	0.001
CY-15	2.623	0.136	15.386	0.012	-0.002	0.071	0.041	0.004
CY-16	0.849	0.018	36.346	0.013	-0.001	0.029	0.097	0.008
CY-70	0.995	0.009	7.236	0.017	-0.011	0.016	0.036	0.017
CY-72	2.170	0.011	12.178	0.043	0.009	0.010	0.032	0.069
CY-73	2.111	0.046	43.500	0.028	0.057	0.062	0.027	0.025
CY-60	1.314	0.062	35.934	0.017	0.053	0.027	0.084	0.084
CY-61	0.976	0.019	37.501	0.019	0.050	0.022	0.090	0.013
CY-17	1.450	0.010	31.244	0.011	0.065	0.013	0.036	0.011
	TiO_2	Cr	V					
CY-3	0.003	-1.353	5.820					
CY-5	0.005	1.187	2.480					
CY-7	0.004	0.287	5.200					
CY-8	0.004	-2.013	4.460					
CY-9	0.007	-1.573	3.320					
CY-13	0.005	-0.713	4.820					
CY-15	0.001	-1.473	7.100					
CY-16	0.001	-2.253	10.020					
CY-70	0.006	-0.853	3.060					
CY-72	0.008	-0.493	12.380					
CY-73	0.027	3.947	4.260					
CY-60	0.002	-0.833	8.160					
CY-61	0.001	-0.813	6.300					
CY-17	0.001	-1.173	6.520					

	Al$_2$O$_3$	CaO	Fe$_2$O$_3$	K$_2$O	MgO	MnO	Na$_2$O	P$_2$O$_5$
CY-1	0.144	0.082	11.698	0.012	0.069	0.024	0.018	0.008
CY-11	0.104	0.038	6.711	0.014	0.045	0.042	0.005	0.006
CY-12	0.099	0.027	6.288	0.014	0.030	0.049	0.004	0.007
CY-62	0.043	0.029	9.908	0.007	0.028	0.007	0.001	0.002
CY-67	0.036	0.023	9.765	0.004	0.035	0.010	0.000	0.002
CY-71	0.052	0.010	3.808	0.001	0.017	0.048	-0.004	0.012
CY-73	0.076	0.034	25.091	0.010	0.065	0.027	0.000	0.011

	TiO$_2$	Cr	Mo	V
CY-1	0.009	4.653	0.507	9.680
CY-11	0.005	0.533	-0.253	3.200
CY-12	0.004	0.773	0.907	2.400
CY-62	0.002	0.573	0.547	6.200
CY-67	0.001	0.733	0.707	5.680
CY-71	0.003	0.173	-0.573	2.440
CY-73	0.015	2.013	2.387	4.560

Rare Earth Elements (ppm)

	La	Ce	Pr	Nd	Sm	Eu	Gd	Tb
CY-1	0.27	0.97	0.082	0.36	0.107	0.0299	0.123	0.0301
CY-6	1.14	3.38	0.241	0.95	0.193	0.0612	0.207	0.0398
CY-11	1.48	4.12	0.298	1.16	0.236	0.0642	0.222	0.0424
CY-12	3.79	11.32	0.691	2.57	0.425	0.085	0.312	0.0473
CY-71	1.6	3.72	0.291	1.15	0.225	0.0607	0.181	0.0283
CY-73A	1.67	2.68	0.282	1.16	0.242	0.0744	0.245	0.0334
CY-73B	1.37	4.18	0.346	1.42	0.347	0.086	0.32	0.0556
CY-77	1.09	2.75	0.213	0.86	0.177	0.0495	0.158	0.0277
CY-62	0.76	2.38	0.166	0.66	0.161	0.0531	0.177	0.0354
CY-67	0.65	2.25	0.174	0.7	0.183	0.06	0.214	0.0418

	Dy	Ho	Er	Tm	Yb	Lu	U
CY-1	0.201	0.0462	0.145	0.0247	0.138	0.0205	0.119
CY-6	0.266	0.059	0.179	0.029	0.159	0.0216	0.192
CY-11	0.296	0.0591	0.185	0.0257	0.158	0.0196	0.083
CY-12	0.316	0.0623	0.191	0.0267	0.157	0.018	0.099
CY-71	0.182	0.0375	0.108	0.017	0.104	0.014	0.144
CY-73A	0.233	0.0473	0.142	0.0217	0.146	0.0216	0.319
CY-73B	0.361	0.0741	0.22	0.0337	0.19	0.0247	0.088
CY-77	0.164	0.0328	0.09	0.0144	0.085	0.0107	0.127
CY-62	0.239	0.0552	0.166	0.0261	0.156	0.0201	0.137
CY-67	0.288	0.0625	0.195	0.0277	0.157	0.0199	0.107

Old School Road

Sample	Lithology
OSR-22	Coarse grained ooidal hematite-rich grainstone
OSR-13	Hematite rich Stromatolite
OSR-12	Hematite rich stromatolite
OSR-5	Brecciated grainstone with hematite-jasper vein
OSR-2	Medium to coarse grainstone

Major Oxides and Trace elements (wt%, ppm)

	Al_2O_3	Fe_2O_3	CaO	K_2O	MgO	MnO	Na_2O	P_2O_5
OSR-22	0.0752	9.8377	0.7220	0.0599	0.1752	0.0670	0.0081	0.0000
OSR-13	0.0083	5.6915	0.0926	0.0143	0.0379	0.1327	-0.0017	0.0090
OSR-12	0.3324	15.2535	0.9190	0.0444	0.3074	0.6270	0.0471	0.0468
OSR-5	0.0151	6.1947	0.2441	0.0274	0.0461	0.3217	0.0069	0.0064
OSR-2	0.0562	9.8377	0.2617	0.0194	0.0832	0.0884	0.0213	0.0000
	TiO_2	Cr	V					
OSR-22	0.0036	31.0133	1.2667					
OSR-13	0.0057	0.0000	3.1467					
OSR-12	0.0209	39.0533	9.3067					
OSR-5	0.0086	23.9333	3.6667					
OSR-2	0.0057	0.0000	9.1867					

Rare Earth Element (ppm)

Sample	La	Ce	Pr	Nd	Sm	Eu	Gd	Tb
OSR-22	1.32	2.568	0.283	1.203	0.283	0.08	0.402	0.075
OSR-13	0.678	1.303	0.14	0.598	0.135	0.042	0.173	0.03
OSR-12	2.364	6.225	0.537	2.366	0.519	0.154	0.625	0.1
OSR-5	0.567	1.517	0.156	0.751	0.177	0.056	0.229	0.036
OSR-2	0.443	1.075	0.118	0.531	0.135	0.05	0.205	0.038
	Dy	Ho	Er	Tm	Yb	Lu	Mo	U
OSR-22	0.496	0.116	0.386	0.064	0.419	0.059	0.107	0.113
OSR-13	0.177	0.036	0.11	0.016	0.104	0.013	1.448	0.145
OSR-12	0.623	0.133	0.379	0.053	0.322	0.042	1.876	0.174
OSR-5	0.224	0.044	0.131	0.016	0.09	0.012	1.871	0.071
OSR-2	0.256	0.055	0.165	0.024	0.131	0.017	0.084	0.125

Magnetic Rock Trail

	D.F.E.S (cm)	Lithology
CY-100	444	Medium to coarse grainstone cross through stratified, with parallel laminat[e] chemical muds
CY-101	410	Coarse grainstone
CY-103	402	Medium to coarse grainstone with mud flasars
CY-104		Coarse grainstone
CY-105	185	Medium to coarse grainstone
CY-106		Medium to coarse grainstone
CY-102		Medium to coarse grainstone with mud flasars
CY-107	96	Massive magnetite layer
CY-108		Medium to coarse, badly silicified grainstone
CY-109		Medium to coarse badly silicified grainstone
CY-80	0	Stromatolite
CY-81		Stromatolite
CY-110	45	Medium to coarse grainstone
CY-111		Medium to coarse grainstone
CY-112		Coarse to fine grainstone with irregular bottoms
CY-113	57	Massive Magnetite layer
CY-114		Coarse grainstone
CY-115		Interlayered grainstone and lapilli
CY-116A		
CY-116B	187	Interlayered grainstone and lapilli
CY-116C		
CY-117A		Coarse grainstone with lapilli
CY-117B		

Major oxides (wt%)

Sample Labels	Al₂O₃	CaO	Fe₂O₃	K₂O	MgO	MnO	Na₂O	P₂O₅
CY-100	0.075	0.349	7.379	0.017	0.287	0.063	0.030	0.010
CY-101	0.118	0.244	19.751	0.008	0.690	0.105	0.144	0.004
CY-102	0.240	2.423	24.649	0.012	1.976	0.353	0.316	0.033
CY-103	0.258	0.963	20.157	0.022	1.233	0.291	0.192	0.025
CY-104	0.165	0.628	30.034	0.009	1.202	0.188	0.179	0.011
CY-105	0.202	1.409	19.872	0.018	0.680	0.335	0.187	0.018
CY-106	0.266	0.428	25.310	0.014	1.003	0.284	0.248	0.018
CY-107	1.183	1.082	49.892	0.166	1.054	0.086	0.838	0.138
CY-108	0.719	1.228	27.491	0.093	0.980	0.316	0.347	0.085
CY-109	0.648	1.089	19.156	0.093	0.830	0.202	0.222	0.018
CY-80	0.772	0.103	18.708	0.014	0.238	0.127	0.004	0.017
CY-81	1.156	0.026	15.048	0.015	0.049	0.113	-0.008	0.008
CY-110	0.343	0.523	27.110	0.025	0.629	0.169	0.356	0.041
CY-111	0.084	0.251	15.422	0.004	0.654	0.142	0.099	0.007
CY-112	0.061	0.396	19.340	0.009	0.488	0.257	0.054	0.008
CY-113	1.086	0.972	51.140	0.164	1.223	0.114	0.662	0.148
CY-114	0.148	2.372	19.415	0.011	1.100	0.289	0.182	0.017
CY-115	0.307	3.372	33.021	0.016	1.614	0.440	0.389	0.026
CY-116A	0.316	12.654	22.695	0.016	3.830	0.314	0.527	0.022
CY-116B	0.394	10.983	23.959	0.020	3.624	0.309	0.709	0.007
CY-116C	0.259	13.737	22.327	0.016	3.714	0.310	0.472	0.013
CY-117A	0.085	0.993	16.447	0.012	0.482	0.246	0.059	0.011
CY-117B	0.445	4.709	27.862	0.032	3.111	0.535	0.591	0.086

Major Oxides and Trace elements cont. (wt%, ppm)

	TiO_2	Cr	V
CY-100	0.006	3.040	10.558
CY-101	0.006	-0.540	10.058
CY-102	0.013	4.700	12.244
CY-103	0.004	0.420	5.978
CY-104	0.004	-1.700	9.164
CY-105	0.004	-0.400	7.824
CY-106	0.005	3.220	8.584
CY-107	0.056	12.560	23.578
CY-108	0.006	60.240	19.178
CY-109	0.004	22.040	11.684
CY-80	0.001	-2.053	1.860
CY-81	0.003	4.627	1.680
CY-110	0.002	16.860	10.218
CY-111	0.001	3.940	5.478
CY-112	0.001	21.760	7.811
CY-113	0.024	-1.760	60.551
CY-114	0.003	13.160	8.938
CY-115	0.008	19.360	21.698
CY-116A	0.003	55.420	24.298
CY-116B	0.005	16.800	17.191
CY-116C	0.003	-2.400	25.391
CY-117A	0.011	11.740	17.011
CY-117B	0.032	0.400	17.131

Rare Earth Elements (ppm)

Sample	La	Ce	Pr	Nd	Sm	Eu	Gd	Tb
CY-100	32.324	101.919	4.84	16.182	2.074	0.447	1.934	0.265
CY-101	2.5	7.612	0.628	2.659	0.669	0.203	0.856	0.173
CY-102	6.835	27.998	2.808	14.66	4.215	1.276	5.913	0.997
CY-103	2.603	8.896	0.808	3.486	0.783	0.211	0.889	0.144
CY-104	4.131	14.229	0.931	3.727	0.798	0.242	0.973	0.164
CY-105	3.742	12.767	1.176	5.009	1.125	0.397	1.352	0.219
CY-106	4.508	12.674	1.007	4.213	0.941	0.319	1.295	0.229
CY-107	24.821	94.423	8.08	36.39	8.364	2.824	10.013	1.535
CY-108	10.594	32.645	3.525	16.044	4.11	2.475	5.141	0.851
CY-109	6.865	23.324	2.374	10.137	2.274	1.857	2.595	0.416
CY-80	0.93	1.68	0.195	0.83	0.185	0.0472	0.35	0.0359
CY-81	2.2	3.32	0.419	1.87	0.409	0.1244	0.27	0.0663
CY-110	24.162	55.43	5.153	21.036	4.583	1.148	5.27	0.884
CY-111	0.643	2.053	0.186	0.901	0.274	0.078	0.368	0.076
CY-112	1.567	4.607	0.609	3.215	1.091	0.32	1.78	0.348
CY-113	50.268	136.666	13.372	59.537	14.499	7.539	18.008	2.954
CY-114	2.427	9.505	0.937	4.337	1.134	0.549	1.351	0.23
CY-115	87.848	290.752	12.835	41.357	5.784	2.124	6.625	1.041
CY-116A	11.441	47.452	4.918	23.562	6.173	3.331	7.839	1.289
CY-116B	7.673	34.6	3.646	17.412	4.446	2.305	5.56	0.912
CY-116C	4.491	17.586	2.3	12	3.437	1.85	4.559	0.76
CY-117A	5.941	14.44	1.53	7.891	2.344	0.684	3.061	0.487
CY-117B	38.802	90.1	8.521	38.865	9.336	2.652	12.051	1.897

	Dy	Ho	Er	Tm	Yb	Lu
CY-100	1.321	0.234	0.65	0.084	0.451	0.055
CY-101	1.243	0.304	1.001	0.146	0.815	0.106
CY-102	6.361	1.397	4.179	0.588	3.419	0.465
CY-103	0.878	0.186	0.579	0.087	0.583	0.088
CY-104	1.064	0.236	0.754	0.116	0.733	0.104
CY-105	1.351	0.29	0.864	0.116	0.671	0.082
CY-106	1.593	0.39	1.48	0.266	1.947	0.317
CY-107	8.876	1.814	5.239	0.686	3.932	0.54
CY-108	5.127	1.091	3.265	0.474	2.818	0.389
CY-109	2.53	0.519	1.592	0.226	1.344	0.18
CY-80	0.216	0.0492	0.157	0.0231	0.137	0.0171
CY-81	0.421	0.0875	0.251	0.0364	0.22	0.027
CY-110	5.331	1.106	3.315	0.455	2.462	0.299
CY-111	0.6	0.15	0.551	0.099	0.702	0.109
CY-112	2.49	0.618	2.152	0.346	2.029	0.263
CY-113	17.661	3.628	10.789	1.518	8.979	1.193
CY-114	1.45	0.3	0.897	0.132	0.815	0.12
CY-115	6.115	1.282	3.956	0.565	3.363	0.469
CY-116A	7.959	1.696	5.029	0.665	3.874	0.525
CY-116B	5.611	1.191	3.512	0.462	2.697	0.379
CY-116C	4.682	1.003	2.918	0.375	2.066	0.282
CY-117A	2.949	0.625	1.819	0.241	1.325	0.157
CY-117B	11.298	2.325	6.736	0.922	5.332	0.738

Current River

	Sample description
CR-7	Grainstone taken 1m above stromatolite layer
CR-8	Grainstone from directly above stromatolite layer
CR-2	Ankertized grainstone with silicified clasts present thoughout
CR-3	Ankeritzed grainstone
CR-11-03	Brecciated grainstone below stromatolites
CR-11-02	Highly pyritiferous brecciated grainstone
CR-11-01 WR	Highly silicified medium to coarse grainstone
CR-11-01 Mn	Manganeese Carbonate at the base of the grainstone

Major Oxides and trace elements (wt%, ppm)

	Al_2O_3	CaO	Fe_2O_3	K_2O	MgO	MnO	Na_2O	P_2O_5
CR-7	0.205	14.617	6.856	0.021	5.818	0.198	0.230	0.011
CR-8	0.128	1.199	1.806	0.023	0.446	0.055	0.018	0.023
CR-2	0.532	13.795	6.953	0.116	5.574	0.404	0.117	0.010
CR-3	0.686	11.618	5.595	0.101	5.229	0.303	0.097	0.002
CR-11-03	2.674	23.634	8.892	0.023	1.852	0.088	0.068	18.918
CR-11-02	1.599	0.950	38.327	0.015	1.694	0.178	0.080	0.095
CR-11-01 WR	0.235	4.059	1.575	0.008	0.844	0.332	0.010	0.009
CR-11-01 Mn	0.464	18.468	4.319	0.012	4.727	1.004	0.029	0.017

	TiO_2	Cr	V
CR-7	0.008	0.000	1.920
CR-8	0.003	0.000	1.720
CR-2	0.023	3.173	5.760
CR-3	0.027	6.333	10.720
CR-11-03	0.070	49.253	345.440
CR-11-02	0.029	21.933	246.760
CR-11-01 WR	0.005	2.293	6.920
CR-11-01 Mn	0.015	3.613	10.480

Rare Earth Elements (ppm)

Sample	La	Ce	Pr	Nd	Sm	Eu	Gd	Tb
CR-7	0.883	2.241	0.212	0.853	0.166	0.056	0.206	0.03
CR-8	0.404	1.065	0.113	0.499	0.104	0.031	0.125	0.018
CR-2	1.643	4.851	0.429	1.858	0.454	0.172	0.575	0.079
CR-3	1.6	4.351	0.334	1.34	0.284	0.116	0.367	0.056
CR-11-03	132.97	230.064	27.882	116.614	22.243	6.354	29.581	4.142
CR-11-02	1.746	3.202	0.483	2.177	0.506	0.117	0.604	0.087
CR-11-01 WR	2.634	3.471	0.451	1.795	0.318	0.18	0.411	0.057
CR-11-01 Mn	7.834	10.81	1.395	5.492	0.958	0.617	1.312	0.175

	Dy	Ho	Er	Tm	Yb	Mo	U	
CR-7	0.162	0.036	0.097	0.013	0.077	0.475	0.405	
CR-8	0.098	0.019	0.055	0.007	0.041	0.632	0.046	
CR-2	0.41	0.076	0.2	0.023	0.136	0.446	2.408	
CR-3	0.311	0.065	0.185	0.024	0.153	0.685	6.558	
CR-11-03	23.093	5.008	14.042	1.683	9.459	8.711	142.223	
CR-11-02	0.5	0.112	0.378	0.054	0.352	16.729	2.711	
CR-11-01 WR	0.311	0.064	0.181	0.021	0.109	1.064	1.834	
CR-11-01 Mn	0.878	0.178	0.512	0.058	0.362	0.539	2.519	

DH 87-3

	D.F.E.S (cm)	Lithology
DH-3 05	130	Medium to coarse grainstone
DH-3 04	0	Red chert stromatolites
DH-3 03	21	Allocthonous conglomerate comprised of clasts cemented by quartz
DH-3 02	300	Carboanceous shales and quartz veining
DH-3 01	424	Medium to coarse grainstone

Major Oxides and Trace Elements (wt%, ppm)

	Al_2O_3	CaO	Fe_2O_3	K_2O	MgO	MnO	Na_2O	TiO_2
DH-3 05	0.085	2.912	19.278	0.010	0.797	0.097	0.029	0.004
DH-3 04	0.579	5.805	20.330	0.275	0.757	0.113	0.150	0.020
DH-3 03	0.084	0.339	7.417	0.019	0.173	0.014	0.010	0.007
DH-3 02	0.432	3.642	17.273	0.054	0.586	0.045	0.030	0.014
DH-3 01	0.173	0.112	15.552	0.039	1.084	0.040	0.021	0.008

	P_2O_5	Cr	V
DH-3 05	0.000	0.000	1.480
DH-3 04	0.017	0.000	12.220
DH-3 03	0.001	0.000	5.340
DH-3 02	0.010	0.140	15.060
DH-3 01	0.001	0.000	3.100

Rare Earth Elements (ppm)

Sample	La	Ce	Pr	Nd	Sm	Eu	Gd	Tb
DH-3 05	1.337	2.887	0.265	1.128	0.245	0.099	0.327	0.052
DH-3 04	4.41	9.796	0.962	4.218	0.892	0.302	1.094	0.178
DH-3 03	0.526	1.156	0.118	0.481	0.096	0.032	0.119	0.02
DH-3 02	1.789	4.2	0.402	1.592	0.296	0.105	0.358	0.052
DH-3 01	0.224	0.565	0.063	0.279	0.064	0.03	0.089	0.013

	Dy	Ho	Er	Tm	Yb	Lu	U	Mo
DH-3 05	0.323	0.064	0.205	0.026	0.158	0.02	0.034	0.342
DH-3 04	1.068	0.217	0.657	0.088	0.532	0.074	0.138	1.116
DH-3 03	0.124	0.026	0.078	0.012	0.077	0.012	0.104	0.631
DH-3 02	0.299	0.063	0.18	0.026	0.148	0.02	0.192	0.602
DH-3 01	0.065	0.016	0.046	0.006	0.04	0.007	0.051	0.493

MC 89-1

Major Oxides and Trace Elements (wt% and ppm)

	Al_2O_3	CaO	Fe_2O_3	K_2O	MgO	MnO	Na_2O	P_2O_5
CY-32	0.284	0.156	9.824	0.191	0.285	0.124	0.062	0.035
MC-CY-04	0.287	0.597	21.131	0.171	0.280	0.145	0.090	0.024
MC-CY-03	0.039	0.763	11.637	0.010	0.052	0.102	0.014	0.015
CY-28	0.130	0.400	13.582	0.070	0.133	0.068	0.031	0.017
MC-CY-02	0.046	0.892	11.872	0.014	0.063	0.077	0.015	0.012
CY-27	1.528	1.155	21.805	0.219	0.911	0.144	0.228	0.061
CY-26	0.220	1.324	15.217	0.137	0.319	0.179	0.085	0.095
MC-CY-01	0.133	1.194	29.697	0.068	0.139	0.101	0.065	0.034
CY-25	0.171	1.304	32.854	0.093	0.212	0.112	0.048	0.191
	TiO_2	Cr	V					
CY-32	0.017	0.000	19.320					
MC-CY-04	0.011	0.000	20.200					
MC-CY-03	0.001	0.000	5.840					
CY-28	0.005	0.893	8.160					
MC-CY-02	0.001	0.000	5.480					
CY-27	0.039	5.493	11.640					
CY-26	0.014	2.013	15.480					
MC-CY-01	0.004	13.533	9.160					
CY-25	0.007	0.000	18.960					

Rare Earth Elements (ppm)

Sample	La	Ce	Pr	Nd	Sm	Eu	Gd	Tb
CY-25	0.922	2.866	0.266	1.216	0.293	0.082	0.392	0.065
MC-CY-01	0.823	2.505	0.243	1.143	0.279	0.086	0.396	0.064
CY-26	1.902	5.797	0.512	2.259	0.51	0.119	0.637	0.097
CY-27	1.025	2.792	0.325	1.554	0.436	0.132	0.572	0.095
MC-CY-02	0.683	1.623	0.158	0.679	0.173	0.059	0.246	0.047
CY-28	0.408	1.092	0.109	0.475	0.112	0.036	0.158	0.026
MC-CY-03	0.626	1.654	0.158	0.686	0.164	0.05	0.214	0.036
MC-CY-04	1.337	3.535	0.321	1.304	0.272	0.096	0.361	0.057
CY-32	0.463	1.706	0.149	0.683	0.184	0.056	0.23	0.037

	Dy	Ho	Er	Tm	Yb	Lu	U	Mo
CY-25	0.421	0.092	0.297	0.044	0.273	0.039	0.088	2.357
MC-CY-01	0.402	0.088	0.273	0.038	0.239	0.035	0.122	0.909
CY-26	0.549	0.115	0.33	0.046	0.297	0.046	0.03	0.881
CY-27	0.555	0.108	0.29	0.04	0.242	0.035	0.176	1.292
MC-CY-02	0.299	0.066	0.207	0.03	0.203	0.029	0.05	1.158
CY-28	0.18	0.04	0.122	0.018	0.112	0.016	0.221	1.252
MC-CY-03	0.235	0.051	0.154	0.022	0.139	0.019	0.065	2.156
MC-CY-04	0.349	0.075	0.228	0.035	0.219	0.029	0.063	1.817
CY-32	0.208	0.044	0.113	0.015	0.094	0.012	0.085	1.525

10.1.3 Upper Exposure Surface
Drill Hole PR98-1

	D.f.E.S* (cm)	Lithology
PR98-23	75	Medium to coarse grainstone
PR98-19	23	Magnetite-rich medium to coarse grainstone
PR98-18	12	Medium to coarse grainstone
PR98-17	0	Medium to coarse grainestone, with quartz filled fractures showing replacment by the iron silicates
PR98-16	30	Green silicate and carbonate
PR98-15	35	Iron carbonate and silicate replacing the grainstone
PR98-14	49	Iron silicate replaced medium to coarse grainstone
PR98-13	53	Rip up clasts within medium to coarse grainstone
PR98-10	92	Oncolite and rip up clasts within medium to coarse grainstone
PR98-7	133	Oncolites present in grainstone
PR98-6	160	Brecciated grainstone with oncolite present on top
PR98-5	176	Brecciated grainstone
PR98-3	207	Purple medium to coarse chert grainstone
PR98-11 CEM	70	Medium to coarse chert grainstone
PR98-11 ONC	70	Oncolite present within the chert
PR98-7 CEM	113	Medium to coarse chert grainstone
PR98-7 ONC	113	Onoclite present within the grainstone
PR98-6 LG ONC	140	Large chert and iron oncolite
PR98-6 SM ONC	132	small chert and iron-rich oncolite

*Distance from exposure surface

Major Oxides and Trace Element (wt% and ppm)

	Al_2O_3	CaO	Fe_2O_3	MgO	MnO	Na_2O	P_2O_5	TiO_2
PR98-23	1.202	1.545	30.066	1.124	0.391	0.505	0.057	0.030
PR98-19	0.537	1.971	24.984	0.124	0.051	0.014	0.017	0.029
PR98-18	0.878	0.848	27.503	0.730	0.301	0.247	0.061	0.016
PR98-17	0.300	5.589	16.569	2.594	0.701	0.267	0.016	0.019
PR98-16	0.438	10.433	25.242	5.786	1.899	0.642	0.017	0.009
PR98-15	0.600	23.552	37.843	1.131	0.351	0.082	0.058	0.030
PR98-14	0.123	1.658	7.871	0.926	0.393	0.098	0.010	0.002
PR98-13	0.101	2.465	10.927	0.985	0.335	0.058	0.023	0.003
PR98-10	0.136	0.176	11.771	0.136	0.108	0.040	0.005	0.002
PR98-7	0.163	3.365	14.304	0.968	0.329	0.107	0.011	0.002
PR98-6	0.195	1.036	13.369	0.365	0.157	0.073	0.024	0.004
PR98-5	0.229	0.777	9.369	0.427	0.196	0.108	0.010	0.004
PR98-3	0.071	0.060	3.624	0.031	0.008	0.017	0.019	0.000
PR98-11C	0.034	1.274	3.556	0.618	0.143	0.041	0.001	0.000
PR98-11 ONC	0.520	1.540	4.742	0.075	0.056	0.046	0.013	0.006
PR98-7 CEM	0.070	1.054	10.167	0.258	0.077	0.023	0.005	0.002
PR98-7 ONC	0.181	1.089	22.425	0.280	0.194	0.104	0.024	0.004
PR98-6 SM ONC	0.240	1.794	19.963	0.466	0.339	0.276	0.047	0.003
PR98-6 LG O	0.123	0.747	22.356	0.252	0.224	0.043	0.050	0.004

Major Oxides and Trace elements (wt% and ppm)

	Cr	V
PR98-23	2.360	12.927
PR98-19	0.780	10.767
PR98-18	2.100	19.927
PR98-17	2.640	14.647
PR98-16	5.860	6.207
PR98-15	6.180	5.367
PR98-14	0.000	2.267
PR98-13	1.600	8.307
PR98-10	0.700	4.027
PR98-7	2.160	3.467
PR98-6	0.000	8.267
PR98-5	0.180	3.147
PR98-3	0.000	1.527
PR98-11C	0.000	1.007
PR98-11 ONC	0.000	12.767
PR98-7 CEM	0.440	2.347
PR98-7 ONC	0.400	6.367
PR98-6 LG O	0.460	10.287
PR98-6 SM ONC	0.440	6.547

Rare Earth elements (ppm)

Sample	La	Ce	Pr	Nd	Sm	Eu	Gd	Tb
PR98-23	2.02	12.924	0.503	2.124	0.518	0.158	0.769	0.105
PR98-19	1.681	4.135	0.304	1.033	0.16	0.046	0.205	0.024
PR98-18	2.252	10.266	0.603	2.64	0.627	0.209	0.896	0.124
PR98-17	1.683	4.181	0.432	1.911	0.445	0.129	0.602	0.087
PR98-16	1.12	3.29	0.337	1.722	0.525	0.129	0.876	0.149
PR98-15	0.479	1.606	0.124	0.542	0.146	0.035	0.215	0.033
PR98-14	2.914	7.458	0.559	2.132	0.385	0.092	0.497	0.065
PR98-13	2.369	5.351	0.486	1.746	0.339	0.067	0.419	0.054
PR98-10	0.288	0.854	0.068	0.275	0.072	0.021	0.109	0.017
PR98-7	1.693	5.948	0.519	2.435	0.648	0.148	0.905	0.159
PR98-6	0.876	2.915	0.212	0.92	0.191	0.056	0.264	0.037
PR98-5	3.045	10.492	0.646	2.657	0.506	0.22	0.624	0.076
PR98-3	0.793	1.493	0.142	0.522	0.101	0.031	0.136	0.019
PR98-11 CEM	0.227	0.615	0.055	0.26	0.055	0.02	0.079	0.012
PR98-11 ONC	0.463	1.213	0.092	0.358	0.058	0.016	0.074	0.009
PR98-7 CEM	0.647	2.004	0.167	0.721	0.176	0.055	0.265	0.042
PR98-7 ONC	1.471	4.57	0.378	1.582	0.365	0.111	0.472	0.064
PR98-6 LG ONC	1.798	6.439	0.512	2.293	0.458	0.148	0.604	0.078
PR98-6 SM ONC	3.442	10.654	0.854	3.501	0.722	0.195	0.868	0.114

	Dy	Ho	Er	Tm	Yb	Lu	Mo	U
PR98-23	0.65	0.128	0.394	0.052	0.325	0.044	0.344	0.324
PR98-19	0.129	0.025	0.08	0.01	0.063	0.008	0.757	0.124
PR98-18	0.82	0.185	0.597	0.089	0.578	0.075	0.222	0.028
PR98-17	0.533	0.113	0.352	0.048	0.276	0.038	0.764	0.518
PR98-16	1.046	0.234	0.763	0.108	0.655	0.09	0.206	0.113
PR98-15	0.218	0.048	0.145	0.021	0.133	0.017	0.584	0.134
PR98-14	0.366	0.081	0.239	0.032	0.193	0.021	0.042	0.023
PR98-13	0.309	0.06	0.171	0.023	0.133	0.017	0.520	0.178
PR98-10	0.105	0.022	0.073	0.008	0.053	0.006	0.348	0.101
PR98-7	1.059	0.218	0.608	0.072	0.391	0.046	0.343	0.086
PR98-6	0.223	0.048	0.146	0.02	0.12	0.015	0.438	0.082
PR98-5	0.417	0.085	0.244	0.032	0.196	0.027	0.638	0.088
PR98-3	0.101	0.023	0.062	0.009	0.046	0.007	0.211	0.016
PR98-11 CEM	0.083	0.018	0.049	0.007	0.051	0.006	0.414	0.595
PR98-11 ONC	0.057	0.01	0.032	0.004	0.02	0.003	0.026	0.016
PR98-7 CEM	0.263	0.058	0.189	0.029	0.142	0.019	0.146	0.045
PR98-7 ONC	0.358	0.074	0.226	0.031	0.172	0.022	0.293	0.133
PR98-6 LG ONC	0.425	0.084	0.248	0.031	0.186	0.024	0.237	0.139
PR98-6 SM ONC	0.612	0.124	0.367	0.047	0.255	0.04	0.107	0.149

Mount Whittlesey Outcrop

	Lithology
14-CY-01	Convolute layer comprised of becciated IF clasts and chert cement
14-CY-14	
14-CY-02	Slaty iron formation
14-CY-03	Slaty iron formation
14-CY-04	Grainstone facies
14-CY-05	Medium to coarse grainstone
14-CY-06	Medium to coarse grainstone
14-CY-07	Grainstone lenses
14-CY-08	Parallel laminated sands and muds
14-CY-09	Parallel laminated sands and muds
14-CY-10	Convoluted layer
14-CY-13	Brecciated convolute layer comprised of clasts
14-CY-11	Laminated muds from directly above the convoluted layer
14-CY-12	Coarse grained sands from above the convoluted layer

Major Oxides (wt%)

	Al_2O3	CaO	Fe_2O_3	K_2O	MgO	MnO	Na_2O	P_2O_5
14-CY-01	0.466	0.046	12.680	0.033	0.388	0.680	0.199	0.009
14-CY-14	0.896	0.209	31.590	0.023	2.129	2.634	0.399	0.027
14-CY-02	1.719	0.541	41.455	0.018	3.248	4.341	0.245	0.262
14-CY-03	1.727	0.191	53.150	0.073	3.370	2.385	0.399	0.028
14-CY-04	1.225	0.156	39.167	0.063	1.797	0.577	0.518	0.098
14-CY-05	0.333	0.023	21.396	0.036	0.047	0.130	0.225	0.013
14-CY-06	0.833	0.169	33.220	0.026	1.072	0.219	0.178	0.127
14-CY-07	1.165	0.070	39.110	0.034	1.431	0.101	0.325	0.053
14-CY-08	1.226	0.074	39.482	0.042	1.439	0.104	0.347	0.054
14-CY-09	3.506	0.285	40.225	0.010	5.267	2.167	0.382	0.138
14-CY-10	0.165	0.040	15.834	0.037	0.047	0.057	0.069	0.015
14-CY-13	0.669	0.162	43.657	0.101	0.312	0.066	0.423	0.116
14-CY-11	1.031	0.138	47.746	0.103	0.817	0.066	0.432	0.075
14-CY-12	3.710	0.073	32.190	0.019	5.018	0.800	0.364	0.027

Major Oxide and Trace Element (wt% and ppm)

	TiO$_2$	Cr	V
14-CY-01	0.040	42.493	6.327
14-CY-14	0.080	10.333	22.367
14-CY-02	0.143	9.953	31.407
14-CY-03	0.145	10.213	30.327
14-CY-04	0.073	4.533	29.927
14-CY-05	0.013	1.153	13.027
14-CY-06	0.059	3.213	31.607
14-CY-07	0.068	4.153	26.367
14-CY-08	0.070	3.853	26.987
14-CY-09	0.522	23.233	67.627
14-CY-10	0.022	1.433	8.407
14-CY-13	0.049	4.193	16.987
14-CY-11	0.070	4.153	27.067
14-CY-12	0.393	21.253	67.027

Rare Earth Elements (ppm)

Sample	La	Ce	Pr	Nd	Sm	Eu	Gd	Tb
14-CY-01	0.752	1.206	0.172	0.684	0.146	0.049	0.154	0.024
14-CY-14	1.762	1.303	0.304	1.259	0.253	0.103	0.314	0.046
14-CY-02	2.465	4.735	0.552	2.234	0.439	0.151	0.546	0.083
14-CY-03	1.617	3.515	0.389	1.643	0.371	0.169	0.448	0.075
14-CY-04	0.663	1.444	0.162	0.667	0.151	0.049	0.163	0.025
14-CY-05	0.457	0.68	0.102	0.406	0.083	0.029	0.09	0.013
14-CY-06	1.088	2.195	0.29	1.234	0.265	0.077	0.288	0.041
14-CY-07	0.796	1.89	0.211	0.862	0.18	0.056	0.195	0.025
14-CY-08	0.642	1.545	0.197	0.854	0.186	0.055	0.192	0.026
14-CY-09	3.159	6.962	0.823	3.358	0.729	0.229	0.852	0.135
14-CY-10	0.319	0.728	0.085	0.363	0.077	0.027	0.078	0.012
14-CY-13	0.677	1.41	0.17	0.745	0.173	0.061	0.222	0.034
14-CY-11	0.835	1.873	0.231	1.011	0.234	0.072	0.266	0.039
14-CY-12	2.059	4.802	0.506	2.028	0.422	0.116	0.396	0.054

Rare Earth Elements (cont.)

	Dy	Ho	Er	Tm	Yb	Lu	U	Mo
14-CY-01	0.139	0.027	0.082	0.013	0.087	0.013	0.059	0.042
14-CY-14	0.27	0.053	0.145	0.019	0.114	0.016	0.017	0.012
14-CY-02	0.466	0.095	0.26	0.034	0.184	0.024	0.033	0.048
14-CY-03	0.467	0.096	0.291	0.046	0.297	0.044	0.13	0.066
14-CY-04	0.124	0.021	0.056	0.007	0.048	0.007	0.021	0.04
14-CY-05	0.067	0.012	0.032	0.005	0.03	0.005	0.012	0.052
14-CY-06	0.19	0.032	0.082	0.011	0.067	0.01	0.021	0.152
14-CY-07	0.125	0.019	0.045	0.007	0.04	0.005	0.025	0.131
14-CY-08	0.127	0.019	0.047	0.007	0.048	0.006	0.024	0.097
14-CY-09	0.737	0.145	0.404	0.057	0.369	0.054	0.144	0.163
14-CY-10	0.058	0.01	0.028	0.004	0.024	0.003	0.01	0.107
14-CY-13	0.187	0.036	0.094	0.012	0.074	0.009	0.019	0.142
14-CY-11	0.204	0.036	0.088	0.013	0.068	0.008	0.024	0.203
14-CY-12	0.269	0.048	0.156	0.025	0.174	0.027	0.07	0.16

Mary Ellen Mine Samples

	Ltihology
ME-01	Red digitate stromatolites
ME-02	Digitate stromatolites
ME-03	Digitate stromatolites
ME-04	Stromatolite
ME-05	Stromatolites
ME-06	Stromatolites and brecciated layer
ME-07	Stromatolites and brecciated layer
ME-15	Weathered layer beneath the stomatolites and breccia
ME-16	Weathered layer beneath the stromatolites andbreccia

Major Oxides (wt%)

	Al2O3	CaO	Fe2O3	K2O	MgO	MnO	Na2O	P2O5
ME-01	0.135	0.045	16.024	0.003	0.032	0.013	0.006	0.015
ME-02	0.213	0.273	35.813	0.004	-0.029	0.012	0.027	0.002
ME-03	0.007	0.144	16.168	0.001	-0.056	0.028	0.007	0.000
ME-04	0.021	0.045	16.437	0.009	-0.054	0.016	-0.004	0.005
ME-05	0.026	0.117	12.526	0.033	-0.039	0.108	0.007	0.012
ME-06	0.252	0.009	9.087	0.005	0.011	0.034	0.002	0.008
ME-07	0.093	0.014	24.102	0.009	0.013	0.041	0.010	0.005
ME-15	0.075	0.008	12.507	0.000	0.006	0.028	0.011	0.022
ME-16	0.020	0.010	10.445	0.000	0.006	0.008	0.002	0.013

Major oxides and Trace Elements (wt% and ppm)

	TiO2	Cr	V	Mo	U
ME-01	0.015	0.000	13.520	0.614	0.097
ME-02	0.024	14.173	5.707	0.536	0.490
ME-03	0.006	0.000	3.627	1.044	2.168
ME-04	0.007	0.000	3.067	22.493	0.149
ME-05	0.012	193.973	5.387	0.896	0.120
ME-06	0.036	0.460	9.680	0.479	0.151
ME-07	0.006	0.000	7.680	1.228	0.255
ME-15	0.005	0.000	2.120	0.688	1.689
ME-16	0.002	0.000	1.700	0.357	0.252

Rare Earth Elements (ppm)

Sample	La	Ce	Pr	Nd	Sm	Eu	Gd	Tb
ME-06	6.685	10.987	1.067	3.939	0.61	0.12	0.574	0.077
ME-07	2.659	6.225	0.529	2.057	0.427	0.101	0.457	0.072
ME-15	3.915	11.272	0.997	4.407	0.952	0.294	1.211	0.197
ME-16	1.502	4.684	0.479	2.194	0.528	0.182	0.725	0.111
ME-02B	0.963	4.139	0.292	1.221	0.361	0.082	0.443	0.083
ME-03	4.791	9.396	0.911	3.343	0.563	0.107	0.539	0.078
ME-04	34.121	68.172	5.892	20.64	2.754	0.42	2.264	0.255
ME-05	5.357	12.349	1.09	4.28	0.812	0.215	0.945	0.137
ME-01	11.691	16.683	1.999	7.727	1.161	0.229	1.086	0.133

Sample	Dy	Ho	Er	Tm	Yb	Lu
ME-06	0.379	0.075	0.27	0.046	0.32	0.051
ME-07	0.407	0.081	0.242	0.034	0.207	0.029
ME-15	1.172	0.254	0.763	0.101	0.608	0.081
ME-16	0.692	0.147	0.406	0.054	0.303	0.039
ME-02B	0.506	0.101	0.297	0.048	0.277	0.039
ME-03	0.355	0.074	0.205	0.03	0.175	0.024
ME-04	0.791	0.131	0.339	0.045	0.262	0.036
ME-05	0.76	0.162	0.457	0.065	0.358	0.05
ME-01	0.56	0.103	0.303	0.048	0.317	0.045